Continuous Plastic Flow Synthesis and Characterization of Nanoscale Bioceramics

Aneela Anwar

A thesis submitted to University College London for the degree of Doctor of Philosophy

Supervised by Professor Quentin Pankhurst

2014

Department of Chemistry,
University College London,
20 Gordon Street,
London, WC1H OAJ

Abstract

The development and use of nanoscale biomaterials offer tremendous potential for future medical diagnosis and analysis. Various types of ceramic biomaterials (bioceramics) have been studied intensively for their potential in numerous biomedical applications. Among others, advances in the synthesis and characterisation of calcium phosphate (CaP) bioceramics have contributed much to this field. The growing demand for CaP bioceramics has stimulated research and production of materials suitable for biomedical applications such as implants. Among all the materials presented by the recent technology, only a very small fraction overcome biological and mechanical limitations rendering them suitable for use as a biomaterial. There is, therefore, a need to develop a clean synthesis methodology which could work under mild conditions to allow the synthesis of high purity, nanoscale bioceramic materials with a fine particle size and controlled surface area.

The work in this thesis involves the use of a continuous plastic flow synthesis (CPFS) technology to synthesise various nano-scale bioceramics. Novel CPFS is a single step, continuous synthesis method for a stable, high purity phase-pure nanosized hydroxyapatite and other calcium phosphates at near ambient conditions (20°C to 80°C). The phase-pure HA nanoparticles obtained from this method possess a substantially superior high-temperature stability (1200°C), with remarkably high surface area (up to 264 m^2/g) and the smallest particle size (20 nm) ever reported. These high surface area nanoparticles have a great range of applications for use in replacement of living hard tissues such as bone and teeth, as bone graft substitutes, injectable, coatings on metallic implants, as fillers or additives in commercial products, such as toothpastes; materials for the controlled release of drugs, or other controlled release therapies; reinforcements in biomedical composites, and in bone and dental cements.

Other calcium phosphate phases (Brushite, β-TCP, CDHA and biphasic HA / β-TCP*)* were also obtained by changing the Ca:P ratio and pH of the precursor solutions. A variety of ion substituted calcium phosphates (Mg, Sr, Ba, Zn, Fe, Mn, Si, CO_3^{2-}), nanocomposite materials (Fe_3O_4-HA, TiO_2-HA) and surface modified organopolymer nano-dental composites have also been developed successfully by using CPFS.

Furthermore, the process has the potential to offer high purity calcium phosphates because the reactor components are made of plastic and therefore will not cause contamination of the product with metals. The *in vitro* biocompatibility analysis indicate that these high surface area nano-sized bioceramics have better performance than commercial products and may have the potential to be used for biomedical applications where bone regeneration / replacement is required.

I certify that the research in this thesis is the product of my own work and that any words and figures from the work of other people are fully acknowledged according to standard referencing.

Aneela Anwar

Acknowledgements

I humbly thank Allah Almighty who gave me the strength and conviction to complete this arduous task. Without His blessings, I would have achieved any thing. The sayings of the holy Prophet Hazart Mohammad (peace be upon him) have been a continuous source of inspiration and comfort for me.

First of all, I offer my sincerest gratitude to my supervisor Prof. Pankhurst, who supported me throughout my PhD. I would also like to thank Prof. Jawwad A Darr and Dr. Ihtesham U. Rehman for their help and guidance.

Furthermore, I would like to thank Prof. Ferranti Wong and Dr. Robin M. Delaine-Smith for their collaboration on radiopacity analysis of nanodental composite materials and biological testing. I would also like to express my gratitude to the group members namely Dr. Christopher J. Tighe and Dr. Aqif Chaudhry for their help in calculations and ordering stuff for CPFS reactor. Dr. Rob Palgrave and Dr. Josie Goodall are thanked for their help with XPS analysis. I would like to express my gratitude to all technicians and staff who have helped with a number of aspects of my PhD. Particularly, I would like to thank Dr. Steven Firth, Martin Vickers and Kevin for their help in TEM, XRD and SEM analysis. Islamic Development Bank and University of Engineering and Technology (Lahore) are thanked for granting scholarship and study leave, respectively.

Members and ex-members of CMTG, On Ying, Jessica, Kalyani, Neel, Fahad, Amin, Nadeem, Abdul Samad and Rob are all thanked for their nice suggestions and help regarding research.

Lastly, I offer my regards and blessings to all of those who supported me in any respect during the completion of the project, especially to my husband Fahad Aftab and kids Muhammad Taha and Hadia Fahad, who had been through thick and thin of this wonderful journey.

Thank you

Table of Contents

List of Figures

List of Tables

List of Abbreviations

Abbreviations	Meaning
BET	Brunauer-Emmitt-Teller
Ca:P	Calcium to Phosphorous molar ratio
FTIR	Fourier Transform Infrared Spectroscopy
CMTG	Clean Materials Technology Group
CDHA	Calcium Deficient Hydroxyapatite
TCP	Tricalcium Phosphate
CaP	Calcium Phosphate
CaHA	Calcium Substituted Hdroxyapatite
CO_3-HA	Carbonate Substituted Hdroxyapatite
Si-HA	Silicon Substituted Hdroxyapatite
Sr-HA	Strontium Substituted Hdroxyapatite
Ba-HA	Barium Substituted Hdroxyapatite
DCPD	Dicalcium Phosphate Dihydrate
PVA	Polyvinyl Alcohol
MA	Methacrylic Acid
VPA	VinylPhosphonic Acid
TEGDMA	Triethylene Glycol Dimethacrylate

BisGMA	Bisphenol Glycidyl Methacrylate
Mg-Whitlockite	Magnesium Whitlockite
CPFS	Continuous Plastic Flow Synthesis
DLS	Dynamic light scattering
HA	Hydroxyapatite
XRD	X-Ray Diffraction
SEM	Scanning Electron Microscope
XPS	X-Ray Photoelectron Spectroscopy
TEM	Transmission Electron Microscopy
JCPD	Joint Committee on Powder Diffraction Standards

Chapter 1

Literature Review on Synthesis and Structural Characterization of Bioceramics

There has been a striking advancement in the field of medicine in past few decades owing to life saving and sustaining drugs, materials and instruments. Among these inventions, bioceramics hold a very special prominence. Dr. L.L. Hench (Hench, 1998b) is of the view that vaccines, antibiotics, chemical treatment of water and similar factors have helped in the improvement of general health, but has increased the incidence of age-related decline in human tissue (Hench and Wilson, 1993).

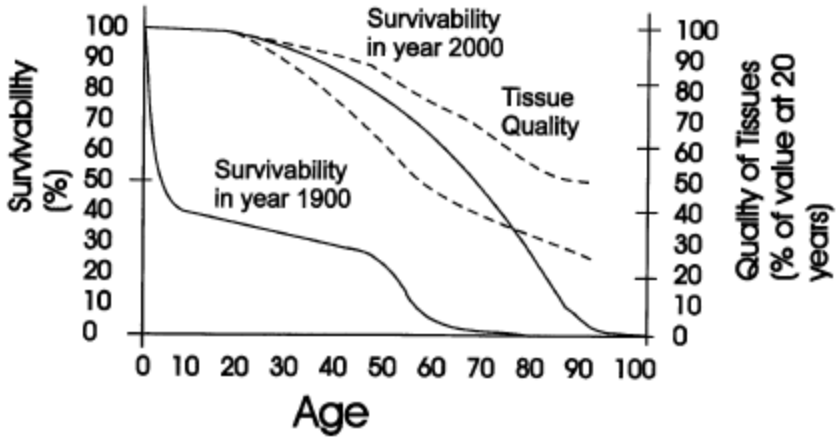

Figure 1-1 Comparison of human survivability in year 1900 vs. 2000 with effects of age on the quality of connective tissue (Hench and Wilson, 1993, Hench, 1998a)

Damaged and fractured body parts have always been problematic but the use of bioceramics in repair, reconstruction, and replacement of diseased body parts has proved vital. Bioceramics need to satisfy a few prerequisites such as good stability, biocompatibility, and biograability (Hench, 1998a). Bioceramic applications rose to prominence as their need in the medical field sparked great deal of research. Hydroxyapatite was researched the most because of its usage in hard tissue replacement [(Hench, 1991, Oonishi et al., 1997, Elliott, 1994, Wu et al., 2004). The reliability of nanomaterials needs to be studied in detail to test their suitability for implementation in human beings, so it is pertinent to introduce the concept of hard tissue biomineralisation

before going over the advancement in the field of bioceramics.

1.1 Introduction to Bones and Teeth

Bone and teeth are naturally occurring biomaterials, which play vital roles in the human body and are termed as hard tissues. Despite wide ranging research, science is still far from producing biomaterials that can entirely substitute the naturally existing materials. Synthetic hydroxyapatite (HA) is a type of calcium phosphate that exhibit similarities to the mineralized mammalian tissues, such as bone and tooth.

1.1.1 Structure, Function and Properties of Bone

Bone is a highly structured porous matrix, composed of nanocrystalline and nonstoichiometric apatite, calcium deficient and carbonated, entangled with collagen fibers and blood vessel (Fratzl et al., 2004, Weiner and Wagner, 1998, Rho et al., 1998). Carbonate-hydroxyapatite, an inorganic nanocrystalline solid, is one of the important compounds of the bone and teeth of all vertebrates and comprises of 65 % of the total bone mass while collagen and water compose 20 and 9 wt% respectively. Additionally, other organic materials, such as proteins, polysaccharides, and lipids are also present in small quantities. Collagen, which forms the organic portion of the bone matrix,, is in the form of small mineral platelets. While rest of the mass is formed by water and organic matter (Weiner and Wagner, 1998). Schematic diagram of this nanocomposite is shown in Figure 1-2.

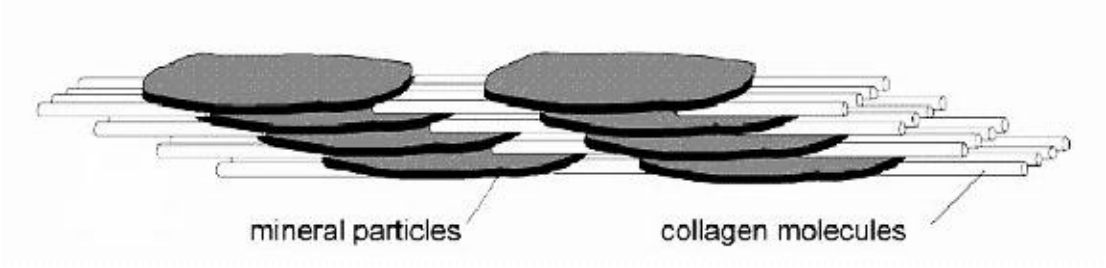

Figure 1-2 Arrangement of mineral particles in collagen fibrils (Fratzl et al., 2004)

The carbonated apatite and organic matrix provide toughness, ability to withstand pressure and elasticity and resistance to stress, bending and fracture (Zaffe, 2005, Hench and Wilson, 1993).

Table 1-1 Composition of human bone (Hench and Wilson, 1993).

Constituent	Bone (wt %)
Calcium, Ca^{2+}	24.5
Phosphorus, P	11.5
Sodium, Na^{+}	0.7
Potassium, K^{+}	0.03
Magnesium, Mg^{2+}	0.55
Carbonate, CO_3^{2-}	5.8
Fluoride, F^{-}	0.02
Chloride, Cl^{-}	0.10
Total inorganic	65.0
Total organic	25.0
Absorbed H_2O	9.7

Bone has a hierarchical structure (Rho et al., 1998, Hench and Wilson, 1993) and is inconsistently dense. The organic-inorganic composite nature of the bone is crucial for different structural arrangements depending on different locations of the skeleton. From the macroscopic point of view, bone can be described into two terms, the outer layer of the bone, cortical or compact bone surrounds a less dense and porous, trabecular or cancellous bone (Figure1-4) which in turn is filled with a jelly tissue called the bone marrow as shown in Figure 1-3 (A).

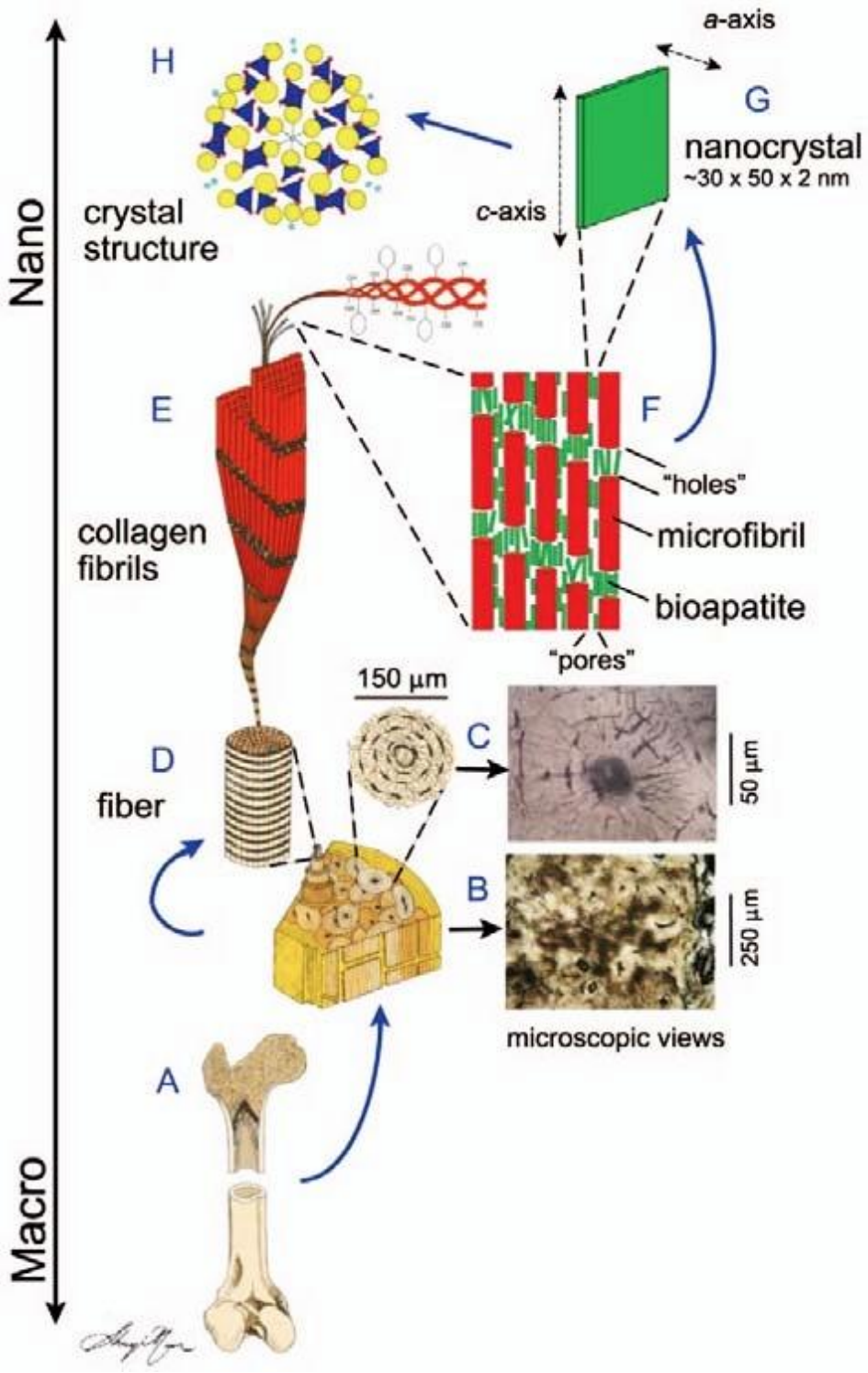

Figure 1-3 Schematic diagram of the hierarchical structure of the bone (Pasteris et al., 2008).

From the microscopic point of view, bone is made up of the basic building blocks called osteons as shown in Figure 1-3 (B, C). Each Osteon consists of lamellae that are formed by bundling fibers, which are built up by numerous collagen fibrils in an array, as indicated in Figure 1-3 (D, E). As represented in Figure 1-3 (G, H), small platelet-like apatite crystals with average dimensions of ~30 × 50 × 2 nm, are fitted in the holes, which are generated by the collagen fibrils with the *c-axis* parallel to the micorfibral long axis (Pasteris et al., 2008, Fratzl et al., 1991, Thompson and Hench, 1998).

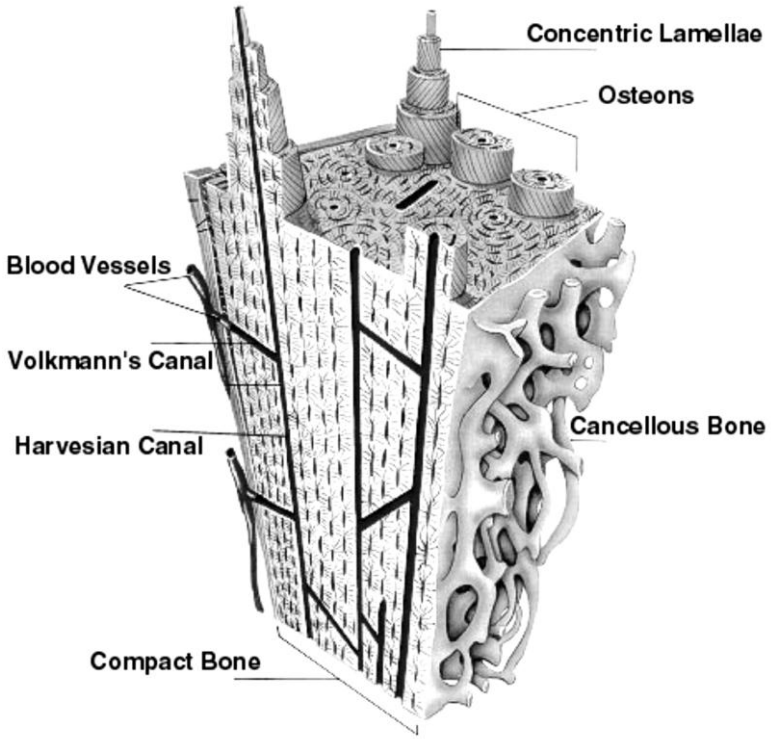

Figure 1-4 Schematic presentation of compact bone cross-section (Martin and Burr, 1989).

1.1.2 Structure, Function and Properties of Teeth

Tooth is a bone like hard tissue. It consists of two parts, the crown and the root (Figure 1-5). The root is covered by a layer of cementum, attached to the bone by periodontal membrane (a layer of fibrous connective tissue). Enamel and dentine form the main two parts of the crown. Enamel is the hardest substance in the body and 97 % (w/w) of which consists of relatively large HA crystals (25 nm thick, 40-120 nm wide, and 160-1000 nm long) and the remaining part organic substances and water (Waters, 1979).

Dentine is the mineralized tissue similar in composition to regular compact bone (Zioupos and Rogers, 2006, Suchanek and Yoshimura, 1998, Pasteris et al., 2008).

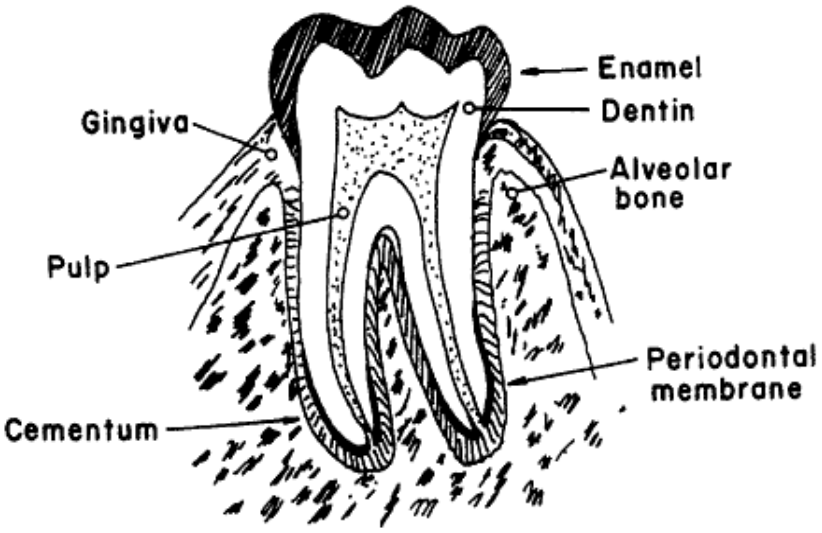

Figure 1-5 Schematic diagram of a tooth (Jones, 2001)

1.2 Types of Bioceramics

Bioceramics are specifically formulated for reconstruction of damaged sections of the skeletal system due to their ability to form a stable interface with surrounding tissues and preform as efficiently as the natural tissue (Hench and Wilson, 1993). In general, bioceramics can be described according to the tissues response in three terms. These are bioinert, bioactive and bioresorbable. Table 1-2 summarized the implant-tissue response of each type of bioceramics.

Bioceramics offer more advantages in terms of biocompatibility, therefore, their application as reinforcements in biomedical composites, polymeric matrices and osteoinductive coatings on metallic implants leads to materials with enhanced biocompatibility. A huge number of clinical applications of bioceramics in the human body (Hench and Wilson, 1993) are summarized in Figure 1-6

Table 1-2 Consequences of implant tissue interactions (Hench and Wilson, 1993) .

Implant-tissue reaction	Consequence	Example
Bioinert	Tissues form a non-adherent fibrous capsule around the implant	Alumina (Al_2O_3), Zirconia (Zro_2) and Carbon
Bioactive	Tissues form an interfacial bond with the implant	Hydroxyapatite, Bioglass, A-W glass
Bioresorable	Tissues replace implant	β-tricalcium phosphate, carbonated hydroxyapatite, calcium carbonate

1.2.1 Bioinert Bioceramics

The term bioinert refers to any material that has minimal interaction with its surrounding tissues post-implantation. This type of bioceramic shows little chemical reactivity, even after long term of exposure to the physiological environment, and therefore forms minimal interfacial bonds with the living tissues (Hench, 1993). Some examples of these bioceramics are stainless steel, zirconia, titanium, alumina and high molecular weight polyethylene. Zirconia and alumina have a great range of applications because of their remarkable corrosion resistance property, high hardness and low friction coefficient properties. Alumina has also been used in dental implantation and for orthopedic products recently (Hench, 1991, Heness and Ben-Nissan, 2004).

1.2.2 Bioactive Bioceramics

Bioactive ceramics are materials, which have the ability to interact with the surrounding tissue or bone upon placement within the human body (Heness and Ben-Nissan, 2004). Upon implantation, surface-reactive ceramics form strong bonds with the closest tissue. The surface reactive implants respond to local pH changes by releasing Ca^{2+}, Na^{+} and K^{+} ions and lead to bonding of tissues at the interfaces. The most common ceramics used are hydroxyapatite (HA) 45S5 Bioglass (Cao and Hench, 1996).

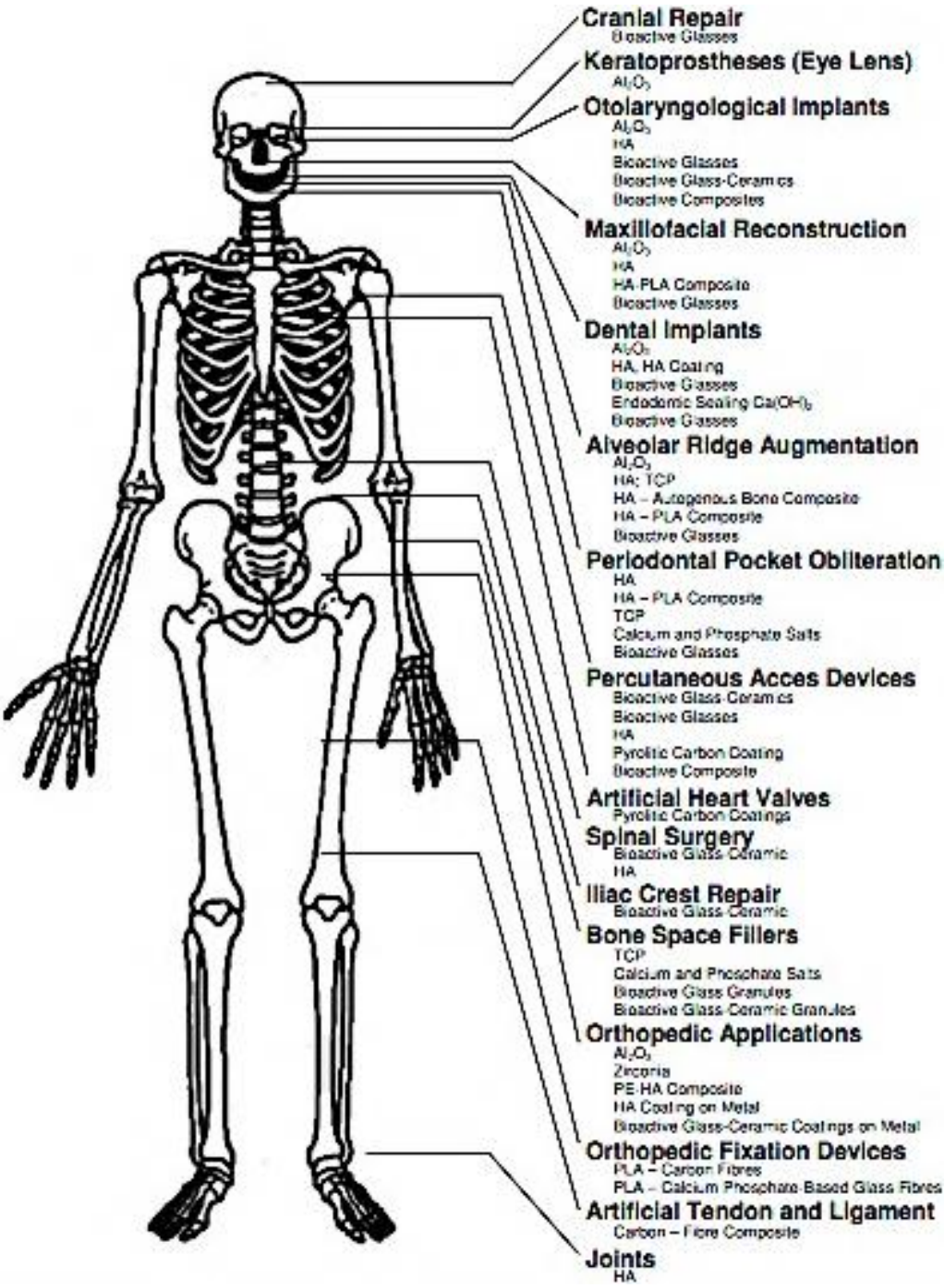

Figure 1-6 Clinical uses of bioceramics (Hench and Wilson, 1993).

1.2.3 Bioresorbable Bioceramics

Bioresorbable refers to a material that has the ability to controllably degrade or dissolve once placed in the body and if required it can gradually be replaced by advancing tissue or bone. In other words, resorbable implants are designed to degrade gradually with time and be replaced with natural tissues (Hench and Wilson, 1993). The rate of degradation varies from one material to another. The advantage of this implant is that it will be replaced by normal, functional bone thus eliminating any long-term biocompatibility problems.

However, during the remodeling process, the load bearing capacity of the implant could possibly be weakened and result in mechanical failure. Therefore, the resorption rates of the material should be matched with the repair rates of body tissues (Hench, 1993). Common examples are tricalcium phosphate, calcium carbonate, gypsum and polylactic-polyglycolic acid copolymers.

1.3 Examples of Bioceramics

1.3.1 Alumina (Al_2O_3), Zirconia (ZrO_2) and Titania (TiO_2)

Alumina is now being widely used in hip prostheses and dental implants. Alumina had already been used extensively as a bioceramic clinically (Thamaraiselvi and Rajeswari, 2004). Alumina exhibits the characteristics, like biocompatibility, high strength, high wear resistance, and high corrosion that make it valuable to the bioceramic industry (Hench, 1998a, Katti, 2004, Hench, 1998b).

Zirconia has great mechanical strength because of its transformation toughening behaviour. In its pure state, zirconia cannot be used in medical applications as the sintering process causes phase transformation, from tetragonal to monoclinic, that takes place during the cooling phase above room temperature (Manicone et al., 2007). This phase transformation, which is associated with a 3-4% volume expansion, engenders internal material stresses and cracks (Marti, 2000, Chevalier, 2006).

Another bioinert bioceramic with excellent biocompatibility is titania (Fidancevska et al., 2007). Different nanostructured porous titania-based devices deliver antiepileptic drugs straight to the central nervous system through the temporal lobe of the human brain

(López et al., 2007). Titania is used in plasma-sprayed bioceramic coatings on Ti-6Al-4V hip endoprostheses and other metallic implants. A bioactive interface is needed for a strong interaction between the implant and tissue. This is a problem found in bioinert bioceramics (Kurzweg et al., 1998, Hench, 2000).

1.3.2 Bioactive Glasses and Glass-Ceramics

Traditionally, bioactive glasses and glass-ceramics are manufactured with SiO_2, Na_2O, CaO and P_2O_5 as base components at high temperature, followed by melting, casting and sintering. Mostly, bioactive glasses, such as SiO_2, are prepared with the 45S5 formula containing 45% SiO_2 (Chen et al., 2006). Glasses with greater quantities of P_2O_5 do not bond with bone. The compositional dependence of bone and soft tissue bonding of bioactive glasses and glass ceramics has been shown in Figure 1-7.

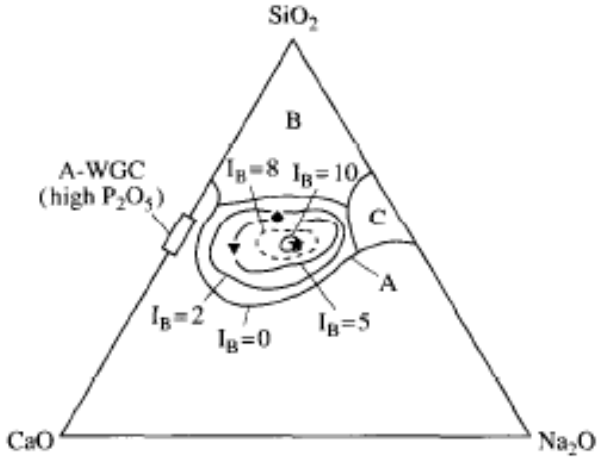

Figure 1-7 Compositional dependence of bone bonding and soft-tissue bonding of bioactive glasses and glass ceramics (Hench, 1991).

As shown in Figure 1-7, glasses in region A are bioactive and bond with bone. In region B, Glasses are inert and result in the formation of a fibrous capsule at the implant-tissue interface. Region C shows glasses, which are resorbed within 10-30 days in tissue. I_B lines represent the index of bioactivity. Depending on composition, therefore, certain glasses are resorbable. The region inside the dashed lines shows compositions which can even bond to soft tissue. The poor mechanical properties of monophase bioglasses inhibit clinical applications (Cao and Hench, 1996).

Bioactive glasses and glass ceramics have been used to replace small damaged bones of the middle ear for more than ten years now. 45S5 bioglass was used to preserve the jawbone of patients who had their teeth extracted prior to being fitted with dentures (Hench and Wilson, 1993).

1.3.3 Calcium Phosphate Ceramics

Calcium phosphates are most widely used bioceramics for implants mainly due to their resemblance to bone mineral in chemical composition and their ability to form strong chemical, physical and biological bonds with the tissue interface. They are well known for their use as bone graft substitutes, coatings on metallic implants, gene therapy, reinforcements in biomedical composites and bone, and as components in dental cements (Elliott, 1994, Hench, 1991).

In 1920, calcium phosphate ceramics were used successfully for bone repair applications in clinical surgery (Albee, 1920). The serious efforts towards the development and commercialisation of calcium phosphates, particularly hydroxyapatite, were made in early 1980s. It is interesting to note that, the lower the Ca:P molar ratio, the more acidic and water soluble the calcium phosphate is, due to the solubility criteria and the kinetics of precipitate formation and transformation (Elliott, 1994). The dissolution and reactions of calcium phosphate bioceramics (*in vivo* and *in vitro*) were found to be largely dependent on the composition, nature of precursors and crystallinity (Aoki, 1991, Hench, 1998b). Variations in pH alter the relative concentrations of the four polymorphs of orthophosphoric acid (Figure 1-8) and thus both the chemical composition and the amount of calcium orthophosphate that forms by direct precipitation (Lynn and Bonfield, 2005).

Hydroxyapatite (HA) and tricalcium phosphate (TCP) are amongst the most common calcium phosphates. Synthetic HA is bioactive and similar to biological apatite, the main mineral constituent of teeth and bone, because of its biocompatibility, bioactivity and low solubility in wet media. Such bioceramics have been employed as scaffold materials to encourage new bone formation for osteoinductive coatings on metal implants and as a bulking agent for bone fillers (Hench, 1991, Hench, 2000, Katti, 2004). In contrast, beta-tricalcium phosphate, β-TCP, [$Ca_3(PO_4)_2$], another bioceramic, has a high dissolution rate compared to HA in vivo (Kannan et al., 2005, Famery et al., 1994).

The use of biphasic calcium phosphate ceramics composed of HA and β-TCP mixtures for bone grafts can assist rapid bone formation around the implant site compared to HA alone (Pan et al., 2003, Ginebra et al., 2004). Calcium deficient hydroxyapatite (CDHA) has also gained importance as a component in injectable bone cements; regulating particle properties is often used to affect cement setting behaviour (Hutchens et al., 2006). In recent studies, brushite ($CaHPO_4.2H_2O$) bioceramic has been considered as a potential bone substitute material and raised great interest because of its high resorbability (Theiss et al., 2005, Bohner, 2000). An important characteristic of brushite is its use as a precursor for synthesizing HA (Ferreira et al., 2003).

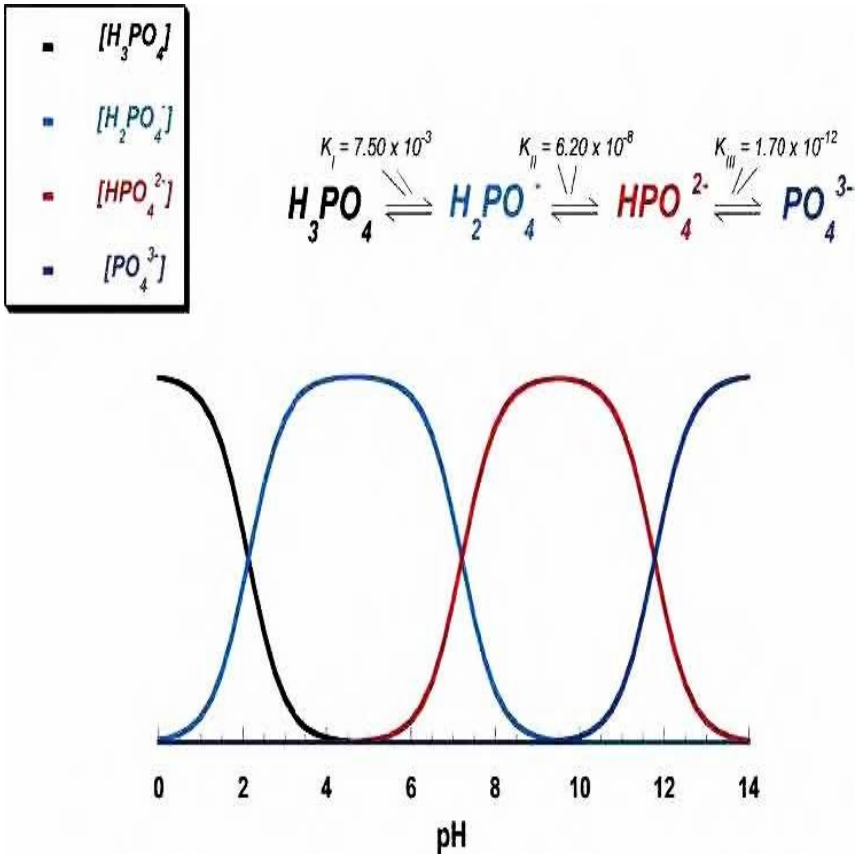

Figure 1-8 pH variation of ionic concentration for phosphoric acids solutions (Lynn and Bonfield, 2005).

Ca/P ionic ratio	Compound	Chemical formula	Solubility at 25 °C, -log (K_s)	pH stability range in aqueous solutions at 25 °C
0.5	Monocalcium phosphate monohydrate (MCPM)	$Ca(H_2PO_4)_2.H_2O$	1.14	0.0 – 2.0
0.5	Monocalcium phosphate anhydrous (MCPA)	$Ca(H_2PO_4)_2$	1.14	[c]
1.0	Dicalcium phosphate dehydrate (DCPD), mineral brushite	$CaHPO_4.2H_2O$	6.59	2.0 – 6.0
1.0	Dicalcium phosphate anhydrous (DCPA), mineral monetite	$CaHPO_4$	6.90	[c]
1.33	Octacalcium phosphate (OCP)	$Ca_8(HPO_4)_2(PO_4)_4.5H_2O$	96.6	5.5 – 7.0
1.5	α-Tricalcium phosphate (α-TCP)	α-$Ca_3(PO_4)_2$	25.5	[a]
1.5	β-Tricalcium phosphate (β-TCP)	β-$Ca_3(PO_4)_2$	28.9	[a]
1.2 – 2.2	Amorphous calcium phosphate (ACP)	$Ca_xH_y(PO_4)_z.nH_2O$, n = 3 – 4.5; 15 – 20% H_2O	[b]	~ 5 – 12
1.5 – 1.67	Calcium – deficient hydroxyapatite (CDHA)[e]	$Ca_{10-x}(HPO_4)_x(PO_4)_{6-x}(OH)_{2-x}$ (0<x<1)	~ 85.1	6.5 – 9.5
1.67	Hydroxyapatite (HAp)	$Ca_{10}(PO_4)_6(OH)_2$	116.8	9.5 – 12
1.67	Fluorapatite (FAp)	$Ca_{10}(PO_4)_6F_2$	120.0	7 – 12
2.0	Tetracalcium phosphate (TTCP), mineral hilgenstockite	$Ca_4(PO_4)_2O$	38 - 44	[a]

[a] These compounds cannot be precipitated from aqueous solutions.
[b] Cannot be measured precisely. However, the following values were found: 25.7 ± 0.1 (pH = 7.40), 29.9 ± 0.1 (pH = 6.00), 32.7 ± 0.1 (pH = 5.28).
[c] Stable at temperatures above 100 °C.
[d] Always metastable.
[e] Occasionally, CDHA is named as precipitated HAp.

Table 1-3 Calcium orthophosphates and their major properties reproduced from Dorozhkin (Dorozhkin, 2009).

1.4 Hydroxyapatite (HA)

Hydroxyapatite [$Ca_{10}(PO_4)_6(OH)_2$] is the most widely used synthetic calcium phosphate (Figure 1-10) for implant fabrication as it is most similar material to the mineral component of bone and has the capability to promote bone regeneration. In recent years, it has attracted much attention because of its biocompatibility, bioactivity and low solubility in wet media (Hench, 2000, Cao and Hench, 1996, Oonishi, 1991)

1.4.1 Structure of Hydroxyapatite

Slightly non-stoichiometric HA has hexagonal symmetry (S.G P63/m) and lattice parameters that are a = 0.95 nm and c = 0.68 nm (Elliott, 1994), whilst stoichiometric HA is monoclinic with $P2_1/b$ space group. The smallest building unit, known as the unit cell, contains a complete representation of HA hexagonal crystal (Sarig, 2004) as shown in Figure 1-9..

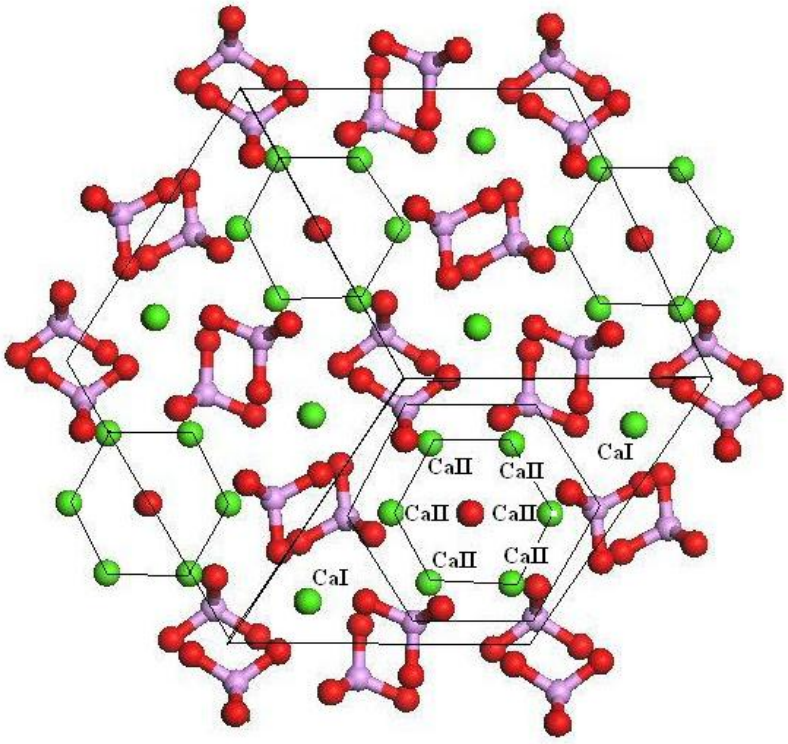

Figure 1-9 Hydroxyapatite structure viewed onto the (0001) surface (Ca = green, O = red, P = purple, H = white) (Narasaraju and Phebe, 1996)

Four calcium (Ca I) ions in the unit cell are generally labeled as columnar calcium as they form single atomic columns perpendicular to the basal plane. Six of the ten calcium ions (Ca II) in the unit cell form hexagonal channels along the *c-direction* of the structure. Each unit cell is based on four OH groups, available in each channel, leading to a 0.5 partial occupancy of each position as shown in Fig. 1-9.

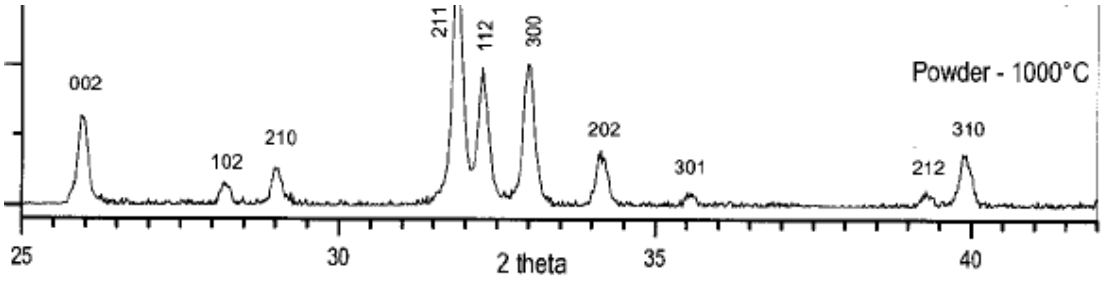

Figure 1-10 XRD pattern of stoichiometric HA powder

1.4.2 Substitutions into Hydroxyapatite

The biological and physiochemical properties of HA can be enhanced by ionic substitutions, some of which are usually present in natural bone apatite. Most natural apatites are non-stoichiometric because of the presence of minor constituents such as metal cations (Mg^{2+}, Mn^{2+}, Zn^{2+}, Na^{+}, Sr^{2+}) or anions (HPO_4^{2-} or CO_3^{2-}). HA is capable of accommodating substitute ions within its lattice. Trace ions substituted in apatites can have a dramatic effect on crystal structure parameters, crystallinity, dissolution kinetics as well as influence the biological response in the final applications (Miao et al., 2005). As a consequence, synthesis of substituted HA has drawn much attention, as substituted HA can show desirable properties and satisfy variety of needs in a wide range of applications (LeGeros, 1990, de Groot, 1983).

1.4.2.1 Carbonate SubstitutionCarbonate Substitution

The carbonate content in human bone is about 8 wt% (Rey et al., 1991)and it depends on the age of the individual (Burnell et al., 1980, Ito et al., 1997). Different levels of substitution can occur for both the hydroxyl and the phosphate ions, giving rise to A-type and B-type substitution, respectively. In 1963, Kuhl and Nebergall suggested the following formula for B-type carbonate-substituted HA (Murugan and Ramakrishna, 2006, Chaudhry et al., 2013).

$$Ca_{10-x+y}(CO_3)_x(PO_4)_{6-x}(OH)_{2-x+2y}$$

B-type substitution is preferred for carbonate as it is found naturally in the bone of a variety of species, with the A/B type ratio in the range 0.7–0.9 (Li et al., 2012, Redey et al., 2000). A higher value of the A/B ratio has been observed in older hard tissues.

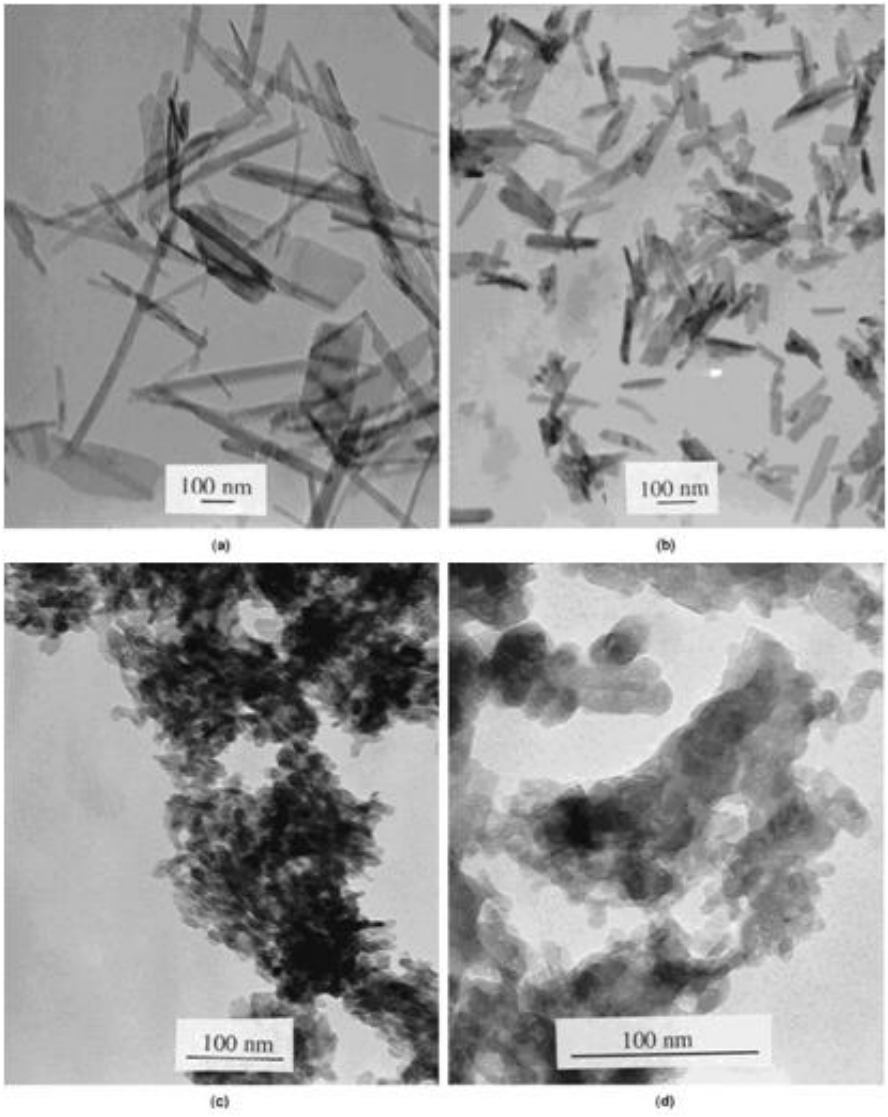

Figure 1-11 TEM micrographs of AB-type CO_3^{2-} apatite with different bicarbonate concentration at 70 °C: (a) 10 mM, (b) 40 mM, (c) 160 mM, and (d) 320 mM (Barralet et al., 1998).

The synthesis of AB-type CO_3^{2-} apatite samples were also investigated by *Barralet and co-workers*, who used different reagents, tri-ammonium orthophosphate, calcium nitrate 4-hydrate, and sodium bicarbonate by using a precipitation method. They observed that with increased bicarbonate concentration from 10 to 160 mM, the apatite crystallite size was slightly decreased, and the morphology of the apatite was changed from needle shape into more spheroidal particles (Barralet et al., 1998) as shown in Figure 1-11.

1.4.2.2 Silicon Substitution

Silicon-substituted HA (Si-HA) has been reported to promote rapid bone mineralization, however, it also leads to a smaller crystallite size and faster dissolution (Thian et al., 2006b, Porter et al., 2003). Many literature reports have shown that with incorporation of Si into HA did not induce direct changes in the crystallographic structure, as same XRD patterns were observed in the HA samples with different Si substitution, ranging from 0 to 1.5 wt% (Botelho et al., 2006). Silicon-substituted HA has been synthesized using wet-precipitation and batch hydrothermal techniques. For example, Gibson et al. produced phase pure Si-HA by an aqueous precipitation of a calcium containing solution and a phosphate containing solution at high pH by using Si acetate as the source of silicate ions (Gibson et al., 1999).

There have also been many reports on the development of silicon- substituted HA coatings on metallic substrates for enhanced osseointegration. Silicon enters the HA lattice in the form of silicate ions which substitute phosphate ions. Silicon levels up to 4 wt% in HA have been identified using a batch hydrothermal process (Patel et al., 2002, Kim et al., 2003, Hing et al., 2006, Leventouri et al., 2003, Thian et al., 2006a, Thian et al., 2007).

Tang and co-workers reported that Si-HA samples with Si substitution ranging from 0 to 4 wt% were prepared by using $Ca(NO_3)_2{\cdot}4H_2O$, $(NH_4)_3PO_4$, and $Si(OCH_2CH_3)_4$ (TEOS) via hydrothermal method. As observed in Figure 1-12, *Tang and co-workers* noticed that the mean crystallite size of apatite was decreased with the content of Tetra ethyl orthosilicate, while the numbers of the need-like apatite crystals were increased (Tang et al., 2005).

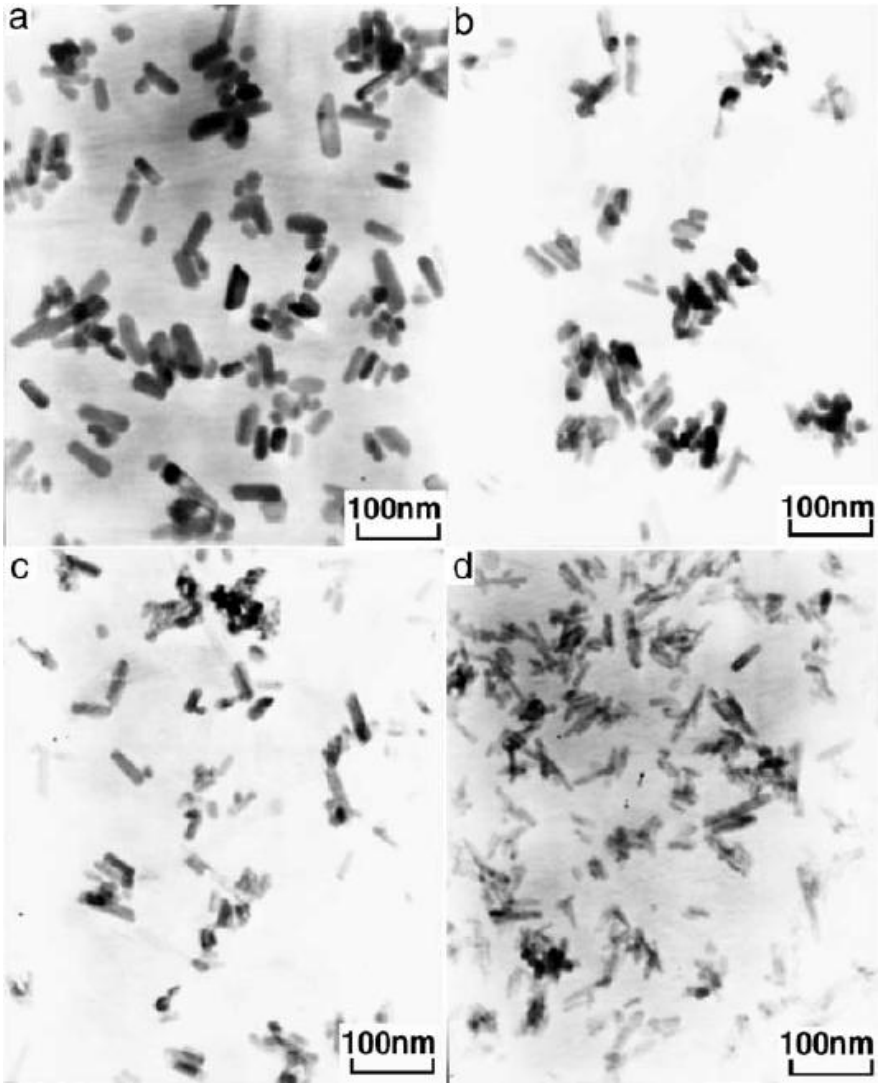

Figure 1-12 TEM micrographs of four Si-HA samples with different Si concentration: (a) HA, (b) HA with 0.8 wt% Si, (c) HA with 1.5 wt% Si, (d) HA with 4 wt% Si (Tang et al., 2005).

1.4.2.3 Magnesium Substitution

Magnesium (Mg^{2+}) is a divalent cationic substitute for calcium (Ca^{2+}) in the HA lattice. Such substitution often inhibits crystallization, increases solubility, and lowers the temperature at which conversion of HA into β-TCP occurs which possibly related to the smaller Mg cation with radius (0.65 Å) substituted larger cation of Ca (0.99 Å) in the HA structure (Suchanek et al., 2004b, Wu et al., 2005, Bertoni et al., 1998, Suchanek et al., 2004a, Chaudhry et al., 2008, Bigi et al., 1993). Yasukawa and co-workers reported various effect of Mg on the crystallite size of apatite and prepared Mg-HA solid solutions with Mg/Ca molar ratio ranging from 0 to 0.5 by wet method,

using the reagents of $Mg(NO_3)_2 \cdot 6H_2O$, $Ca(OH)_2$, and H_3PO_4. They observed that the crystallite size of apatite increased with increasing Mg/Ca ratio from 0 to 0.31 (Yasukawa et al., 1996). When the ratio reached 0.38, amorphous morphology was observed as shown in Figure 1-13.

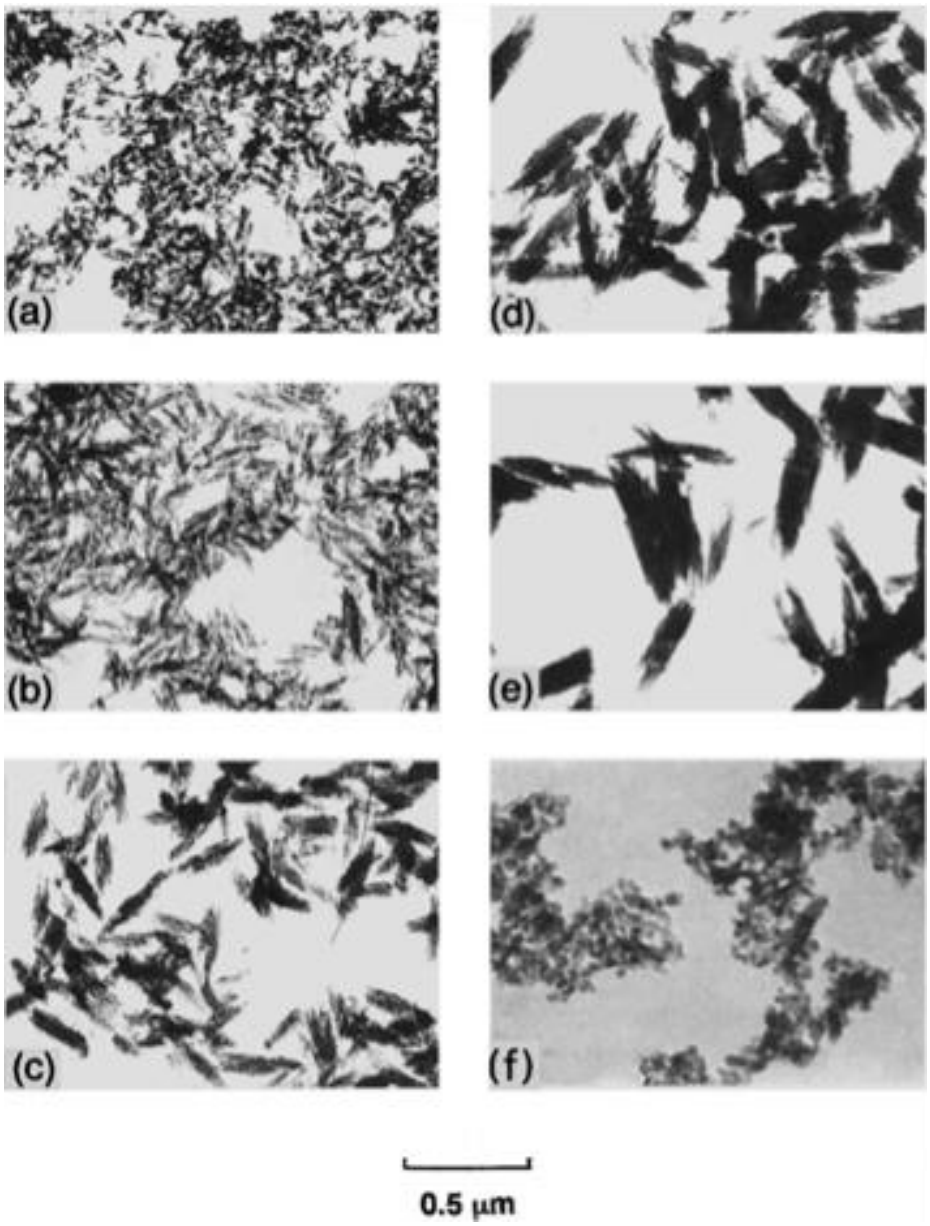

Figure 1-13 TEM images of Mg-HA samples with different Mg content: (a) 0, (b) 0.09 mol %, (c) 0.16, (d) 0. 23, (e) 0.31, (f) 0.38 (Yasukawa et al., 1996).

Fadeev and co-workers synthesized Mg substituted HA samples using wet precipitation methods with chemical formula $Ca_{10-x}Mg_x(PO_4)_6(OH)_2$, where NH_4OH was used to adjusted pH of the solution. They also found that Mg exhibited destabilizing effect on the apatite structure, since the transition temperature from hydroxyapatite to whitlockite decreased with increasing Mg substitution from 1 to 10 atom % (Fadeev et al., 2003).

1.4.2.4 Strontium Substitution

Strontium is present in the mineral phase of bone and connective tissue at levels of 320-400 mg of strontium. Unlike the trace elements of Zn, and Mg, the synthesis of phase pure apatite can be achieved with the incorporation of Sr substitution in the whole range of compositions (Bigi et al., 2007). It was reported that the larger cation Sr^{2+} (1.18 Å) substituted in the HA structure for the smaller Ca^{2+} (1.00 Å) cation. Due to the size difference between these two cations, modification of the lattice parameters of HA were therefore expected (O'Donnell et al., 2008, Li et al., 2007). Clinically, strontium has been observed to confer beneficial effects on bone growth especially at the regions where high metabolic turn-over occurs (McEwan, 1997). In vitro, strontium increases the number of osteoblast cells followed by the reduction osteoclast cells, whereas strontium administration decreases bone resorption and stimulates bone formation (Canalis et al., 1996, Dahl et al., 2001, Grynpas et al., 1996).

Bigi and co-workers reported variations in crystallite size with Sr substitution. They prepared a group of Sr-HA samples using $Ca(NO_3)_2{\cdot}4H_2O$, $Sr(NO_3)_2$, and $(NH_4)_2HPO_4$ via a coprecipitation method. They observed that with increased Sr substitution from 0 to 100 %, a systematic changes of the crystallite size and crystallinity of the Sr-HA samples were evident in TEM images, as shown in figure 18 (Bigi et al., 2007).

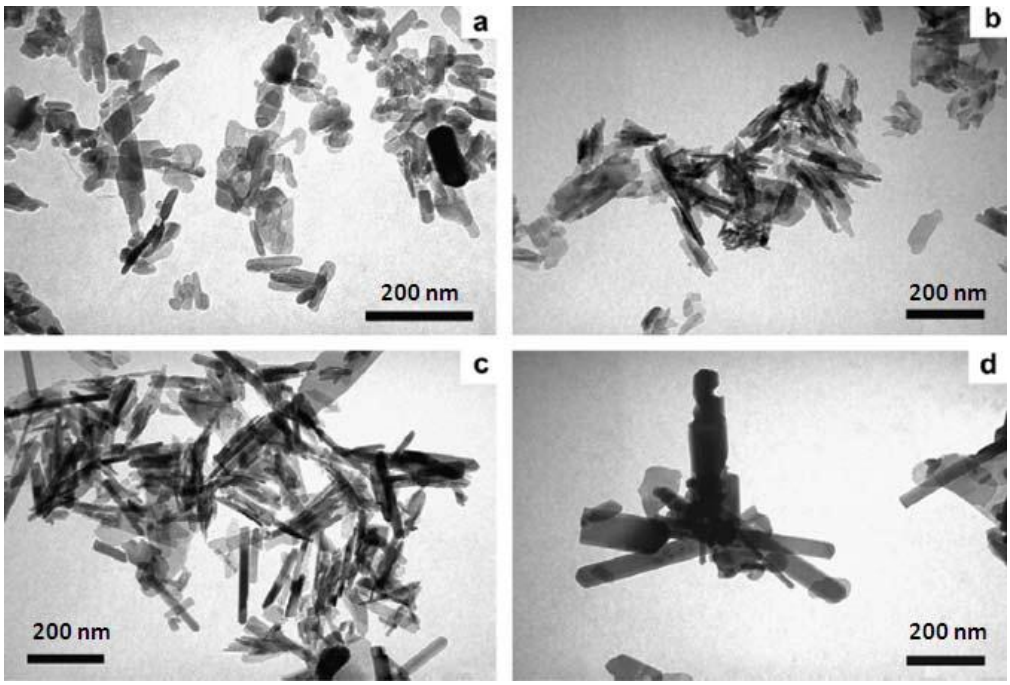

Figure 1-14 [a-d] TEM images of Sr-HA samples with different Sr concentration: (a) HA, (b) HA with 20 % Sr, (c) HA with 70 % Sr, (d) HA with 100 % Sr (Bigi et al., 2007).

As indicated by figure 1-14, that the HA sample contained 0% Sr substitution exhibited plate-like crystals, while with 20 % Sr substitution, ill-defined apatite shapes were observed in Figure 1-14 (b). It was observed that by increasing Sr substitution to 70 % or higher, the apatite crystallite size was increased. When the Sr substitution reached 100 %, fully Sr substituted elongated apatite crystals were observed (Bigi et al., 2007).

1.4.3 Surface Functionalization

Surface properties of hydroxyapatite (HA) play an important role in its applications, as its surface is in direct contact with the body fluids once placed inside a body. Surface modified HA has gained much attention from researchers in recent years. Surface modified groups are commonly employed to avoid agglomeration of nanoparticles and give controlled particle growth. These functional groups make the surface more suitable to the host tissue in biomedical applications. (Lu et al., 2007, Arcís et al., 2002).

Surface functionalization of HA by organic molecules or polymers provides an efficient way to control the surface properties of HA. There are two common methods

to modify the HA surface by organic molecules. The first approach is surface adsorption as many polymers and proteins can be formally adsorbed onto the surface of HA (Hlady and Füredi-Milhofer, 1979). Secondly, grafting of organic molecules through covalent bonding to the hydroxyl groups, which are available on the crystal surface of HA. These surface grafted nanoparticles including methyl methacrylate, vinylphosphonic acid, polyethylene, and polyurethane have great range of applications in the field of HA/polymer composites, column chromatography of protein, cell culture carrier and carriers of catalysts in chemical engineering(Schaad et al., 1994, Haque et al., 2007, Puvvada et al., 2010).

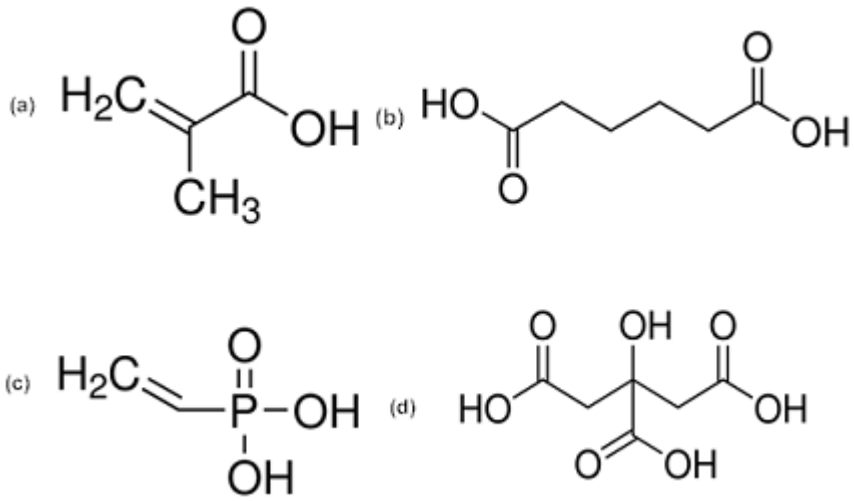

Figure 1-15 Coupling agents used hydroxyapatite and other phosphate grafting: (a) methacrylic acid, (b) adipic acid, (c) vinylphosphonic acid, (d) citric acid.

1.4.4 Nano-biocomposites

Hydroxyapatite has been widely used as a bioactive filler component phase in nanocomposites, particularly in dental applications. Numerous HA-polymer based nano-biocomposites have been produced to enhance the mechanical and biological properties of bone. Chemical coupling of a polymer matrix with HA and creating reactive sites on the surface of inorganic filler particles can improve the interfacial bonding of a composite. (Arcís et al., 2002, Willems et al., 1992). Dental resin with HA particles as a filler component, is considered to be a potential restorative material for non-load bearing human tooth tissues. Dental composites are mainly based on an organic polymer matrix (BisGMA and TEGDMA) in Figure 1-16, coupling agents,

inorganic filler particles and initiators. Liang Chen and coworkers reported that impregnating a small fraction of HA (5-10 wt%) into BisGMA/TEGDMA dental resins can significantly enhance the biaxial flexural strength of the resulting composite (Saito et al., 1994, Chen et al., 2011).

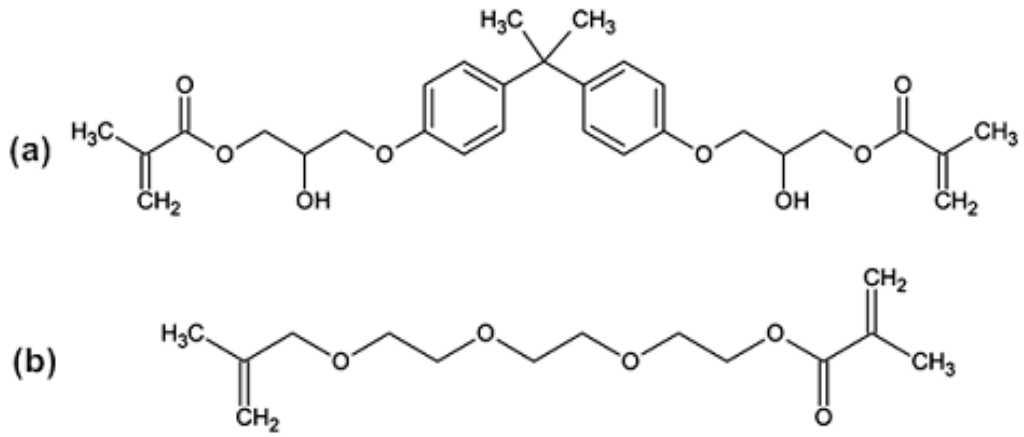

Figure 1-16 Bisphenol glycidyl methacrylate (BisGMA) and triethylene glycol dimethacrylate (TEGDMA).

1.4.5 Synthesis of Hydroxyapatite

Multiple techniques have been used for the preparation of HA including solid state synthesis (Güler et al., 2011), coprecipitation methods (Afshar et al., 2003), sol gel techniques (Hench and West, 1990), emulsion synthesis (Kimura, 2007) and batch hydrothermal synthesis (Manafi and Joughehdoust, 2009). More recently, the authors pioneered the continuous hydrothermal flow synthesis (CHFS) (Zhang et al., 2010, Chaudhry et al., 2008, Chaudhry et al., 2006) of bioceramics containing HA or its doped phases under supercritical conditions of high temperature and pressure.

1.4.5.1 Solid-State Reactions

The solid state route is the high temperature synthesis of hydroxyapatite using solid precursors of calcium and phosphate. Synthesis of hydroxyapatite using calcium nitrate and tri-sodium phosphate by heating in microwave oven was reported by Cao and co-workers (Cao et al., 2005). In this method, the stoichiometric ratio of solid calcium and phosphate precursors were mixed in a ball mill followed by a heat-

treatment step under suitable temperature and pressure. A spherical morphology of synthesized HA particles were observed after a short heating time of 0.5 minutes which changed into nano-rods upon continuous heating for one minute as shown in Figure 1-175.

Mechanochemical methods are also considered as solid state routes wherein, mechanical mixing leads to chemical reactions. Chemical reactions occur due to favorable temperature and pressure. The time required to synthesize HA varies from a few hours to 60 hours. After initial mixing, powder mixture may require a heat treatment step to transform into phase pure HA. This heat treatment results in lower surface area hydroxyapatite as reported by Chen and coworkers had saw a reduction in surface area from 175 m^2g^{-1} for as synthesized HA to 7.2 m^2g^{-1} after heat treatment at 900 ˚C for one hour (Chen et al., 2004). Ion substituted hydroxyapatite powders have also been synthesized using similar methods (Getman et al., 2004).

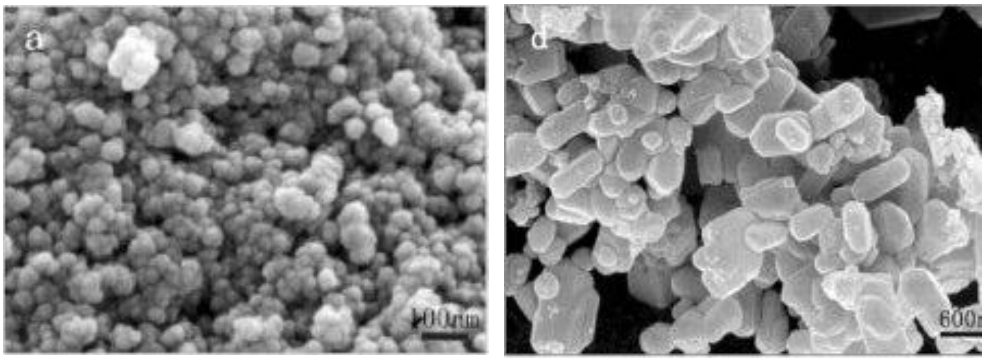

Figure 1-17 FE-SEM image of HA nanoparticles prepared by (a) microwave heating with 15 second intervals for 0.5 minutes (b) continuous microwave heating for 1 minute (Cao et al., 2005).

1.4.5.2 Co-precipitation Method

Co-precipitation is one of the oldest methods used for the synthesis of HA nanoparticles. These reactions usually involve a mixture of soluble calcium and phosphorous sources and the addition of base to result in precipitation of crystalline HA (Haque et al., 2007). Hence co-precipitation refers to the simultaneous occurrence of nucleation, growth and agglomeration processes. In these types of reactions, sparingly soluble products are generally formed under high super saturation. As a result, a large number of small particles are formed by nucleation (a major step in this reaction).

This is followed by the second step of Ostwald ripening (consumption of smaller particles by larger ones) and aggregation, which largely affects the size, morphology and properties of the final obtained particles. The product size, morphology and particle size distribution are mainly influenced by reaction conditions like mixing rate, rate of reactant addition, concentration, temperature and stirring rate (Cushing et al., 2004). Typical calcium ion sources include calcium nitrate [$Ca(NO_{3)2}$], calcium chloride [$CaCl_2$] and calcium hydroxide [$Ca(OH)_2$]. Typical phosphate ion sources include diammonium hydrogen phosphate [$(NH_4)_2HPO_4$], phosphoric acid (H_3PO_4), di-sodium hydrogen phosphate [Na_2HPO_4] and potassium dihydrogen phosphate. The Ca^{2+} and PO_4^{3-} sources react immediately to yield an amorphous precipitate. Reactions carried out in basic conditions (NH_4OH) with a Ca:P molar ratio of 1.67 (at pH 10-11) result in formation of stoichiometric HA (Donadel et al., 2005).

Two precipitation methods have been reported in the literature for HA production (Hench and Wilson, 1993). Rathje, Hayek, and Newesly proposed the first method. They employed a reaction involving 0.6 M phosphoric acid solution into 1 M Calcium hydroxide solution.

$$10[Ca(OH)_2] + 6\ H_3PO_4 \longrightarrow [Ca_{10}(PO_4)_6(OH)_2] + 18\ H_2O$$

The second batch process described by Hayeck and Stadlman was based on the addition of diammonium hydrogen phosphate into a solution of calcium nitrate and ammonium hydroxide solution as an agent for pH adjustment. The similar work has been done by Changsheng Liu and his co-workers in April 2000 (Liu et al., 2001a). They described the mechanism and kinetics of hydroxyapatite precipitation at pH 10-11 which were greatly affected by variation in time and Ca:P ratio under different temperatures.

$$10[(Ca(NO_3)_2.4H_2O] + 6[(NH_4)_2HPO_4] + 8NH_4OH \longrightarrow [Ca_{10}(PO_4)_6(OH)_2] + 20\ NH_4NO_3 + 6H_2O$$

Based on their research, it can be summarized that heating at 60 °C for a batch process of calcium nitrate [$Ca(NO_3)_2.4H_2O$] and diammonium hydrogen phosphate [$(NH_4)_2HPO_4$] then the reaction can be completed in 5 minutes.

From this premise, it may be possible to carry out a flow synthesis (rather than batch) in which temperature of reagents reaches 60 °C and thereafter there is a residence time of at least 5 minutes. The properties, nature and crystallinity of the precipitated HA powder depended significantly on the temperature, pH, time and other precipitation conditions like aging time, variation in Ca:P ratio (Raynaud et al., 2002, Rodríguez-Lorenzo et al., 2001, Arends et al., 1987).

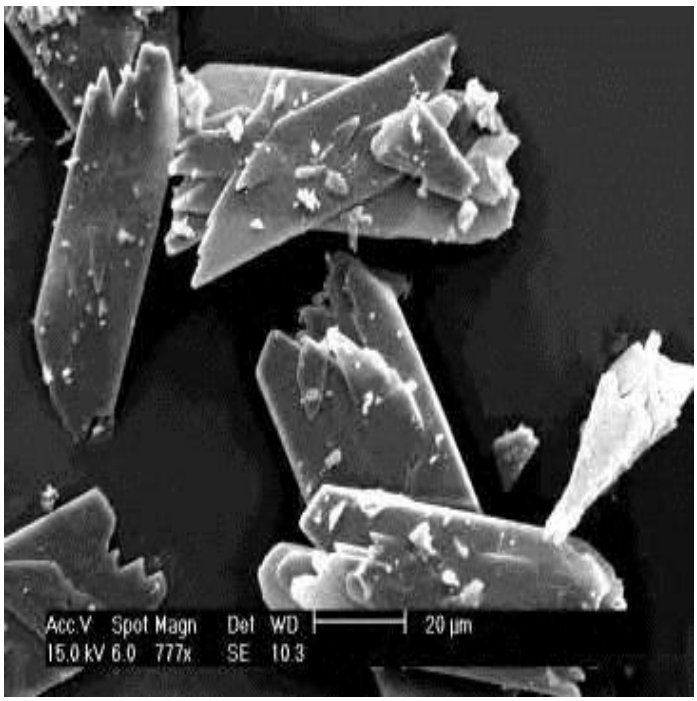

Figure 1-18 SEM of pre-sintered HA particles produced by coprecipitation at room temperature (Donadel et al., 2005).

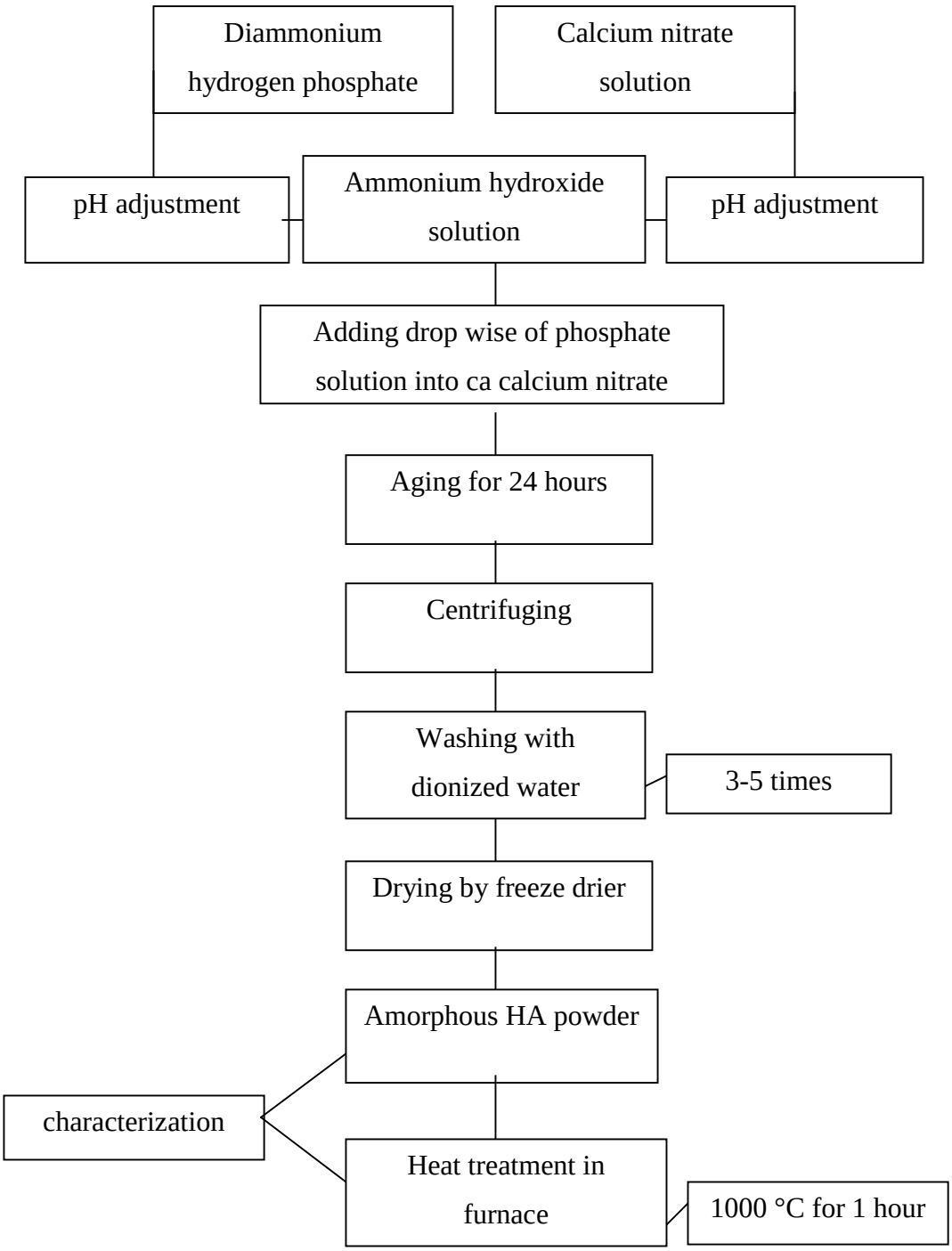

Figure 1-19 Flow chart for the synthesis of hydroxyapatite powder made via coprecipitation method at room temperature.

1.4.5.3 Sol-gel Method

The earliest Sol-gel process was done by Ebelmen in 1846 and formed the basis of modern sol-gel synthesis. This involved the hydrolysis of $SiCl_4$ complexed with alcohols to make SiO_2 (Dislich, 1986). In the late 1930's, oxide films were prepared from sol-gel precursors, which proved useful in the synthesis of stained glass (Geffcken and Berger, 1939). The sol-gel process involves three distinct steps. The first step is the formation of sol (a stable solution of alkoxide or metal precursor) followed by gelation (formation of oxide or alcohol- bridged network), which causes an increase in the viscosity of the solution. The transformation of gel to solid mass takes place in the third step leading to drying and dehydration (Cushing et al., 2004).

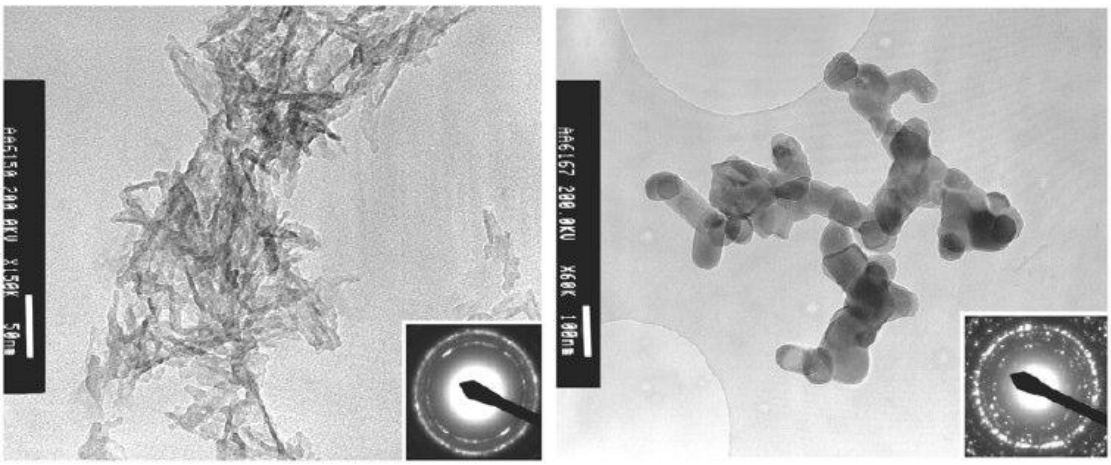

Figure 1-20 TEM images of (a) amorphous co-precipitated HA "needles" (b) heat-treated at 900 °C for two hours (Phillips et al., 2003)

The sol-gel chemistry has also been used to synthesize HA particles but includes aging up to 24 hours and subsequent heat treatment as shown in Figure 1-20. As a consequence of this heat treatment, highly agglomerated particles with changed morphology are formed (Liu et al., 2001b).

1.4.5.4 Emulsion Synthesis

Emulsion is a homogenous combination of water, oil and a surfactant. Emulsion syntheses are used to produce a large variety of metal and metal oxide nanoparticles. By using Stobber method, SiO_2 particles were prepared in ethanol at room temperature (Stöber et al.). The droplet size can be controlled by tailoring the water and the solvent

phases, which can be useful in order to control the product (López-Quintela and Rivas, 1993). HA has been synthesized using emulsion synthesis. However, this needs a large amount of surfactants with organic solvent (oil) and subsequent heat treatment is needed to obtain crystalline HA product (Koumoulidis et al., 2003).

Sun and co-workers also reported (Sun et al., 2007) the synthesis of rod-like HA using microemulsions under hydrothermal conditions of 160 °C for 12 hours under autogenous pressure at neutral pH. They found that by increasing reaction pH almost spherical particles were obtained as shown in Figure 1-21.

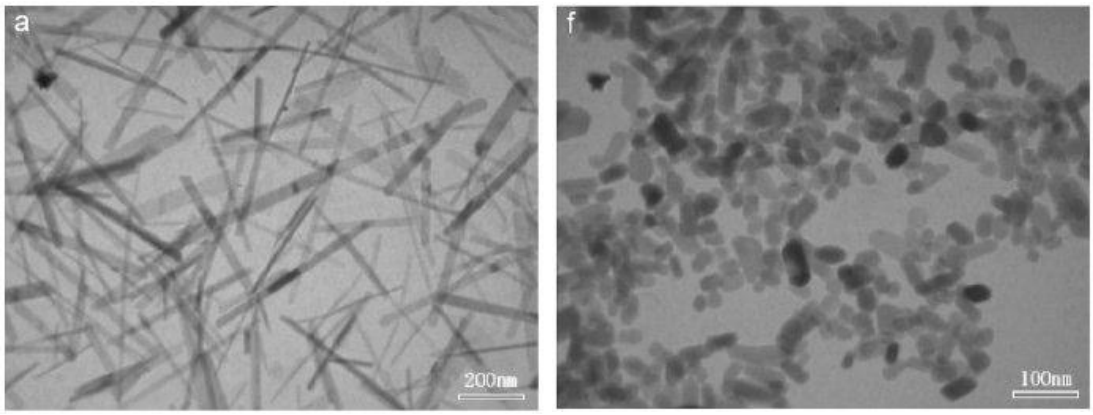

Figure 1-21 Transmission electron microscope images of HA obtained using a microemulsion technique under hydrothermal conditions at (a) pH 7 [bar = 200 nm] and (b) pH 11 [bar = 100 nm] (Sun et al., 2007).

1.4.5.5 Batch Hydrothermal Synthesis

Hydrothermal processes are one of the earliest synthesized methods and can take several hours or days to complete, typically at 150-260 °C. The reactions are typically done in the closed container in order to increase temperature above the boiling point and achieve crystals. However for safety purpose, the pressure should be estimated after heating in the sealed container. In supercritical water [water above both of its critical pressure (Pc) and critical temperature (Tc)], the reaction can proceed in a cleaner and greener way. We can manipulate the phase behavior of the mixture and also change the morphology of the products (Byrappa and Adschiri, 2007).

Hydroxyapatite has also been synthesized using batch hydrothermal methods by mixing and pouring Ca^{2+} and PO_4^{3-} into a sealed container. As compared to other

methods, batch hydrothermal synthesis produces crystalline, well defined and phase pure HA in a single step. Ageing times vary between a few hours to 24 hours with synthesis temperature of 90 to150 °C (Guo and Xiao, 2006).

Zhou and co-workers reported on the decrease in particle size of rod-like HA from 75 x 25 nm to 65 x 26 nm (Figure 1-22) when a dendrimer (polyamidoamine, PAMAM) was used during the hydrothermal batch reaction between calcium nitrate [$Ca(NO_3)_2$] and diammonium hydrogen phosphate [$(NH_4)_2HPO_4$] at 150 °C for 10 hours (Zhou et al., 2007).

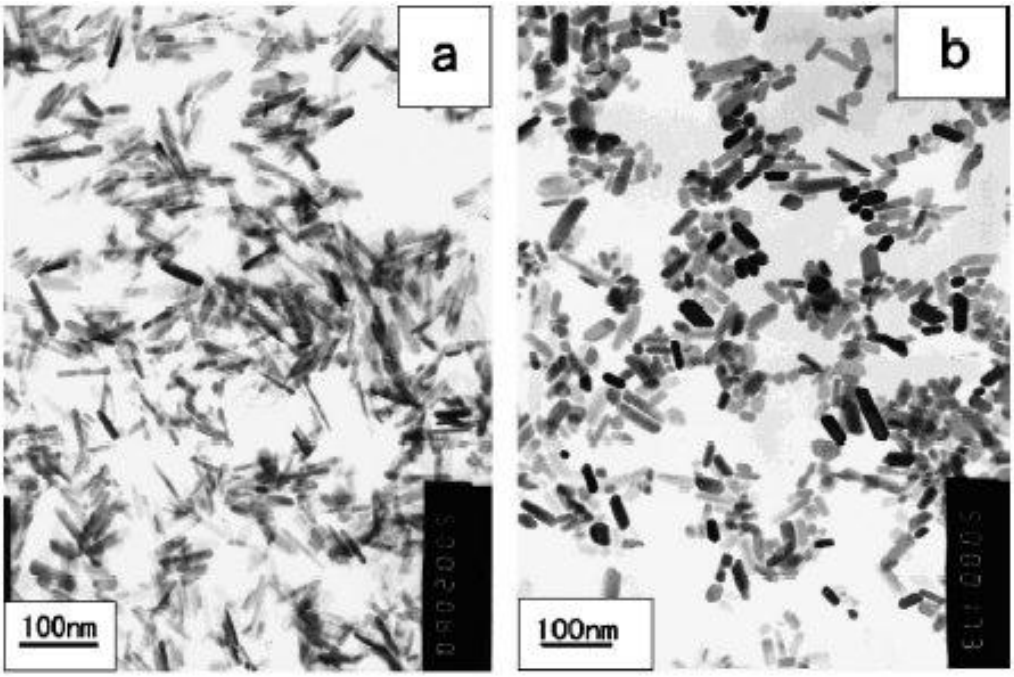

Figure 1-22 Transmission electron microscope images of HA synthesised by a batch hydrothermal reaction (a) without and (b) with a dendrimer (PAMAM) (Zhou et al., 2007).

Zhang and co-workers also reported the hydrothermal synthesis of HA rods employing anhydrous dicalcium phosphate ($CaHPO_4$, DCPA) and $CaCO_3$ in the temperature range from 120 to 180°C. They found the resulting material was mostly HA with slight traces of β-TCP as a by product (at 140 °C for 24 hours). Figure 1-23 shows the morphology of HA rods with width of approximately 200 nm and length of several microns (Zhang and Vecchio, 2007).

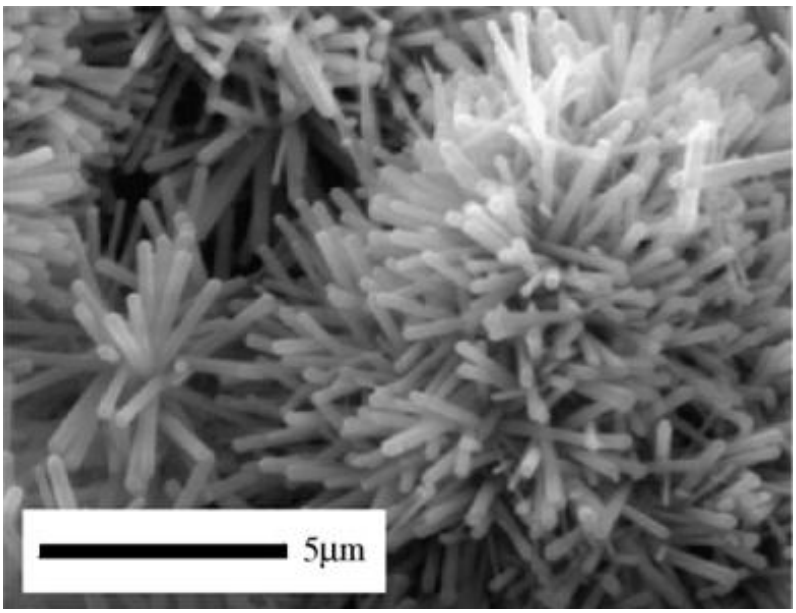

Figure 1-23 SEM image of HA rods synthesized by a hydrothermal reaction between DCPA and calcite at 140 °C for 24 h (Zhang and Vecchio, 2007)

HA particles morphology and crystallinity is affected by pressure, temperature, pH and ageing time. In order to evaluate the influence of pH and temperature on the structure and morphology of HA, different pH values ranging from 6 to 14, and the different temperatures in the range from 60 to 140 °C, were used, during the synthesis (Liu et al., 2003). It was observed that pH greatly affected the morphology, and crystallinity of HA as shown in Figure 1-24 [a-c] .

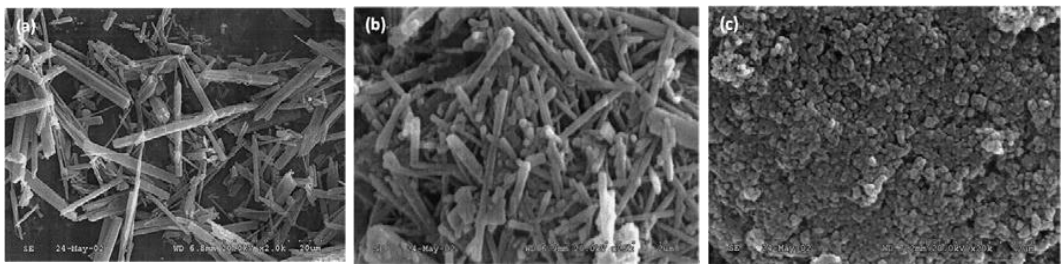

Figure 1-24 [a-c] SEM images of HA whiskers and crystals grown at different pH value at 140 °C: (a) pH = 6, (b) pH = 9, (c) pH =14 (Liu et al., 2003).

Synthesis of various ion-substituted hydroxyapatites using batch hydrothermal processing has also been reported in literature (Jokanović et al., 2006). A decrease in surface area (126 to 50 m^2g^{-1}) was observed by increasing synthesis temperature from 50 to 200 °C in batch process (Riman et al., 2002). By lowering pH below 10, and the Ca:P ratio below 1.67, calcium deficient HA is usually obtained (Andres-Verges et al., 1998).

1.4.5.6 Continuous hydrothermal flow synthesis

Continuous hydrothermal flow synthesis (CHFS) has recently gained interest as a fast and controllable method for producing inorganic nanomaterial (Chaudhry et al., 2006, Sue et al., 2003). Previous examples include the rapid synthesis of nanomaterials that normally require long synthesis times or those are difficult to manufacture using more conventional methods.

In continuous hydrothermal flow synthesis, the starting materials are formed in aqueous solution and secondly the reactants are combined at a mixing point with high temperature and pressure as shown in Figure 1-25. Water becomes supercritical at this high temperature and pressure. As a result, this rapid heating of reactants allows hydrothermal synthesis, precipitation and crystallization [(Darr and Poliakoff, 1999).

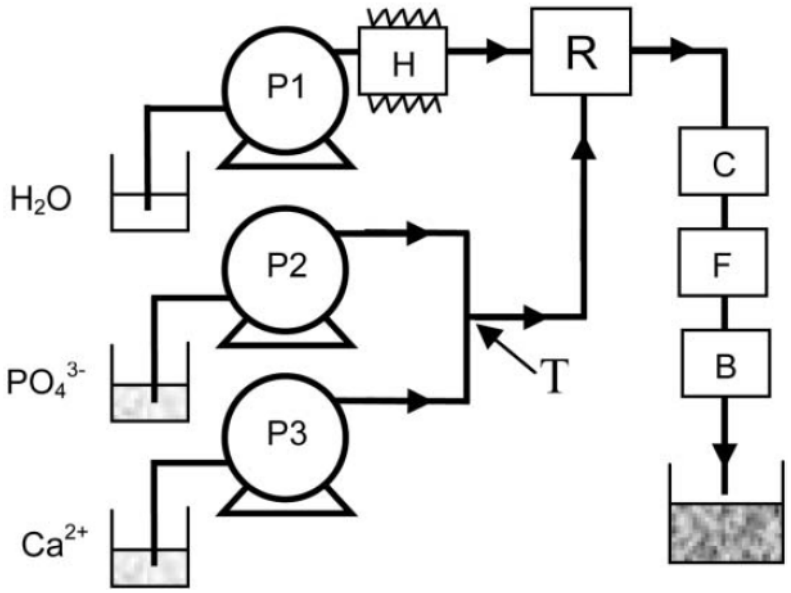

Figure 1-25 Schematic diagram of a CHFS system (Chaudhry et al., 2006)

The crystalline nanoparticle hydroxyapatite rods were obtained in a continuous hydrothermal flow system using water at 400 °C and 24 MPa pressure. In this process, basic solutions of calcium nitrate and ammonium phosphate, respectively, were pumped to meet at a 'Tee'' piece mixer.

This initial mixture was then brought to meet a superheated water feed in a counter current reactor, whereupon, rapid ageing occurred. The apatite suspension was collected at the exit of the backpressure regulator after first passing though the in-line cooler and a 7 mm filter. The collected particles were centrifuged and the wet solids were freeze-dried prior to further analysis. The CHFS process was successfully used to synthesize nano-sized HA rods as well as a great range of ion substituted calcium phosphates (Chaudhry et al., 2006, Chaudhry et al., 2011, Chaudhry et al., 2013, Chaudhry et al., 2008) as shown in Figure 1-26 and Figure 1-27.

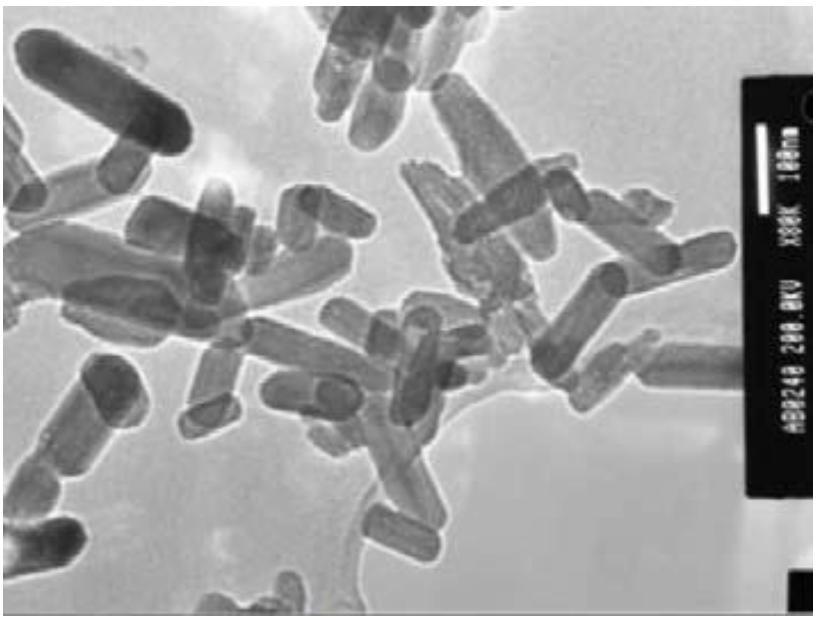

Figure 1-26 TEM image of nano HA rods prepared using a three pump continuous hydrothermal flow system at 400°C and 24MPa (bar = 100nm) (Chaudhry et al., 2006).

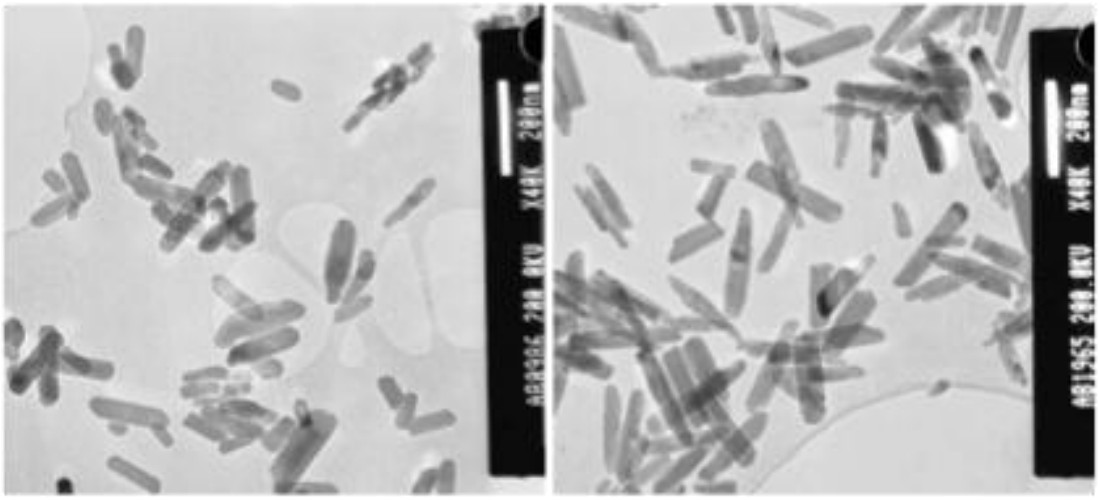

Figure 1-27 Transmission electron microscope images of (a) HA at x40k magnification [bar = 200 nm] and (b) 5SiHA at x40k magnification [bar = 200 nm](Chaudhry et al., 2012a).

Furthermore, the CHFS process has also been refined and scaled to Kg/h scale production of nanomaterials (Gruar et al., 2013). In particular, this group of authors, published the first ever synthesis of HA using CHFS (Chaudhry et al., 2006) and more recently, Mg doped HA (Chaudhry et al., 2008) and the carbonate and silicate doped HA (Chaudhry et al., 2012a) and also HA/ZrO_2 nanocomposites (Chaudhry et al., 2012b). This work by Darr and Chaudhry has clearly shown that if the temperature is sufficiently high enough, the conversion from precursors to the stoichiometric HA can be achieved near instantaneously (Chaudhry et al., 2006). Another problem with this process was the use of metal pipes, which were needed due to the high temperature and pressure. This work did not however explore the possible use of lower temperatures and pressures for the same reactions.

1.5 Hypothesis and Aims

The majority of room temperature batch synthesis methods for phase pure HA and other calcium phosphates tend to be multi-step, energy intensive or time consuming processes. For example, in wet chemical syntheses of HA, a maturation step (>18 h), followed by a heat treatment of 650 °C, is required. Failure to allow sufficient maturation, gives a phase-separated product upon heat treatment, which can adversely affect biological properties *in vivo*. Emulsion synthesis is suitable for small sized powdered product however it is also time consuming and needs subsequent heat-treatment and it uses solvents. Although batch hydrothermal process facilitates a simple, low temperature and efficient way to synthesize phase pure HA however, most of the time it requires templating agents along with long reaction time (up to 24 hours).

Continuous production of HA are carried out at temperatures in excess of the range of 200-400 °C, which is energy intensive. Furthermore, at such high temperatures, although nucleation occurs, there is substantial growth or agglomeration of smaller nuclei to form substantially larger particles, typically >100 nm in size (i.e. the length of needles). Additionally, there is a disadvantage of having to use high temperature continuous reactors, in that they are conducted in metal pipes due to the high reaction temperatures and therefore if such a process were used to make bioceramics, they would contain substantial levels of leached metals from the steel (e.g. Fe, Cr, etc). This would mean that the bioceramics may not be acceptable for clinical use according to the latest international standards and guidelines. Furthermore, many of the particle sizes obtained in such reactors are not particularly small and indeed are very similar to those obtained using more conventional synthesis methods. Smaller particles would open up and improve many applications such as more rapid dissolution (due to higher surface area) or use as injectable or as a hard filler for bone replacement. Consequently, a need arises to develop smaller nano-sized calcium phosphates using methods, which allow for fine control over particle sizes, preferably under relatively mild conditions of temperature and pressure, and with purity acceptable for use in a clinical setting such as for bone replacement. One known method of HA production at near ambient conditions (20-60 °C) was reported in the patent literature that involves the mixing of reagents in multiple stages using a multiple step reactor with strong stirring (Bozhevolnov et al., 2007).

Therefore, attempts have been made to develop a simple, low cost, clean, synthesis technique, which could work under mild conditions and allow the synthesis of high purity stoichiometric HA and other bioceramic materials in a considerably short time period with a fine and controllable particle size (range from 20-150 nm) and controlled surface area (typically range from 95-300 m^2g^{-1}), depending on reaction conditions and containing trace contaminating elements which are well below acceptable levels as stipulated by international recognized standards for clinical use of bioceramics [ISO13779-3].

Based on these inferences, the main aims of this work can be outlined as follows

- To prepare phase pure stoichiometric hydroxyapatite (<100nm) and other bioceramics as fast as possible and at alow temperature as possible.
- The HA must be very stoichiometric, ie No decomposition of HA into other phases after heating at 1200ºC in air for 2h
- To demonstrate control over particulate properties using CPFS system parameters.
- To evaluate the effects of different size particles by biological testing.
- To produce ion-substituted calcium phosphates with variable properties and explore the substitution limits in a quick and controllable manner using CPFS system parameters.
- To avoid corrosion and blockage in flow synthesis
- To obtain specific products/phases with controlled particle size and shape by tailoring temperature, time and reaction pH.
- To prepare high purity product in a plastic flow system; suitable for biomedical applications.
- To use low cost and using readily available precursors, to fulfill the need of simplified production methods under mild conditions for developing countries like Pakistan.

Chapter 2
Materials and Methods

This chapter describes the materials and experimental procedures used in this thesis. This includes details of chemicals used for reactions in the continuous plastic flow synthesis (CPFS) system, synthesis methodology (calculations, reaction parameters), characterization techniques (sample preparation and measurement details) and *in-vitro* cell viability studies.

2.1 Chemicals and Methods

The following chemicals were used for the preparation of phase pure calcium phosphates.

- Calcium nitrate tetrahydrate [$Ca(NO_3)_2.4H_2O$, 99%] and Calcium hydroxide [$Ca(OH)_2$, 99.99%] precursors supplied from Sigma Aldrich, Chemical Company (Dorset, UK.) were used as a calcium ion sources.
- Diammonium hydrogen phosphate [$(NH_4)_2HPO_4$, 99%] and Phosphoric acid [H_3PO_4, 99.99%] precursors supplied from Sigma Aldrich, Chemical Company (Dorset, UK.) were used as phosphate ion source.
- To synthesize ion substituted calcium phosphates, surface grafted and nanocomposite materials the following chemicals were used.
- Urea [$(NH_2)_2CO$, 99.5%] supplied by VWR International (UK) was used as a carbonate ion source.
- Silicon tetraacetate [$Si(OCOCH_3)_4$, 98%] purchased from Sigma-Aldrich Chemical Company (Dorset, UK) was used as a silicate ion source.
- Magnesium nitrate hexahydrate [$Mg(NO_3)_2.6H_2O$, 98%] purchased from Sigma-Aldrich Chemical Company (Dorset, UK.) was used as a magnesium ion source.

- Zinc nitrate hexahydrate [$Zn(NO_3)_2.6H_2O$, 97%] purchased by Sigma-Aldrich Chemical Company (Dorset, UK.) used as a zinc ion source.

- Strontium nitrate hexahydrate [$Sr(NO_3)_2.6H_2O$, 98%] supplied by Sigma-Aldrich Chemical Company (Dorset, UK.) used as a strontium ion source.

- Barium hydroxide octahydrate [$Ba(OH)_2.8H_2O$, 98%] supplied by Sigma-Aldrich Chemical Company (Dorset, UK.) used as a barium ion source.

- Silver nitrate [$AgNO_3$, 99 %] supplied by Sigma-Aldrich Chemical Company (Dorset, UK.) used as a silver ion source.

- Iron citrate [$C_6H_5O_7Fe.3H_2O$, 98%] obtained from Scientific Fischer, UK was used as an iron source.

- Manganese nitrate tetrahydrate [$Mn(NO_3)_2.4H_2O$,97%] obtained from Scientific Fischer, UK was used as a manganese ion source.

- Methacrylic acid [$C_4H_6O_2$, 99+%] Polyvinyl alcohol [$(C_2H_4O_X)$, 99+%], Adipic acid [$C_6H_{10}O_4$, 99%], Citric acid [$C_6H_8O_7$, 99%] and Vinyl phosphonic acid [$CH_2=CHP(O)(OH)_2$, 97%] were purchased from Sigma Aldrich Chemical Company (Dorset, UK).

- Triethylene glycol di-methacrylate [TEGDMA, $C_{14}H_{22}O_6$, 95%], Bisphenol A diglycidyl ether dimethacrylate [Bis-GMA,$C_{29}H_{36}O_8$], and Camphorquinone [CQ, $C_{10}H_{14}O_2$, 97%] were purchased from Sigma Aldrich, Steinheim, Germany.

- Dimethyl aminoethyl methacrylate [DMAM] and N, N-Dimethyl-p-toluidine [$C_9H_{13}N$, >98%] were supplied by Merck, Hohenbrunn, Germany.

Ammonium hydroxide solution (NH_4OH, 28%) was used to adjust pH where required supplied by VWR International (UK). Deionised water was used throughout all experimentation.

2.2 Synthesis Method for Nanopowders

2.2.1 Continuous Plastic Flow Synthesis System

The continuous plastic flow synthesis (CPFS) system is a simple, single step method that was used for the synthesis of HA and other high purity bioceramics under near ambient conditions with affordable and readily available reagents.

The CPFS system consists of two HPLC Gilson pumps (Gilson Model 307 Pumps with 25 SC Pump heads), connected to 8 m long Polyflon™ PTFE tubing which was coiled inside an oil bath with one end of the tubing splitting via a T-junction connection into precursor reservoir and the other end emerging from the heating system (oil bath) in a collection beaker.

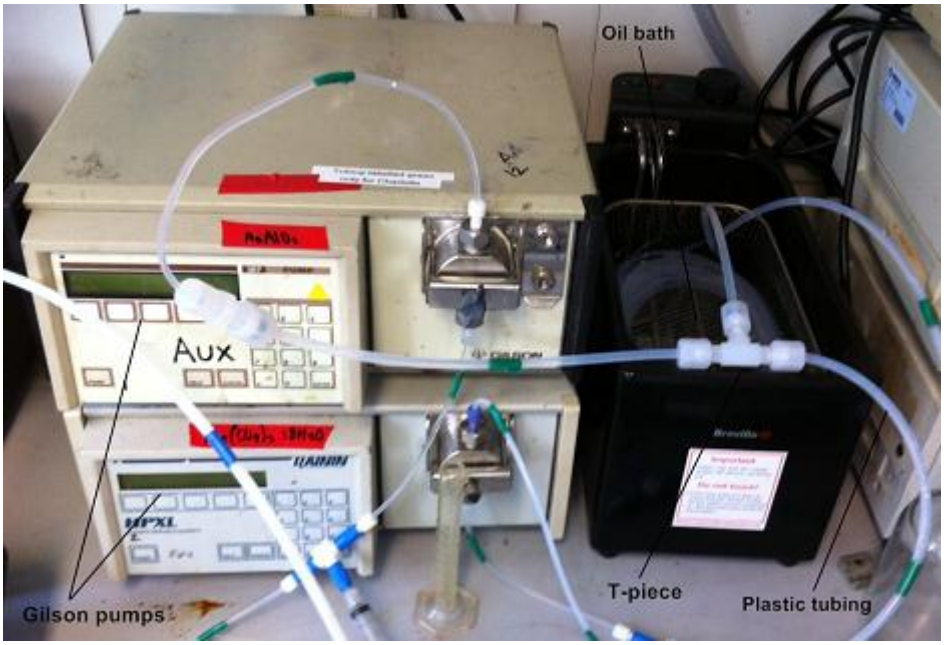

Figure 2-1 Two pump (P1, P2) plastic flow system used for the synthesis of nano-bioceramics.

In the CPFS process, precursor solutions were pumped to meet at a 1/16 inch Polyflon™ T-piece through a 1/8 in. Polyflon™ straight union reducer (D6-D1/8", PFA). This initial mixture was connected to 8 m long 1/16 inch Polyflon™ PTFE tubing (internal diameter 4.0mm x outer diameter 6.0mm) which was coiled inside an oil bath which gave an effective 5 minutes from the tee to the exit of the pipe. The reactor tube is made of a fluoropolymer which gives good resistance to strong pH and is easy to clean. For

given flow rates for the two pumps of 10 mL per minute (total flow= 20 mL min^{-1}), gives an approximate residence time of five minutes as a typical set of process parameters. Preferably, the tube is heated externally via a heat exchanger placed downstream of the T-junction mixing point. The tube is located inside an oil bath which acts as a heat exchanger downstream of the mixing point, allowing the reaction to go to completion.

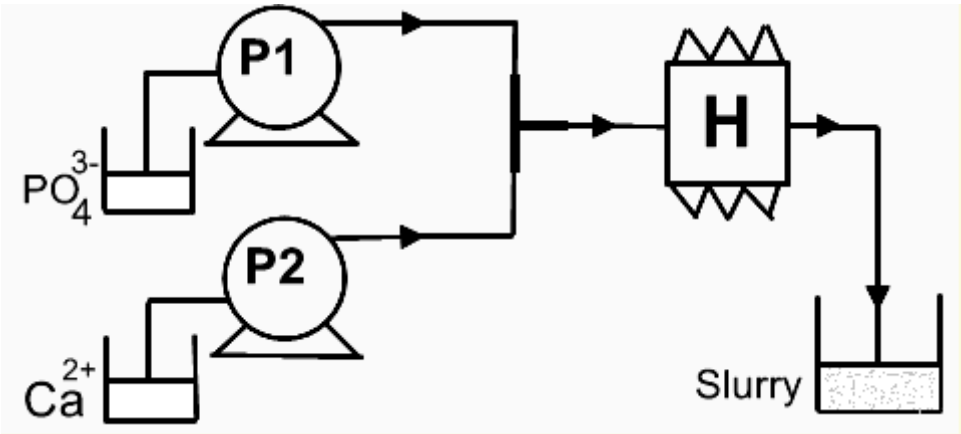

Figure 2-2 Scheme of the two pump (P1, P2) plastic flow system used for the synthesis of nano-bioceramics Key: P = pump, H = heat exchanger, T = ‘‘Tee’’ piece mixer.

The product is collected from the end of the tube at ambient pressure. The tube diameters, type of heat exchanger and flow rates and types of pumps differ considerably depending on what is required to achieve similar performance and lab scale. The CPFS system allows access to the range of reaction conditions required for rapid and continuous synthesis of calcium phosphates (summarized in table 2-1). Dr. Chris Tighe, a chemical engineer in the CMTG materials chemistry group, calculated all CPFS reactor parameters.

Table 2-1 Parameters for continuous plastic flow system

Flow rate $F = V/\tau$	**Residence time** $T = v/F$	**Outer diameter of tubing (do)**	**Inner diameter of tubing (di)**	**Length of tubing used** $L = 4F\tau/\pi d^2$	**Heat required** $Q = \rho FCp (T_{out} - T_{in})$	**Heat transfer area required** $L' = Q/U\pi d\Delta T_{LMTD}$	**Surface area** $S = \pi d\, L'$
$mLmin^{-1}$	**minutes**	**cm**	**cm**	**cm**	**J/s**	**cm**	**cm^2**
5	5	0.60	0.40	199	13.95	100.43	126.20
10	5	0.60	0.40	398	27.90	200.86	252.41
15	5	0.60	0.40	597	41.85	301.29	378.62
20	5	0.60	0.40	796	55.80	401.72	504.82
25	5	0.60	0.40	995	69.75	502.16	631.03
30	5	0.60	0.40	1194	83.71	602.59	757.24

2.3 Synthesis Methodology

In this section, exact amounts of chemicals used to make solutions, synthesis conditions for the CPFS systems (temperature, concentration, pH, flow rates), clean up, centrifugation parameters and freeze drying and thermal stability study parameters are described.

2.3.1 Synthesis of High Surface Area Nano-sized Hydroxyapatite and Effect of CPFS System Parameters

2.3.1.1 Synthesis of Phase Pure Stoichiometric Nanohydroxyapatite

Method 1: The pure nano-hydroxyapatite (HA) was prepared at 60°C using a simple continuous plastic flow synthesis system (CPFS). 0.3 M phosphoric acid solution and 0.5 M calcium hydroxide solutions were used (Ca : P molar ratio: 1.67). Both reagent solutions were made in 500mL deionised water and pumped at 20 mL min^{-1}, to meet at a 1/16 in. Polyflon™ T-piece through a 1/8 in. Polyflon™ Straight union reducer (D6-D1/8", PFA). This initial mixture was connected to 8 m long 1/16 in. Polyflon™ PTFE tubing surrounded by a heating jacket whereupon reaction completed in 5 minutes which was the residence time for the reaction. The resulting precipitates were collected from the exit point. The precipitation of HA can be described by the following equation.

$$10[Ca(OH)_2] + 6\ H_3PO_4 \longrightarrow [Ca_{10}(PO_4)_6(0H)_2] + 18\ H_20$$

Method 2: In this process, 0.3 M diammonium hydrogen phosphate solution and 0.5 M calcium nitrate solutions were used (Ca : P molar ratio: 1.67). The pH of both the solutions prior to the reaction was kept above pH 10. 15.0 ml of ammonium hydroxide were added to calcium nitrate (500 mL) and diammonium hydrogen phosphate solutions (500 ml), respectively. Both reagent solutions were pumped at 20 mL min^{-1}, to meet at a T-piece. This initial mixture was connected to 8 m long tubing surrounded by heating jacket. The flow rates used for calcium nitrate and diammonium hydrogen phosphate solutions for pump 1 and pump 2, respectively, were selected to give a total residence time of 5 minutes. The precipitation of HA can be described by the following equation.

$$10\ [Ca(NO_3)_2.4H_2O] + 6\ [(NH_4)_2HPO_4] + 8\ NH_4OH \longrightarrow [Ca_{10}(PO_4)_6(OH)_2] + 20NH_4NO_3 + 6H_2O$$

The slurries were collected from the exit (at the end of the CPFS system) in 50 mL Falcon tubes. Between consecutive collections, the CPFS system was purged with clean water for 20 minutes. Each slurry was centrifuged at 4500 rpm for five minute (per 50 mL suspension), *ca.* 45 mL of liquid was removed from each sample and *ca.* 45 mL deionised water was added followed by vigorous shaking using a vortex mixer. Each sample was then recentrifuged at 4500 rpm for five minutes and *ca.* 45 mL liquid was removed for a final time to give a concentrated slurry. The wet residue was frozen in liquid N_2 and then freeze-dried using a VirTis Genesis Pilot Lyophilizer 35XL at 0.3 Pa for 24 hours.

Table 2-2 Reaction conditions for the synthesis of phase pure hydroxyapatite

Temperature	**Initial pH of solution 1**	**Initial pH of solution 2**
Temp. (60 °C)	$Ca(NO_3)_2$ ~ 8 $Ca(OH)_2$ ~ 13	$(NH_4)_2HPO_4$ ~ 8.5 H_3PO_4 ~ 3
Dropping Mechanism	**Flow Rate (variable)**	**Residence Time**
Gilson pump	20 mL min^{-1}	5 min.
Ca:P ratio	**Drying Method**	**pH Adjustment**
1.67	Freeze drying	NH_4OH (28% vol)

The powders were also separately heat–treated to show that the as-prepared materials were able to form phase pure synthetic hydroxyapatite that was stable at 1200°C in air (this suggested that it was stoichiometric hydroxyapatite as it did not decompose).

2.3.1.2 Disc Preparation

The obtained as prepared and sintered powders were compacted into cylindrical discs of 13 mm diameter and 2 mm thickness by using a laboratory hydraulic press at 5 MPa. These samples were used for cell viability studies after sterilization in 70 % ethanol for 1 hour.

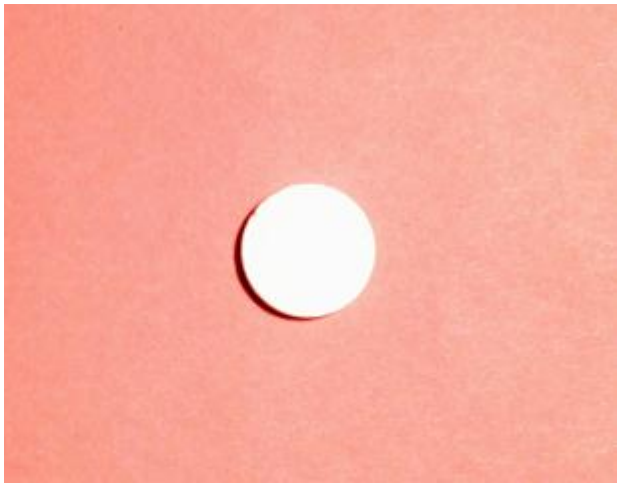

Figure 2-3 Cylindrical HA disc made for cell viability analysis

(a) Effect Of Temperature

Six separate reactions were carried out to study the effects of reaction temperature on the end products. For each case, samples were synthesized under basic pH 10 conditions with Ca/P ratio 1.67.

59 g (0.25 moles) and 19.8 g (0.15 moles) of calcium nitrate and diammonium hydrogen phosphate were separately dissolved in 1000 mL deionised water for stock solution. In total, 6 different reactions were carried out using 150 mL of calcium nitrate and diammonium hydrogen phosphate solutions for each case. The pH was adjusted to pH 10 by adding 30 mL ammonium hydroxide solution to each solution.

The samples were labeled as HA30, HA40, HA50, HA60, HA70 and HA80 depending on reaction temperatures ranges from 30 to 80 °C, respectively. The numbers in the sample ID specifies the different temperatures on which reactions are carried out. The pH values were measured from suspensions immediately after collection.

Table 2-3 Effect of temperature on the synthesis of hydroxyapatite

Sr. #	Sample ID	Flow rate ($mLmin^{-1}$)	Reaction temperature	Product formed
1	HA30	20	30	Impure Product
2	HA40	20	40	HA/TCP
3	HA50	20	50	HA/Traces of TCP
4	HA60	20	60	Pure HA
5	HA70	20	70	Pure HA
6	HA80	20	80	Pure HA

These reactions were carried out using the CPFS system as explained in section 2.2.1. Pump rates of 20 mL min^{-1} were used for calcium nitrate and diammonium hydrogen phosphate solutions, respectively. All reactions were carried out at atmospheric pressure. Results have shown that apatite obtained below 60 °C after heat-treatment at 1200 °C for 1 hour was not phase pure synthetic hydroxyapatite, as shown in Table 2-3.

(b) Effect of Flow rates

59 g of calcium nitrate were dissolved in 1000 mL deionised water to result in 0.25 M stock solution. The pH of this solution was adjusted to pH 10 by adding 30 mL of neat ammonium hydroxide solution. 19.8 g of diammonium hydrogen phosphate were dissolved in 1000 mL of deionised water to result in a 0.15M stock solution. In total, five different reactions were carried out using 200 mL of calcium nitrate and diammonium hydrogen phosphate solutions for each case.

Table 2-4 Effect of different flow rates on the synthesis of hydroxyapatite

Sr. #	Sample No.	Flow rate	Product formed
1	HA1	50	Impure
2	HA2	40	HA/TCP
3	HA3	30	Pure HA
4	HA4	20	Pure HA
5	HA5	10	Pure HA

All samples were centrifuged, washed and freeze-dried as explained earlier; see section 2.3.1.1.

(c) Effect of Concentration

A series of experiments (six in total) were carried out by varying concentration and by keeping all other parameters the same. For each case, samples were synthesized under basic pH 10 conditions with Ca:P ratio 1.67.

The fine HA powder obtained from all reactions using different concentration were hereafter referred to as 1HA, 0.5HA and 0.25HA and 0.125HA, respectively. All reactions were carried out at 60 °C and atmospheric pressure. It was observed that tailoring reaction concentration while keeping the reaction time as five minutes in all reactions greatly influenced the particle size and specific surface area as shown in Table 2-5. The dried product was a fine, free flowing white powder.

It was observed that the method works very well at higher concentrations of precursors. However, the particle size increases, with a subsequent lowering of surface area. Therefore, at higher concentrations of precursors, the method can still be used for the rapid and continuous manufacture of stoichiometric hydroxyapatite or other bioceramics (e.g. calcium phosphates and their derivatives).

Table 2-5 Effect of reaction concentration on the final product

Sr. #	Sample ID	CaN ($molL^{-1}$)	DAHP ($molL^{-1}$)	Ca/P ratio	Flow rate ($mLmin^{-1}$)	Product formed (g)	BET Surface Area (m^2g^{-1})
1	1HA	1	0.6	1.67	20	Impure (~150g/h)	50-100
2	0.5HA	0.5	0.3	1.67	20	Pure HA (~75g/h)	100-150
3	O.25HA	0.25	0.15	1.67	20	Pure HA (~35g/h)	100-200
4	0.125HA	0.125	0.075	1.67	20	Pure HA (~20g/h)	200-300

Under such conditions, the particles are typically around one hundred nanometers or more in length and surface areas are about 100 m^2g^{-1}. The properties of the precipitated material depended on the temperature, concentration, pH, time and other precipitation conditions such as variation in Ca:P ratio and residence time. By tuning the reaction parameters, products of any required particle size (ranging from 20-150 nm) and surface area (ranging from 95-300 m^2g^{-1}) can be produced.

2.3.1.3 Synthesis of Other Phase Pure Calcium Phosphates (DCPD, CDHA, TCP)

(a) Synthesis of Brushite

Brushite (DCPD: dicalcium phosphate dihydrate: $CaHPO_4.2H_2O$) nanoparticles (<100nm) were rapidly synthesised using a novel two pump continuous plastic flow synthesis (CPFS) at room temperature (22 °C) in 3 minutes (residence time) at pH 5.5 from aqueous solutions of calcium nitrate tetrahydrate and diammonium hydrogen phosphate. The product was obtained as a phase pure material with a Ca:P molar ratio for the reagents of 0.8, and without the need for an initial prolonged ageing step. Brushite is transformed into monetite by losing its crystal water upon heating above 110

°C. The transition of monetite into pyrophosphate typically occurs at temperatures above 400 °C. The product obtained was fine white powder with ~ 85 % yield.

(b) Synthesis of Calcium Deficient HA and β- Tricalcium Phosphate

Other calcium phosphate phases (β-TCP, CDHA) were also obtained by changing the Ca:P ratio (1.5~ 1.67) by keeping other conditions as shown in Table 2-6. β-TCP was obtained by the heat-treatment of as-prepared CDHA at 1100 °C. The influence of initial Ca:P molar ratio, pH and precipitation temperature on the phase evolution and crystallinity of the nanopowder were systematically investigated and optimized. The product obtained was a fine white powder with ~ 85 % yield.

Table 2-6 Synthesis of various phase purse calcium phosphates made on CPFS

Ca/P	Name	Formula	Acronym	pH range
1.67	Hydroxyapatite	$Ca_{10}(PO_4)_6(OH)_2$	HA	9.5-12
1.5-1.67	Calcium-deficient hydroxyapatite	$Ca_{10-x}(HPO_4)_x(PO_4)_{6-x}(OH)_{2-x}$	CDHA	6.5-9.5
1.0	Dicalcium phosphate dihydrate (brushite)	$CaHPO_4.2H_20$	DCPD	2.0-6.0
1.5	β-tricalcium phosphate	β-$Ca_3(PO_4)_2$	B-TCP	7.4
1.0	Dicalcium phosphate anhydrous (monetite)	$CaHPO_4$	DCPA	2.0-6.0
1.0	Calcium pyrophosphate	$Ca_2P_2O_7$	CPP	4-6

2.3.1.4 Synthesis of Phase Pure Strontium and Barium Hydroxyapatite

(a) Synthesis of Strontium Hydroxyapatite

The as-prepared phase pure strontium and barium hydroxyapatite (containing no calcium) were prepared at 60°C using a simple continuous (plastic) flow synthesis

system (CPFS). 52.9g (0.25 moles) of strontium nitrate and 19.8 g (0.15 moles) of diammonium hydrogen phosphate were dissolved in 1000 mL deionised water and the pH of the solution was adjusted to pH 12 by adding 30 mL neat ammonium hydroxide solution.

CPFS system was used for these reactions and pump rates of 20 mL min^{-1} were used for calcium nitrate/urea and diammonium hydrogen phosphate solutions, respectively. All reactions were carried out at 70 °C and atmospheric pressure. All samples were centrifuged, washed and freeze-dried as explained earlier; see section 2.3.1.1. The dried product was free flowing white powder with ~ 85 % yield.

(b) Synthesis of Barium Hydroxyapatite

In the synthesis process, 78.8 g (0.25 M) basic solutions of barium hydroxide solutions with (Ba:P molar ratio: 1.67) and 19.8 g (0.15 M) diammonium hydrogen phosphate, respectively, were pumped to meet at a T-piece. This initial mixture was connected to an 8 m long pipe which was coiled inside an oil bath which gave an effective 5 minute residence time from the tee to the exit of the pipe. The pH of both the solutions prior to the reaction was ideally kept above pH 12.

The CPFS system was used for these reactions and pump rates of 20 mL min^{-1} were used for barium hydroxide and diammonium hydrogen phosphate solutions, respectively. All reactions were carried out at 70 °C (reaction temperature) and atmospheric pressure. All samples were centrifuged, washed and freeze-dried as explained earlier; see section 2.3.1.1. The product obtained was a fine white powder with ~ 85 % yield.

2.4 Synthesis of Ion Substituted Calcium Phosphates

2.4.1 Synthesis of Magnesium Substituted Calcium Phosphates

All samples were made using a novel continuous plastic flow synthesis (CPFS) system, which consisted of two HPLC Gilson pumps as explained in section 2.2.1. In the synthesis process, separate reservoirs of calcium nitrate with different wt% of metal ions (Ca + Mg)/P = 1.67) ranging from 1 to 10 wt%, and diammonium hydrogen phosphate, respectively, were pumped to meet at T-piece. Ammonium hydroxide was used to maintain the pH of both the solutions prior to the reaction above pH 10. The residence time from the T-piece to the exit of the tubing was 5 minutes.

The product was collected as a suspension in a beaker at the exit point. All samples were centrifuged, washed and freeze-dried as explained earlier; see section 2.3.2. The dried powders were then heat-treated at 1000 °C for 2 hours in air at a heating rate of 10 °C/min. The samples were labelled as 1Mg-CaP, 2Mg-CaP, 3Mg-CaP, 4 Mg-CaP, 5Mg-CaP, 6 Mg-CaP, 7Mg-CaP, 8Mg-CaP, 9Mg-CaP and 10Mg-CaP. The numbers in the sample IDs represent the expected magnesium content (wt%). The dried product was fine white powder with ~ 85 % yield. The as prepared and heat-treated powdered samples were compacted into cylindrical discs of *ca.* 13 mm diameter and 2 mm thickness by using a hydraulic press at 5 MPa.

2.4.2 Synthesis of Carbonate and Silicate Substituted Calcium Phosphates

(a) Synthesis of Carbonate Substituted Calcium Phosphates

A series of carbonate substitution reactions were carried out for this study. The continuous plastic flow synthesis was carried out as previously described ; see section 2.2.1. 59 g (0.25 moles) of calcium nitrate were dissolved in 1000 mL deionised water and the pH of this solution was adjusted to pH 11 by adding 30 mL neat ammonium hydroxide solution. Urea (carbonate ion source) was added to diammonium hydrogen phosphate (adjusted to pH 10). This solution was reacted with calcium nitrate solution (adjusted pH 11). A Ca:[PO_4^{3-}+CO_3^{2-}] molar ratio of 1.67 was maintained in all precursor solutions. All calculations were based on the formula $Ca_{10}(PO_4)_{6-}$

$_x(CO_3)_x(OH)_2$, wherein carbonate ions partially replace phosphate ions in the HA lattice. Samples are labelled as 2CHA, 4CHA, 6CHA and 8CHA. The initial numbers in the sample IDs show the nominal carbonate content (wt%).

CPFS system was used for these reactions and pump rates of 20 mL min^{-1} were used for calcium nitrate/urea and diammonium hydrogen phosphate solutions. All reactions were carried out at 70 °C and atmospheric pressure. All samples were centrifuged, washed and freeze-dried as explained earlier; see section 2.3.1.1. The product obtained was fine white powder with ~ 85 % yield.

(b) Synthesis of Silicate Substituted Calcium Phosphates

A similar procedure to carbonate substitution was adopted for the synthesis of silicon-substituted calcium phosphates using the CPFS system. In total, nine reactions were carried out using silicon acetate as a silicate ion source. For a typical reagent solution, silicate tetra-acetate and calcium nitrate were accurately weighed and added to 200 mL deionised water so that the combined ratio of calcium nitrate with silicate ion and diammonium hydrogen phosphate was 1.67. For these reactions it was assumed that silicate ions partially substitute phosphate ions in HA lattice [$Ca_{10}(PO4)_{6-x}(SiO_4)_x(OH)_{2-x}$].

The pH of this solution was adjusted to pH 10 by adding 10 mL of neat ammonium hydroxide solution. The samples are labeled as 1Si-HA, 2Si-HA, 3Si-HA, 4Si-HA, 5Si-HA, 6Si-HA, 7Si-HA, and 8Si-HA. The numbers in the sample IDs represent the nominal silicon content (wt%) according to how much silicate precursor was used in the precursors. All samples were centrifuged, washed and freeze-dried as explained earlier; see section 2.3.1.1. The product obtained was fine white powder with ~ 85 % yield.

2.4.3 Synthesis of Strontium and Barium Substituted Calcium Phosphates

(a) Synthesis of Strontium Substituted Calcium Phosphates

A customized synthesis of strontium substituted calcium phosphates was made using A CPFS system which has capacity to prepare nanobioceramic materials with controllable particle size by tailoring the reaction parameters like temperature, pH and flow rates of precursors. All samples were made using the continuous plastic flow synthesis as previously described in section 2.2.1. In the synthesis process, basic solutions of calcium nitrate with different wt% of metal ions (Ca + Sr)/P = 1.67 strontium and diammonium hydrogen phosphate were used.

A CPFS system was used for these reactions and pump rates of 20 mL min^{-1} were used for calcium nitrate/strontium nitrate and diammonium hydrogen phosphate solutions, respectively. All reactions were carried out at 70 °C and atmospheric pressure. All samples were centrifuged, washed and freeze-dried as explained earlier; see section 2.3.1.1. The product obtained was a fine white powder with ~ 85 % yield.

(b) Synthesis of Barium Substituted Calcium Phosphates

All samples were made using a CPFS system as previously described in section 2.2.1. In the synthesis process, basic solutions of calcium nitrate and strontium nitrate (total conc. = 0.5M and (Ca + Ba)/P = 1.67) and diammonium hydrogen phosphate, respectively, were pumped to meet at T-piece. The pH of both the solutions prior to the reaction was kept above pH 10.

The CPFS system was used for these reactions with pump rates of 20 mL min^{-1} for the calcium nitrate/barium hydroxide and diammonium hydrogen phosphate solutions. All reactions were carried out 70 °C and atmospheric pressure. All samples were centrifuged, washed and freeze-dried as explained earlier; see section 2.3.1.1.

Table 2-7 Synthesis of various Ion substituted calcium phosphates made on CPFS

Serial #	Substituted Ions	Substitution site	Temp(°C)	Residence time (minutes)
1	Carbonate (CO_3^{2-})	Phosphate (PO_4^{3-})	70	5
2	Silicate (SiO_4^{4-})	Phosphate (PO_4^{3-})	70	5
3	Magnesium (Mg^{2+})	Calcium (Ca^{2+})	70	5
4	Strontium (Sr^{2+})	Calcium (Ca^{2+})	70	5
5	Barium (Ba^{2+})	Calcium (Ca^{2+})	70	5
6	Silver(Ag^{2+})	Calcium (Ca^{2+})	70	5
8	Iron (Fe^{2+}, Fe^{3+})	Calcium (Ca^{2+})	70	5
9	Manganese (Mn^{2+})	Calcium (Ca^{2+})	70	5

A CPFS reactor was used to successfully synthesize ion substituted calcium phosphates from calcium nitrate tetrahydrate [$(Ca(NO_3)_2.4H_2O)$], and diammonium hydrogen phosphate [$(NH_4)_2HPO_4$)] precursor solutions at (near) ambient conditions in a rapid single step.

2.5 Synthesis of Hydroxyapatite Based Nanocomposites

2.5.1 HA-Magnetite Nanocomposites

(a) Synthesis of Magnetite

Magnetite nanoparticles were rapidly synthesised using a novel two pump continuous plastic flow synthesis at 70 °C in 5 minutes (residence time) at pH above 10. In our process, 20.2g Iron nitrate and 11.52 g citric acid were pumped to meet at a ‘‘Tee’’ piece mixer. This initial mixture was connected to 8 meter plastic tubing surrounded by

a heating jacket whereupon reaction will be completed in 5 minutes, which is the residence time for the reaction. The suspension was collected in a beaker at the exit point. The precipitates were centrifuged and dried by using freeze drier as explained earlier; see section 2.3.1.1. The product obtained was a dark brown powder with ~ 85 % yield.

(b) Synthesis Of HA-Magnetite Nanocomposites

Hydroxyapatite nanoparticles were prepared using a similar method as described in section 2.3.1.1. Composite materials of magnetite-HA were made by passing HA and magnetite through a CPFS system with a total flow rate of 40 mL min^{-1} at 70 °C.

2.5.2 HA-Titania Nanocomposites

(a) Synthesis of Titania

Titania samples were made using a CPFS system, which consists of two HPLC Gilson pumps fitted with 25 mL pump heads. In the synthesis process, 0.25 M titanium oxysulfate solution and 0.20 M basic solution of potassium hydroxide were pumped to meet at a T-piece. The pH of both the solutions prior to the reaction was kept above pH 10. This initial mixture was connected to 8 m long PTFE tubing which was coiled inside an oil bath which gave an effective 5 minutes from the tee to the exit of the pipe. The suspension was collected in a beaker at the exit point and then centrifuged as described in section 2.3.1.1. The product obtained was a white powder dark with ~ 85 % yield.

The obtained powder was compacted into cylindrical discs of 13 mm diameter and 2 mm thickness using a laboratory hydraulic press at 5 MPa. These samples were used for cell viability studies after sterilization in 70 % ethanol for 1 hour.

(b) Synthesis of HA-Titania Nanocomposites

The hydroxyapatites nanoparticles were obtained following a similar procedure as described in section 2.3.1.1. Composite materials of Titania-HA were made by passing HA and titania suspensions through a CPFS system. The details of which are described in section 2.2.1. The reactions were carried out by setting the total flow rate to 40 mL min^{-1} at 70 °C. The final precipitates were centrifuged and freeze dried as explained in section 2.3.1.1. The product obtained was a white powder with ~ 85 % yield.

The obtained powder was compacted into cylindrical discs of 13 mm diameter and 2 mm thickness using a laboratory hydraulic press at 5 MPa. These samples were used for cell viability studies after sterilization in 70 % ethanol for 1 hour.

2.5.3 HA Based Dental Nanocomposites

(a) Synthesis of Surface grafted hydroxyapatite

The surface modified hydroxyapatites were obtained following a similar procedure as for pure nano-HA (mentioned above in section 2.3.1.1), except the calcium containing precursor additionally contained the appropriate amount of (0.05 M) functionalised carboxylic acid or organic phosphoric acid. The resulting nanopowders were termed PVA-HA (polyvinyl alcohol), AA-HA (adipic acid), CA-HA, (citric acid), VPA-HA (vinylphosphonic acid) and MA-HA (methacrylic acid).

(b) **Synthesis of surface grafted strontium hydroxyapatite**

The surface modified strontium (containing no calcium) hydroxyapatite nanopowders were prepared at 60°C using a simple continuous (plastic) flow synthesis system (CPFS). In the synthesis process, 0.5M basic solutions of strontium nitrate with organic surface modifier ($Sr+RCO_2^-R$) / P = 1.67) and 0.3 M diammonium hydrogen phosphate, respectively, were pumped to meet at a T-piece. The pH of both the solutions prior to the reaction was ideally kept above pH 12. This initial mixture was connected to an 8 m long pipe which was coiled inside an oil bath which gave an effective 5 minute residence time from the tee to the exit of the pipe. The product obtained was white fine powder with ~ 85 % yield.

(c) Synthesis of surface grafted barium hydroxyapatite

A similar procedure was adopted for the synthesis of Ba-hydroxyapatite using CPFS system as described earlier in section 2.2.1. In the synthesis process, basic solutions of barium hydroxide with organic surface modifier ($Ba+RCO_2^-R$) /P = 1.67) were used. The pH of both the solutions prior to the reaction was ideally kept above pH 12. This initial mixture was connected to an 8 m long plastic tube, which was coiled inside an oil bath that gave an effective 5 minutes residence time from the tee to the exit of the pipe. The obtained precipitates were centrifuged and freeze dried as described previously (section 2.3.1.1). The product obtained was dark brown powder with ~ 85 % yield.

2.5.4 Dental composite preparation

The organic matrix consisted of 60 wt% Bis-GMA and 40 wt% diluent TEGDMA as a comonomer. Various mass fractions of surface-modified hydroxyapatite, nanoparticles were added into the monomer. The solution was stirred for 24 hrs and shifted to a light sensitive vial to avoid photocuring prior to addition of further components (initiator, coinitiator, filler). 0.5 wt% camphorquinone and 2 wt% dimethylaminoethyl methacrylate along with 0.2 wt% N, N-Dimethyl-p-toluidine were added into the monomer solution as the initiator and coinitiators, respectively. After mixing thoroughly for 2 hours, the mixture was carefully transferred into a disk shaped Teflon mold (diameter 6mm, thickness 1 mm). Then samples were photo-cured using a blue LED activation light (Demetron LC, Ser no 66004022, KERR corporation, Danbury). X-ray images were then taken of the samples after leaving the sample to cure for at least 30 minutes. A similar procedure was repeated for surface modified strontium and barium phosphates.

2.5.4.1 Depth of Cure Measurement

The degree of cure of visible light activated dental resins was recognized as important to the clinical success of these materials soon after these materials were introduced. The scraping off technique has been codified as the depth of cure measure in the ISO standard 4049. Three specimens of each material type, 4 mm in diameter and 6 mm deep were condensed into Teflon mould.

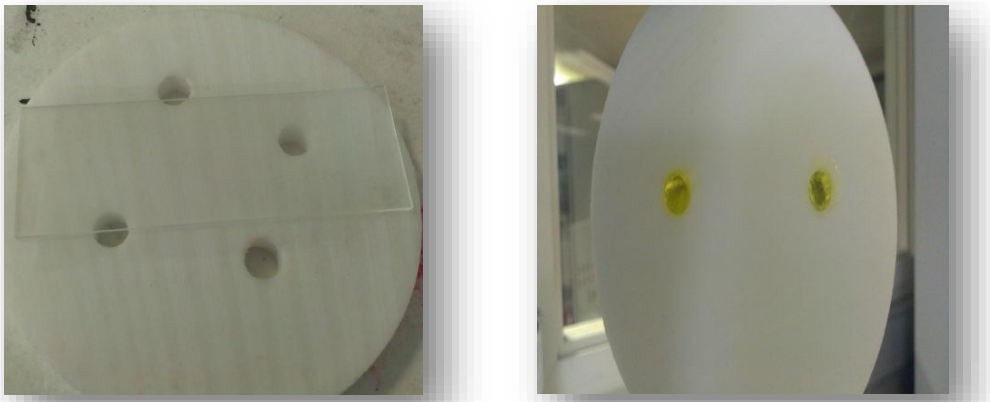

Figure 2-4 Showing the composite material condensed into Teflon mould.

A microscope glass slide was placed on top of the mould to hold the tip of the activating light 1 mm away from the surface of the resin. The specimens were activated for 20 secs using a blue LED activation light (Demetron LC, Ser no 66004022, KERR corporation, Danbury).

After activation, the specimens were immediately removed from the mould and the uncured material was scraped off with a spatula. The length of the remaining material was measured with a digital micrometer in three different places and an average length was obtained. This value was then divided by 2 to obtain the ISO 4049 depth of cure. The ISO 4049 standard requires that the result should be at least 1.5 mm for non-opaque shades and 0.5 mm for opaque shades.

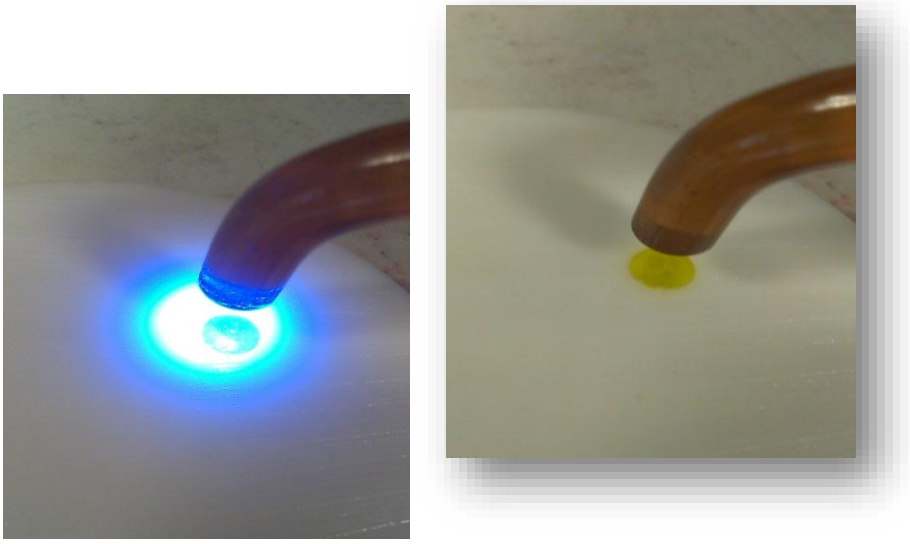

Figure 2-5 Light curing of composite for 20 sec using a high power blue LED activation light.

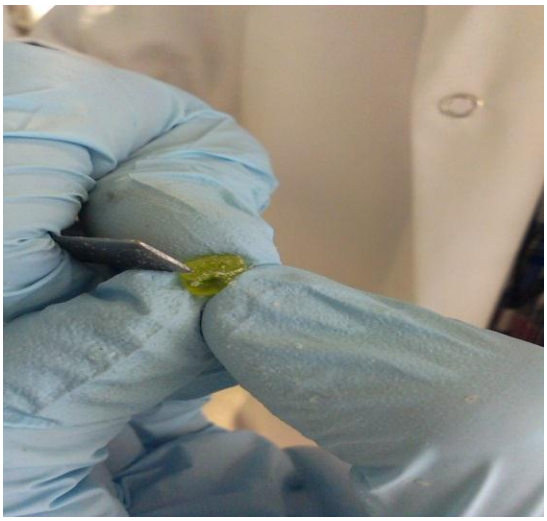

Figure 2-6 Peeling off the uncured material from the bottom of the sample using the spatula.

Figure 2-7 Measurement of the remaining thickness of the sample using a micrometer

2.5.4.2 Radiopacity image investigations

For each sample, a Teflon mould was used to produce three disks, measuring 6 mm in diameter and 1 mm in thickness, in accordance with ISO 4049. The specimens were photopolymerized using a blue LED light (Demetron LC, Ser no 66004022, KERR corporation, Danbury). The specimens were hand ground for few minutes using 150-grit sandpaper to create a flat surface. Specimens were measured using a digital micrometer. One specimen of each sample along with an aluminium wedge were placed side by side on an occlusal radiographic film. The Al step wedge served as a standard for each radiographic exposure. Films were exposed for 0.6 milliseconds using a radiography unit at 70 kV and 8 mA, the object to film distance was 300 mm.

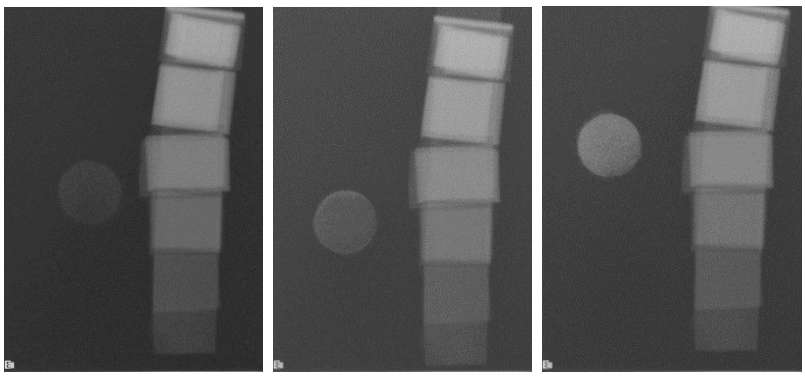

Figure 2-8 Radiographic images of calcium, barium and strontium-hydroxyapatite based dental composite

2.6 Characterization

The following are the techniques used to characterize all the samples obtained from the CPFS method.

2.6.1 Centrifugation

A Sigma 4K15 Centrifuge with a rotor housing four buckets, having a capacity of seven 50 mL Falcon tubes each, was used to centrifuge the aqueous slurries at 4500 rpm for 10 minutes (per 50 mL suspension), *ca.* 45 mL of liquid was removed from each sample and *ca.* 45 mL deionised water (>10 Mega Ohm) was added followed by vigorous shaking using a vortex mixer. Each sample was then recentrifuged at 4500 rpm for five minutes and *ca.* 45 mL liquid was removed to give concentrated slurry. Steps were repeated ca. 3-5 times to ensure the removal of all residual ions with neutral pH. The obtained concentrated slurry was then freeze dried for further analysis.

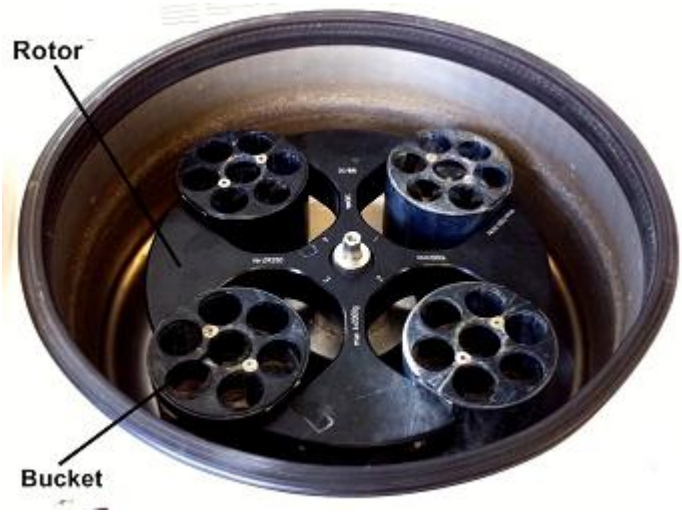

Figure 2-9 Centrifuge showing the rotor with a capacity of four buckets.

2.6.2 Freeze Drying

After centrifugation all samples were freeze dried using a VirTis Genesis Pilot Lyophilizer 35XL (SP Scientific UK) at 0.3 Pa for 24 hours. The samples obtained were first frozen in liquid N_2 prior to freeze drying.

2.6.3 Chemical analysis

Chemical analysis of all samples were carried out using Thermo Scientific K-Alpha X-ray photoelectron spectrometer with a two chamber vacuum system (loadlock and analysis chamber). The XPS used a monochromated Al K-alpha source (E = 1486.6 eV) with maximum power of 72 W. X-rays were microfocused at source to give a spot size on the sample in the range of 30–400 µm. The monochromator comprised of a single toroidal quartz crystal set in a Rowland circle with a radius 250 mm. The surface sensitivity (typically in the range 40-100 Å) makes this technique ideal for measurements of elemental ratio as oxidation states. The vacuum analysis chamber pressure was set at ~ 3x 10^{-8} Torr. The spectra were collected at an energy of 150 eV for survey scans and at 50 eV for high resolution regions. The detector used was a 128 channel position sensitive detector. The spectral intensity of the Ag 3d 5/2 peak from a clean metal sample was >2.5 Mcps at a FWHM of 1.0 eV. The XPS spectra were processed using the Casa^{TM} software. The binding energy scale was calibrated by a C 1s peak at 285.0 eV.

2.6.4 Scanning Electron Microscopy

A JEOL JS-6301F scanning electron microscope located at Department of Archaeology, University College London (UK) was used to analyse the nanoparticles prepared by the CPFS process. The SEM was operated at 25 kV and all samples were carbon coated prior to measurements.

2.6.5 Transmission Electron Microscopy

Transmission electron microscope (TEM) images were collected using a JEOL JEM-1200EX II Electron Microscope. Digital images were taken with a side mounted AMT 2K high sensitivity digital camera (Debens, East Grinstead, UK). A small amount of sample (< 10 mg) was dispersed in 10 mL neat methanol (Merck, Darmstadt, Germany) and then ultrasonicated (Model USC100T, VWR, East Grinstead, UK) for 2 minutes to yield a very dilute suspension. A few drops of the resulting suspension were then deposited on a carbon-coated copper grid (Agar Scientific, Stansted, UK) which was used as the TEM specimen. The grid was dried in air at room temperature prior to use

in the double tilt holder of the TEM. Image J™ software (version 5.0) was used for estimating particle sizes, using a sample of 200 particles for each measurement.

2.6.6 Powder X-ray Diffraction

A Bruker AXS D4 Endeavour™ XRD diffractometer was used for XRD collection of all samples. The data were collected in the 2θ range from 5 to 80 ° with a scanning step of 0.05 ° and a count time of 2 sec.step^{-1} using Cu-Kα radiation (λ = 1.5406 Å). DIFFRACplus Eva™ software was used for the phase analysis of the data by spectral matching with standard reference patterns. The crystallite sizes were estimated by using the Scherrer equation.

$$\mathbf{L = 0.9\ \lambda\ /\ \beta\ \cos\ \theta}$$

Where L = crystallite size, β = full-width half maximum, λ = wavelength of X-rays (1.5406 nm for Cu- Kα), and θ is the angle corresponding to the peak.

2.6.7 FTIR Spectroscopy

Chemical structural properties of HA and other Group 2 metal phosphates were analysed using Fourier Transform Infrared spectroscopy (FTIR), Nicolet 6700 FTIR (Thermo Nicolet, UK). A Photo-Acoustic sampling accessory was used, which allowed analysis of neat samples, without the need for any sample preparation. The sample chamber was purged with helium gas. The FTIR spectra were collected in the range 4000 - 400 cm^{-1} at 4 cm^{-1} resolution averaging 256 scans. Background was obtained using carbon black.

2.6.8 Raman Spectroscopy

A Confocal Raman Thermo Nicolet DXR™ Spectrometer, equipped with a 780nm laser was used in order to obtain further confirmation of chemical structural properties and in addition provide supplementary crystallographic data and confirm substitutions in the apatite lattice. Samples were analysed in powder form as neat materials without any

sample preparation. The spectral Acquisition parameters used were; 100 scans, 5.4 mw laser power, and the spectra obtained at 4 cm^{-1} resolution.

2.6.9 BET Surface Area Analysis

BET surface area (N_2 adsorption) measurements of all samples were made using an ASAP 2420 micromeritics BET machine which is capable of analysing six samples simultaneously, whilst degassing twelve additional samples. Prior to use, sample tubes were washed with methanol and then dried overnight in an oven at 100 °C. The powder samples were accurately weighed and degassed for 12 hours at 180 °C prior to BET analyses.

After degassing, they were weighed again and then analysed for nitrogen absorption. Liquid N_2 was supplied by BOC, UK. The absorption isotherm data and surface area were recorded for different samples.

Figure 2-10 BET surface area analysis measurement

2.6.10 Dynamic light scattering

DLS measurements were taken using a Malvern Instruments Zetasizer operated in backscatter (173 °) mode. The sample slurry produced by the CPFS process (solid content ~ 1% by volume) was diluted with methanol then placed in an ultrasonic bath for 10 minutes to disperse the sample. Square cuvettes with a path length of nominally 10 mm were used for measurements. The intensity of light scattered by the sample was recorded with the measurement angle of 173 °). The hydrodynamic diameter was taken as an average of at least ten measurements.

2.6.11 Zeta potential measurements

Zeta potential measurements were taken using a Malvern Instruments Zetasizer operated in backscatter mode (173 °). The electrical charge on the particle surface which provides information about the colloidal stability of the system was performed by using a procedure based on the knowledge of zeta potential, by application of the Helmholtz-Smoluchowski model [30-32]. The relationship between electrophoretic mobilitiy and zeta- potential is shown by this equation.

$$Ue = 2\varepsilon z f(Ka) / 3\eta$$

where Ue is the electrophoretic mobility, ε is the dielectric constant, z is the zeta potential, *f(Ka)* is Henry's function, and η is the viscosity.

The measurements were carried out using an electrophoretic technique in which the sample slurry produced by the CPFS process (solid content ~ 1% by volume) was diluted with methanol then placed in an ultrasonic bath (Model USC100T, VWR, East Grinstead, UK) for 5 minutes to disperse the sample. A clear disposable zeta cell was used as a measurement chamber for analysis and the colloidal stability was determined by measuring electrophoretic mobility of the dispersed particles in the applied electric field. The reported values for zeta potential are the average of at least three repeat measurements.

2.6.12 Electrophoretic deposition

Electrophoretic deposition was carried out in a self-made EPD cell, consisting of a 250 ml glass beaker and a holder for fixing electrodes. The electrodes were parallel to each other connected to a MA410 3DC power supply. Both the cathode and anode were of the same dimensions. The deposition electrode was the cathode. The deposition of HA particles on the 316L stainless steel substrate was performed at the constant voltage of 50 V and various deposition times ranging from 1 min. to 20 min. For this purpose, a 2 wt% suspension of HA was prepared by suspending 2g of the powder in 100 mL ethanol. Electrodes were dipped in the suspension and the distance between two electrodes was kept at 2 cm. For a uniform deposition and acquirement of stable suspension, the suspension was ultrasonicated for 10 minutes prior to deposition on the metal substrate.

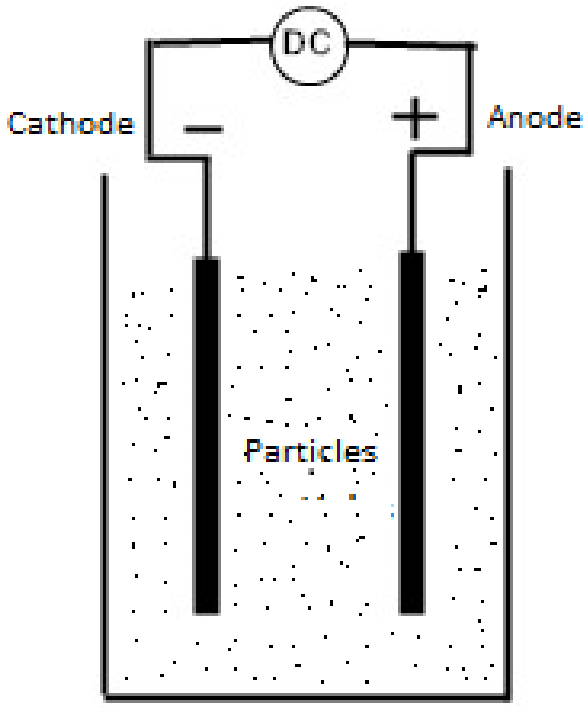

Figure 2-11 Schematic diagram of electrophoretic deposition of dispersed nanoparticles

2.7 In vitro biocompatibility

2.7.1 Culture of human osteoblast cells

MG63 human osteocarcoma-osteoblast cells were expanded in complete culture medium consisting of Dulbecco's Modified Eagle's Medium (DMEM) (Biosera, Uckfield, East Sussex, UK) supplemented with 10 % fetal calf serum (FCS), 2 mM L-glutamine and 100 $mg.mL^{-1}$ penicillin and streptomycin (Sigma-Aldrich, Dorset, UK). Cells were kept incubated at 37 ^{o}C with a 95 % oxygen and 5 % CO_2 humidified atmosphere and media changes were performed every 2-3 days. The disc-shaped sample pellets (13 mm diameter) were sterilised in 70 % ethanol for 1 hour followed by PBS washes. Sample discs were then seeded with 25,000 cells and cultured for 7 days with media changes every 2-3 days. MG63 cells were used between passages 60-65 and cellular responses to the sample discs were evaluated by cell viability assay and cell morphological appearance.

2.7.1.1 Cell viability

Cell viability of MG63 cells on sample discs was assessed at days 1, 4 and 7 of culture using Resazurin (7-hydroxy-3H-phenoxazin-3-one-10-oxide) assay. The Resazurin assay incorporates an oxidation-reduction (REDOX) indicator that fluoresces in response to metabolic activity from growing cells. Briefly, culture medium was removed from cells and a known amount of fresh medium containing 0.1 mM Resazurin sodium salt (Sigma-Aldrich, Dorset, UK) was added and cells were incubated at 37 ^{o}C for 4 h. Negative controls or sample discs with no cells showed a blue coloured solution (oxidised) while samples with cells showed a purple-pink coloured solution (reduced). Reduction of Resazurin was detected using fluorescence in opaque 96-well plates on a FLx800 microplate fluorescence reader (BioTek, Potton, Bedfordshire, UK) using wavelengths of 540 nm excitation and 635 nm emission.

2.7.1.2 Cell morphology

Cellular morphology of MG63 cells on sample discs was visualized at day 7 using fluorescence microscopy. Briefly, cells were fixed in 3.7 % formaldehyde and permeabilized with 0.5 % Triton-X100 before staining with DAPI (4′,6-diamidino-2-phenylindole dihydrochloride) (1 µg mL^{-1}) and phalloidin-TRITC (phalloidin-tetramethylrhodamine B isothiocyanate) (1 µg mL^{-1}) (Sigma-Aldrich, Dorset, UK) for cell nucleus and actin-cytoskeleton respectively. Images were captured using an Image Express™ epifluorescent microscope (Axon Instruments/Molecular Devices, Union City, CA, USA) using the built in x20 objective. Individual images of nucleus and cytoskeleton were compiled together using Image J™ (Image Processing and Analysis in Java, National Institute of Health, Bethesda, Maryland, U.S.).

2.7.1.3 Statistics

All material characterization techniques were performed on all samples using the CPFS reactor. Cell experiments were performed twice in triplicate and samples made at different reaction conditions were compared for significant differences using one-way ANOVA followed by Tukey's post-hoc test. All quantitative data are presented as mean ± standard deviation. Significant differences are marked as * $p < 0.05$.

Chapter 3
Rapid and Continuous Plastic Flow Synthesis of Phase Pure Nano-Hydroxyapatite

3.1 Introduction

Calcium phosphates (CaP) are well known for their use as bone graft substitutes, coatings on metallic implants, as reinforcements in biomedical composites and as components in bone and dental cements (Elliott, 1994, Hench, 1991, Willems et al., 1992). Hydroxyapatite (HA) [$Ca_{10}(PO_4)_6(OH)_2$] is chemically similar to biological apatite, the main mineral constituent of teeth and bone (Liu et al., 2001a), and exhibits comparable biocompatibility, bioactivity and low solubility in wet media. HA and other calcium phosphates have been employed as scaffold materials to encourage new bone formation for osteoinductive coatings on metal implants and as a bulk bone filler (Hench, 1998b, Hench, 2000, Katti, 2004). The dissolution of calcium phosphate bioceramics (*in vivo* and *in vitro*) is highly dependent on the particle size, composition, and crystallinity of the powder as well as the pH of the solution in question (Klein et al., 1990, Ducheyne et al., 1993).

Multiple techniques have been used for the preparation of HA powders and coatings including solid state syntheses (Güler et al., 2011), spray pyrolysis (Jokanović and Uskoković, 2005), sol gel techniques (Hench and West, 1990), chemical vapour deposition (CVD) (Darr et al., 2004), solvothermal processes (Wang et al., 2006b), microwave synthesis (Nazir et al., 2013) and wet precipitation methods (Haque et al., 2007). The majority of the described literature methods for the production of nano-sized HA powders are either multi-step, inconsistent, energy intensive or time consuming (Wang et al., 2006b, Pang and Bao, 2003, Phillips et al., 2003, Lim et al., 1997, Kothapalli et al., 2005, Kim et al., 2005) and the wet chemical methods almost always require very careful control over reaction pH during the mixing of two or more reagents. For example, batch hydrothermal syntheses of HA powders have normally been performed in the temperature range 60 – 150 °C for up to 24 h to produce crystalline HA rods that are usually agglomerated (Arce et al., 2004). For room temperature batch syntheses, failure to permit enough maturation time for the reagents

gives a non-stoichiometric as-prepared powder, which then phase separates into two phases upon heat-treatment, which can affect biological properties *in vivo* (Li-yun et al., 2005). Thus, there is an interest in developing simple, low cost, and reproducible techniques, which could work under relatively mild conditions to synthesize high purity HA and other ceramic materials in a short timeframe with well-defined particle size.

Hydroxyapatite synthesized by the different aforementioned literature techniques is considered to be an ideal and frequently studied biomaterial for coating depositions on metallic implants. Multiple techniques have been used for the preparation of HA coating deposition on metallic implants such as sputter coating (Lacefield, 1988), plasma spraying (Dey et al., 2009), pulse laser deposition (Paital et al., 2010), dip coating (Wang et al., 2010), doctor blade (Yano et al., 1998) and electrophoretic deposition (Stoch et al., 2001). The major problems related to high temperature deposition processes, such as plasma spraying, besides the HA decomposition, are associated with difficulties to produce a uniform coating over the complex substrate geometry. To overcome these issues the electrophoretic deposition (EPD) of high surface area of as-prepared HA nano-precipitates can be used. This is an alternative to using commercially available pre-calcined powders, which densify at temperatures typically higher than 1200 °C on metal substrates (Kaminski et al., 1968, Balla et al., 2010, Kim et al., 1997).

Electrophoretic deposition (EPD) is a versatile, cost effective, simple and rapidly expanding method attracting increasing interest as an important tool in advanced materials processing and nanotechnology for a wide range of technical applications (Ryan et al., 2006, Iqbal et al., 2012, Zhitomirsky and Gal-Or, 1997). In order to effectively apply this technique to process materials, it is essential to produce a stable suspension containing charged particles free to move when an electric field is applied. Therefore EPD can be applied to any solid that is available as a fine powder or as a colloidal suspension, including metals, polymers, ceramics and glasses. However, a post-sintering step is normally needed to further densify the deposit, to eliminate porosity and to enhance the bonding strength between coating and metal substrate (Paital and Dahotre, 2009, Sygnatowicz and Tiwari, 2009, Fathi and Doostmohammadi, 2009). Metals are frequently used as orthopedic implants because of their mechanical properties and formability (Sarkar and Nicholson, 1996, Wei et

al., 2001). However, metals are nonbioactive with poor adhesion strength and release toxic ions when in direct contact with surrounding living tissue (Boccaccini and Zhitomirsky, 2002, Van der Biest and Vandeperre, 1999). Therefore, coating of metal implants with bioceramics, such as hydroxyapatite (HA) or bioactive glass encourages natural bone growth at the interface of the prosthetic device (Heavens, 1990, Besra and Liu, 2007).

The UCL Clean Materials Technology Group has prior expertise in use of high temperature routes to HA and its variants, and they recognize the limitations of the process, namely that the CHFS process uses high temperatures and pressures to generate bioceramics which are likely to be contaminated with metals from the reactors at levels that are far above those which would be acceptable for their use in clinical applications. Furthermore, many of the particle sizes obtained (65-150 nm) in such reactors are not particularly small indeed are very similar to those obtained using more conventional synthesis methods (Chaudhry et al., 2006, Chaudhry et al., 2008, Darr and Poliakoff, 1999). Smaller particles would open up and improve many applications such as more rapid dissolution (due to higher surface area) or use as injectable or as a hard filler for bone replacement. Therefore, there is a desire to be able to produce smaller nano-sized calcium phosphates using methods which allow for fine control over particle sizes, preferably under relatively mild conditions of temperature and pressure, and with a purity acceptable for use in a clinical setting such as for bone replacement.

In this chapter, the rapid and continuous plastic flow synthesis (CPFS) reactor for the production of phase pure stoichiometric HA at (near) ambient conditions (room temperature to up to 80 °C), and at atmospheric pressure over a period of a few minutes is described. In this new flow system, aqueous solutions of calcium nitrate tetrahydrate and diammonium hydrogen phosphate were mixed and heated for a residence of 5 minutes at a pH in the range ca. 10-11. It was observed that particle properties could be affected, e.g. such as particle size and shape, by selection of conditions such as the bath temperature, reaction pH, reaction time in flow and variation in Ca:P ratio [UK Patent Filed Application No. 1317747.2].

3.2 Experimental

3.2.1 Synthesis of Stoichiometric Nano-Hydroxyapatite

Method 1: Phase pure nano-hydroxyapatite (HA) was prepared using a simple CPFS system as described in section 2.2.1. The experimental process involved pumping 0.3 M phosphoric acid solution and 0.5 M calcium hydroxide solutions into the CPFS reactor (Ca:P molar ratio 1.67) via separate Gilson pumps. Both reagent solutions were pumped at 20 mL min^{-1}, to meet at a T-piece. This initial mixture was connected to 8 m long tubing (surrounded by an oil bath set at the desired temperature). The flow rates used for calcium hydroxide and phosphoric acid solutions for pump 1 and pump 2, respectively, were selected to give a total residence time of 5 minutes. The product suspension was collected in a beaker at the exit point of the process. The precipitation of HA can be described by equation.

$$10[Ca(OH)_2] + 6\ H_3PO_4 \longrightarrow [Ca_{10}(PO_4)_6(OH)_2] + 18\ H_2O$$

Method 2: Pure nano-hydroxyapatite (HA) was-prepared using a CPFS system the design of which is described in section 2.2.1. The reagents used in the process were 0.3 M diammonium hydrogen phosphate solution and 0.5 M calcium nitrate solution, respectively (gives Ca:P molar ratio 1.67). The pH of the precursors was made up to 10 by adding 5.0 mL and 15.0 mL of ammonium hydroxide to calcium nitrate (500 mL), and diammonium hydrogen phosphate solutions (500 mL), respectively. Both reagent solutions were pumped at 20 mL min^{-1}, The flow rates used for calcium nitrate and diammonium hydrogen phosphate solutions for pump 1 and pump 2, respectively, were selected to give a total residence time of 5 minutes and the product suspensions were collected in a beaker at the exit point of the process. The precipitation of HA can be described by the following equation.

$$10[Ca(NO_3)_2.4H_2O] + 6[(NH_4)_2HPO_4] + 8NH_4OH \longrightarrow [Ca_{10}(PO_4)_6(OH)_2] + 20NH_4NO_3 + 46\ H_2O$$

The aqueous suspension obtained from both procedures were washed, centrifuged, frozen and then freeze-dried. Details are given in section 2.3.2. The as prepared HA samples were each heat-treated at 1200 °C for 1hr according to ISO standard methods [ISO13779-3] to confirm the thermal stability and phase purity of the obtained nanopowders.

3.2.1.1 HA Disc Preparations

For cell biocompatibility studies, the obtained as-prepared powder was compacted into cylindrical discs of 13 mm diameter and 2 mm thickness by using a laboratory hydraulic press at 5 MPa.

3.2.1.2 Electrophoretic Deposition Procedure

A 2 wt% suspension of HA was prepared by suspending 2 g of the powder in 100 mL ethanol. Electrodes were dipped in the suspension and the distance between the two electrodes was kept 2 cm. For a uniform deposition and acquirement of stable suspension, the suspension was utrasonicated for 10 minutes prior to deposition on metal substrate.

Electrophoteric deposition was carried out in a self-made EPD cell, consisting of a 150 mL glass beaker and a holder for fixing electrodes at a distance of 15 mm. The electrodes were parallel to each other connected to a MA410 3DC power supply (Iskra). Both the cathode and anode were of the same dimensions. The deposition electrode was the cathode. The electrophoretic deposition of HA particles on the 316L stainless steel substrate plates was performed at a constant voltage of 50 V, since it was determined to be optimal for EDP of HA deposition onto the 316L steel. The experiments were performed at various deposition times ranging from 1 min. to 20 min. at constant voltage of 50 V. The current density of 1 mA was recorded during the deposition process. The coated substrate was withdrawn from the suspension and dried in a convection oven at 80 °C for 24 h. In order to obtain a thick HA coating, a repeated deposition method was employed instead of single deposition to overcome deposit spalling problem. The quality of coatings not only depends strongly on the applied current density and the corresponding voltage but also on the conductivity and Zeta potential of the HA

suspension. Coating morphology was studied by scanning electron microscopy (Jeol, model JSM-6301F).

3.2.2 Synthesis of Hydroxyapatite and Effect of System Parameters

3.2.2.1 Effect of Reaction Temperature

Six separate reactions were carried out to study the effects of different reaction temperatures on the end products using the CPFS system and keeping all other parameters same. The CPFS system is described in section 2.2.1.

For each case, samples were synthesized under basic pH 10 conditions with a Ca:P ratio of 1.67. 59 g (0.25 moles) and 19.8 g (0.15 moles) of calcium nitrate and diammonium hydrogen phosphate were separately dissolved in 1000 mL deionised water for stock solution. The pH was adjusted to pH 10 by adding 30 mL ammonium hydroxide solution to each solution. The samples were labeled as HA30, HA40, HA50, HA60, HA70 and HA80 (where the number represents the bath temperature), depending on reaction temperatures ranges from 30 to 80 °C, respectively. The pH values were measured from suspensions immediately after collection.

Pump rates of 20 mL min^{-1} were used for calcium nitrate and diammonium hydrogen phosphate solutions. All reactions were carried out at atmospheric pressure. Results showed that apatite obtained below 60 °C after heat-treatment at 1200 °C for 1 hour was impure synthetic hydroxyapatite whilst phase pure hydroxyapatite was obtained at 60, 70 and 80 °C, respectively. Details are summarized in Table 2-3.

3.2.2.2 Effect of Different Flow rates

In total, five different reactions were carried out using the CPFS system (described in section 2.2.1). 59 g of calcium nitrate were dissolved in 1000 mL deionised water to result in 0.25 M stock solution. The pH of this solution was adjusted to pH 10 by adding 30 mL of neat ammonium hydroxide solution. 19.8 g of diammonium hydrogen phosphate were dissolved in 1000 mL of deionised water to result in a 0.15M stock solution. Reactions were carried out using 200 mL of calcium nitrate and diammonium hydrogen phosphate solutions for each case.

The calcium nitrate and diammonium hydrogen phosphate solutions were pumped at 50, 40, 30, 20 and 10 mL min^{-1}, respectively at 60 °C and atmospheric pressure. After collection, all samples were centrifuged, washed and freeze-dried as explained earlier; see section 2.3.1.1. The product was obtained as a free flowing fine white powder with ~ 85 % yield.

3.2.2.3 Effect of Precursor Concentration

A series of experiments (six in total) were carried out by varying concentration and by keeping all other parameters the same. For each case, samples were synthesized under basic pH 10 conditions with Ca:P ratio 1.67.

The fine HA powder obtained from all reactions using different concentration were hereafter referred as 1HA, 0.5HA and 0.25HA and 0.125HA.. It was observed that tailoring reaction concentration while keeping the reaction time at five minutes in all reactions greatly influenced the particle size and specific surface area (summarized in Table 2-5). All reactions were carried out at 60 °C and atmospheric pressure. The product was obtained as fine white powder with ~ 85 % yield.

3.2.2.4 Effect of System Parameters on Surface Area and Yield

In total, seventeen different reactions were carried out by changing reaction temperature, flow rate and concentration using the CPFS system described in section 2.2.1. For each case, samples were prepared under pH 10 conditions with Ca:P ratio 1.67. All temperature, flow rate and concentration regime designations are summarized in detail in tables 2-4, 2-5 and 2-6, respectively.

The surface area and product yield of all these reactions were calculated and it was observed that by increasing reaction concentration and temperature, surface area decreased, whereas particle size increased with almost the same product yield (~ 85 %).

3.3 Results and discussion

3.3.1 Synthesis of Hydroxyapatite (Effect of Temperature)

3.3.2 Transmission Electron Microscopy

Transmission electron microscope images of sample HA60 as shown in Figure 3-1 confirmed that small crystallites had been obtained.

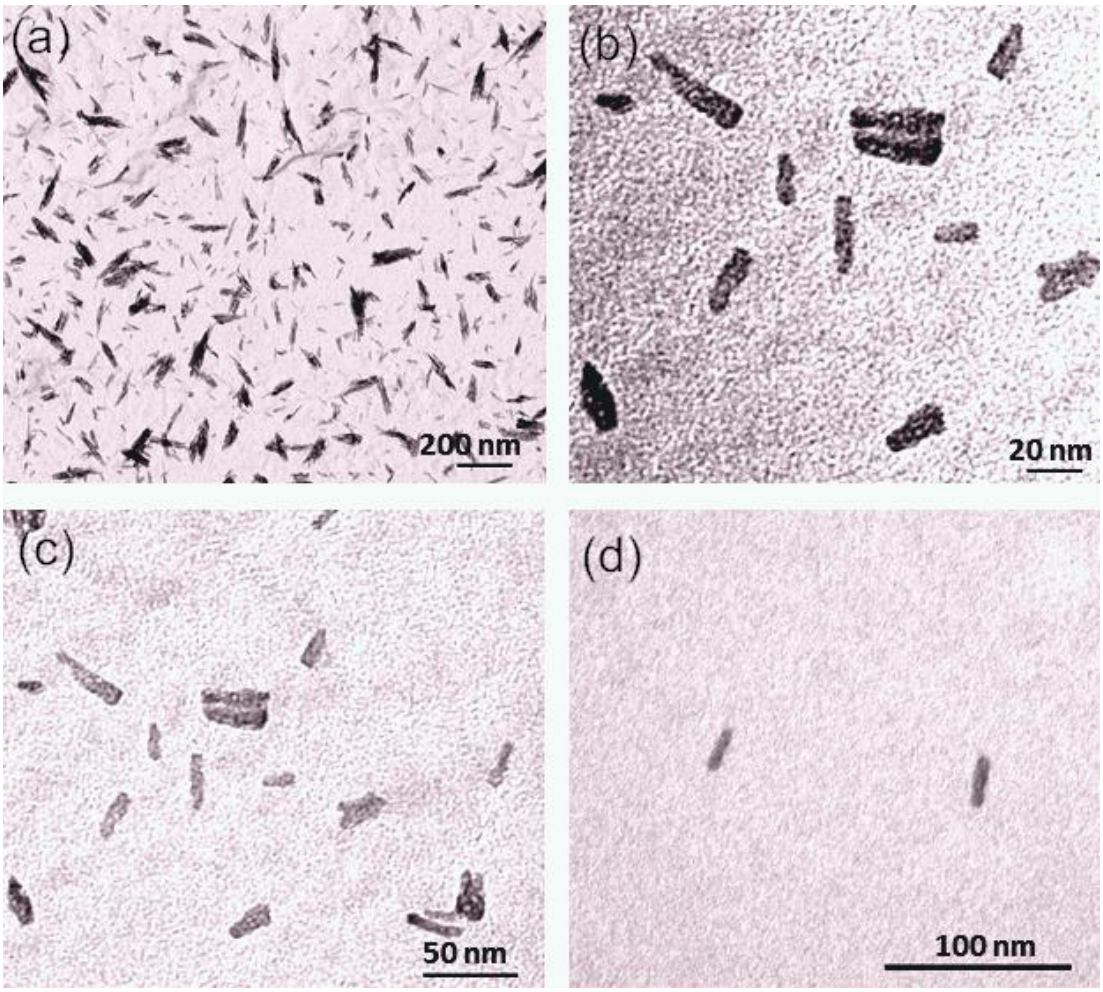

Figure 3-1 Transmission electron microscope images of hydroxyapatite nano-rods of sample HA60 synthesized using calcium nitrate and diammonium hydrogen phosphate precursors at 60 °C and five minutes residence time via CPFS (a), bar = 200 nm, (b), bar = 20 nm, (c), bar = 50 nm and (d), bar = 100 nm.

Phase pure as prepared HA synthesized using calcium nitrate and diammonium hydrogen phosphate solutions as starting materials at 60 °C in the CPFS system had a rod like particulate morphology and average length along the longest axis of each particle was *ca.* 25 ± 5 nm and 5 ± 1 nm along the smaller axis (200 particles sampled). The phase pure HA particles synthesized using calcium hydroxide and phosphoric acid solutions as starting reagents as shown in Figure 3-2, had almost the same particle size (*ca.* 20 ± 5nm) and surface area (254 m^2g^{-1}). This study revealed that the CPFS process works equally well with different nature of precursors (acidic or basic).

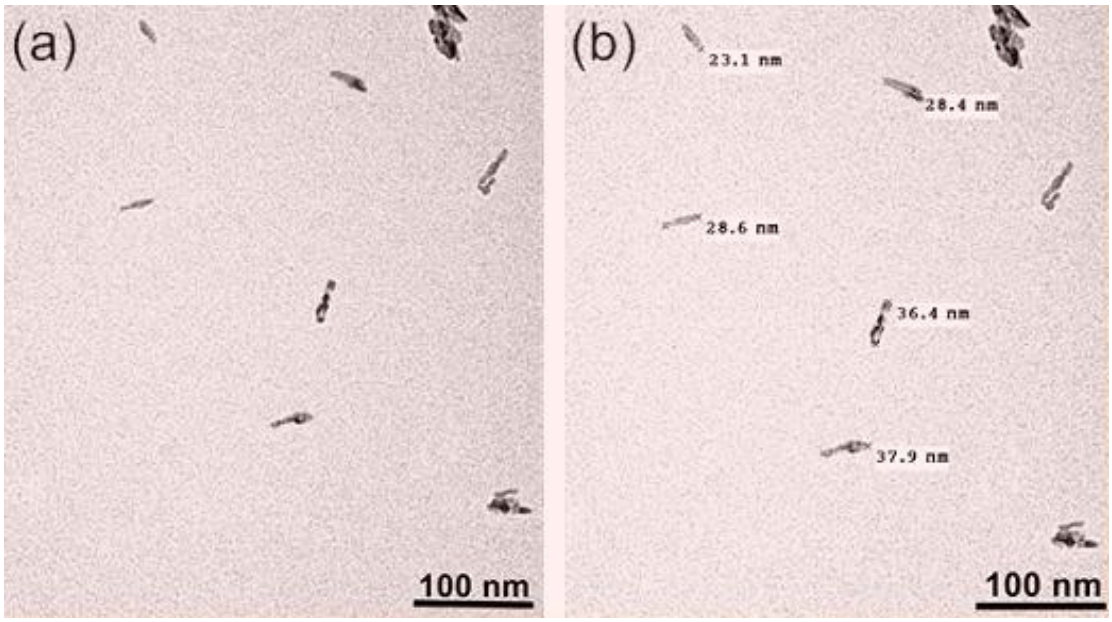

Figure 3-2 Transmission electron microscope images of hydroxyapatite nano-rods of sample HA60 synthesized using calcium hydroxide and phosphoric acid precursors at 60 °C and five minutes residence time via CPFS (bar = 100 nm).

Hydroxyapatite nanoparticles obtained at 70 and 80 °C possessed particle size of ~ 80 ± 15 nm and ~ 95 ± 15 nm along the longest axis *ca.* 12 ± 5 nm and 15 ± 5 nm along the smaller axis (200 particles sampled) as shown in Figure 3-1. These results showed that reaction temperature is one of the key factor for attaining different particle sizes.

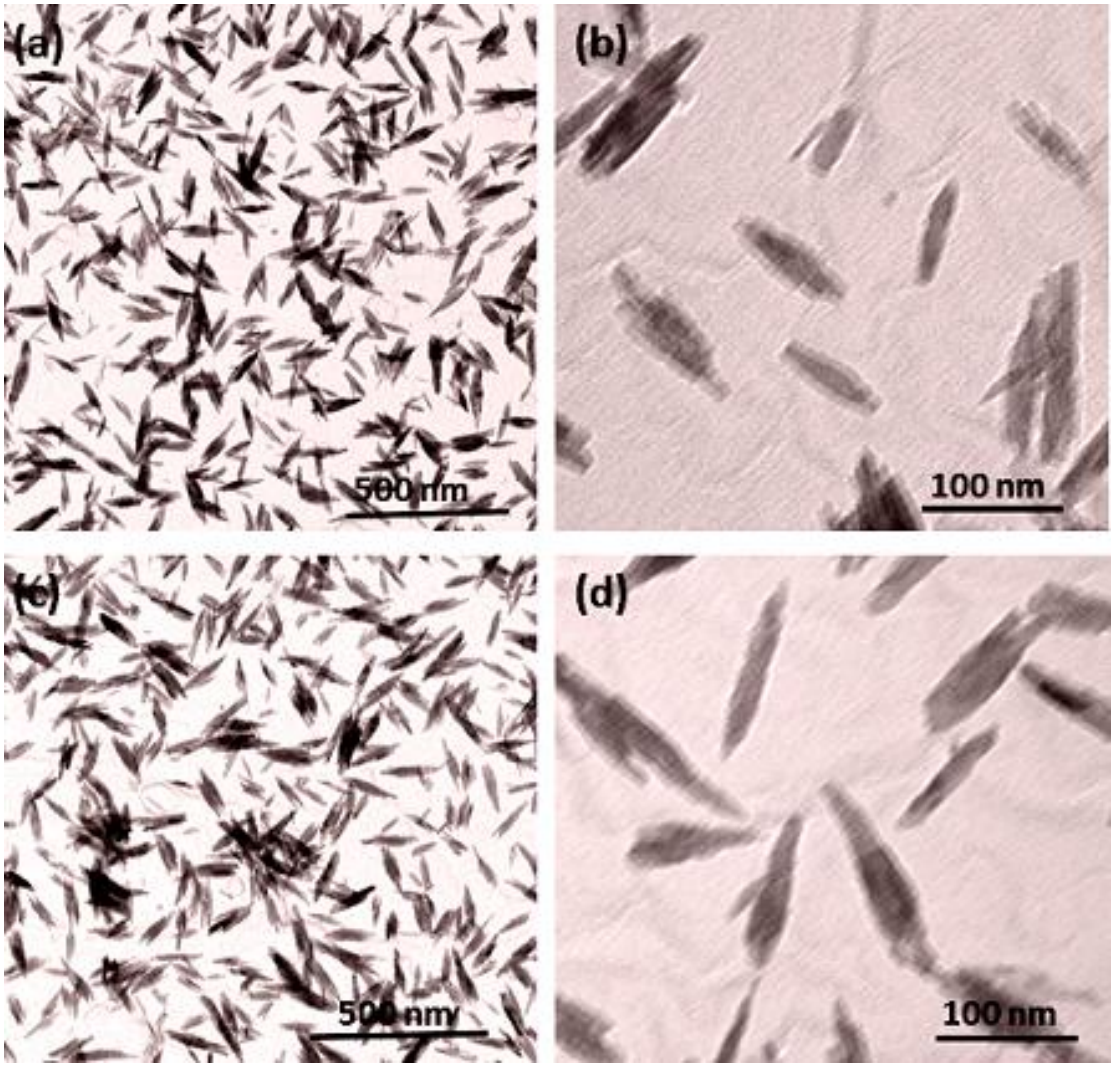

Figure 3-3 Transmission electron microscope images of hydroxyapatite nano-rods of samples HA70 and HA80 synthesized at 70 and 80 °C in five minutes residence time via CPFS (a), (bar = 500 nm), and for (b), (bar = 100 nm).

3.3.3 Scanning Electron Microscopy

Hydroxyapatite sample synthesized at 60 °C in five minutes residence time and heat-treated at 1200 °C for 1 hr possessed particle sizes of *ca.* 120 ± 15 nm along the longest axis and 60 ±10 nm along the smaller axis (200 particles sampled) as shown in Figure 3-4 (a) and (b). SEM images were also captured for both as prepared and heat-treated (1200 °C, 1h) HA60 samples as shown in Figure 3-4 (c) and (d) respectively.

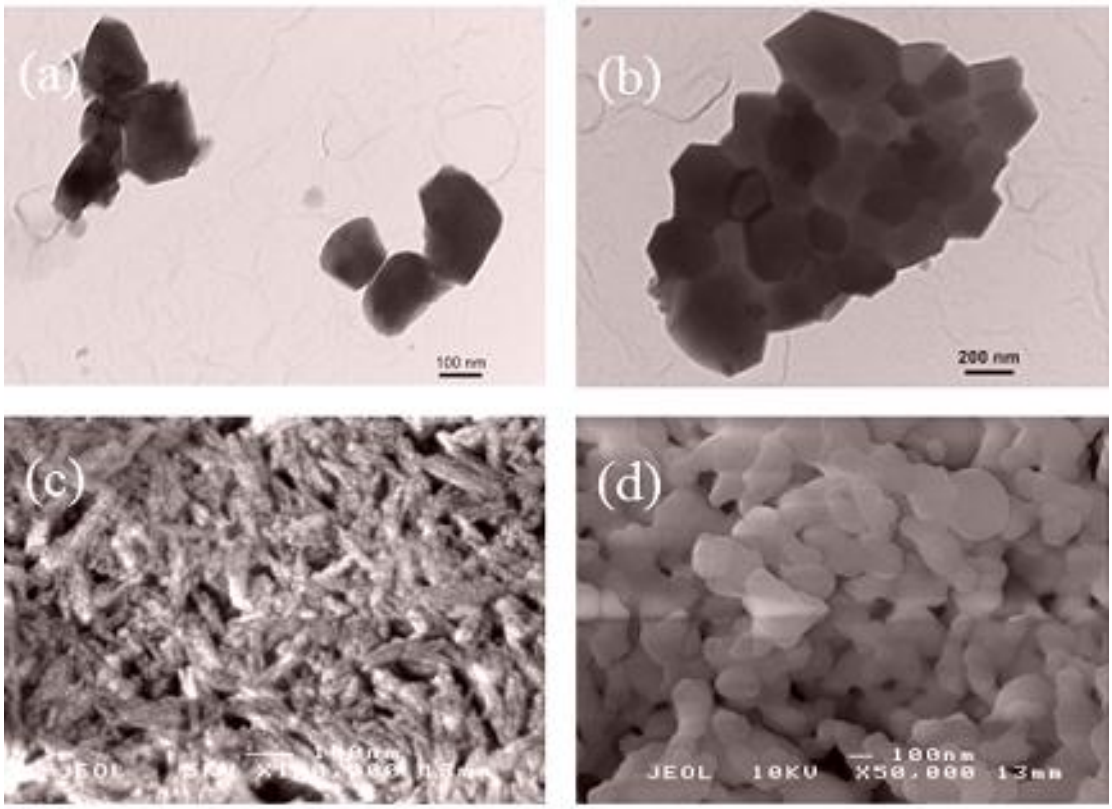

Figure 3-4 TEM images (a,b) and SEM images (c,d) of heat-treated hydroxyapatite nano-rods of samples HA60.

3.3.4 BET Surface Area Analysis

It was observed that tailoring the reaction temperature (60 – 80 °C), while keeping the reaction time constant at 5 minutes, greatly influenced the particle size and specific surface area as shown in Fig. 3-3. BET surface area measurements of as prepared HA60 possessed a remarkably high surface area of 263.9 m^2g^{-1}. To the best of our knowledge this is one of the highest surface areas ever reported in the current literature for as prepared phase pure HA powdered needles. HA70 and HA80 samples made with the same residence time of 5 minutes, revealed smaller suface areas of 195.48 and 113 m^2g^{-1} respectively. On the other hand, heat-treated HA60, HA70 and HA80, revealed surface areas of 9.5 ± 0.1, 5.9 ± 0.1 and 4.9 ± 0.1 m^2 g^{-1}, respectively.

3.3.5 Powder X-ray Diffraction

The powder X-ray diffraction data of phase pure hydroxyapatites generally displayed broad peaks due to the apatite structure as shown in Figure 3-5. Post synthesis heat-treatment studies were performed on all three as prepared HA samples made at 60, 70 and 80 °C respectively, to confirm the phase purity and stoichiometry of as prepared samples.

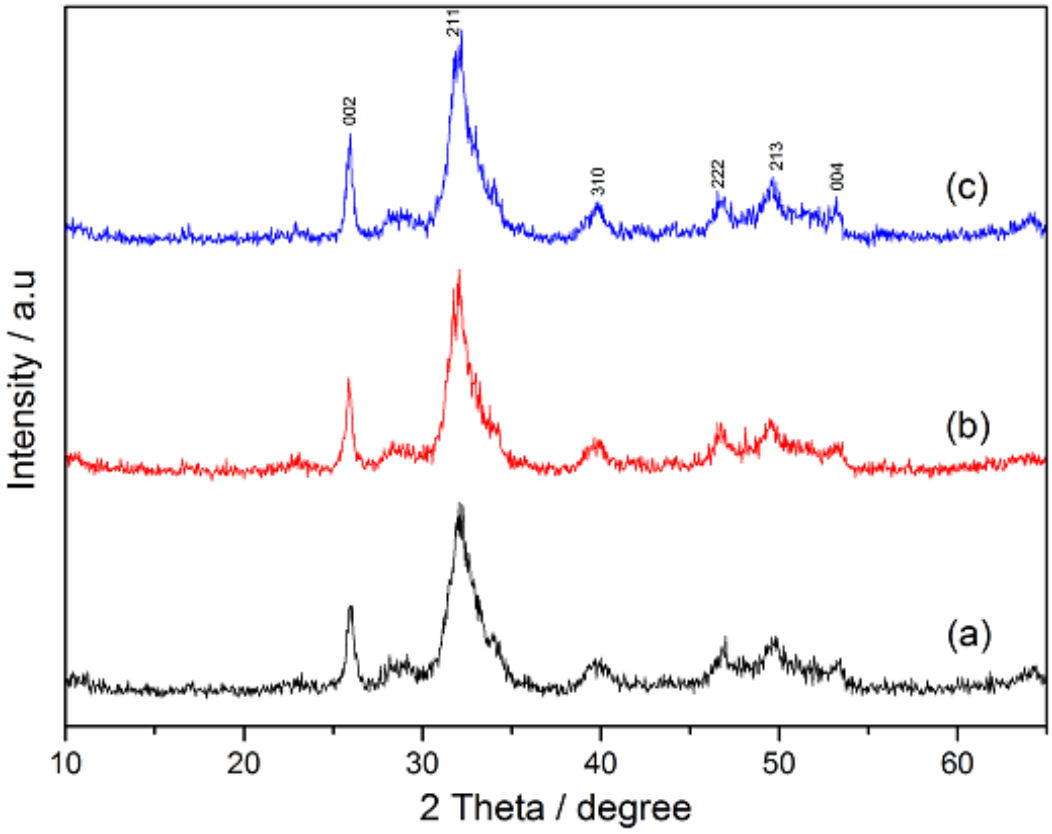

Figure 3-5 Powder X-ray diffraction patterns of phase pure as prepared hydroxyapatite made at temperature (a), 60 °C (sample HA60), (b), 70 °C (sample HA70), and (c), 80 °C (sample HA80).

Non-stoichiometric HA generally gives the phase- separated product upon additional heat-treatment above 1000 °C which can significantly affect biological properties *in vivo* and *in vitro*. Figure 3-7 showed that upon heat-treatment at 1200 °C for 1 hour, the X-ray diffraction peaks became considerably sharper and well resolved and gave a good match to the phase pure hydroxyapatite (reference pattern JCPDS [09-432]).

Other studies carried out by lowering temperature (below 60 °C and time (below 5 minutes) have shown that apatite obtained below 60 °C after heat-treatment at 1200 °C for 1 hour was not phase pure synthetic hydroxyapatite as shown in Figure 3-6. This observation showed that the residence time is an important factor in order to achieve a stoichiometric hydroxyapatite and that CPFS can confer high-temperature stability of the apatite powders if the correct conditions are used.

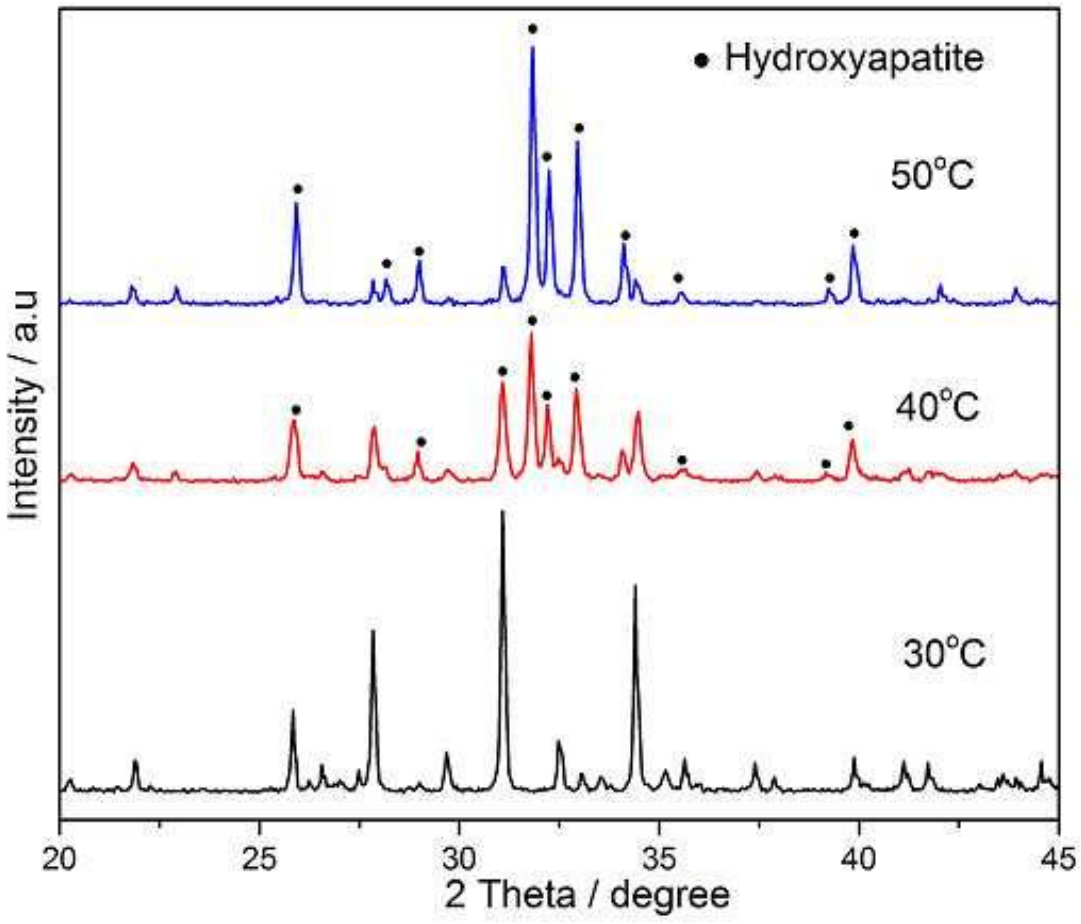

Figure 3-6 Powder X-ray diffraction patterns of products made at temperature (a), 30 °C (b), 40 °C and (c), 50 °C, respectively.

3.3.6 Heat-treatment Studies

No additional peaks were observed in heat-treated samples of HA60 (synthesized at 60 °C, five minutes residence time via CPFS) even at 1200 °C for one hour which revealed excellent high temperature stability of as prepared HA powders made via CPFS. Figure 3-7 depicted the heat-treatment studies of HA60 at different temperatures ranging from 200 to 1200 °C.

It was observed that the conduction of reactions at 60 ºC required a maturation time of at least 5 minutes in the flow system, and that, for the lowest temperature of 60 °C, particle nucleation dominated, however, the particles had insufficient energy to grow larger via Ostwald ripening. So small particulates with very high surface area are obtained at 60 °C.

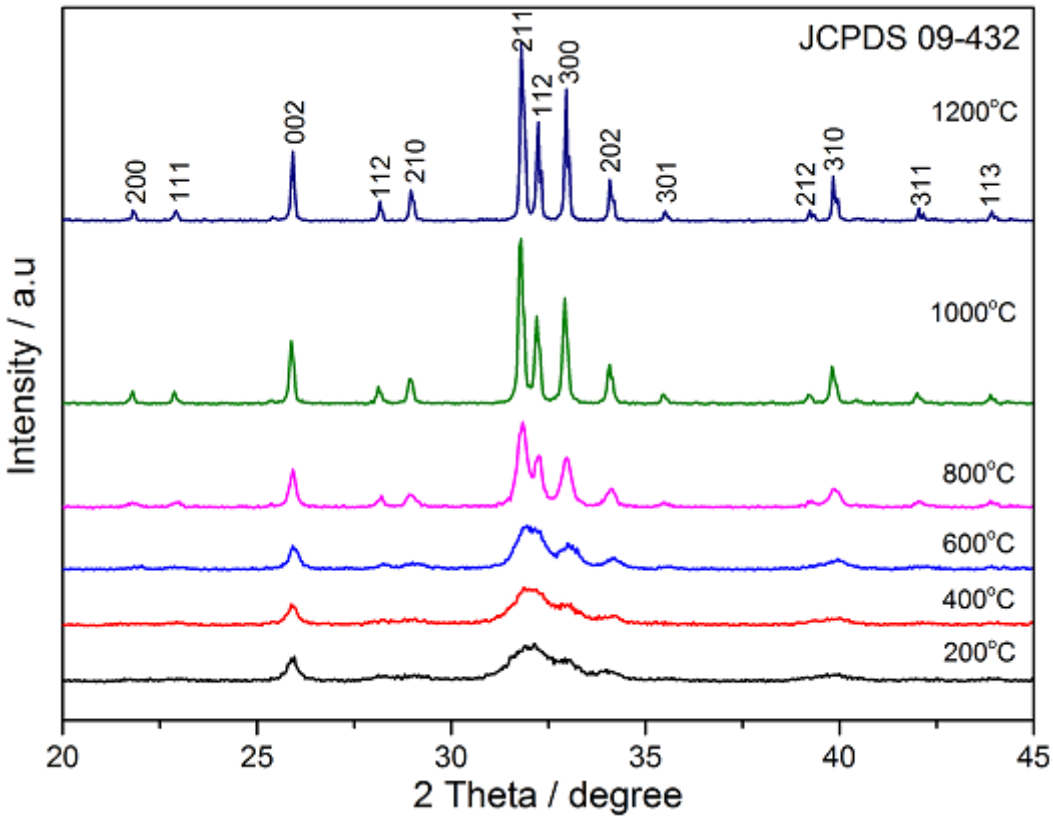

Figure 3-7 Heat treatment of phase pure HA60 at different temperatures made at 60 °C via CPFS.

3.3.7 Effect of Reaction Temperature

The properties of the precipitated material depended on the temperature, concentration, pH, time and other precipitation conditions such as variation in Ca:P ratio and residence time. It was observed that by increasing reaction temperature, the particle size increased whereas surface area decreased as shown in Figure 3-8. It was observed that by tuning the reaction parameters, products of any required particle size (ranging from 20-150 nm) and surface area (ranging from 95-300 m^2g^{-1}) can be produced using CPFS system.

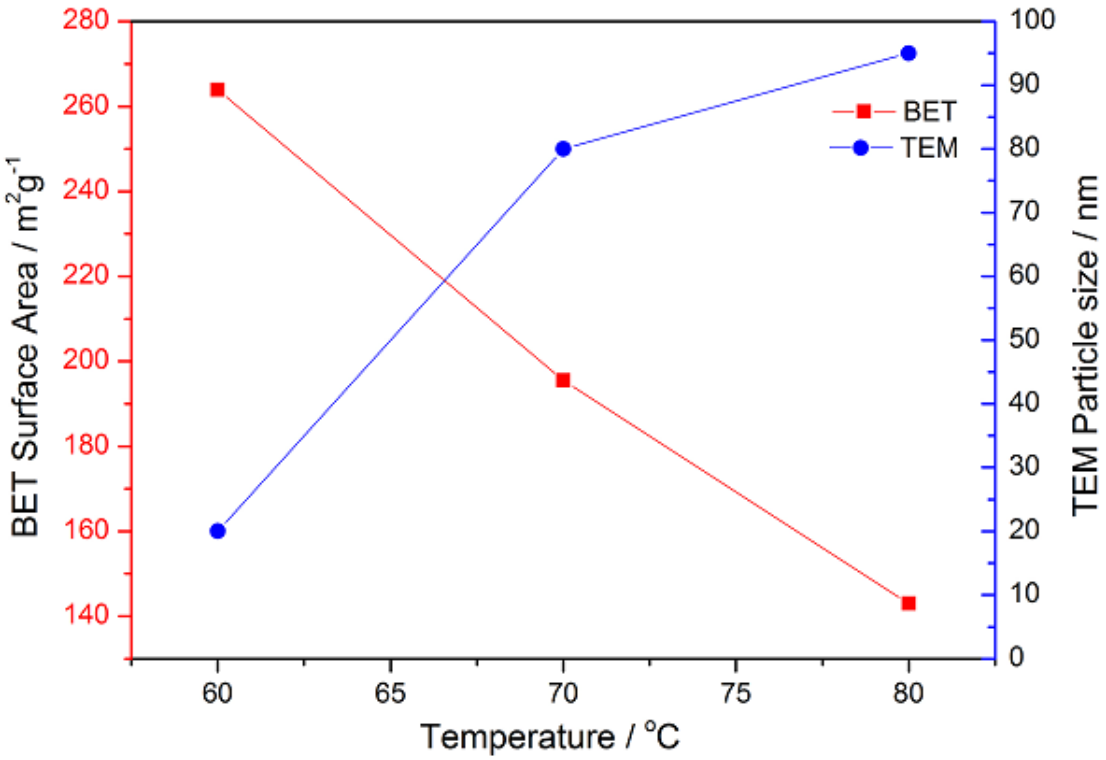

Figure 3-8 Effect of temperature on BET surface area and TEM particle size analysis

3.3.8 X-ray Photoelectron Spectroscopy

A chemical analysis of phase pure HA sample HA60 was done by using XPS analysis as shown in Figure 3-9. The peaks at 134 eV corresponded to P 2p spectra of hydroxyapatite. While the binding energy values for O 1s and Ca 2p were measured as 532 and 347 eV, respectively. The Ca 2p spectrum as shown in Figure 3-10 (a) could be resolved into two peaks for Ca $2p_{3/2}$ and $2p_{1/2}$ (two spin-orbit pairs) at 347.4 and 351.3 eV, respectively, which are related to hydroxyapatite. In Figure 3-10 (b), the 2p peak can also be deconvoluted into two peaks with a spin orbit splitting for $p_{1/2}$ and $p_{3/2}$ levels with binding energy values of 134.2 and 133.4 eV, respectively. Figure 3-10 (c), depicts the core level spectrum of O 1s and the peaks at 530.4 and 531.8 eV are attributed to the phosphate group, and contribution of hydroxyl group in hydroxyapatite crystal, respectively (Mahabole et al., 2005, Costescu et al., 2010a, Lu et al., 2000).

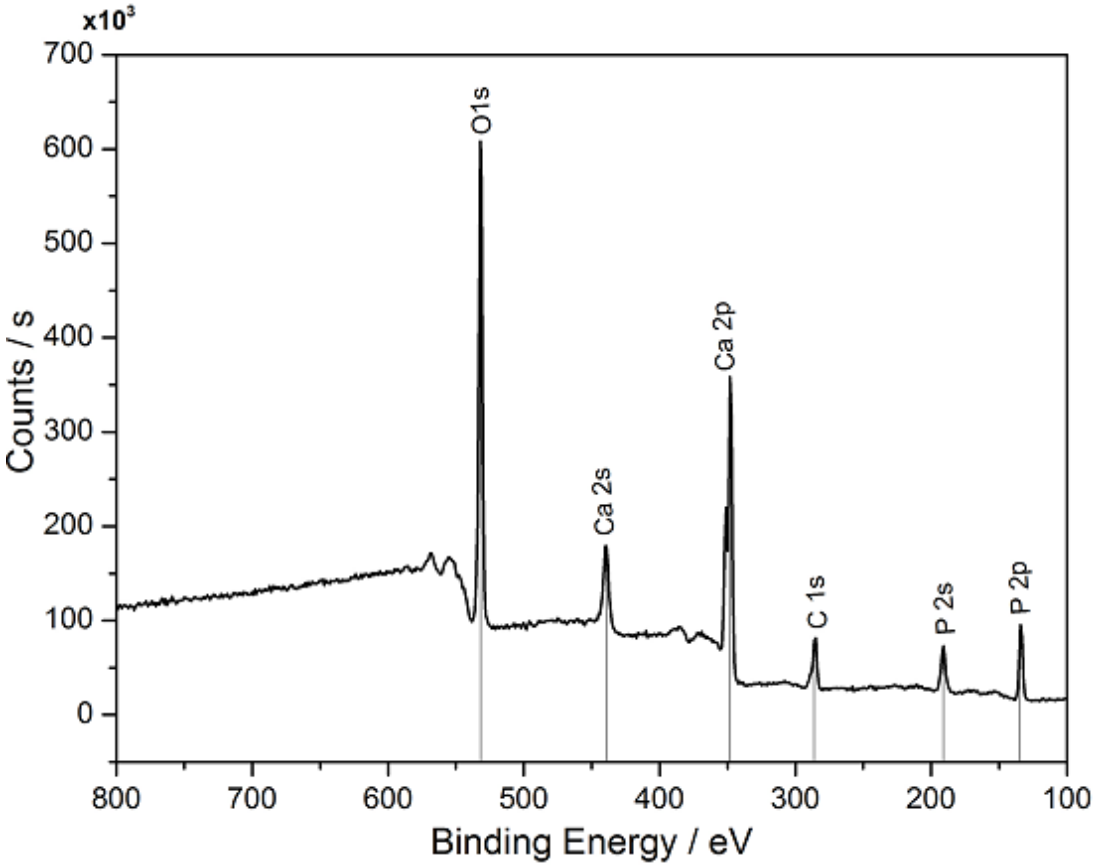

Figure 3-9 XPS survey spectrum of phase pure HA60 sample made via continuous plastic flow synthesis

3.3.9 Fourier Transform Infrared Spectroscopy

FTIR and Raman spectroscopy were used to analyse the samples and aid identification of different calcium phosphates. FTIR data of as-prepared HA samples (HA60, HA70 and HA80) showed characteristic peaks of phase pure, stoichiometric HA. The peak at 3569 cm^{-1} was assigned to the O-H stretching mode (ν_s) of the hydroxyl group (Rehman and Bonfield, 1997) in the spectra of HA60, HA70 and HA80 as shown in Fig. 3-11. The hydroxyl band at 3569 cm^{-1} in the spectrum of HA60 has a lower intensity compared to HA70 and HA80, which is also masked by broad H_2O absorption (Figure 3-11). It was observed that the hydroxyl peak grew stronger and sharper with increasing synthesis temperature from 60 to 80 °C as shown in Figure 3-11. The intensity of peak 1639 cm^{-1} corresponding to the bending mode (ν_2) for absorbed water was observed to decrease with increasing synthesis temperature. This suggested that loosely bonded OH^-

groups became more incorporated into the lattice with an increase in reaction temperature.

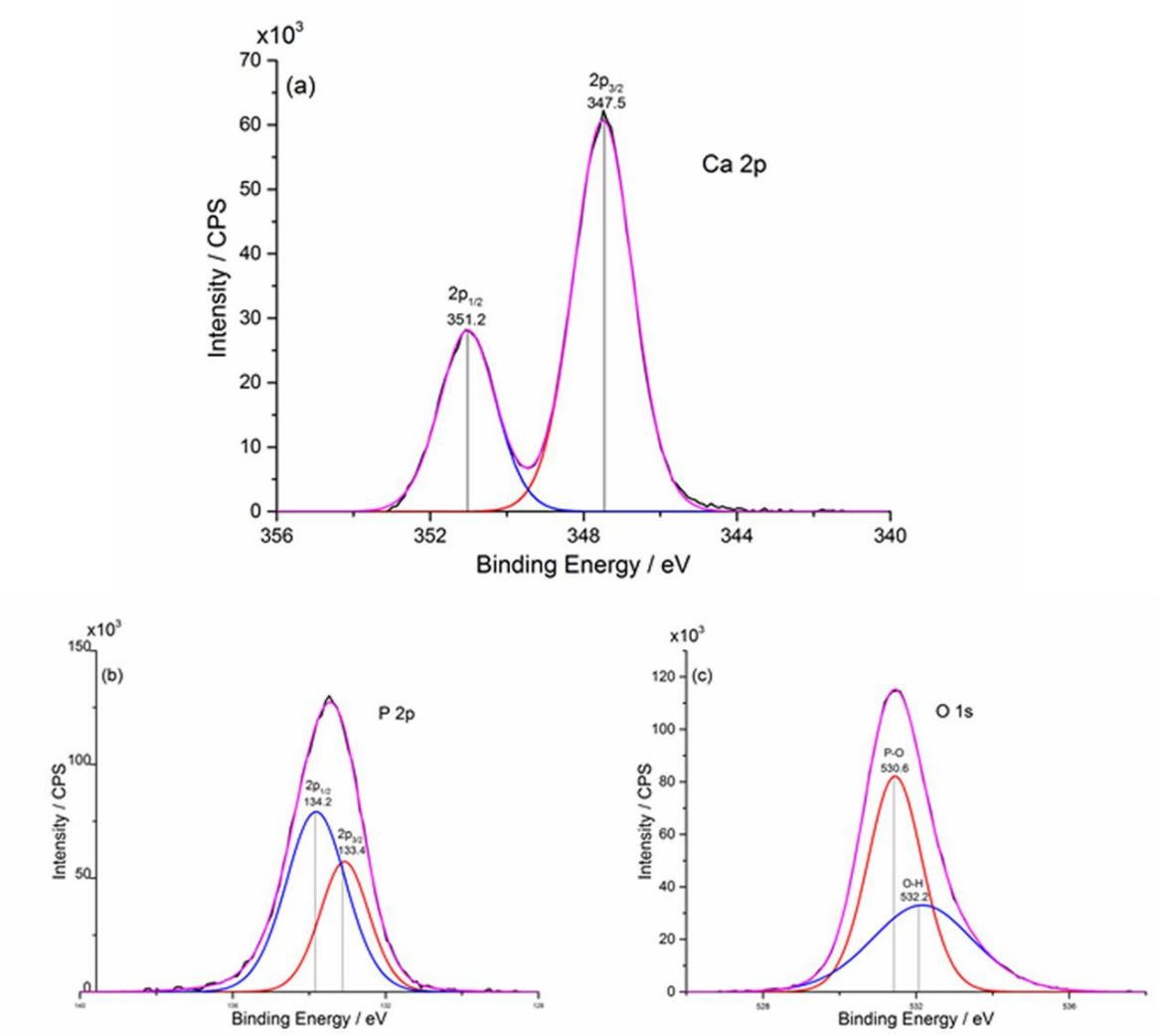

Figure 3-10[a-c] XPS Spectra of Ca 2p,O 1s and P 2p recorded from the phase pure HA60

Peaks at 1453 and 1414 cm^{-1} were assigned to the stretching modes (ν_3) of some adsorbed carbonate ions on the surface of HA. No HPO_4^{2-} vibration at 867 cm^{-1} was observed. However, the carbonate vibration at 872 cm^{-1} corresponding to the bending mode (ν_2) of the O-C-O linkage in carbonate also became weaker in the HA80 sample with increasing synthesis temperature. The peak at 637 cm^{-1} corresponded to the ν_L vibration mode of hydroxyl group in all HA samples made at 60, 70 and 80 °C, respectively using novel CPFS reactor.

Peaks at 1100 and 1031 cm^{-1} corresponded to the (P–O) asymmetric stretching mode (ν_3) of phosphate, whilst the peak at 961 cm^{-1} corresponds to the symmetric stretching (ν_1) of the same bond. The sharpness and intensity of peaks at 602, 564 and 466 cm^{-1} corresponding to the bending mode of the O-P-O linkage in phosphate, increased with increasing reaction temperature from 60 to 80 °C as shown in Fig 8c. The most obvious change in the spectrum of HA80 is the increase in the hydroxyl peak centered at 3569 cm^{-1} compared to the HA60 and HA70 samples made on the CPFS reactor.

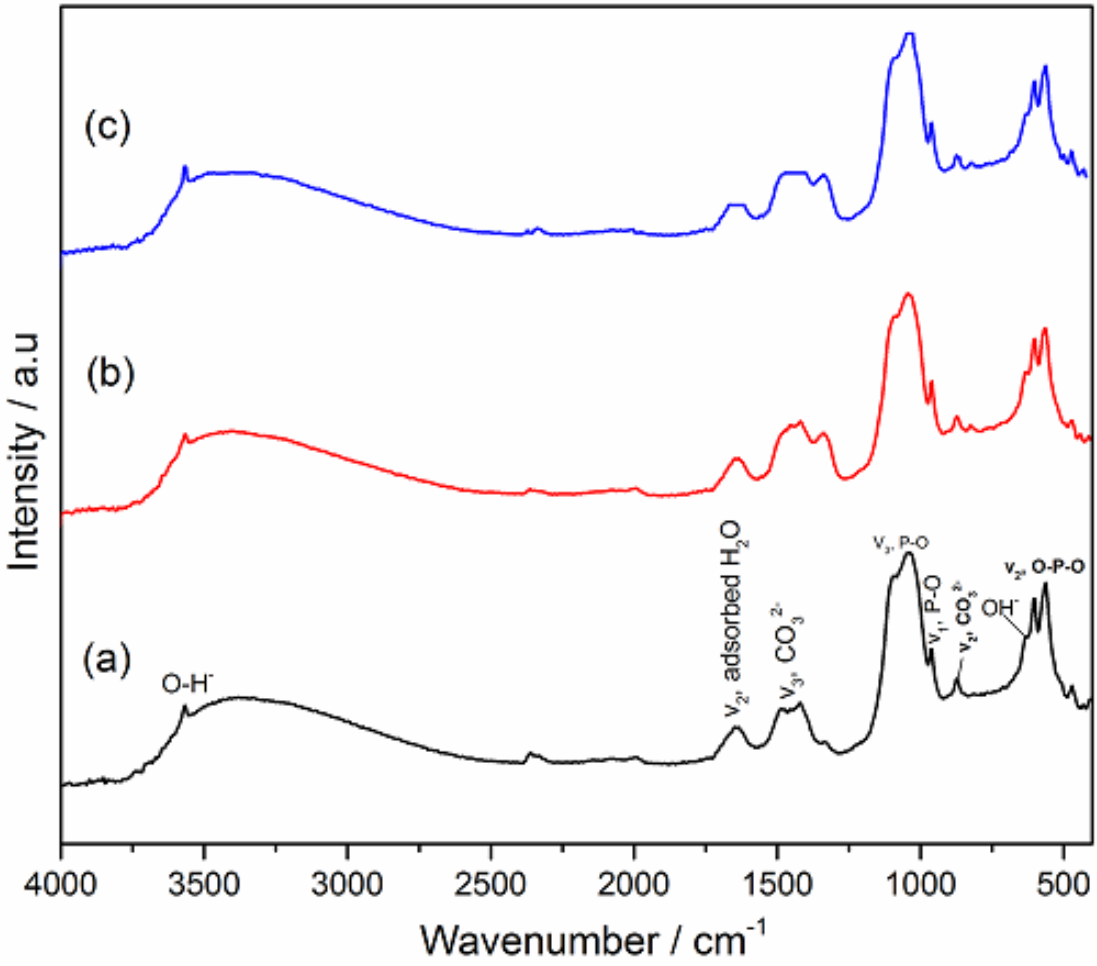

Figure 3-11 FTIR spectra of phase pure hydroxyapatite synthesized at (a), 60 °C(HA60) (b), 70 °C (HA70) and (c), 80 °C (HA80), respectively

3.3.10 Raman Spectroscopy

Raman spectroscopy was conducted in order to supplement crystallographic data and detect substitutions in the apatite lattice. The peaks in the Raman spectra shown in Figure 3-12 corresponded to those normally observed for HA (Penel et al., 1998). The peak at 965 cm^{-1} for HA60, HA70 and HA80 corresponded to a symmetric stretching mode (v_1) of the P-O bond in phosphate.

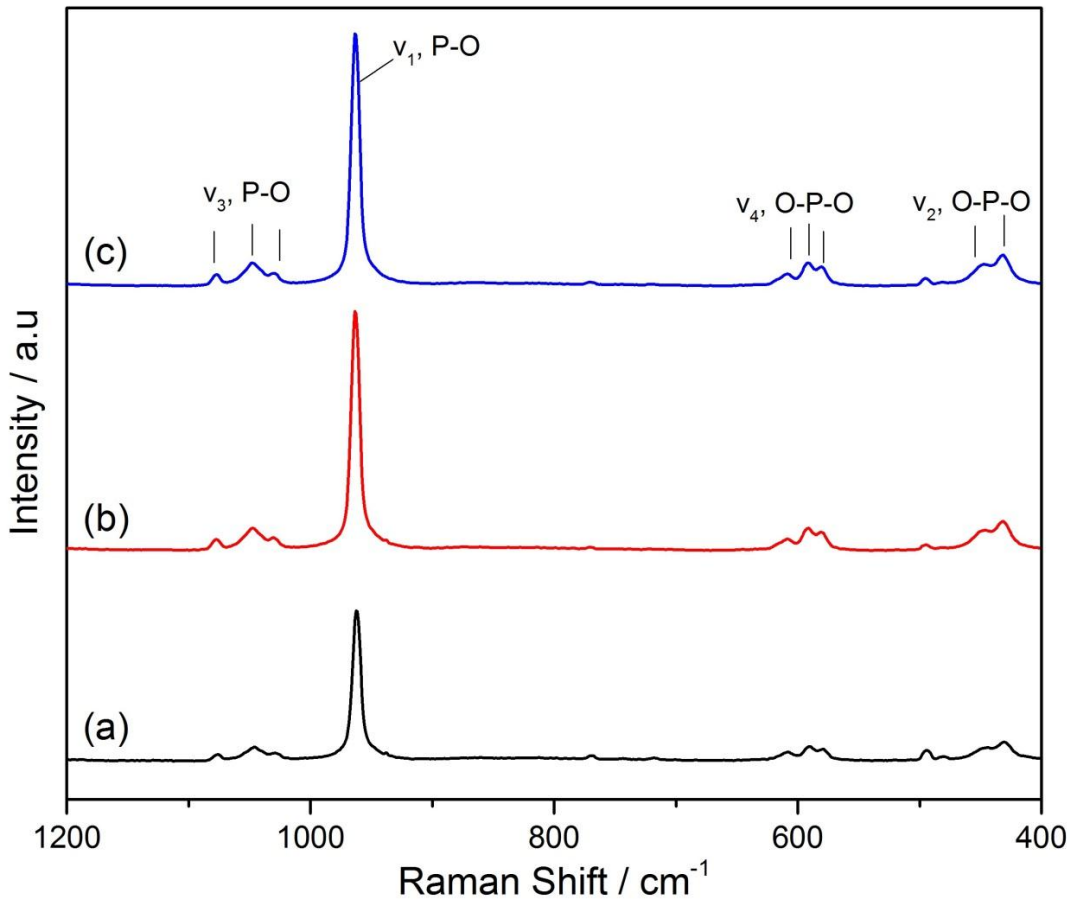

Figure 3-12 Raman spectra of phase pure hydroxyapatite synthesized at (a), 60 °C (HA60) (b), 70 °C (HA70) and (c), 80 °C (HA80), respectively.

It was observed that peaks became narrower and more intense with increasing synthesis temperature in the sample HA80 as compared to the samples HA70 and HA60 made via CPFS. Peaks at 610, 593 and 583 $cm^{-1}$are likely to correspond to the bending mode (v_4) of the O-P-O linkage in phosphate as shown in Figure 3-12. Peaks at 1078, 1049 and 1030 cm^{-1} corresponded to asymmetric stretching modes (v_3) of the P-O bonds in

phosphate. An increase in intensity and sharpness of these peaks with temperature, indicated an increase in crystallinity with increasing temperature.

3.3.11 Cell Viability Study

Human osteoblast cells (MG63) were cultured on CPFS HA disks from and cell viability was studied over the course of 7 days (Figure 3-13). At day 1, cell viability was similar on all HA disk samples indicating that initial cell attachment was not enhanced by any surface. At day 4, cell viability increased on both HA 60 and HA 70, while it remained constant on HA 80, when compared with day 1.

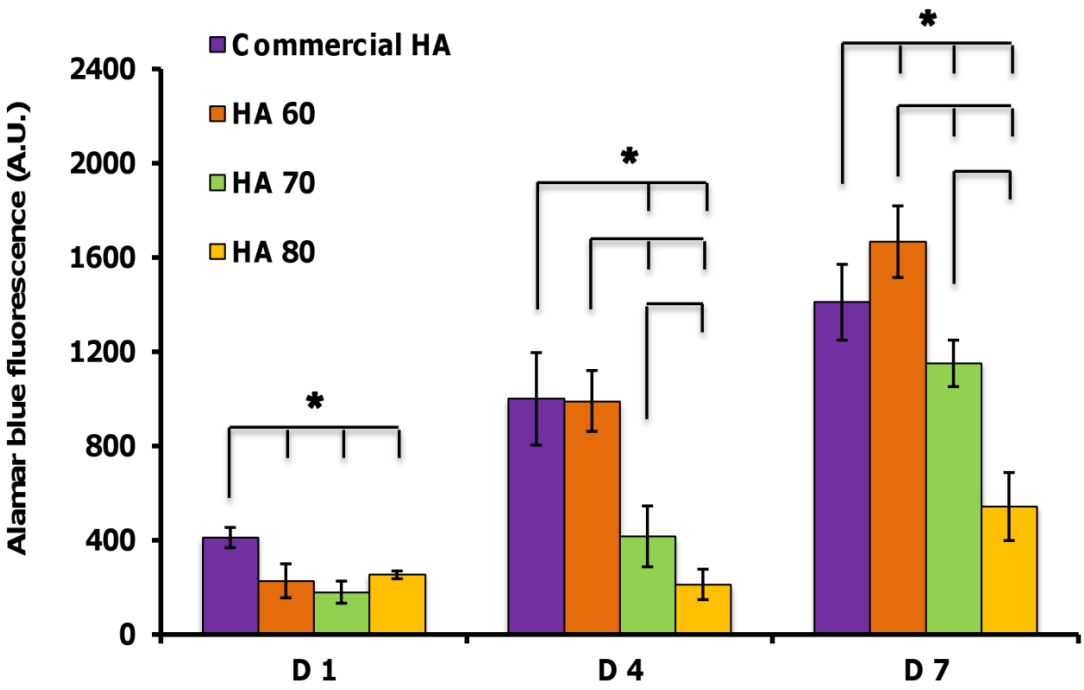

Figure 3-13 MG63 viability on HA discs. Cell viability was measured at days 1, 4 and 7 via Alamar blue assay for MG63s cultured on HA 60, HA 70, HA 80 and cHA (Mean ± SD, n = 6). * $p < 0.05$.

A similar trend was observed at day 7, however, all HA samples had an increased cell viability compared with day 1 and 4. At both days 4 and 7, HA 60 had significantly higher cell viability then both HA 70 and HA 80, while HA 70 had significantly higher cell viability than HA 80. MG63 viability on commercial HA (cHA) was compared with HA samples prepared using novel CPFS method and was initially higher (day 1) than

all prepared HA samples. Cell viability on cHA remained higher than HA 70 and HA 80 at all time points but at days 4 and 7 it was equal to and less than HA 60. These results indicate that the newly developed CPFS technique for the production of HA, has made samples which are biocompatible and that support osteoblast proliferation. However, for these samples, cell viability at day 7 was dependent on preparation temperature (60 > 70 > 80).

3.3.12 Cell Morphology

MG63 morphology was observed at day 7 (Figure 3-14) on each HA type. Cells were evenly distributed on cHA and showed a typical square-like osteoblast morphology. MG63s were also evenly spread across the surface of HA 60 and showed an osteoblastic morphology but the cell cytoskeleton was also more elongated than on cHA and the cells appeared to form cell-cell bridges.

On HA 70, cells were more spares and generally less-well spread than those on cHA and HA 60, with the majority showing a rounded morphology. MG63s on HA 80 were also generally quite rounded and formed clusters. These results indicate that even cell spreading and anostoeblastic morphology are favoured on HA60 compared with HA70 and HA80 and that they compare well with cHA.

3.3.13 Zeta Potential Measurements

Zeta potential measurements were performed in order to investigate the colloidal stability related to surface charge of the pure HA.

Zeta potential gives the electrostatic potential of particles which is directly related to their dispersion stability; the higher the zeta potential values the greater the electrostatic repulsion and therefore the higher will be the colloidal stability of the suspension. The pH value has been shown to influence the Zeta potential and conductivity of HA suspension. This implies that we can adjust the pH value of suspension by the addition of acid or alkaline (HNO_3,NaOH) to a desirable one, so as to obtain an ideal and stable suspension of HA particles.

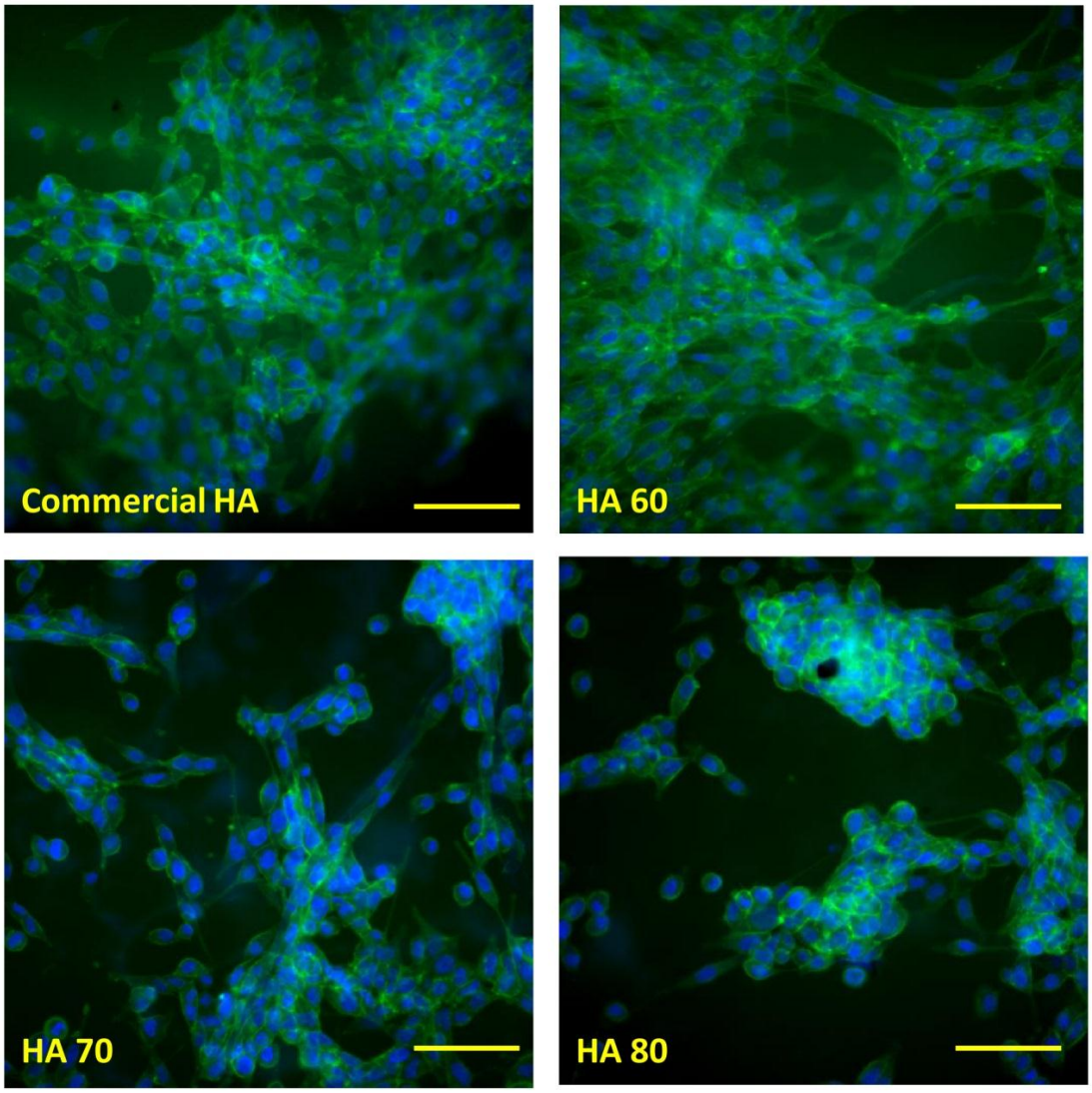

Figure 3-14 MG63 morphology on HA discs. Cells were visualised at day 7 for cell nucleus (DAPI in blue) and cytoskeleton (phalloidin-FITC in green) for MG63s cultured on HA 60, HA 70, HA 80 and commercial HA. Scale bar is 100 µm.

The Zeta potentials of HA suspension at different pH were analysed using a zeta potential analyser. A zeta potential of -70 mV was measured for as prepared HA at pH 10.5 which indicated a high negative surface charge as shown in Figure 3-15. The higher surface charge would be expected to stablise the particles from agglomeration.

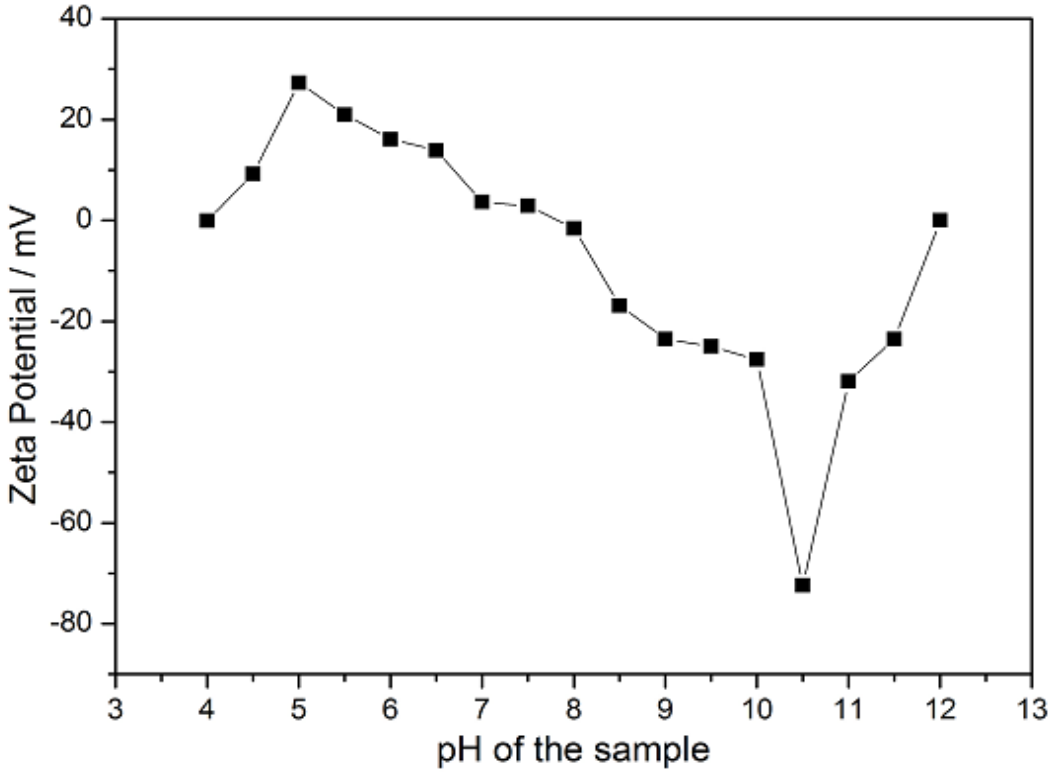

Figure 3-15 Zeta potential measurement of as prepared HA at different pH

3.4 Electrophoretic Deposition on Metallic Implants

The SEM image in Figure 3-16 shows the as prepared HA coating on 316L stainless steel substrate by EPD at 50 V for 5 min. The coating was found to be homogenously deposited on the surface with no major visible cracks and a few surface level pores.

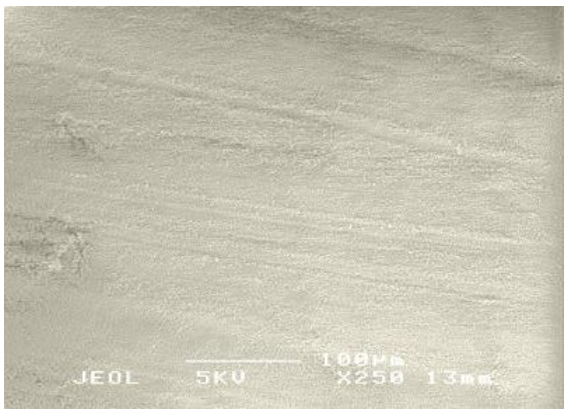

Figure 3-16 HA coating on 316L Stainless steel before heat-treatment

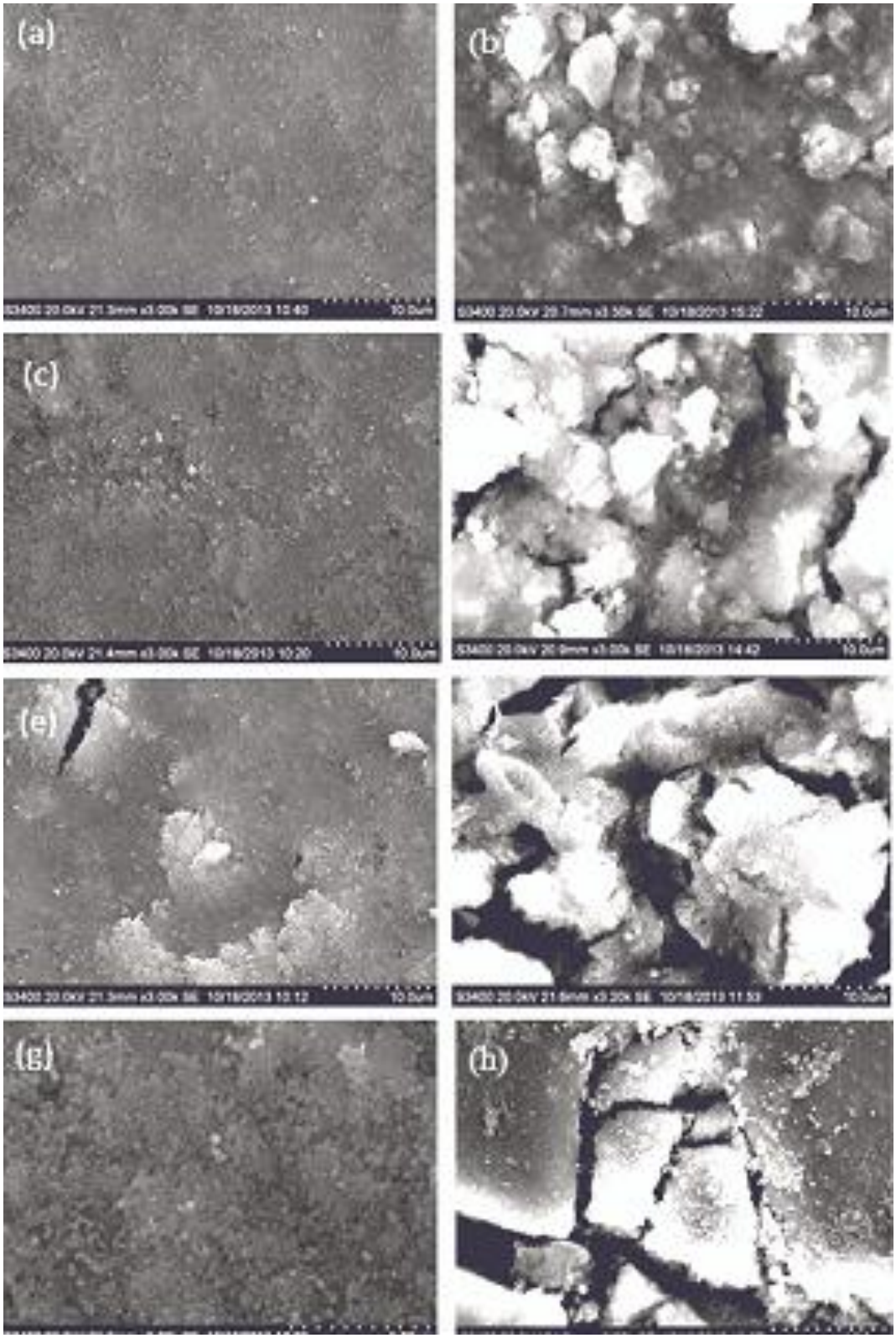

Figure 3-17(a-h) Scanning electron micrographs of surface morphologies of different coatings, (a), (b) 5 min. deposition time, (c), (d) 10 min. (e), (f) 15 min. and (g), (h) 20 min. deposition time at 50V.

Surface analysis of the deposition carried out at the fixed voltage of 50 V for 5, 10, 15 and 20 min revealed that the surface is packed with agglomerates resulting in a rough porous surface (Figure 17e to h). The presence of surface pores is considered beneficial for promoting osteointegration and providing pathways for diffusion of nutrients. It was observed that by increasing deposition time (20 min.), the adhesive strength and smoothness of coating reduced as shown in Figure 3-18.

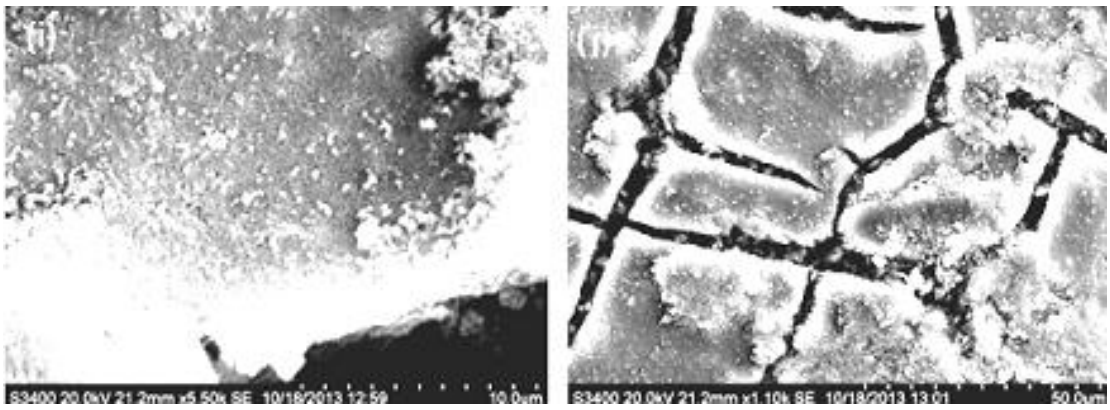

Figure 3-18 HA coating on 316L SS for 20 min. deposition time at 50 V.

Examination of the cross-section of the coating of HA onto 316L SS at 50 V for 10 min (Figure 3-19) showed well compact layer of coated HA onto the substrate, furthermore no evidence of delamination of the coating was observed at the interface, indicating that the coating is strong enough to tolerate imposed stresses which results from the constrained volume shrinkage during the drying cycle.

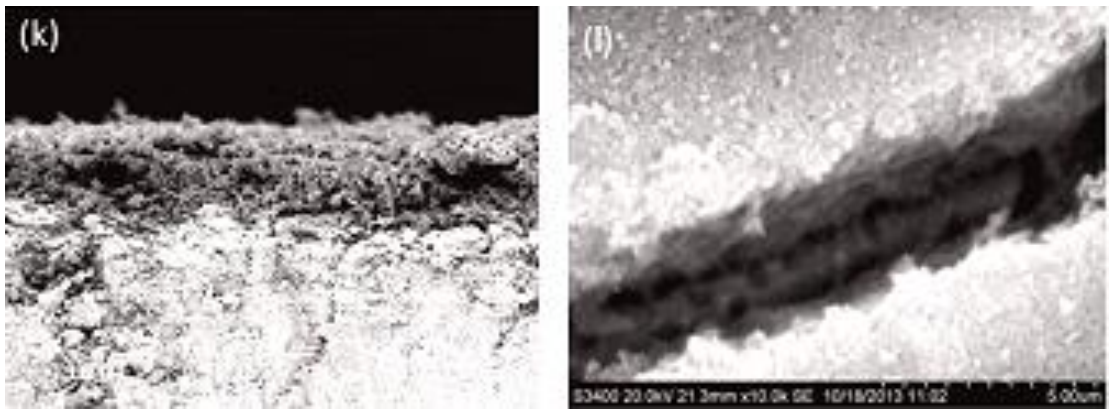

Figure 3-19 Cross section morphology of HA coating on 316 L SS substrate for 10 min. at 50V.

3.4.1 Effect of other System Parameters on the Properties of Hydroxyapatite

3.4.1.1 Effect of Different Flow rates / Residence Time

Residence time is considered an important factor to get the phase pure nanosized hydroxyapatite particles. A series of different reactions were performed using a CPFS system at different residence time ranging from 0 to 50 minutes as shown in Figure 3-20. It was observed that at 60 °C, the system takes 5 minutes to produce phase pure hydroxyapatite with remarkably high surface area and very small particle size. While if we go above 60 °C, we get phase pure product in considerably less time period (even less than one minute at 80 °C).

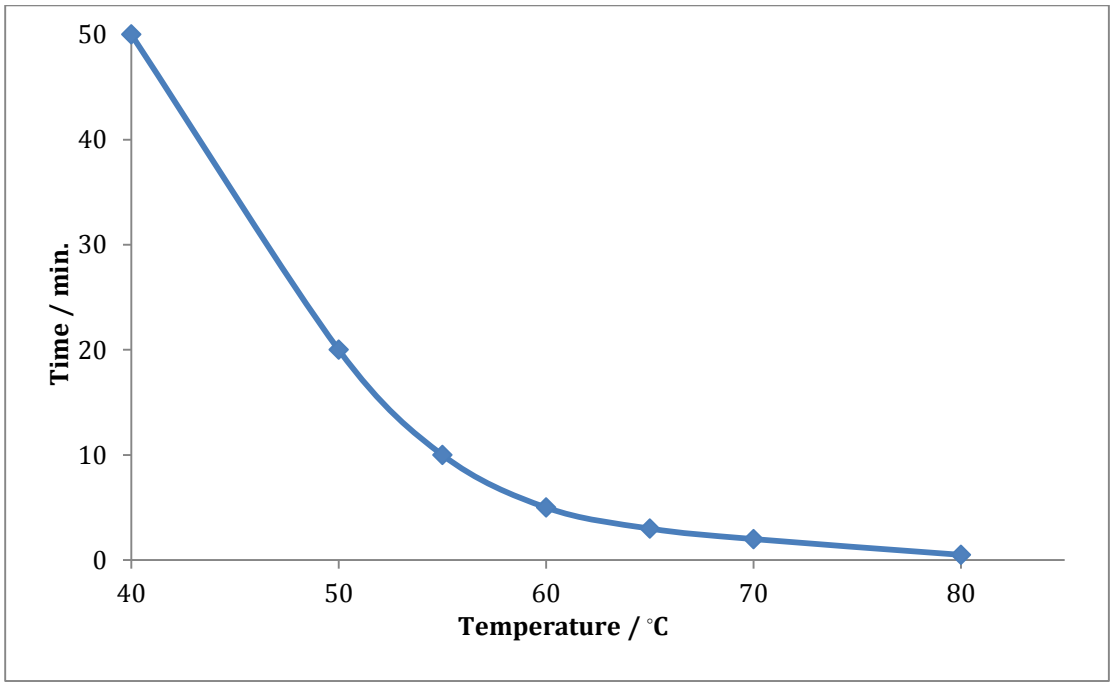

Figure 3-20 Relationship between residence time and reaction temperature on the phase purity of product.

3.4.1.2 Effect of Reaction Concentration

The reaction concentration is also considered a key factor after temperature to obtain phase pure nano-sized hydroxyapatite of required surface area and size. The method worked at all concentration ranging from mMoles to Moles. It was observed that at lower reaction concentration, the particles with high surface area (~ 265 m^2g^{-1}) and small particle size (~20 nm) were obtained. The method worked equally well at higher concentrations of precursors. However, the particle size increases, with a subsequent lowering of surface area as shown in Figure 3-21. Therefore, at higher concentrations of precursors, the method can still be used for the rapid and continuous manufacture of stoichiometric hydroxyapatite or other bioceramics (e.g. calcium phosphates and their derivatives). Under such conditions, the particles are typically around one hundred nanometers or more in length and surface areas are about 100 m^2g^{-1}as shown in Figure 3-21.

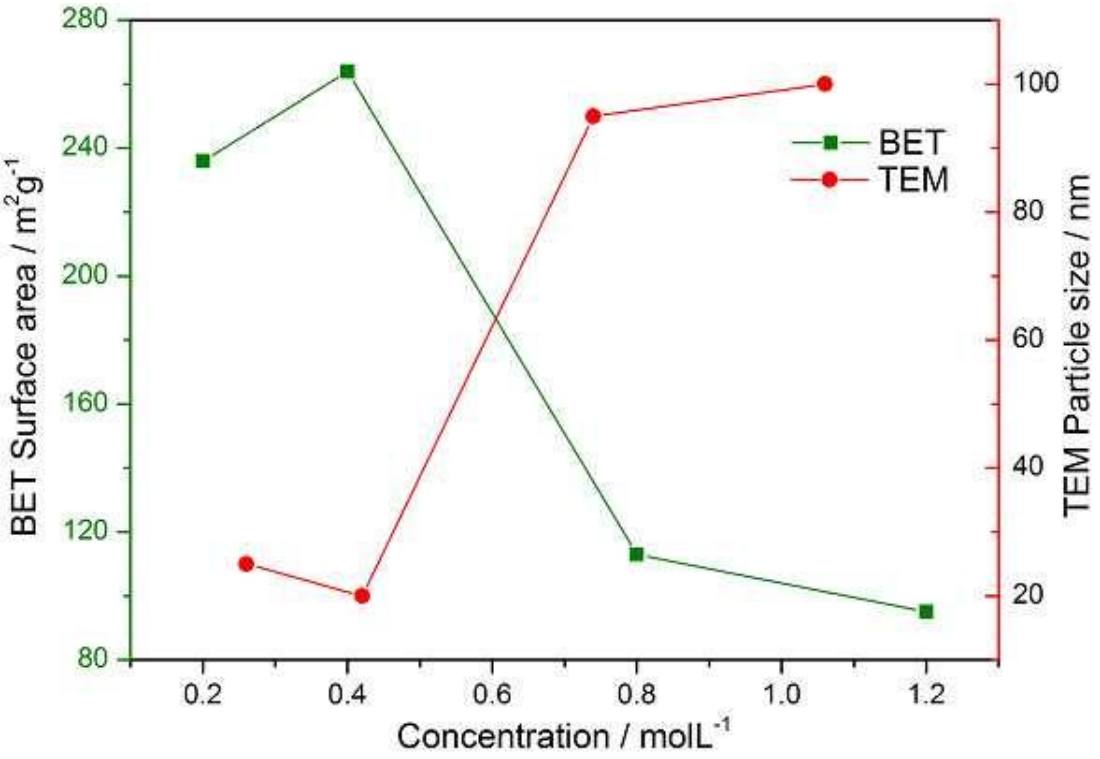

Figure 3-21 Effect of concentration on BET surface area and TEM particle size analysis

3.4.1.3 Effect of System Parameters on the Surface Area and Yield

For this study, a series of reactions were carried out by changing reaction parameters one at one time to see the effect of each system parameters on the surface area, particle size and yield (%). It was observed that the variation in flow rates, residence time and temperature regimes gave minimal or no variation in product yield (~ 85 %) in all reactions. However these system variations in system parameters affected the particle size and surface area as summarized in table 2-3, 2-4 and 2-5. It was observed that by tailoring reaction temperature, any specific products can be obtained with controlled particle size (in the range 25 - 95 nm) within 5 minutes at a synthesis temperature in the range of 60 to 80 °C with approximately the same yield (~ 85 %).

3.5 Conclusions

The work in this chapter constitutes the first ever report on synthesis of high surface area (95-300 m^2g^{-1}), nano-sized phase pure hydroxyapatite (20-150 nm) in a continuous plastic flow at near ambient conditions (room temperature to 80 °C and atmospheric pressure). Continuous (plastic) flow synthesis (CPFS) technique provides a rapid, facile and economical pathway to obtain high surface area, nano-sized HA and other calcium phosphate bioceramics and then coating these bioceramics onto metallic substrates.

Cell toxicity analyses confirm the biocompatiblity of this material. Cell culture experiments on HA discs using human origin osteocarcoma osteoblast cells showed diffrentiation into various cell types depending on the surface and culture conditions. Cell adhesion on HA60 (highest surface area) was substantially greater than HA70 and HA80. So these results indicate that high surface area nanosized HA rods have potential to be used in bone regeneration /replacement applications.

Electrophoretic deposition studies performed at 50 V for 5 min furnished *ca.* 200 nm thick coating of 5% PVA coated HA on 316L SS. It was noticed that the addition of 5% PVA into HA powder successfully improved the adhesion of the powder on the substrate and thus eliminating the need for heat treatment of the coated substrate. Coating thickness and surface morphologies were effectively controlled by varying deposition time.

It was observed that all apatites made at CPFS at or above 60 °C, five minutes residence time, were phase pure. However, increasing reaction temperature and concentration above 60 °C, resulted in lower surface area and lager particle size and.

It was observed that samples synthesized at 60 °C or above this temperature at pH 10 were all phase pure with a wide range of particle size and surface area. Other samples made below 60 °C and pH 10, resulted in the phase separated product (with traces of β-TCP). It is concluded that in the CPFS system, reaction temperature was the dominating factor for attaining more thermally stable apatites.

From the literature reports of high temperature synthesis of HA we can see that at such high temperatures (200-300 °C), substantial growth or agglomeration of smaller nuclei occurs to form substantially larger particles typically > 100 nm in size. Additionally, there is a disadvantage of having to use high temperature continuous reactors, in that they are metal pipes due to the high reaction temperatures and therefore if such a process were used to make bioceramics, they would contain substantial levels of leached metals from the steel. This would mean that the bioceramics may not be acceptable for clinical use according to the latest international standards and guidelines. Therefore this CPFS process represents a low cost, clean, synthesis technique, which works relatively under mild conditions and allows the synthesis of high purity stoichiometric HA and other bioceramic materials in a considerably short-time period with fine control over particle size)and surface area), well below 100 nm in size.

3.6 Future Work

Future work will address the ability of the CPFS nano-HA to support osteogenic differentiation. The combined cell observations indicate that high surface area

nanosized HA rods made via CPFS may have the potential to be used for biomedical applications where bone regeneration /replacement is required.

Furthermore, this high surface area HA products will be utilized to make porous scaffolds by freeze casting process by the addition of polyvinyl alcohol (PVA) as a binder and emulsifying agent. The purpose of study is to enhance the mechanical strength of HA for applications in bone tissue engineering. It would be interesting to perform reactions at different reaction pH to obtain different HA morphologies.

The high temperature stability (stable up to 1200°C) of these hydroxyapatite made via CPFS with remarkably high surface area (up to 263.9 m^2g^{-1}) and small particle size (typically 20nm) compared to that reported in the literature would make these nanobioceramics more promising materials for use in injectables, coatings on metallic implants, as fillers or additives into commercial products such as toothpastes, materials for the controlled release of drugs or other controlled release therapies, reinforcements in biomedical composites and in bone and dental cements.

Chapter 4

Synthesis and Characterization of Phase Pure Brushite, Clacium Deficient HA and Tricalcium Phosphate Bioceramics

4.1 Introduction

Calcium phosphate (CaP) bioceramics are well known for their use in bone repair applications for use as bulk defect fillers, injectables, the hard phase of biocomposites and coatings on implants because of their excellent biocompatibility and osteoconductivity. There are numerous forms of CaP structures which typically form a family of compounds called 'apatites'(Elliott, 1994). The general formula $Ca_{10-x}(HPO_4)_x(PO_4)_{6-x}(OH)_{2-x}$, with $0 \leq x < 2$, is non-stoichiometric apatite, while calcium phosphates have a Ca:P molar ratio starting from 0.5 for $[Ca(H_2PO_4)_2]$ to 2.0 for $[Ca_4(PO_4)_2O]$. Compounds such as brushite $[CaHPO_4.2H_2O]$ and hydroxyapatite $[Ca_{10}(PO_4)_6(OH)_2]$ have been the focus of many recent studies (Kundu et al., 2010a, Kundu et al., 2010b). Hydroxyapatite (HA) and brushite (DCPD) have been considered as potential bone substitute materials, of which the latter raised great interest in recent times because of its high resorbibility (Lemaitre et al., 1987, Lemaitre, 1995, Bohner, 2000, Lu et al., 2002). Brushite powders are resorbed more quickly as compared to HA (Nilsson et al., 2002) as brushite is a metastable compound when used under physiological conditions (Vereecke and Lemaître, 1990). A significant characteristic of brushite is its use as a precursor for producing HA (Roop Kumar and Wang, 2001)[10-12]. In addition, it is a common CaP phase stable under weakly acidic environments of pH range 4–6. However, its storage stability is questionable due to its instantaneous transformation to form HA. It can lose water to form monetite $[CaHPO_4]$ upon storage. However, in order to exploit the potential use of brushite for gene delivery, it is enormously important that the phase not only be synthesized under physiological conditions but also remain stable under those environments (Kumar et al., 1999, Fulmer et al., 2002)

The most common method in the literature for synthesizing brushite is by the addition of a water soluble calcium source (e.g., $CaCl_2.2H_2O$, $Ca(NO_3)_2.4H_2O$, or $Ca(CH_3COO)_2.H_2O$) and a phosphate source (e.g., $NH_4H_2PO_4$, $(NH_4)_2HPO_4$, Na_2HPO_4, NaH_2PO_4, KH_2PO_4 or K_2HPO_4) at a Ca:P molar ratio of 1 under acidic conditions of pH in the range of 5-6. The precipitated product is typically washed with deionized water, and air-dried (Ngankam et al., 1999, Sivakumar et al., 1998, Skytte Sørensen and Lundager Madsen, 2000, Xie et al., 2002). In contrast, phase pure brushite powders can also be prepared by reacting $Ca(OH)_2$ suspension with a stoichiometric amount of H_3PO_4 (Ca:P ratio 1.67) and maintaining the solution pH in the range 5-6 (Martin and Brown, 1997, Ferreira et al., 2003). Brushite can also be prepared by combining two phosphate powders in the presence of water (Charriere et al., 2001, Mirtchi et al., 1989, Van Landuyt et al., 1999) e.g. β-TCP ($Ca_3(PO_4)_2$) and monocalcium phosphate monohydrate ($Ca(H_2PO_4)_2 \cdot H_2O$) in the presence of sodium pyrophosphate ($Na_2H_2P_2O_7$) as a setting regulator. Mixing of the powders is done in a sulfuric acid solution and brushite form is transformed into dehydrated monetite form by losing its water of crystallization upon heat-treatment at 110 ^oC (Linde, 1991). Based on the experimental solubility values of different calcium phosphate phases recently described by Tang et al. it is noted that phase pure brushite has a 3.4 times higher dissolution rate compared to TCP at pH 5.5 (Tang et al., 2003).

Calcium deficient hydroxyapatite, CDHA) has also attracted much attention as components in injectable bone cements; regulating particle properties is frequently used to control cement setting behaviour (Hench, 1998b, Chaudhry et al., 2006). Natural bone consists of calcium deficient HA (Ca:P molar ratio <1.67) and possesses the high ion-exchange ability of various cations. Therefore, calcium-deficient HAP is extremely used as an ion-exchange media, such as the distillation of water and soil contaminated with heavy metals as well as biomedical applications (Nakahira et al., 2004, Nakahira et al., 2006). The dissolution of calcium phosphate bioceramics (in vivo and in vitro) was found to be dependent on the Ca:P ratio, crystallinity, and pH of the solution (Kannan et al., 2005, Yoshida et al., 2005, Kannan and Ferreira, 2006, Pan et al., 2003).

In contrast, beta-tricalcium phosphate, β-TCP, [$Ca_3(PO_4)_2$], another resorbable CaP

bioceramic, has a greater dissolution rate compared to HA in vivo. Thus, the use of biphasic calcium phosphate ceramics composed of HA and β-TCP mixtures for bone grafts can support rapid bone formation around the implant site compared to HA alone (Ginebra et al., 2004, Klein et al., 1983).

TCP powders were commonly synthesized by solid state or thermal decomposition reactions. In thermal decomposition, calcium deficient hydroxyapatite was generally used for the synthesis under acidic conditions. TCP powder cannot be precipitated directly from an aqueous solution under room temperature, but it (also called whitlockite) can only be obtained when some of the calcium ions are replaced by Mg^{2+}or Mn^{2+} ions (LeGeros, 1986, LeGeros, 1990, Dorozhkin, 2000).

Hydroxyapatite has become the most extensively studied calcium phosphate bioceramic but that of a biphasic HA/TCP powder is still under analysis. Biphasic HA /TCP powders can be synthesized as by product during the synthesis of pure HA and pure TCP or by the thermal treatment of calcium deficient HA (Ca/P = 1.5~ 1.67) above 700 °C (Kohri et al., 1993, Ducheyne et al., 1993, Radin and Ducheyne, 1993).

In this chapter, the novel, continuous plastic flow synthesis process is used to synthesize phase pure brushite, beta-tricalcium phosphate and calcium deficient hydroxyapatite nanoparticles. The effect of changing pH and Ca:P molar ratio in solution on the final product is also addressed. Furthermore, use of brushite nanoparticles for the production of monetite and calcium pyrophosphates by additional steps such as heat treatments is also investigated.

4.2 Experimental

4.2.1 Synthesis of Brushite Calcium Phosphate

Phase pure brushite was prepared at room temperature using a simple CPFS system as described in section 2.2.1. 0.6 M diammonium hydrogen phosphate solution and 0.5 M calcium nitrate solutions were pumped in the CPFS (Ca:P molar ratio 0.8) using pump 1 and pump 2, respectively. Both reagent solutions were pumped at 20 mL min^{-1}, to meet at T-piece. This initial mixture were connected to 5 m long tubing surrounded by an oil bath at the desired temperature. For flow rates of calcium nitrate and diammonium hydrogen phosphate for pump 1 and pump 2, respectively, this gives a total time of 3 minutes for the reaction. The pH of the reaction was maintained at 5.5 to obtain phase pure product. The final suspension was collected in a beaker at the exit point. A Sigma 4K15 Centrifuge with a rotor housing four buckets, having a capacity of seven 50 mL Falcon tubes each, was used to centrifuge the aqueous slurries at 4500 rpm for 10 minutes. After centrifugation, all samples were freeze-dried as described in section 2.3.1.1.

4.2.2 Synthesis of Calcium Deficient Hydroxyapatite

Other calcium phosphate phases (β-TCP, CDHA) were also obtained by changing pH and Ca:P ratio (1.5~ 1.67) and by keeping other conditions same as summarized in Table 2-6. The as-prepared calcium deficient hydroxyapatite was prepared at 70 °C using a simple continuous (plastic) flow synthesis system (CPFS). Details of the CPFS process are described in section 2.2.1. In this process, 0.3 M diammonium hydrogen phosphate solution and 0.48 M calcium nitrate solutions were used (Ca:P molar ratio: 1.6). The pH of both the solutions prior to the reaction was kept above pH 8.5. 5.0 mL of ammonium hydroxide were added to calcium nitrate (500 mL) and diammonium hydrogen phosphate solutions (500 mL), respectively. Both reagent solutions were pumped at 20 mL min^{-1}, to meet at a T-piece. This initial mixture were connected to 8 m long tubing surrounded by heating jacket. The flow rates used for calcium nitrate and diammonium hydrogen phosphate solutions for pump 1 and pump 2, respectively, were selected to give a total residence time of 5 minutes.

The pump rates of 20 mL min^{-1} were used for calcium nitrate and diammonium hydrogen phosphate solutions. The reaction was carried out at 70 °C and atmospheric pressure. The resulting suspension was centrifuged, washed and freeze-dried as explained earlier; see section 2.3.1.1. The product obtained was a fine white powder with ~ 80 % yield.

4.2.3 Synthesis of β-Tricalcium Phosphate

In this process, 0.3 M diammonium hydrogen phosphate solution and 0.45 M calcium nitrate solutions were used (Ca : P molar ratio: 1.5). Both reagent solutions were pumped at 20 mL min^{-1}, to meet at a T-piece. This initial mixture were connected to 8 m long tubing surrounded by a heating jacket. The reaction was carried out at 70 °C and atmospheric pressure. The resulting product was centrifuged, washed and freeze-dried as explained earlier; see section 2.3.1.1. The product obtained was fine white powder with ~ 80 % yield. Phase pure crystalline product (β-TCP) was obtained by the heat-treatment of as-prepared powder at 1100 °C.

The as prepared and heat-treated powdered samples were compacted into cylindrical discs of *ca.* 13 mm diameter and 2 mm thickness by using a hydraulic press at 5 MPa.

4.3 Results and Discussions

The precipitation of brushite from solution does not always take place at the start of the reaction. Ferreira and coworkers (Ferreira et al., 2003) reported that various steps are required in the formation of brushite. The first step is the quick precipitation of HA (Equation.1) and as a result of the decrease in pH, this is followed by the formation of brushite nuclei. At this stage, two species, brushite and HA coexist in the solution. Recent reports have shown that the crystallization rate of brushite is much greater than that of HA at room temperature (Singh et al., 2010).

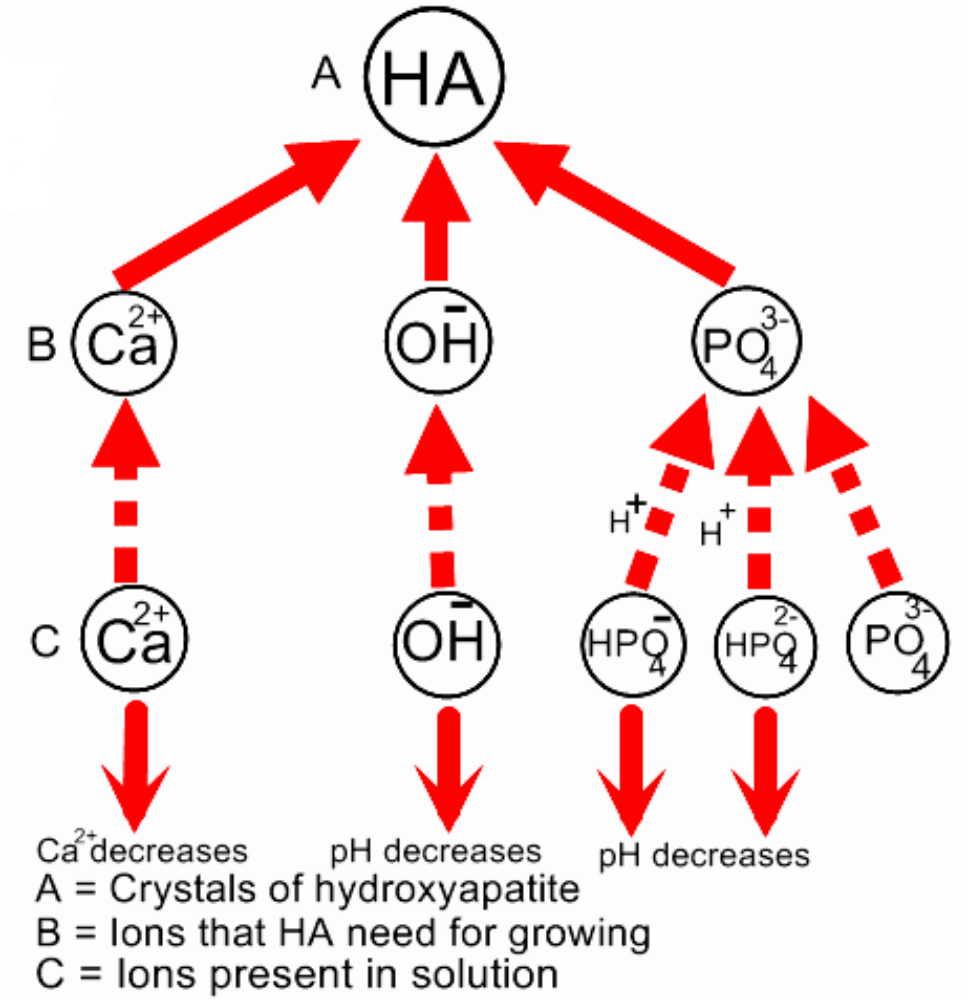

Figure 4-1 Ions needed for the growth of HA [reproduced from Ferreira (Ferreira et al., 2003)

Thus, the existing HA can be transformed into dehydrated brushite form, resulting in an increase of pH as shown in Equation 2.

$$5Ca(OH)_2 + 3H_3PO_4 \longrightarrow Ca_5OH(PO4)_3 + 9H_2O \quad (1)$$

$$Ca_5OH(PO_4)_3 + 2H_3PO_4 + 9H_2O \longrightarrow 5CaHPO_4 + 2H_2O \quad (2)$$

$$Ca(OH)_2 + H_3PO_4 \longrightarrow CaHPO_4\ 2H_2O \quad (3)$$

4.3.1 Transmission Electron Microscopy

Transmission electron microscope images of the samples are shown in Figure 4-2. This confirmed the synthesis of small crystallites with an average particle size along the longest axis of each particle of *ca.* 35 ± 15 nm (200 particles sampled) for CPFS phase pure brushite, with the particles having a roughly spherical morphology.

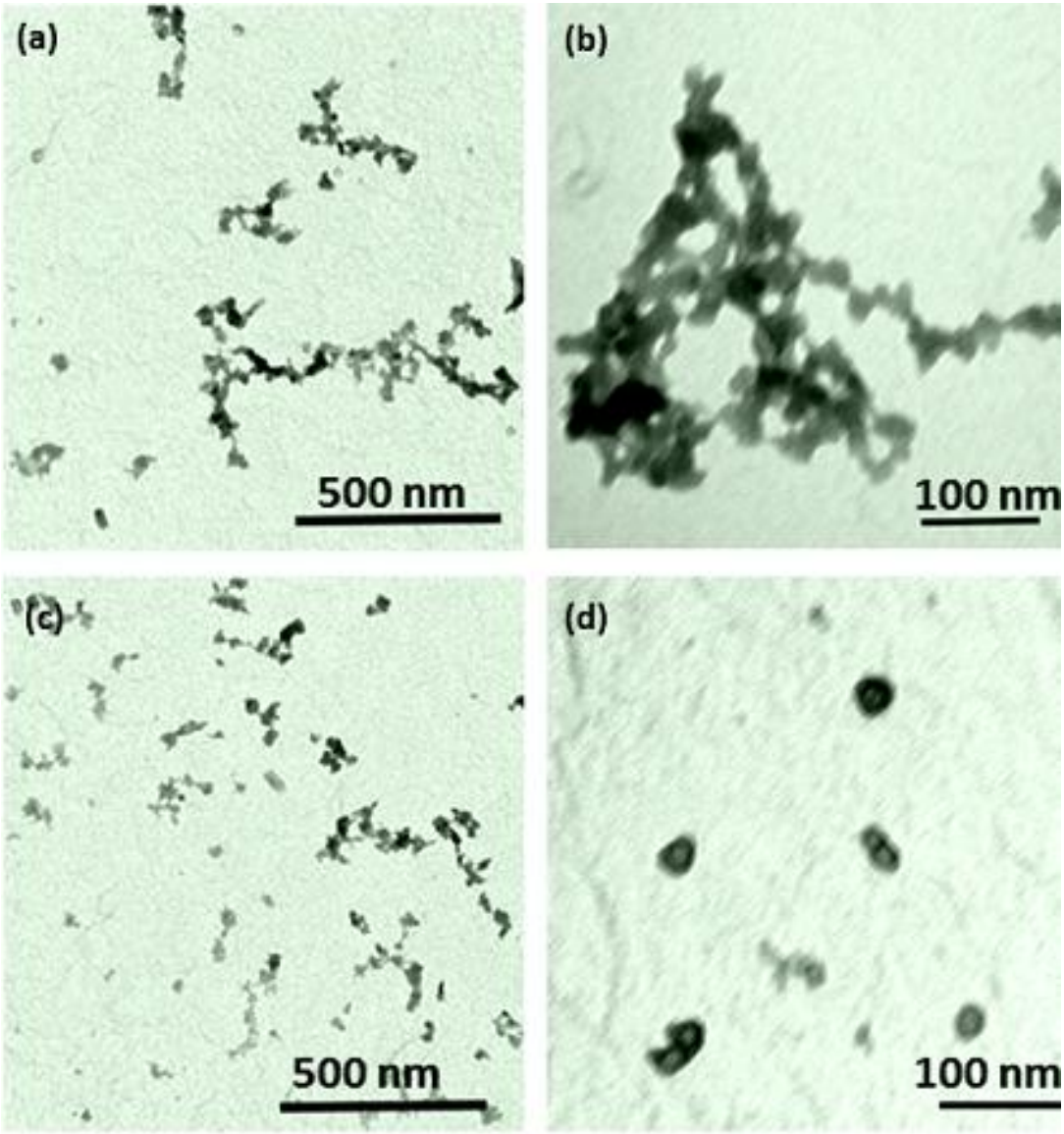

Figure 4-2 Transmission electron microscope images of brushite synthesized at room temperature in 3 minutes residence time via CPFS (a,c) magnification 50k (bar = 500 nm), (b,d) magnification 200k (bar = 100 nm)

On the other hand, particles obtained from CDHA had flower like, tubular morphology and possessed particle size of *ca*. 95 ± 15 nm as shown in Figure 4-3. TEM images of sample whitlockite possessed spherical morphology with the average particle size of ~ 45 ± 15 nm (100 particles sampled).

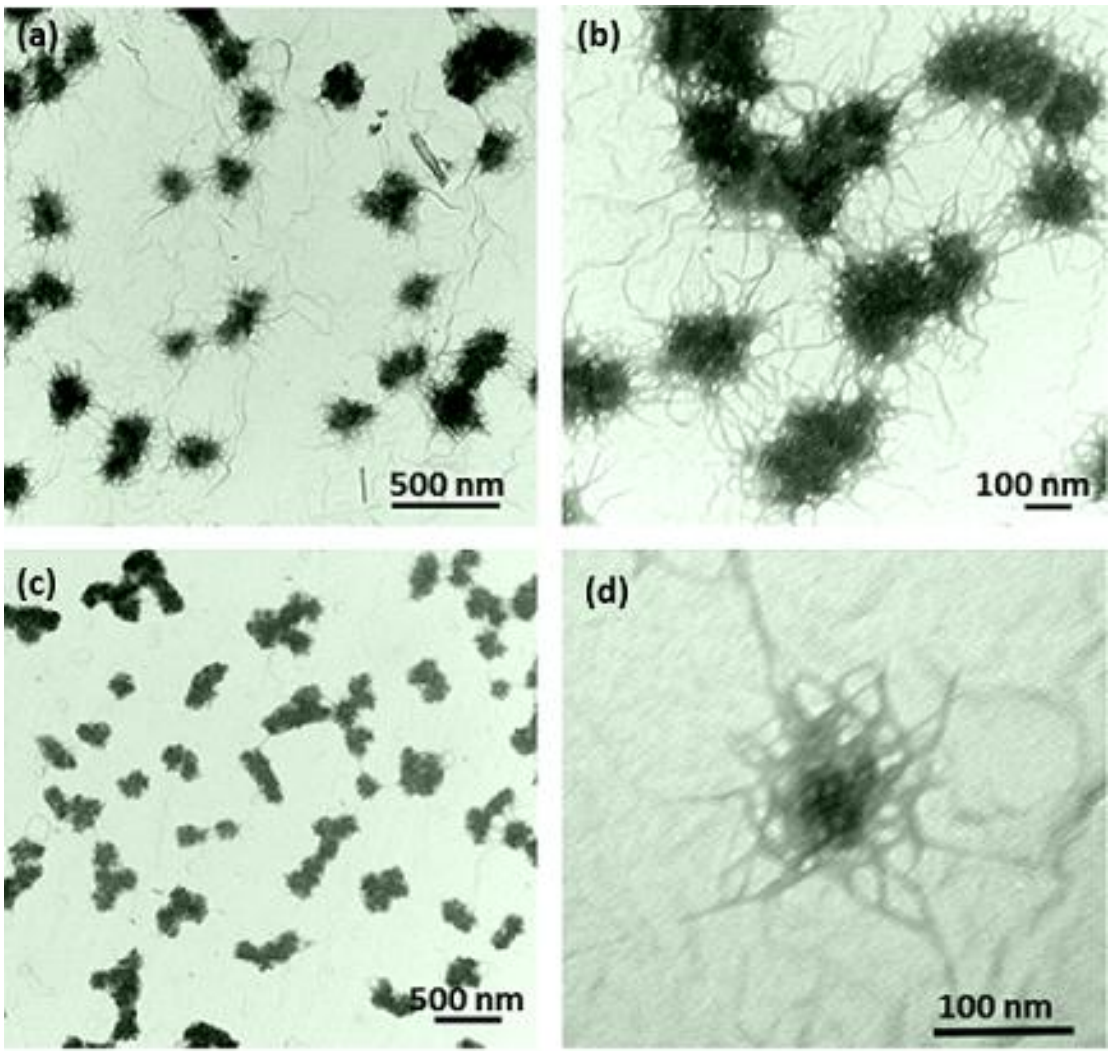

Figure 4-3 Transmission electron microscope images of calcium deficient HA made at 70 °C in five minutes residence time via CPFS (a,c) magnification 50k (bar = 500 nm), (b,d) magnification 200k (bar = 100 nm)

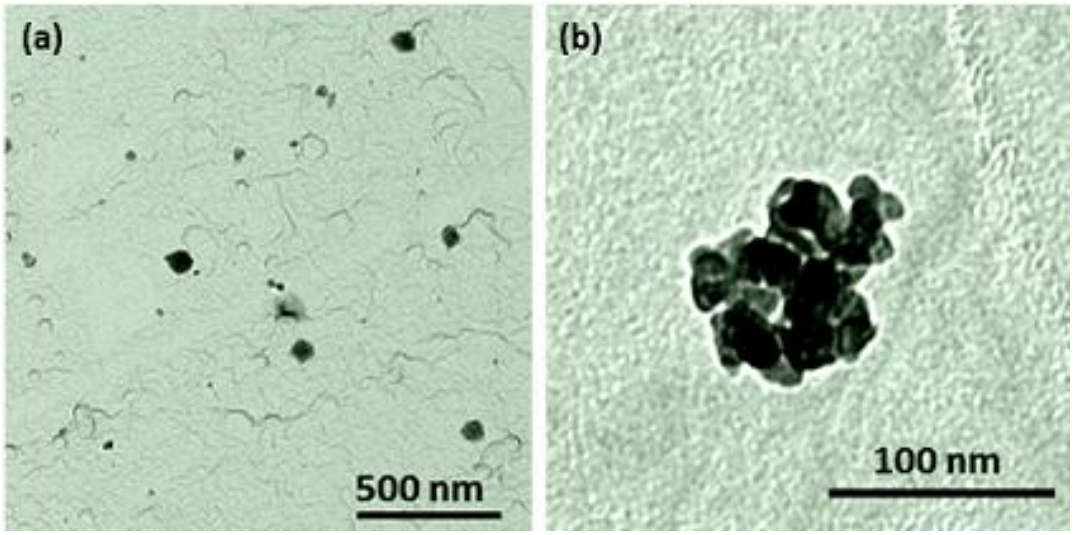

Figure 4-4 Transmission electron microscope images of beta-tricalcium phosphate (a) magnification 50k (bar = 500 nm), (b) magnification 200k (bar = 100 nm)

BET surface area measurements (N2 adsorption) of as precipitated HA and CDHA samples yielded sufrace areas of ca 195 and 80 m^2 g^{-1}, respectively while heat-treated samples at 1000 °C for one hour revealed surface areas of 4.9 ± 0.1 and 5.9 ± 0.1 m^2 g^{-1}, respectively. The results of the present study are in agreement with previous reports that indicate that the amorphous HA made at ambient conditions possesses a surface area of 90 m^2 g^{-1} after oven-drying and 113 m^2 g^{-1} after freeze-drying (Chaudhry et al., 2006).

4.3.2 Powder X-ray Diffraction

XRD analysis indicated that the as-synthesized products obtained at a lower temperature of 22 °C were exclusively brushite particles (Safronova et al., 2009). The XRD patterns shown in Fig. 4-5 show the most intense peaks are at 2θ values of *ca.* 11.6, 20.9, 23.6 and 29.3° assigned to the (020), (121), (040) and (112) Miller indices of brushite. The XRD data, confirmed that the products obtained were fairly well-crystallized.

Brushite is readily transformed into monetite ($CaHPO_4$) by losing its water of crystallization upon heating above 110 ^oC [40] as described in Equation 4. The presence of calcium pyrophosphate ($Ca_2P_2O_7$) in a heat-treated sample indicates the presence of HPO_4^{2-}. This phase can be formed by the loss of one H_2O molecule from two HPO_4^{2-} groups of brushite under high-temperature conditions. The transition of monetite into

pyrophosphate typically occurs at temperatures above 400 °C as described in Equation 5.

$CaHPO_4 \cdot 2H_2O \rightarrow CaHPO_4 + 2H_2O$ (4)

$2CaHPO_4 \rightarrow Ca_2P_2O_7 + H_2O$ (5)

The results of the present study are in agreement with previous reports (Tas and Bhaduri, 2005) that indicate that the brushite can be transformed into monetite (in this case at *ca.* 180 °C) and the monetite to calcium pyrophosphate transition is possible (here it was completed above 440 °C). Thus, an alpha calcium pyrophosphate phase was observed at both 500 and 700 °C. Furthermore, a beta-calcium pyrophosphate phase was obtained after heat treatment at 850 or 1000 °C, respectively.

The presence of calcium pyrophosphate in a heat-treated brushite sample indicates the presence of HPO_4^{2-}. Calcium pyrophosphate is formed by the loss of one H_2O molecule from two HPO_4^{2-} groups of brushite under heat treatments at various conditions. The transition of monetite into pyrophosphate typically occurs at temperatures above 400 °C.

The powder X-ray diffraction results confirmed that the products obtained at 70 °C in five minutes residence time using CPFS reactor (HA, β-TCP, CDHA and biphasic HA / β-TCP) were phase pure. The lattice constants of HA were similar to reference JCPDS Pattern no. 09-432. No decomposition of HA into other phases was observed even after heating at 1200 °C in air for 1h.
The XRD plot obtained for the sample Whitlockite showed good agreement and excellent match with JCPDS pattern 09-0426 Syn $Ca_{3(}PO_4)_2]$.

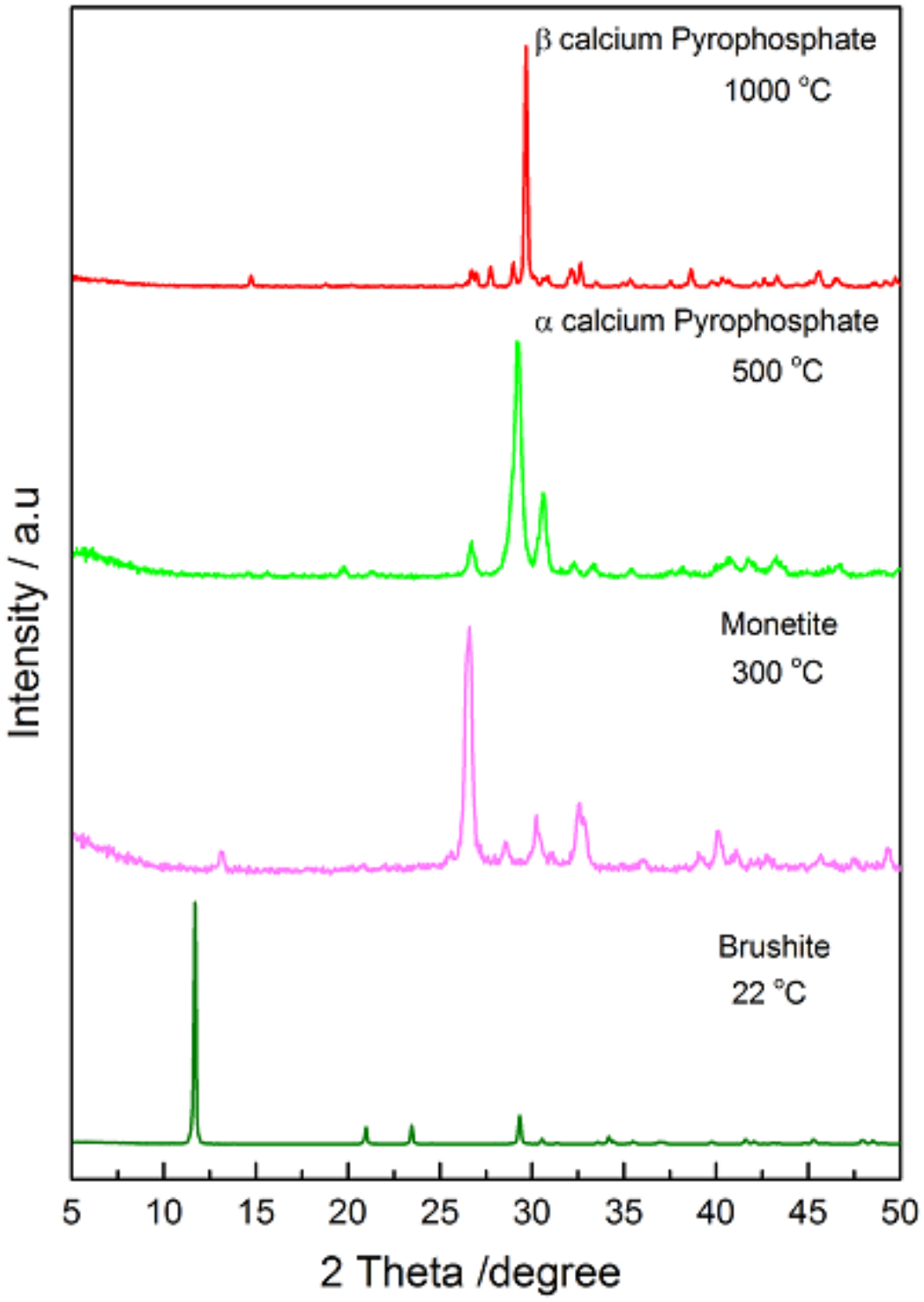

Figure 4-5 Brushite nanoparticles made at room temperature in five minutes residence time via CPFS and heat-treated at 300 °, 500 ° and 1000 °C.

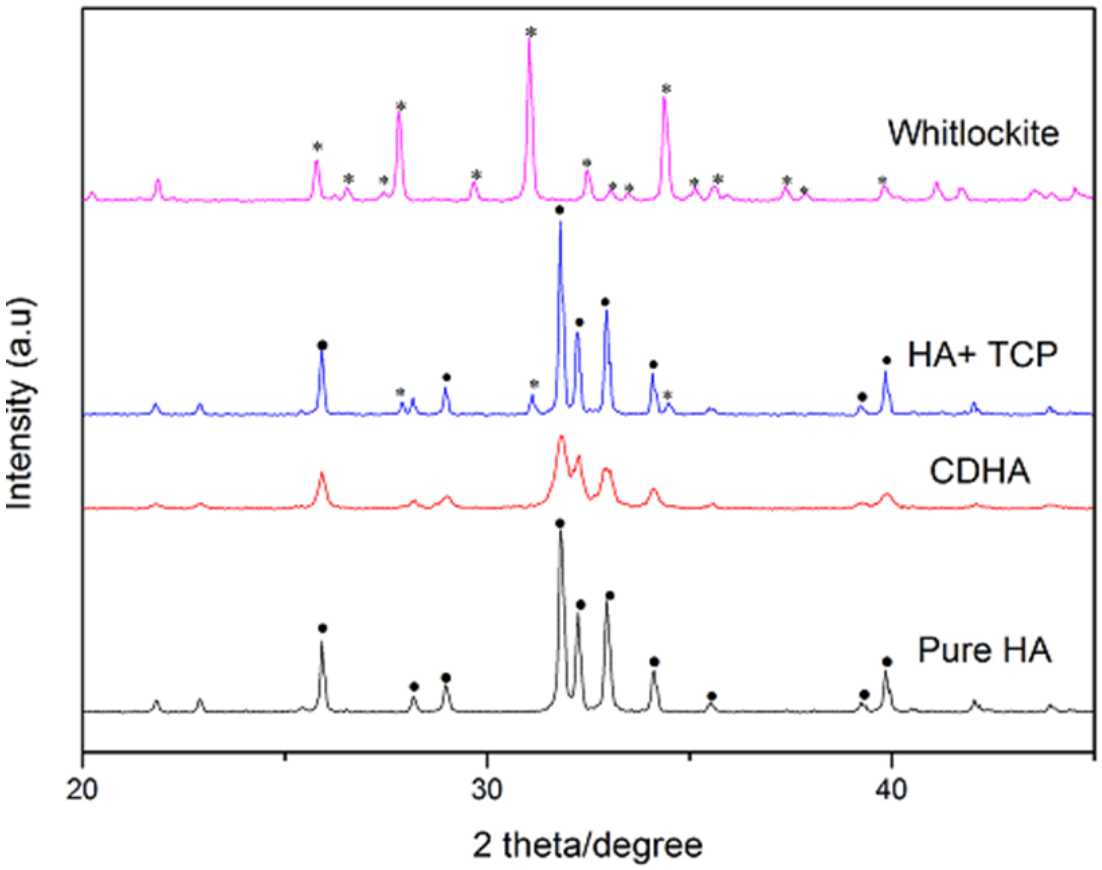

Figure 4-6 X-ray diffraction patterns of pure HA, CDHA, HA+TCP and β-TCP

4.3.3 FTIR Spectroscopy

Brushite formation was also confirmed by FTIR spectral analysis. Figure 4-7 shows the FTIR spectra of products obtained at different temperatures. The spectra exhibit easily distinguishable bands attributed to PO_4^{3-} for the non heat-treated form of brushite. Bands at *ca.* 525 and 575 cm^{-1} were attributed to the v_4 bending vibrations of the P-O-P linkage. Peaks at 873 and 1225 cm^{-1} were assigned to the HPO_4^{2-} group of brushite were observed in all samples.

The data were in good agreement with the previous reports of Vallet-Regi and Gonzalez-Calbet (Joshi and Joshi, 2003, Vallet-Regi and González-Calbet, 2004) and Lu and coworkers (Lu et al., 2006). A band at 985 cm^{-1} was due to the P-O(H) v_1 symmetric stretching vibration of PO_4^{3-}. Whilst a peak at 1060 cm^{-1} was due to the v_3 vibration of the PO_4^{3-} group. A broad band in the range 3400–3600 cm^{-1} was observed, due to the stretching (ν_s) mode of H-bonded OH^- or water. The FTIR spectra thus show

that the nano-particles obtained in the as-synthesized samples were brushite, whereas calcium pyrophosphate was obtained after calcination.

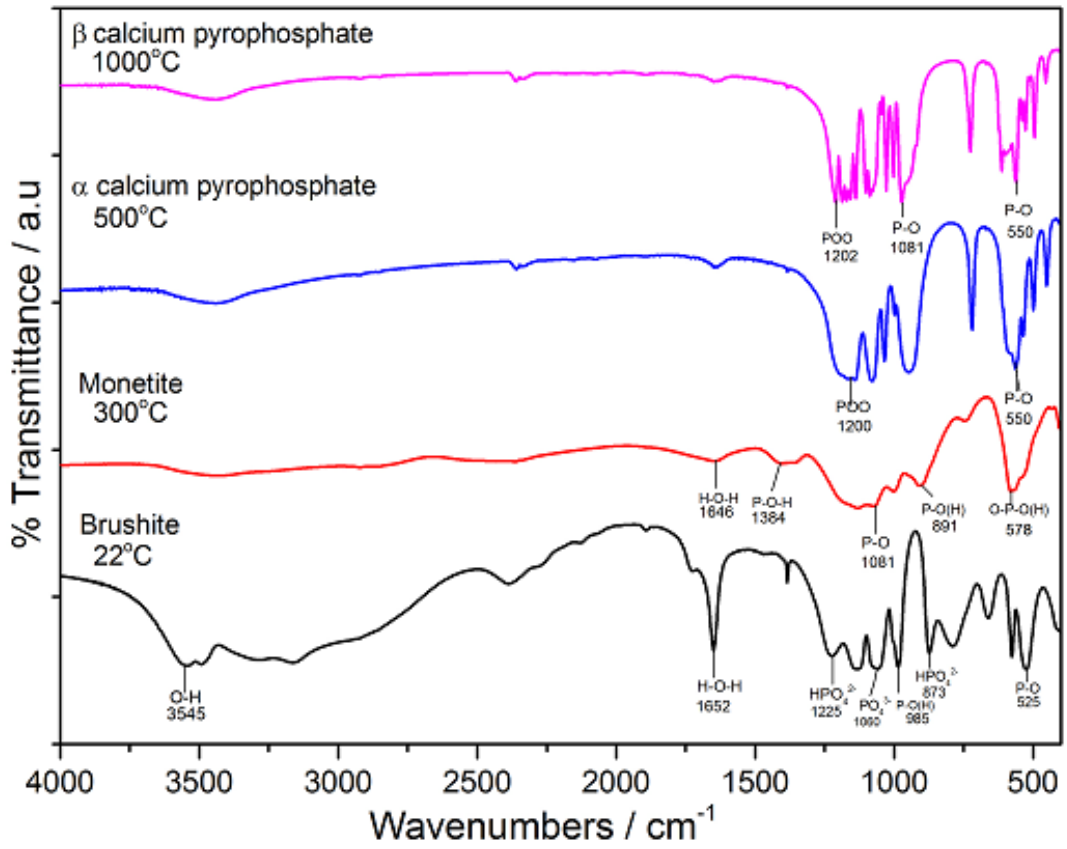

Figure 4-7 FTIR spectra of brushite nanoparticles obtained at different temperatures

FTIR and Raman spectroscopy were used to analyze the different calcium phosphates samples (made at 70 °C in five minutes residence time via CPFS) and aid identification of different calcium phosphates as shown in Figure 4-8. FTIR data revealed peaks at 3420 and 632 cm-1 (corresponding to stretching vibrations of the hydroxyl group in HA. The intensity of a peak at 1637 cm^{-1}, corresponding to the bending mode for lattice water, was observed to decrease with increasing synthesis temperature. Peaks at 1453 and 1414 cm^{-1} correspond to the stretching modes, respectively, of some substituted carbonate in the HA.

The weak absorption peak at 880 cm^{-1} was assigned to the P–O–H vibration in the HPO_4^{2-} group which exists in non-stoichiometric HA. Peak at 1031 cm^{-1} corresponds to the P–O asymmetric stretching mode of phosphate, whilst the peaks at, 534 and 466 cm^{-1} correspond to O–P–O bending modes. An increase in intensity and sharpness of these peaks with temperature, indicates an increase in crystallinity.

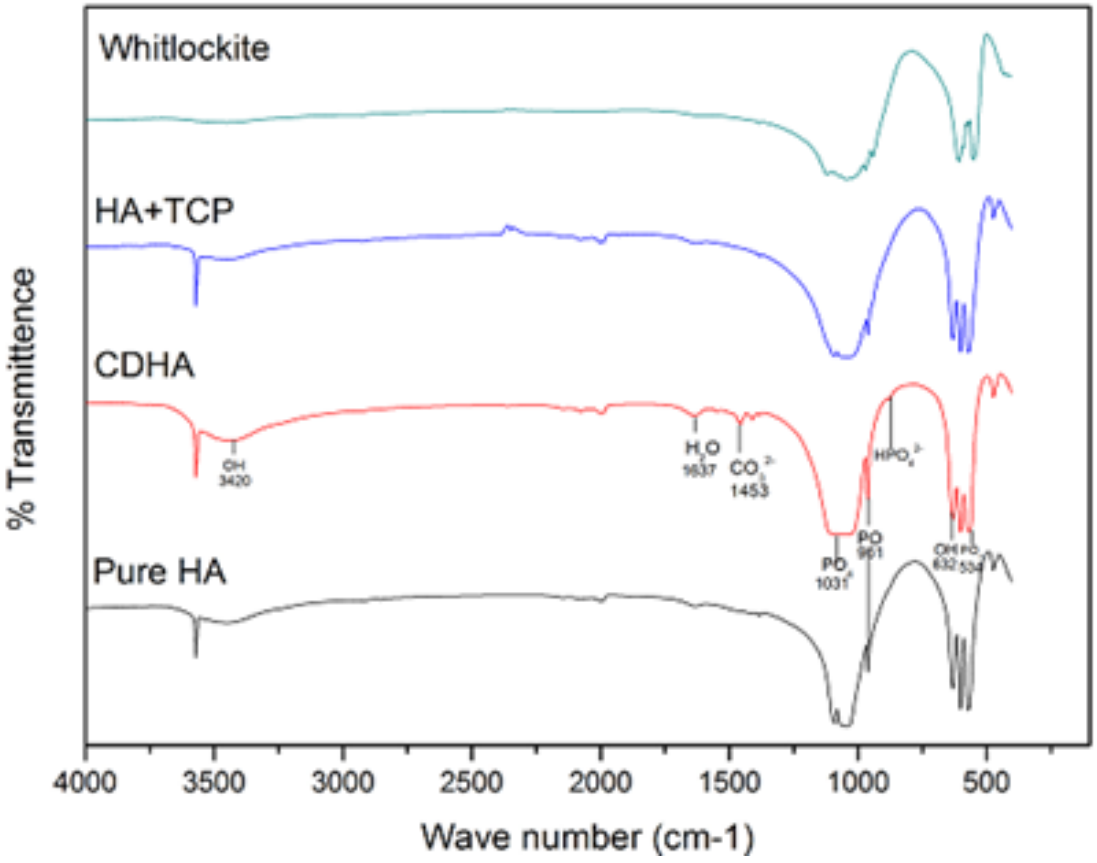

Figure 4-8 FTIR spectra of pure HA, CDHA, HA+TCP and β-TCP nanoparticles obtained at different temperatures

4.3.4 *In-vitro* Biocompatibility

The osteoblast cells cultured on phase pure as prepared brushite samples (pressed discs) showed continuous proliferation as shown in Figure 4-9. The cells were seen to attach, spread and grow on the surface which indicated that material was non-toxic to the cells. A significant increase in the growth of osteoblast cells with culturing time was observed.

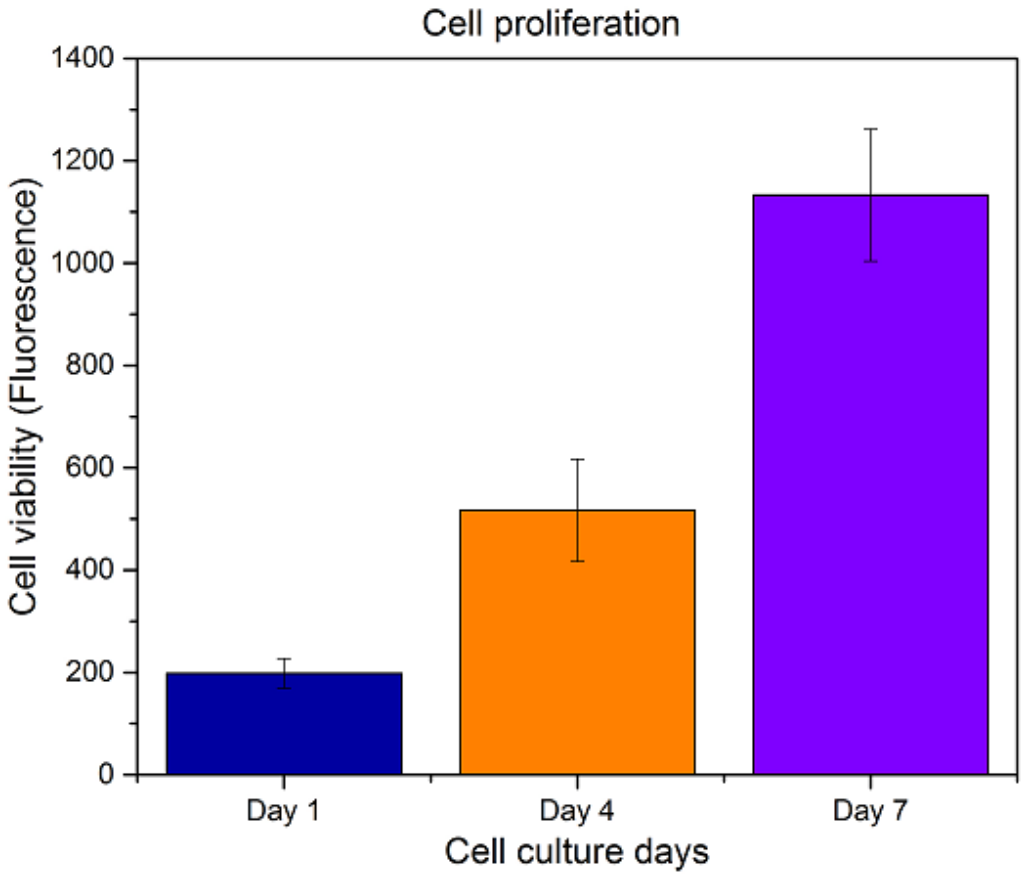

Figure 4-9 Human osteoblast cell proliferation as pressed discs of brushite nanopowder after 1, 4 and 7 days of culture

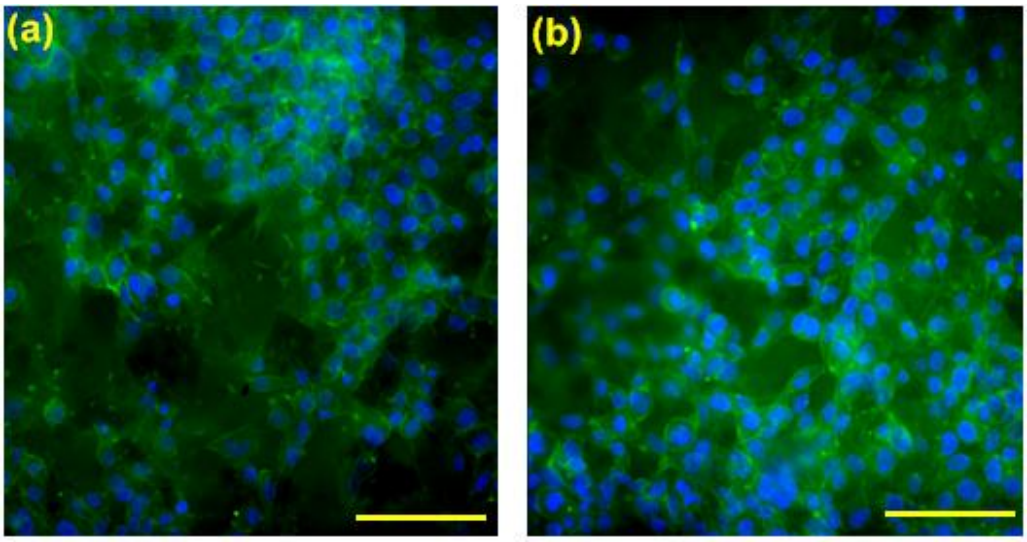

Figure 4-10 Pressed discs of brushite nanopowder imaged at day 7, MG63 nucleus (blue) and cytoskeleton (green)

Morphological images taken of these cells on day 7 are shown in Fig. 4-10. The cells were round and almost flattened against the surface that showed the colony formation and was attributed to continuous proliferation.

A human osteoblast cell proliferation study was conducted on all 4 samples (pure HA, CDHA, HA+TCP and β-TCP). The osteoblast cells cultured on all ceramic samples showed continuous proliferation. Cells were seen to attach, spread and grow on all types of samples as shown in fig. 4-11. A significant increase in the growth of osteoblast cells with culturing time was observed on all samples, and the highest level of viability was observed for whitlockite. This could be due to the faster dissolution rate of whitlockite sample as compared to pure HA.

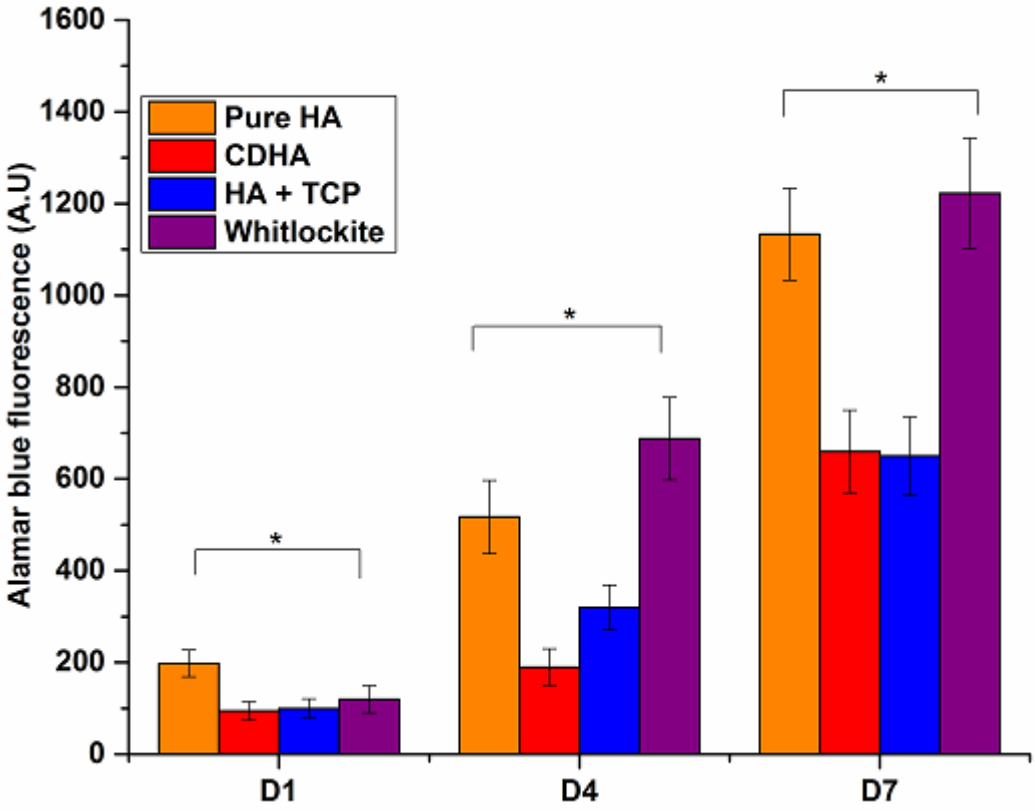

Figure 4-11 MG63 viability on HA discs. Cell viability was measured at days 1, 4 and 7 via Alamar blue assay for MG63s cultured on pure HA, CDHA, HA+TCP and whitlockite (β-TCP).

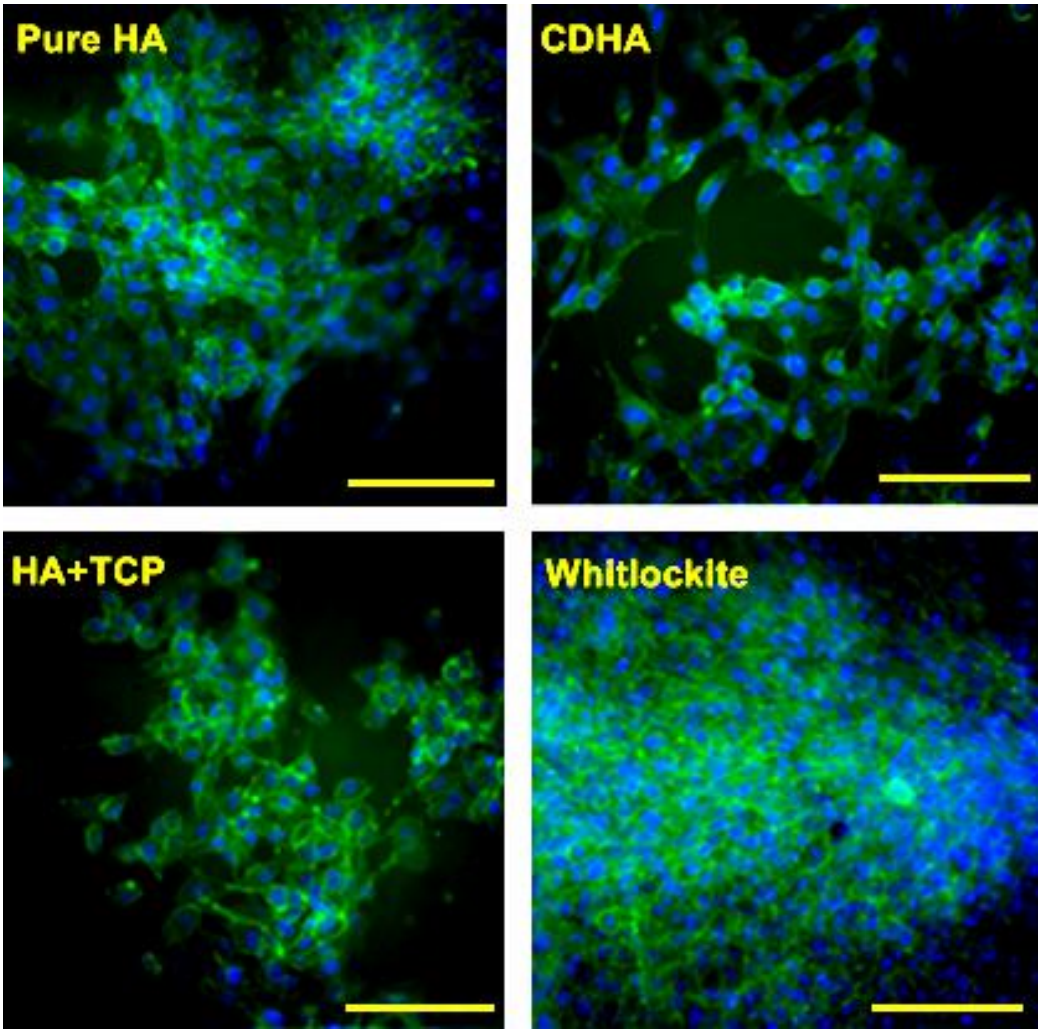

Figure 4-12 MG63 morphology on HA discs. Cells were visualised at day 7 for cell nucleus (DAPI in blue) and cytoskeleton (phalloidin-FITC in green) for MG63s cultured on pure HA, CDHA, HA+TCP and pure whitlockite (β-TCP).

4.3.5 X-ray Photoelectron Spectroscopy

A chemical analysis of the phase pure brushite sample was performed by using XPS analysis. The XPS survey spectrum of brushite is shown in Figure 4-13. Besides the expected Ca, P and O peaks, a small C 1s peak was also observed which was due to carbon tape used for all analysis. The binding energy scale was calibrated by a C 1 s peak at 285.0 eV. The peaks at 134 eV corresponded to P 2p spectra of hydroxyapatite. The binding energy values for O 1s and Ca 2p were measured as 532 and 347 eV,

respectively. The Ca/P elemental ratio in the analysed sample was the expected one i.e 0.8.

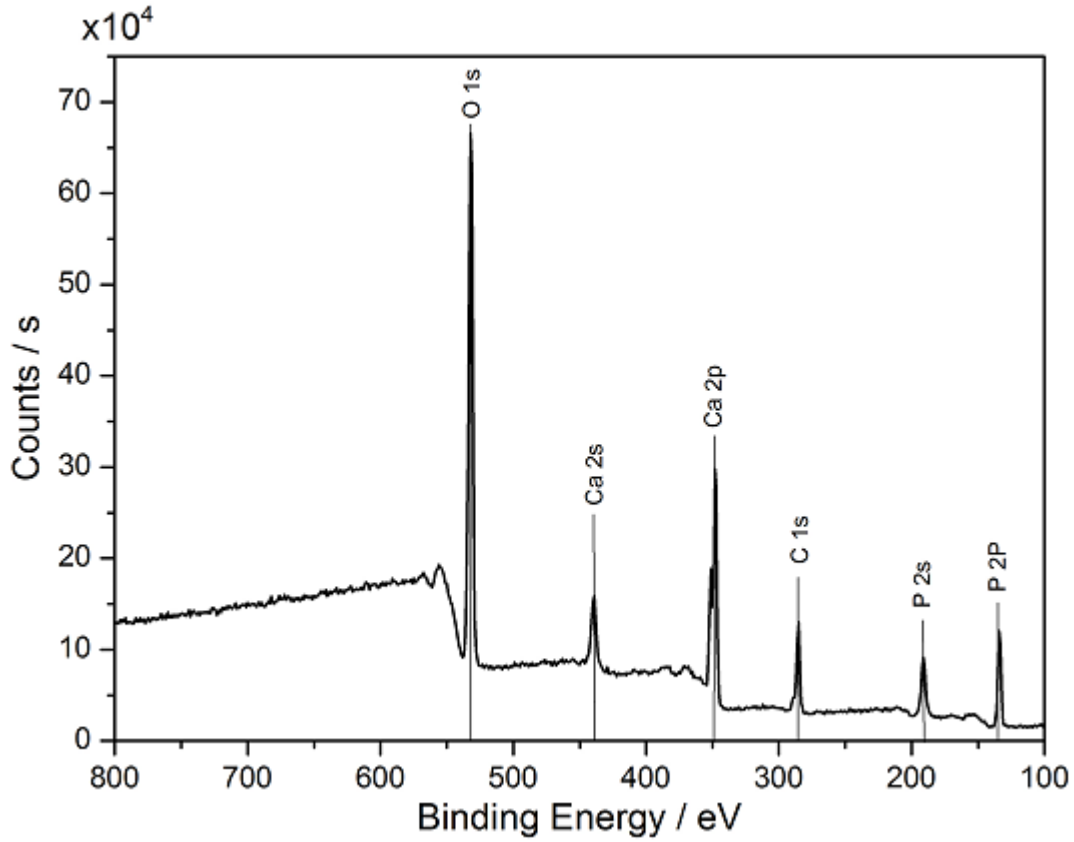

Figure 4-13 XPS Survey spectrum of phase pure brushite nanopowder

The Ca 2p spectrum could be resolved into two peaks for Ca $2p_{3/2}$ and $2p_{1/2}$ (two spin-orbit pairs) at 347.5 and 351.2 eV, respectively, which are related to calcium apatite [44]. In Fig. 4-15b, the 2P peak at 133.8 eV can also be deconvoluted into two peaks with a spin orbit splitting for $p_{1/2}$ and $p_{3/2}$ levels with binding energies of 134.2 and 133.4 eV, respectively (Lee et al., 2003, Lu et al., 2000).

Figure 4-15c, shows the XPS spectrum of O 1s and the peaks at 530.6 and 532.2 eV that are attributed to the phosphate group, and adsorbed water in apatite crystal, respectively [46]. These values were consistant with those measured for standard brushite powders (within the 0.2 eV precision of the measurements) (Mahabole et al., 2005, Landis and Martin, 1984).

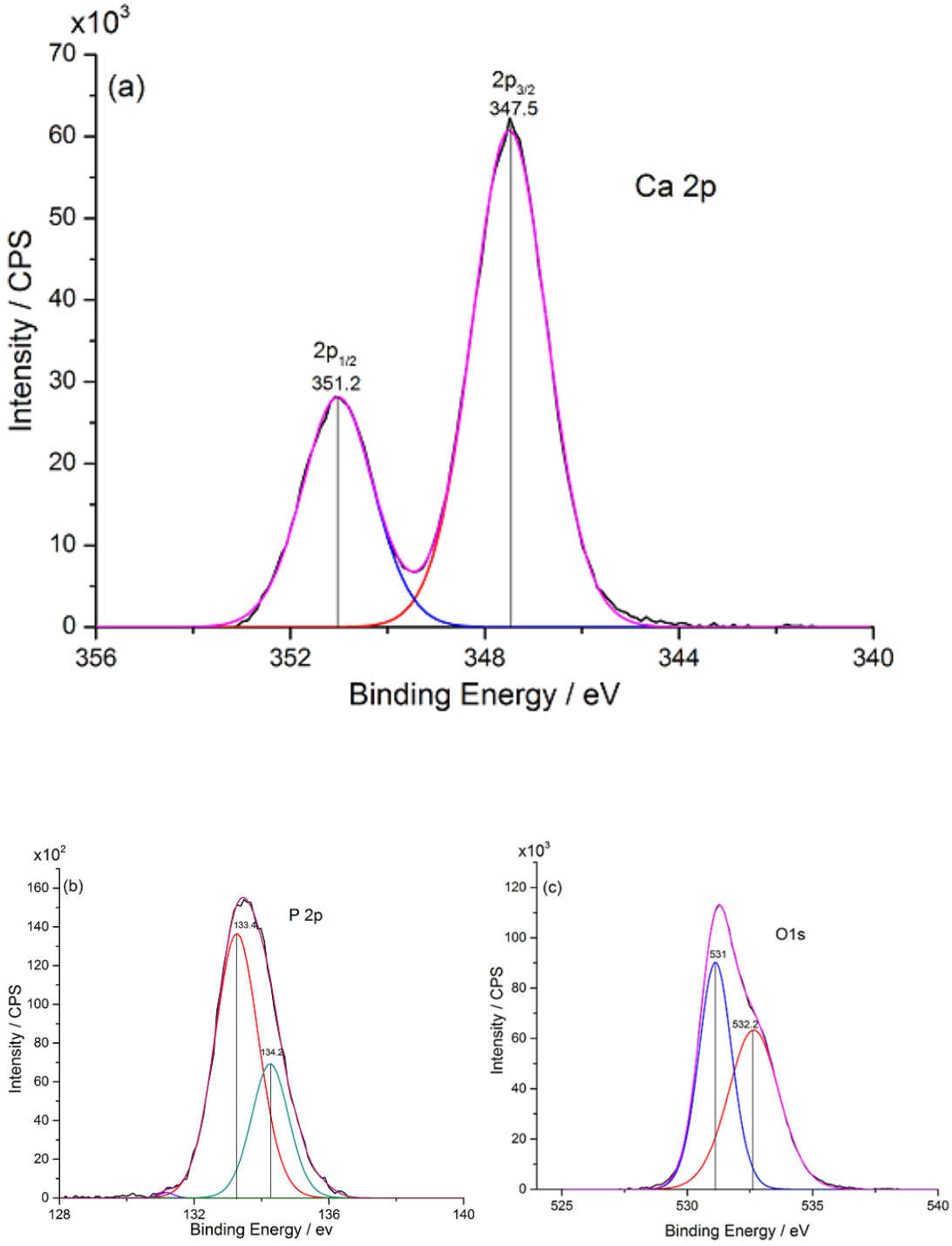

Figure 4-14 [a-c] XPS Spectra of Ca 2p,O 1s and P 2p recorded from the phase pure brushite made at room temperature in 3 minutes residence time via CPFS system.

4.4 Conclusions

The reactive crystallization and thermal decomposition study of brushite was conducted in a plastic flow reactor. Different phases were observed in the synthesis of brushite. The first phase that was formed in situ was HA followed by the appearance of few crystals of brushite. Both phases coexist in the solution for first two minutes of the flow reaction. However after a reaction time of at least two minutes at room temperature and pH 5.5 HA transformed to phase pure stable brushite crystals. The reaction pH and temperature were shown to play an important role in the formation of single phase brushite.

Cell toxicity analysis of the brushite as pressed discs confirmed the biocompatibility of this material as a consequence of cell proliferation up to 7 days. Thus the obtained brushite nanopowder is a promising candidate material to be considered for further use in biomedical applications where bone substitution or controlled resorbibility of bone grafts is requied.

It was observed that by tailoring Ca:P ratio and pH and by keeping other reactor parameters the same, any phase pure calcium phosphate product with contolled particulate properties can be achieved using CPFS system.

In summary, Continuous (plastic) flow synthesis (CPFS) technique provides a rapid (as low as 3 minutes), facile and economical pathway to obtain brushite and other calcium phosphate bioceramics with high purity, suitable size and ultra low level of impurities. The results of the in vitro studies showed that the all synthesized samples (pure HA, CDHA, HA+TCP and pure whitlockite) are biocompatible. Hence the current work deals with the preparation of synthetic calcium phosphates with optimum properties closer to those of living hard tissues like bone and teeth, aiming at better and more effective biomedical ceramics for use as powders or as nanocomposites in future efforts.

4.5 Future Work

Since the solution pH was determined to be the dominating factor in order to get the accurate phase along with Ca:P ratio It would be interesting to use different pH ranges (acidic and basic) for attaining a range of different calcium phosphates and their nano-composite mixtures.

The current work deals with the preparation of synthetic phase pure calcium phosphates with optimum properties closer to those of living hard tissues like bone and teeth, aiming at better and more effective biomedical ceramics for use as powders or as nanocomposites in future efforts.

Chapter 5
Continuous Plastic Synthesis and Characterization of Nano-sized Magnesium and Strontium Substituted Calcium Apatite

5.1 Introduction

Calcium phosphate bioceramics are well known for their use in bone repair applications for example as bulk defect fillers, injectables, the hard phase of biocomposites and biocompatible coatings on implants. Synthetic hydroxyapatite (HA), $[Ca_{10}(PO_4)_6(OH)_2]$, is chemically similar to the mineral component of hard tissues (biological apatite) and is widely used in hard tissue augmentation and replacement with slow resorption (Elliott, 1994, Wu et al., 2004, Hench and Wilson, 1993). HA can physiochemically bond to bone and promote bone formation, which is necessary for implant osseointegration. Osseointegration is needed to repair bone loss and to increase implant efficiency and stability (Norhidayu et al., 2008).

Biological and physiochemical properties of HA can be tailored by the substitution of Ca with certain ions, some of which are present in the natural apatites of bone. Most biological apatites are non-stoichiometric because of the presence of minor constituents which include cations e.g. Mg^{2+}, Mn^{2+}, Zn^{2+}, Na^{+}, Sr^{2+} or anions e.g. HPO_4^{2-} or CO_3^{2-}. HA is capable of accepting substitute ions within its lattice and trace ions substituted in apatites can effect lattice parameters as well as crystallinity, dissolution kinetics, surface charge and other physical properties (Miao et al., 2005).

Magnesium (Mg^{2+}) is a divalent cationic substitute for calcium (Ca^{2+}) in the HA lattice. Such substitution often reduces crystallinity, increases solubility, and lowers the temperature at which conversion of HA into β-Tricalcium phosphate (β-TCP) occurs (Suchanek et al., 2004b, Wu et al., 2005, Bertoni et al., 1998, Suchanek et al., 2004a). As the amount of substituted magnesium affects thermal stability of apatite or other phases, this has implications for sintering behavior [3]. For example, the β-TCP to α-TCP phase transformation normally occurs at *ca.* 1180°C for the pure Ca compounds. However, Mg^{2+} substitution for Ca^{2+} can increase the transformation temperature up to

ca. 1500 °C (Chaudhry et al., 2008, Bigi et al., 1993, Yoshida et al., 2005). This enables enhanced sintering of β-TCP at elevated temperatures without deleterious formation of α-TCP (the latter is a less bioactive polymorph). Magnesium substitution levels of up to 1.6 wt% have been reported using wet precipitation reactions (BLUMENTHAL, 1989). Surprisingly, as much as 28.4 wt% in HA has also been demonstrated in previous studies using mechano-chemical synthesis routes (Mayer et al., 1997). However, an excess of Mg^{2+} can also be detrimental as it is known to reduce bioactivity *in vivo* in certain biomaterials (Suchanek et al., 2004b). The complete substitution of Mg^{2+} for Ca^{2+} in HA has been shown to prohibit the formation of an extracellular matrix and has deleterious effect on bone cells (Yang et al., 2005, Zyman et al., 2006, Serre et al., 1998).

Mg^{2+} as one of the key substitutes for Ca^{2+} in natural apatites and is expected to have reasonable biocompatibility and favorable biological properties. Human bone, enamel and dentine comprise 1.0, 0.4, and 1.2 wt% of Mg^{2+}, respectively, and it is believed that Mg^{2+} ions may play an important role in the initial formation of tooth apatites and have a significant effect on their physiochemical properties. As well as Mg-HA, other phases such as Mg-whitlockite can also be made from precipitation reactions at relatively low temperatures (< 95°C) which has been known as a promising bone replacement material because of its high bioactivity and resorbable properties. (Serre et al., 1998, Chaudhry et al., 2008).

Among the group 2 cations that can replace calcium in HA, Sr^{2+} has gained interest for its possible beneficial biological role. Strontium is present in the mineral phase of bone and connective tissue at levels of 320-400 mg of strontium. Clinically, strontium has been observed to confer beneficial effects on bone growth especially at the regions where high metabolic turn-over occurs (Blake et al., 1986). It also known to be beneficial in the treatment of osteoporosis. In vitro, strontium increases the number of osteoblast cells followed by the reduction osteoclast cells whereas strontium administration decreases bone resorption and stimulates bone formation. Furthermore, in addition to its antiresorptive activity, strontium has been found to have anti-osteoporosis and antiosteopenic acitivity in animal models. The beneficial effects in osteoporosis were as a result of mechanical strength of bone (in animal models). Strontium treatment increased bone mineral density (BMD), bone mineral content

(BMC), bone volume and microarchitecture, reduced bone fracture risk and improved the mechanical performance of whole bone without affecting the estimated material properties of the bone tissue (Canalis et al., 1996, Panzavolta et al., 2008, Grynpas et al., 1996, Marie et al., 2001, Dahl et al., 2001, Marie, 2005).

Strontium can replace calcium in the HA structure across the compositional range. The solid solutions, which have previously been obtained by hydrothermal methods or by treatment at high temperatures, display a linear variation in the lattice parameters with composition. Other literature reports suggested the replacement sites of Sr for Ca in Ca-HA (Zhu et al., 2006, Kikuchi et al., 1994, Bigi et al., 1998).

In this chapter, CPFS system is successfully used to synthesize magnesium and strontium substituted calcium phosphate bioceramics with unique physical and compositional attributes (ion substitution level, particle size, crystallinity and phase composition) that possess novel properties, which would be useful in the development of bioceramics.

5.2 Experimental

5.2.1 Synthesis of Magnesium Substituted Calcium Phosphates

All samples were made at 70 °C using a novel continuous plastic flow synthesis (CPFS) system. The details of the CPFS system are described in section 2.2.1. In the synthesis process, separate reservoirs of calcium nitrate with different wt% of metal ions (Ca + Mg)/P = 1.67) ranging from 1 to 10 wt%, and diammonium hydrogen phosphate, respectively, were pumped to meet at a Polyflon™ T-piece through a Polyflon™ straight union reducer. Amonium hydroxide was used to maintain the pH of both the solutions prior to the reaction above pH 10. The residence time from the T-piece to the exit of the tubing was 5 minutes. All reactions were carried out at 70 °C and atmospheric pressure. The product was collected as a suspension in a beaker at the exit point and centrifuged, washed and freeze dried as explained earlier in section 2.3.1.1. The dried free flowing white powders were then heat-treated at 1000 °C for 2 hours in air at the heating rate of 10 °C/min.

In total, ten reactions were carried out using magnesium nitrate as magnesium ion source. The samples were labelled as 1Mg-CaP, 2Mg-CaP, 3Mg-CaP, 4 Mg-CaP, 5Mg-

CaP, 6 Mg-CaP, 7Mg-CaP, 8Mg-CaP, 9Mg-CaP and 10Mg-CaP, respectively. The numbers in the sample IDs represent the expected magnesium content (wt%). The dried white powders were then heat-treated at 1000 °C for 2 hours in air at the heating rate of 10 °C/min.

5.2.2 Synthesis of Strontium Substituted Calcium Phosphates

Strontium-substituted calcium phosphates were made using CPFS system, the details of which are described in section 2.2.1. In the synthesis process, basic solutions of calcium nitrate and strontium nitrate (total conc. = 0.5M and (Ca + Sr)/P = 1.67) and diammonium hydrogen phosphate, respectively, were pumped to meet at a 1/16 inch Polyflon™ T-piece through a 1/8 in. Polyflon™ straight union reducer. The pH of both the solutions prior to the reaction was kept above pH 10. This initial mixture was connected to 8 m long 1/16 inch Polyflon™ PTFE that was coiled inside an oil bath, which gave an effective 5 minutes from the tee to the exit of the pipe. The suspension was collected in a beaker at the exit point and was then centrifuged at 4500 rpm for 10 minutes. All samples were washed and freeze-dried as explained earlier; see section 2.3.1.1. The product was obtained as white fine powder with approximately 85% yield.

In total, seven reactions were carried out using strontium nitrate as strontium ion source. The samples were labelled as 1Sr-HA, 5Sr-HA, 10Sr-HA, 15Sr-HA, 20Sr-HA, 25Sr-HA, 30Sr-HA, respectively. The numbers in the sample IDs represent the expected strontium content (wt%).

5.2.2.1 Disc Preparation

The obtained powders from magnesium and strontium substituted calcium phosphate reactions were compacted into cylindrical discs of *ca.* 13 mm diameter and 2 mm thickness by using a hydraulic press at 5 MPa. These samples were used for cell viability studies after sterilization in 70 % ethanol for 1 hr.

5.3 Results and Discussions

5.3.1 Transmission Electron Microscopy

The novel CPFS system was successfully used for cation substitutions (Mg^{2+}, Sr^{2+}) of calcium phosphates. For selected samples, TEM images were collected to investigate the particle morphology with increasing magnesium content or with changes in phase. TEM images of sample pure HA, shown in Figure 5-1 (a) and (b), reveal distinct nanorods of size ~ 85 ± 15 nm (200 particles sampled), along the longest axis and ~ 15 ± 5 nm (100 particles sampled), along the smaller axis.

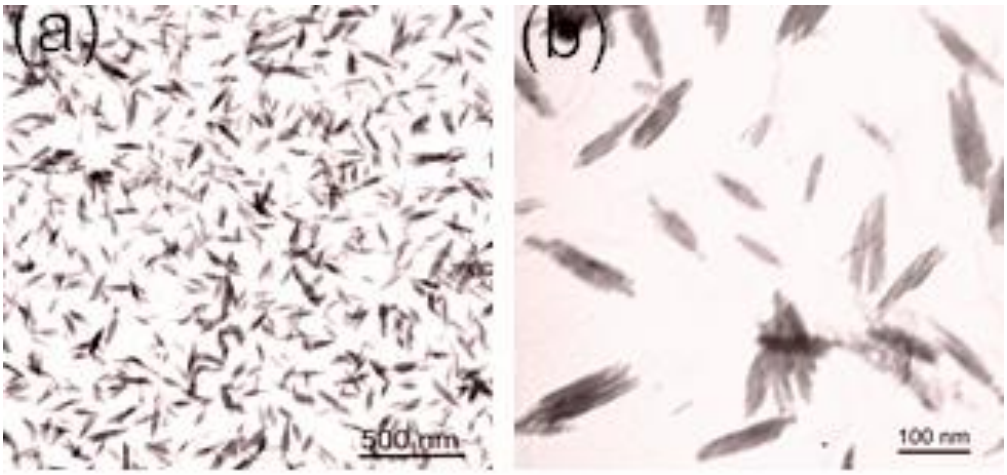

Figure 5-1 Transmission electron microscope images of phase pure hydroxyapatite made at 70 °C in five minutes residence time via CPFS (a) = bar = 500 nm, (b) = bar = 100 nm.

TEM images of sample 1Mg-CaP [Figure 5-2 (a) and (b)] revealed small rod shaped agglomerates with the average particle size of ~ 70 ± 16 nm (200 particles sampled). Sample 6Mg-CaP [Figure 5-2 (c) and (d)] revealed semi-spherical shaped morphology, suggesting a deviation from the rod like morphology.

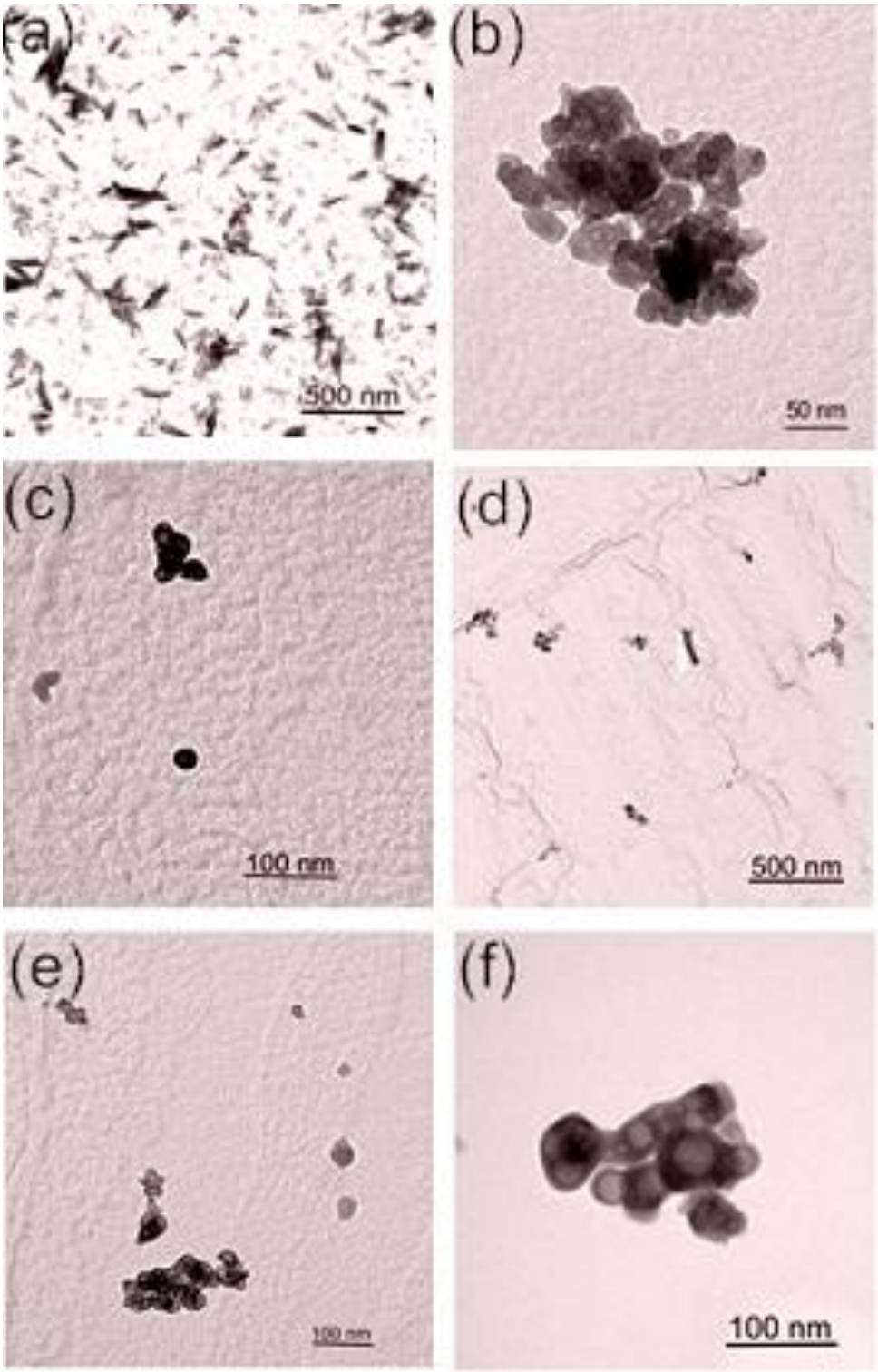

Figure 5-2 Transmission electron microscope images of sample (a), = Pure HA, bar = 500 nm, (b) = Pure HA, bar = 100 nm, (c), = 1Mg-CaP, bar = 500 nm, (d) = 1Mg-CaP, bar = 100 nm, (e) = 6Mg-CaP, bar = 500 nm, (f) = 6Mg-CaP, bar = 100 nm, (g), (h) = 10Mg-CaP, bar = 100 nm.

In contrast, TEM images of sample 10Mg-CaP possessed spherical morphology in large agglomerations with the average particle size of ~ 35 ± 15 nm (100 particles sampled). The TEM images reveal that rounded Mg-whitlockite (identified from PXRD) particles are possibly hollow as shown in Figure 5-2 (e) and (f).

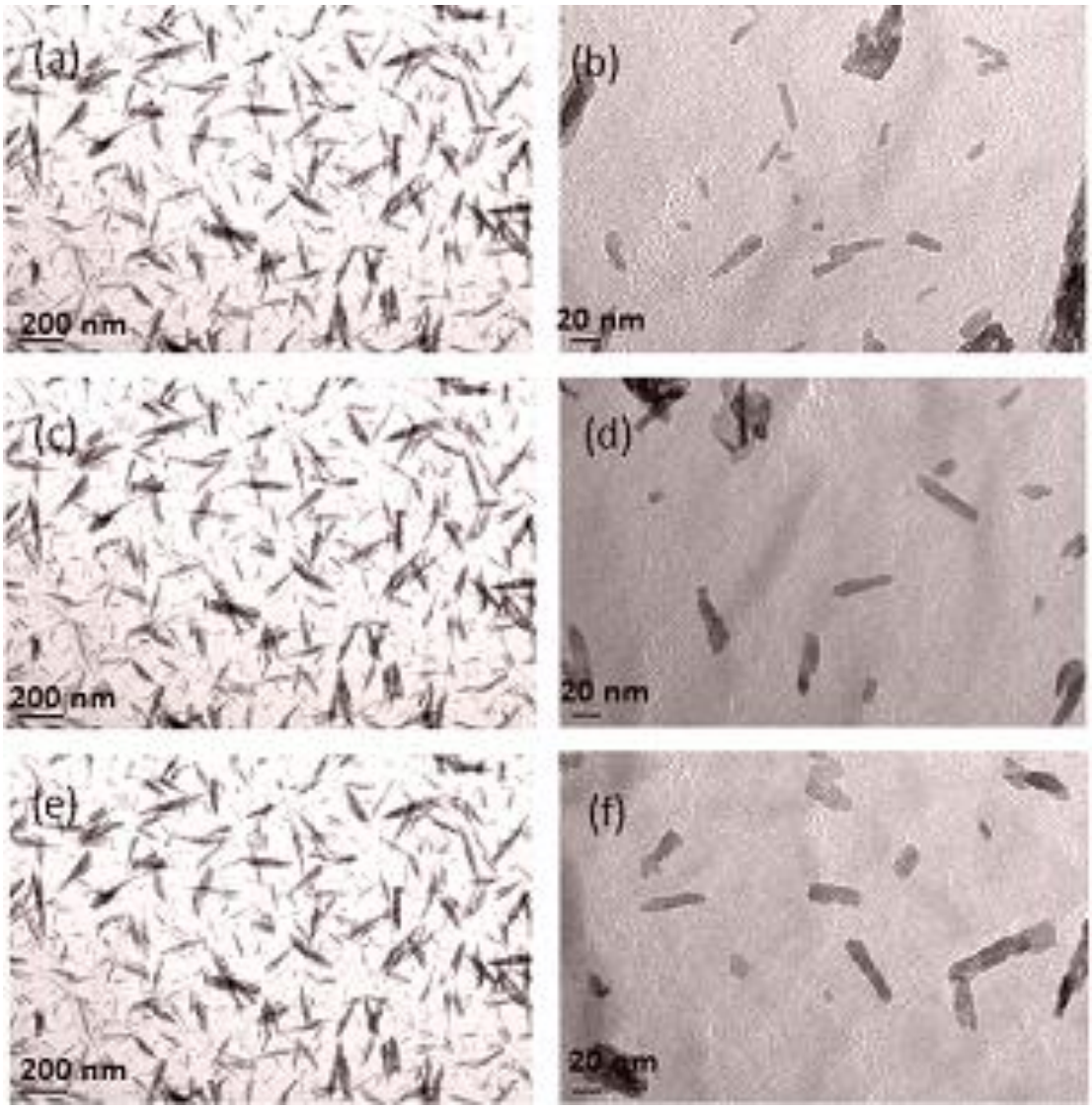

Figure 5-3 Transmission electron microscope images of strontium substituted calcium phosphates made at 70 °C in five minutes residence time via CPFS 10Sr-HA (a) = bar = 200 nm, (b) = bar = 20 nm, 20SrHA (c) = bar = 200 nm, (d) = bar = 20 nm, 30Sr-HA (e) = bar = 200 nm, (f) = bar = 20 nm.

TEM images were also collected for Strontium substituted HA to investigate the particle morphology and size. Figure 5-3 (a) and (b) for sample 5Sr-CaP reveal distinct nanorods of size ~ 75 ± 15 nm (100 particles sampled), along the longest axis. Further increase in strontium concentration lead to larger particles with rod like morphology as observed in Figures 5-3 (c) to (f) for samples 10Sr-CaP [~ 90 ± 15 nm] to 30Sr-CaP [100 ± 20 nm], respectively. It was observed that the presence of strontium in the HA lattice slightly increased the particle size as compared to pure HA as shown in Figure 5-1 (a) and (b).

5.3.2 Powder X-ray Diffraction

The presented novel CPFS system was successfully used for magnesium substitution of calcium phosphates. Powder X-ray diffraction (XRD) data were collected for all samples to investigate how Mg substitution affected phase composition and phase purity. The PXRD data for samples up to 3 wt% Mg-CaP, shown in Figure 5-4, gave a good match to the standard line pattern for crystalline HA [ICDD pattern 09-0432, $Ca_5(PO_4)_3(OH)$]. Samples 4Mg-CaP, 6Mg-CaP and 7Mg-CaP were identified as biphasic mixtures, with a good match to the aforementioned pattern for HA and whitlockite, respectively.

Increasing the magnesium content further (8Mg-CaP and 10Mg-CaP) resulted in significantly broader peaks, which were assigned as phase pure Mg-whitlockite. This was not surprising, as magnesium is known to impede the crystallization and growth of calcium phosphates in solution and also to stabilize whitlockite. Table 5-1 also showed the different XRD phases along with measured magnesium contents in the product. The XPS analysis was used to determine the substitution level of magnesium in different calcium phosphate samples. It was observed from detailed measurement analysis that the measured magnesium contents in all samples were very close to the expected value as shown in Table 5-1.

It was noticed that particles with low magnesium contents were generally rod shape. Whilst more rounded agglomerates were observed by increasing magnesium concentration in reagent solution.

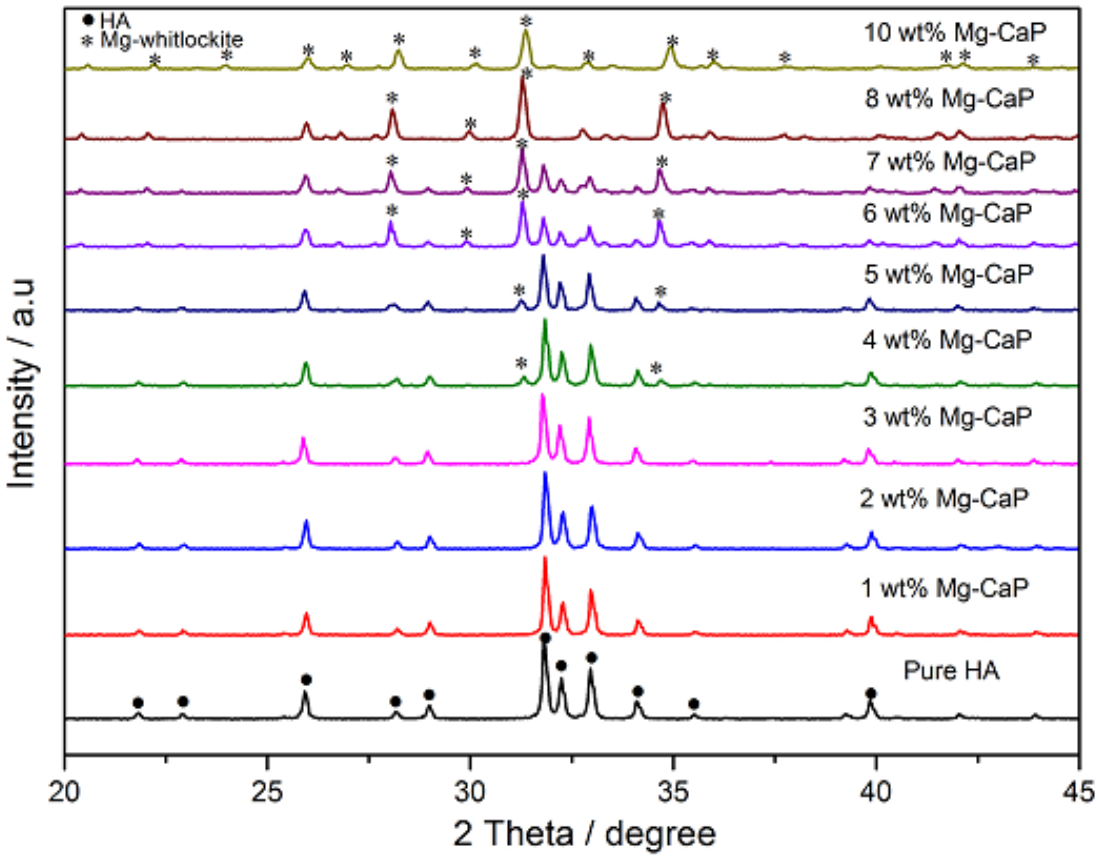

Figure 5-4 Powder X-ray diffraction patterns of heat treated (1000 °C, 1hr in air) Mg-substituted calcium phosphates. The wt% values quoted are based on the amount of magnesium in the precursor feed.

These results suggested that CPFS is an efficient method to obtain a variety of products by varying the substitution level (pure HA, biphasic mixture and pure whitlockite).

The powder X-ray diffraction patterns of the dry heat treated (1000 °C in air for 1h) products with different strontium contents are shown in Figure 5-5. All the patterns indicated that they are constituted of hydroxyapatite as a unique crystalline phase. The XRD patterns of the HA samples containing both Ca^{2+} and Sr^{2+} ions together generally exhibit broader diffraction peaks, in agreement with a reduced degree of crystallinity.

Table 5-1 Sample identification corresponding to wt% based on XPS analysis along with XRD and BET surface area analysis. Key: HA = hydroxyapatite, Mg-HA = magnesium substituted hydroxyapatite, MgW = magnesium whitlockite, BCP = Mg-HA + Mg-W.

Sample ID	**Mg Added (wt%)**	**Mg Measured (wt%)**	**XRD Phase**	**BET Surface Area (m^2g^{-1})**
Pure HA	0	0	HA	195
1Mg-CaP	1	0.8	Mg-HA	160
2Mg-CaP	2	2.1	Mg-HA	139
3Mg-CaP	3	2.9	Mg-HA	119
4Mg-CaP	4	3.7	BCP	91
5Mg-CaP	5	5	BCP	95
6Mg-CaP	6	5.8	BCP	80
7Mg-CaP	7	6.5	BCP	75
8Mg-CaP	8	7.4	MgW	81
10Mg-CaP	10	9.1	MgW	102

The broadening is more evident for the samples with smaller Sr content, suggesting a greater difficulty for Ca-HA to accomodate the larger strontium ion than for SrHA to host the smaller calcium ion.

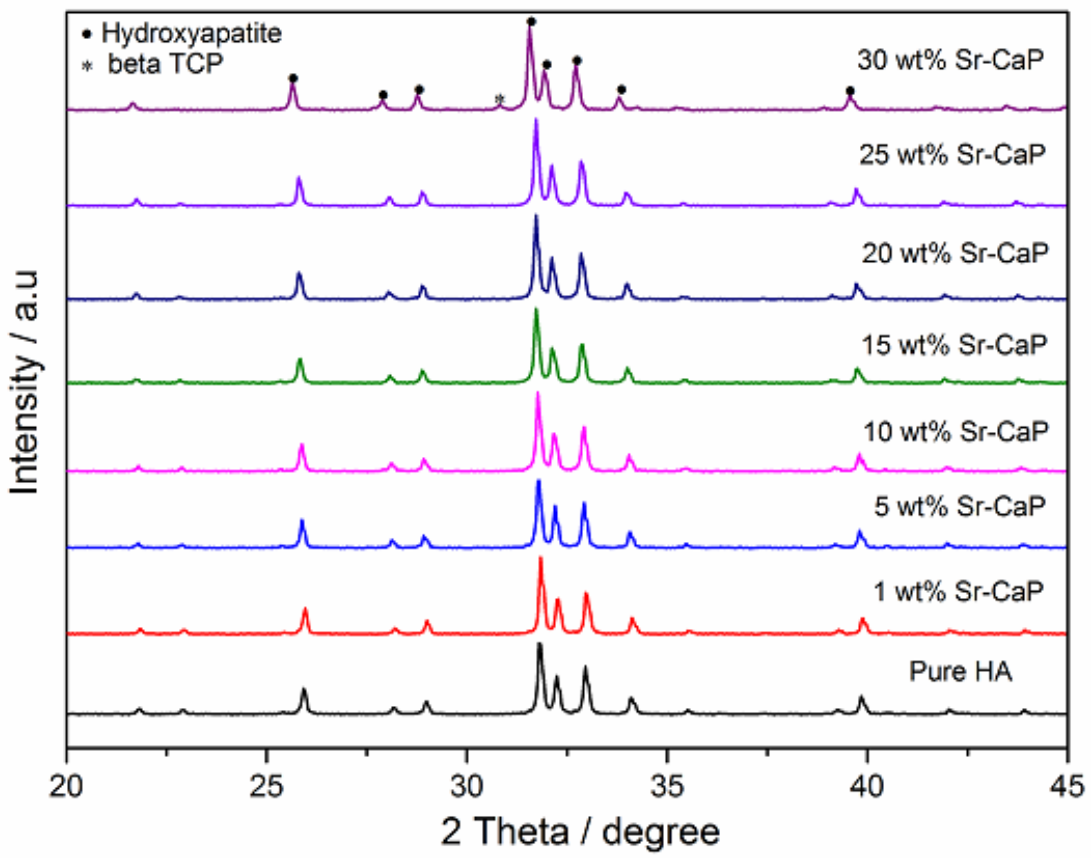

Figure 5-5 Powder X-ray diffraction patterns of heat-treated (1000 °C, 1hr in air) Sr-substituted calcium phosphates. The nominal wt% values quoted are named according to the amount of strontium ions in the precursor feed.

5.3.3 BET Surface Area Analysis

Figure 5-6 shows the trends in BET surface areas for the magnesium substituted calcium phosphate samples. For phase pure HA and 1Mg-CaP, the BET surface area were recorded as 195 m^2g^{-1} and 160 m^2g^{-1}, respectively. Samples from 4Mg-CaP and 7Mg-CaP (biphasic mixture) had lower surface areas of 91 and 75 m^2g^{-1}. whilst phase pure 10Mg-whitlockite had a surface area of 102 m^2g^{-1}. One of the possible reasons for the lower surface area is the increased particle agglomeration observed in TEM images (fig. 2 c-f). On the other hand, samples 8Mg-CaP and 10Mg-CaP (phase pure Mg-whitlockite) revealed a noticeable increase in surface area (102 m^2g^{-1}) compared to biphasic mixture (see table 5.1). The afformentioned results can be supported by XRD and TEM as shown in Figure5-4 and Figure 5-2 (e, f).

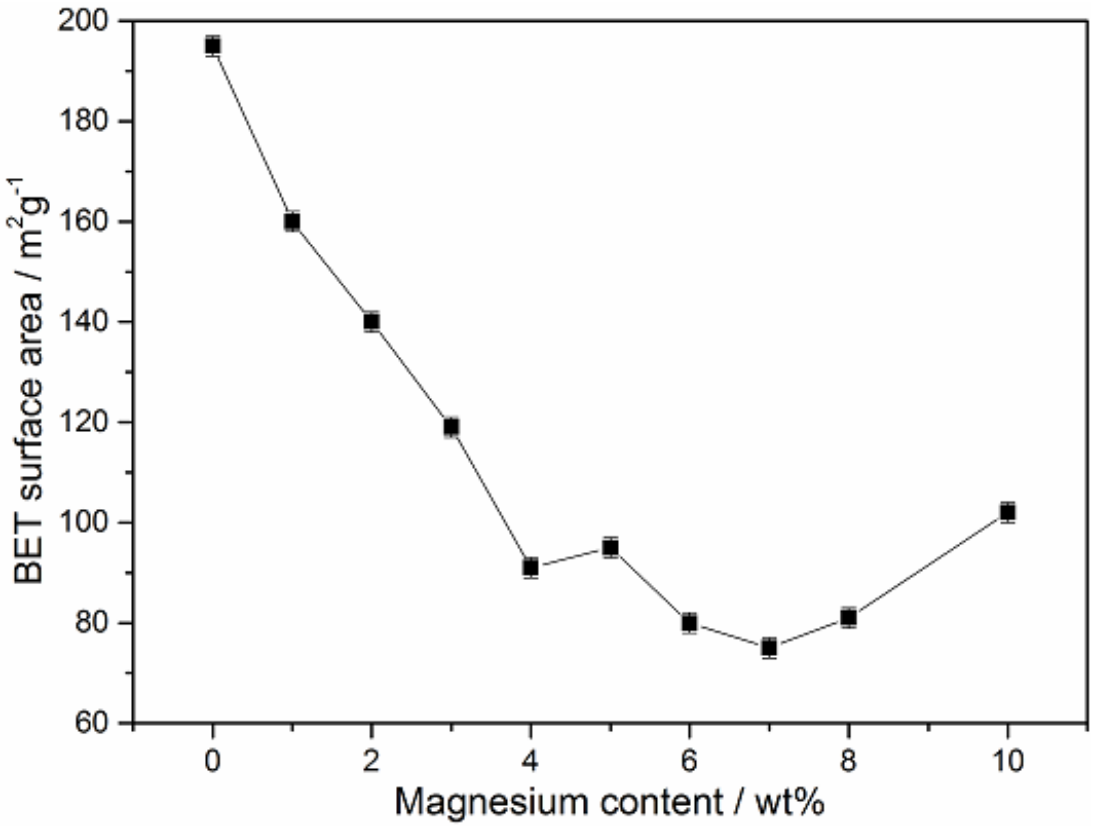

Figure 5-6 BET surface area of as prepared HA, Biphasic Mg-HA and Mg-whitlockite calcium phosphates. The data points from left to right corresponded to samples Pure HA, 1Mg-CaP, 2Mg-CaP, 3Mg-CaP, 4Mg-CaP, 5Mg-CaP, 6Mg-CaP, 8Mg-CaP, 10Mg-CaP.

Table 5-2 shows the measured strontium contents and their effect on BET surface area of strontium substituted calcium phosphates. It was observed that the measured contents of strontium in the final product were lower than the actual contents added as shown in Table 5-2. By increasing strontium concentration, BET surface area decreased whereas particle size increased as shown in Figure 5-3.

Table 5-2 Sample identification corresponding to wt% based on XPS analysis along with BET surface area analysis

Sample ID	**Sr Added (wt%)**	**Sr Measured (wt%)**	**BET Surface Area (m^2g^{-1})**
Pure HA	0	0	195
1Sr-CaP	1	0.4	154
10Sr-CaP	10	7.1	143
15Sr-CaP	15	11.9	138
20Sr-CaP	20	14.2	132
25Sr-CaP	25	18.5	135
30Sr-CaP	30	21.1	121

5.3.4 X-ray Photoelectron Spectroscopy

Chemical analyses of magnesium substituted calcium phosphate sample (8Mg-CaP) were performed using XPS analysis as shown in Figure 5-7. The P 2p, Ca 2p, O 1s, and Mg 2p core level spectra of Mg-HA was taken as shown in Fig. 5. The Ca 2p spectrum could be resolved into two peaks [Figure 5-8 (a)] for Ca $2p_{3/2}$ and $2p_{1/2}$ at 347.4 and 351.3 eV, respectively, which are related to hydroxyapatite. In Figure 5-8 (b), the 2p peak can also be deconvoluted into two peaks for $p_{1/2}$ and $p_{3/2}$ levels with binding energies of 134.2 and 133.4 eV, respectively. Figure 5-8 (c), depicts the core level spectrum of O 1s and the peaks at 530.4 and 531.8 ev are attributed to the phosphate group, and hydroxyl group or adsorbed water in hydroxyapatite crystal (Mahabole et al., 2005, Costescu et al., 2010a, Lu et al., 2000), respectively. The Mg 1s core level spectrum can be deconvoluted into two peaks with the binding energies of 1304 and 1307 eV, respectively as shown in Figure 5-8 (d).

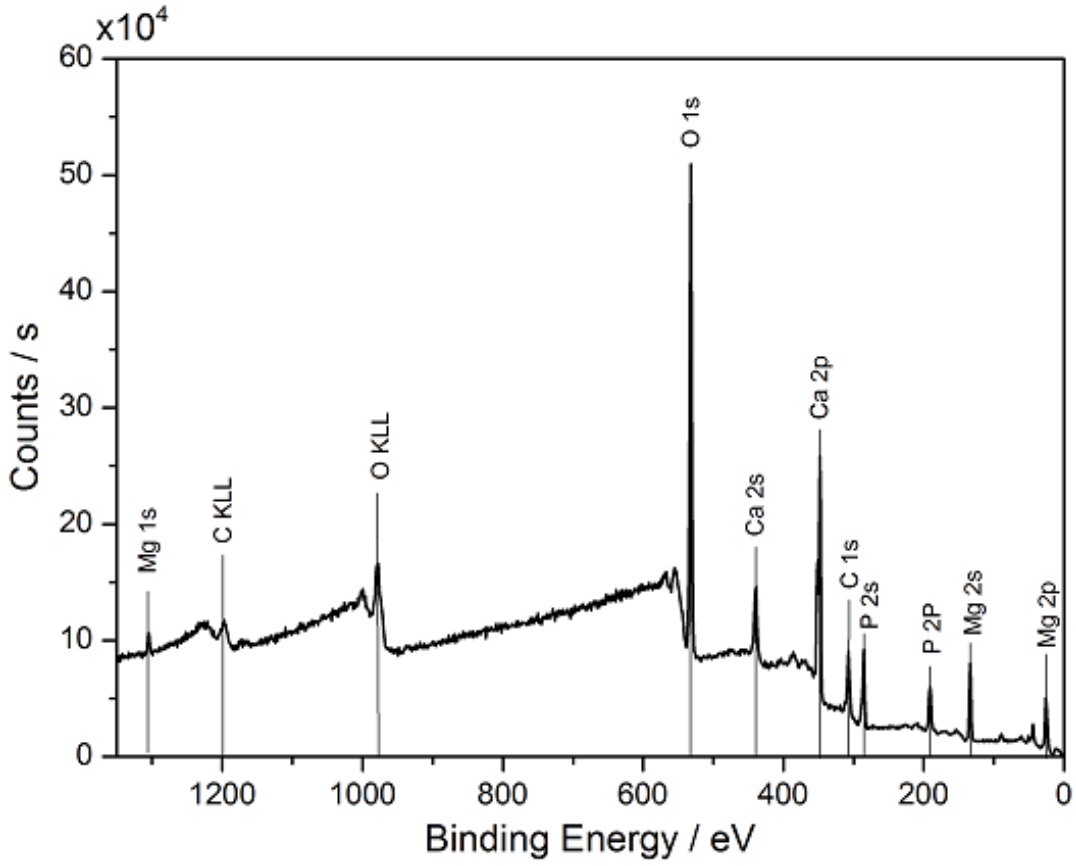

Figure 5-7 XPS survey spectrum of magnesium substituted calcium phosphate (8Mg-CaP) sample made at 70 ˚C in a continuous plastic flow reactor

A representative survey spectrum for strontium substituted hydroxyapatite (10SrHA) made at 70 °C is presented in figure 5-9. The peak at 134 eV was an overlap of Sr 3d and P 2p because Sr $3d_{5/2}$ and Sr $3d_{3/2}$ with binding energies of 133.2 and 134.8 eV were very closed to P $2p_{3/2}$ and P $2p_{1/2}$ peaks with binding energies of 133.4 and 134.2eV, respectively. The deconvoluted spectra for O, Ca, P and Sr are presented in figure 5-10. The peaks at 134 eV corresponded to P 2p of the phosphate groups in hydroxyapatite.

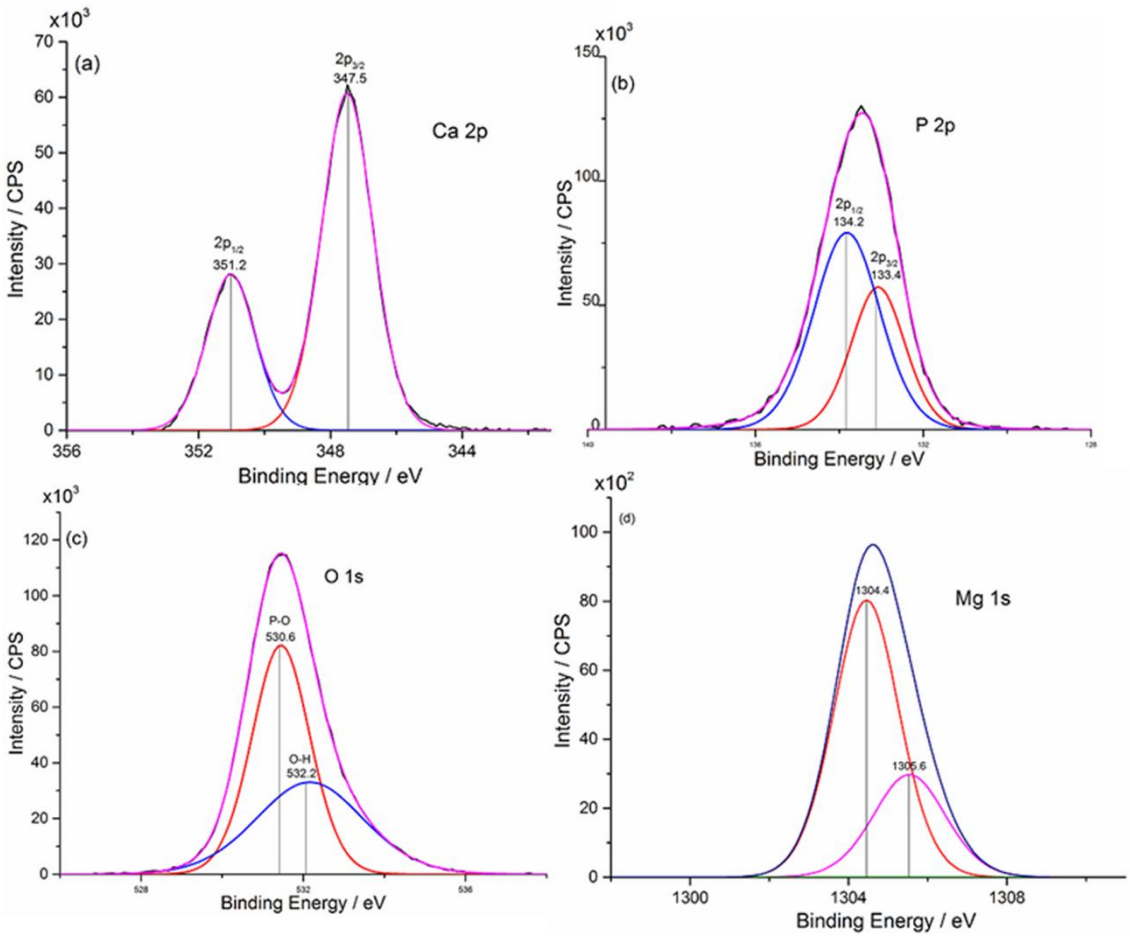

Figure 5-8 [a-d] XPS Spectra of Ca 2p,O 1s and P 2p and Mg 1s recorded from the synthesized CaP sample 8Mg-CaP.

The Ca 2p spectrum could be resolved into two peaks for Ca $2p_{3/2}$ and $2p_{1/2}$ (two spin-orbit pairs) at 347.4 and 351.3 eV, respectively, which are related to hydroxyapatite [36] In Figure 5-10 (b), the 2P peak can also be deconvoluted into two peaks with a spin orbit splitting for $p_{1/2}$ and $p_{3/2}$ levels with binding energies of 134.2 and 133.4 eV, respectively [37]. Figure 5-10 (c), depicts the core level spectrum of O 1s and the peaks at 530.4 and 531.8 eV are attributed to the phosphate group, and adsorbed water in hydroxyapatite crystal, respectively. The binding energy values for the Sr 3d spectrum were measured as 133.2 and 134.8 eV, respectively [38].

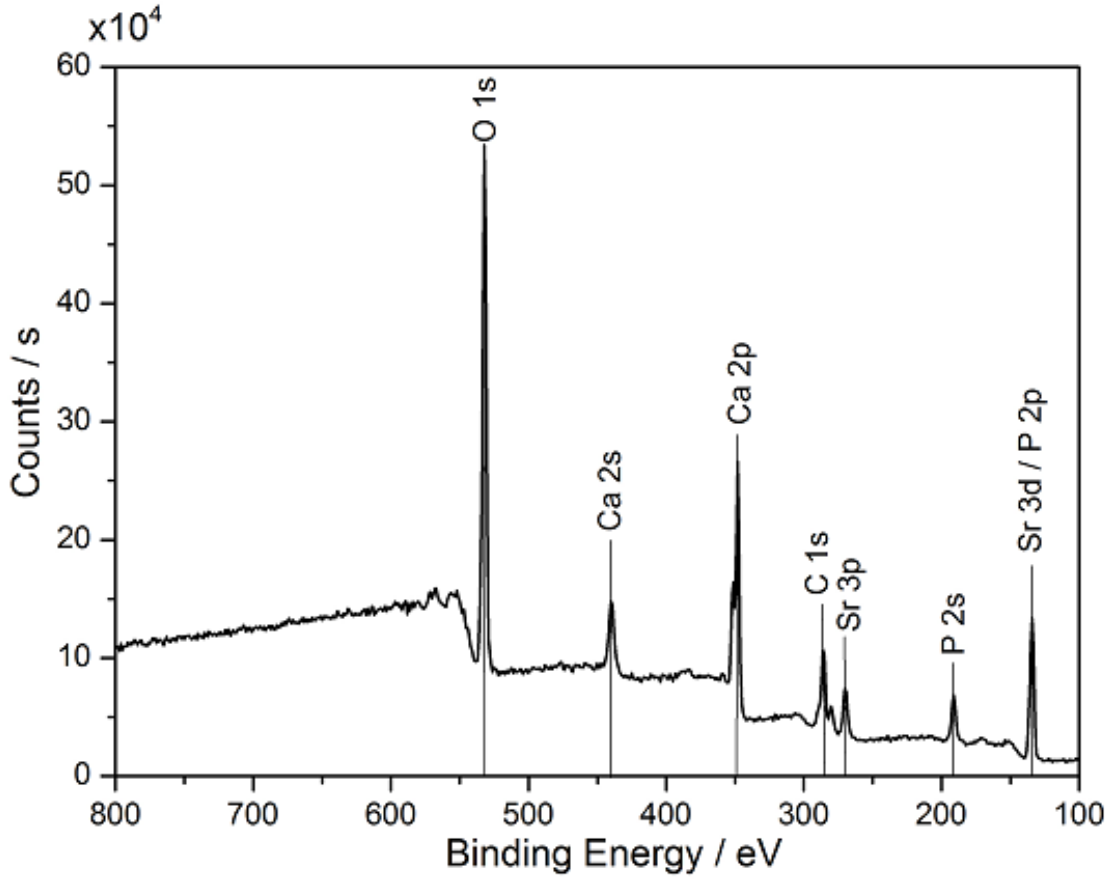

Figure 5-9 XPS survey spectrum of strontium substituted calcium phosphate (10Sr-CaP) made at 70 °C in 5 minutes residence time via CPFS

5.3.5 Fourier Transform Infrared Spectroscopy

The FTIR spectrum for sample 1Mg-CaP as shown in Figure 5-11 showed peaks similar to those normally seen for HA. Peaks at 3570 cm^{-1} and 636 cm^{-1} corresponds to the hydroxyl group, whilst the peaks at 1150-990 cm^{-1} and 964 cm^{-1} correspond to asymmetric and symmetric P-O stretching of the phosphate group, respectively. The peaks at 605 and 567 cm^{-1} correspond to the O-P-O bending mode. The intensity of hydroxyl peaks at 3570 and 633 cm^{-1} generally decreased with increasing content of magnesium in the corrersponding FTIR spectra.

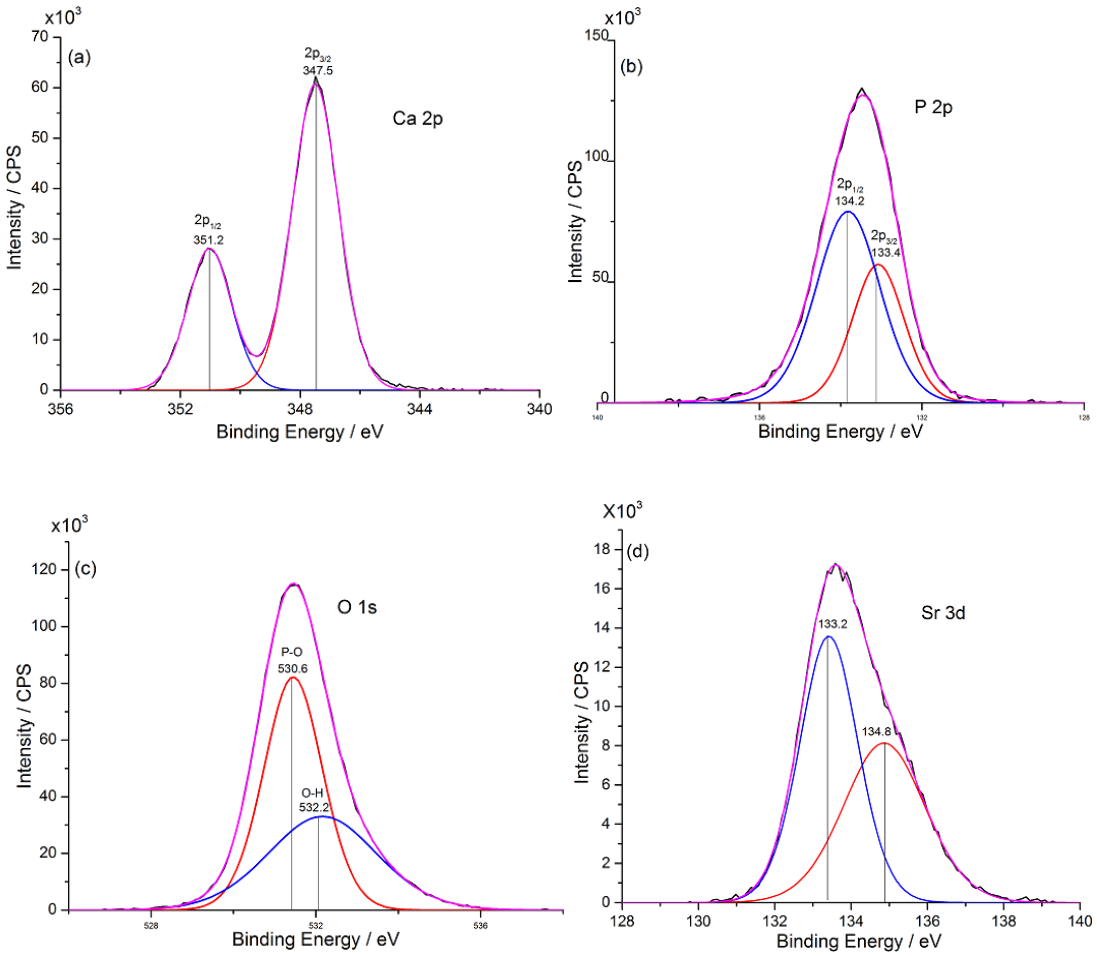

Figure 5-10 [a-d]. XPS Spectra of Ca 2p,O 1s and P 2p recorded from 10Sr-CaP made via CPFS at 70 °C in five minutes residence time

The samples with magnesium substitution of 6 wt% or higher revealed a broader phosphate peak in the range of 1550-1450 cm^{-1} which coincided with a decrease in crystallinity of Mg-whitlockite (as shown in XRD data, Figure 5-4). The band at 871 cm^{-1} corresponding to ν_2 stretching vibrations of the carbonate or hydrogen phosphate groups. Since the intensity of the major carbonate bands between 1420 and 1450 cm^{-1} samples decreases with increasing magnesium as shown in Figure 5-11, this band can be attributed to the carbonate groups.

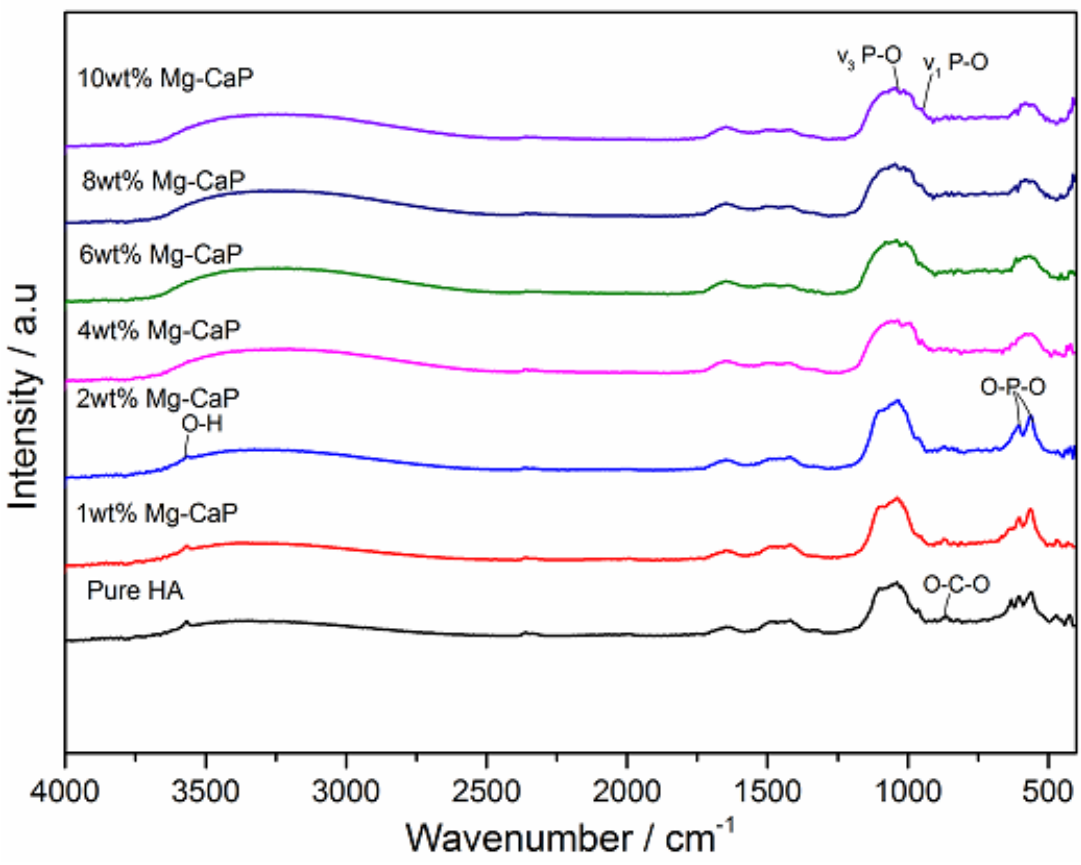

Figure 5-11 FTIR spectra of pure HA and Mg substituted calcium phosphates made at 70 ˚C in a CPFS reactor.

The FT-IR spectra for strontium-substituted calcium phosphate nanoparticles were also measured. It was observed that the solid solutions show a decrease in the relative intensity of the absorption bands due to O-H stretching and libration modes. Furthermore, the OH stretching band, which is at 3572 cm^{-1} in Ca-HA, progressively shifts to higher wave numbers on increasing the strontium content, up to 3590 cm^{-1} for Sr-HA, whereas the OH^- libration band shifts from 630 to 537 cm^{-1}, in agreement with the results previously reported for Ca-HA and Sr-HA [39]. The infrared absorption bands due to phosphate groups shift to lower wave numbers on increasing the relative content of strontium. Figure 5-12 shows how the bands due to the symmetric stretching (ν_1) and bending (ν_4) modes of phosphate groups move, respectively, ν_1 from 962 (Ca-HA) to 947 cm^{-1} (Sr-HA) and ν_4 from 603 (Ca-HA) to 592 cm^{-1} (Sr-HA).

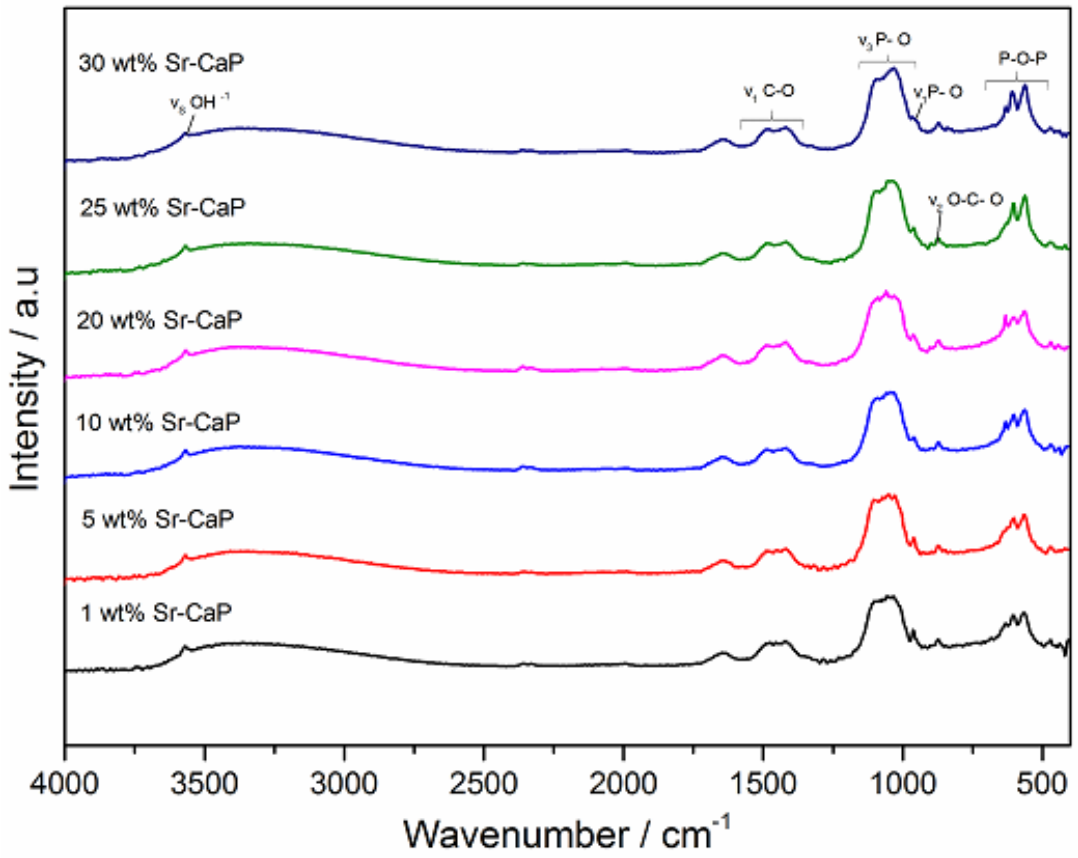

Figure 5-12 FTIR spectra of strontium-substituted hydroxyapatite made at 70 ˚C in a CPFS reactor.

5.3.6 Raman Spectroscopy

Raman spectroscopy was conducted in order to supplement crystallographic data and detect substitutions in the apatite lattice. Figure 5-13 shows Raman spectra for magnesium substituted calcium phosphates. Peaks from 1 to 3 wt% Mg-CaP are very similar to those observed for phase pure HA. Peaks at *ca.* 1080 and 1054 cm^{-1} in the Raman spectra, for these samples were attributed to asymmetric stretching of the P–O bond in phosphate. The peak around 970 cm^{-1} corresponds to the symmetric stretching mode of the P–O bond of the phosphate group. In pure HA, this peak normally appeared at 963 cm^{-1}. This peak shifting could be because of the increased incorporation of magnesium in the HA lattice.

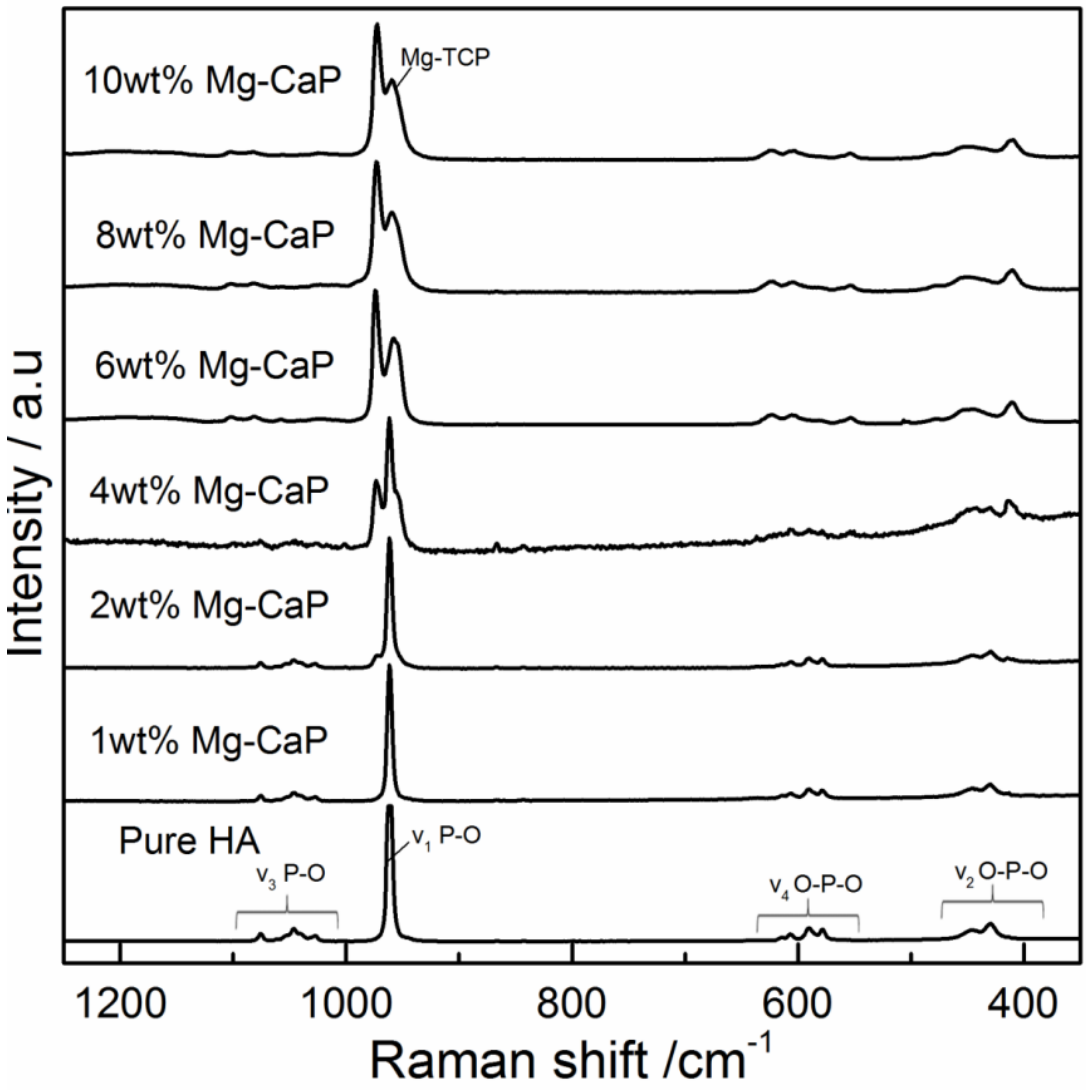

Figure 5-13 Raman spectra of pure HA and Mg- substituted CaPs made at 70 ˚C in a CPFS reactor.

Figure 5-14 shows the Raman spectra of strontium substituted calcium phosphates. The peak at 965cm^{-1} corresponds to a symmetric stretching mode of the P-O bond in phosphate. Peaks at 610 and 483 cm^{-1} are likely corresponded to the bending mode of the O-P-O linkage in phosphate. Peaks at ca. 1080 and 1054 cm^{-1} in the Raman spectra correspond to asymmetric stretching of the P–O bond in phosphate.

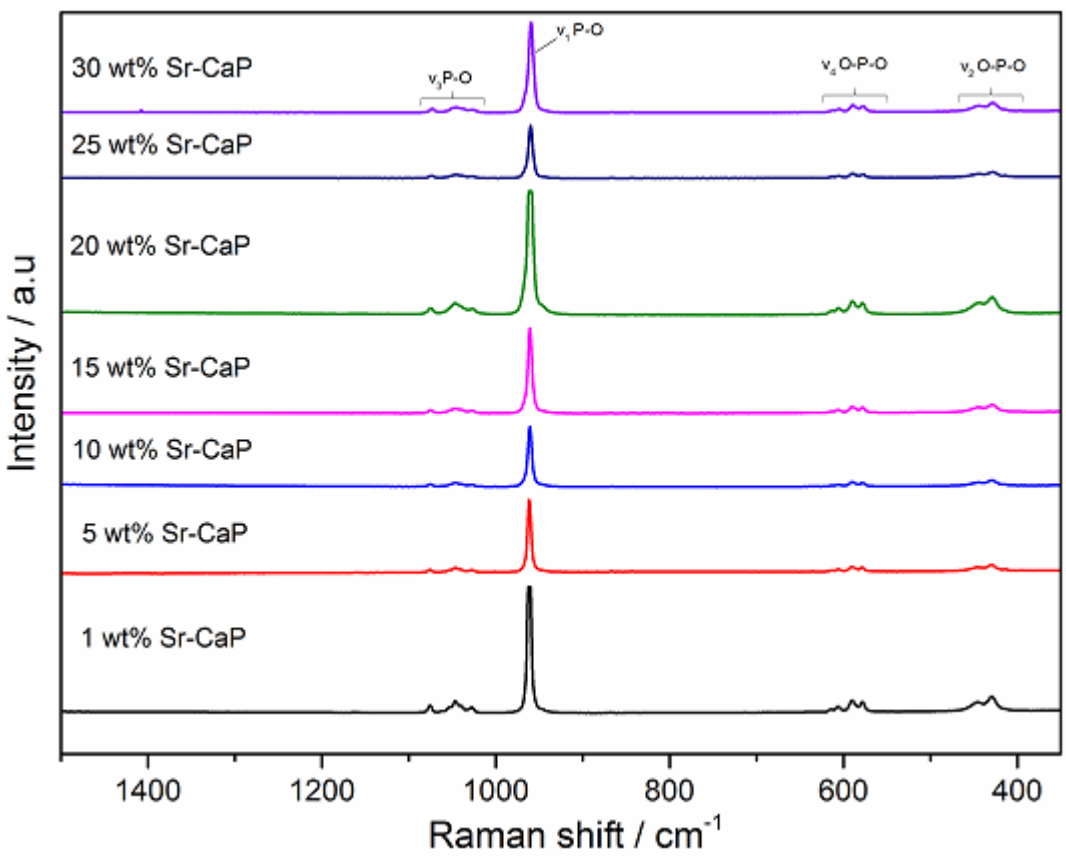

Figure 5-14 Raman spectra of strontium-substituted calcium phosphates made at 70 ˚C in a CPFS reactor.

5.3.7 Zeta Potential Measurements

Zeta potential measurements were performed in order to investigate the colloidal stability related to surface charge of the pure HA and strontium substituted HA. Zeta potential therefore can be considered as a measure of colloidal stability as it give the electrostatic potential of particles which is directly related to their dispersion stability by the electrostatic repulsion.

The greater the electrostatic repulsion, the higher the zeta potential values and therefore higher will be the colloidal stability of the suspension. A zeta potential of 28 mV was obtained for pure HA and 33 and 35 mV for 10 and 20 mol % strontium substituted HA, respectively which indicates the high positive surface charge. The higher surface charge shows the high zeta potential value, which protects the particle agglomeration resulting in a more stable dispersion.

5.3.8 Cell Viability Study

Cell viability studies were investigated for 13mm diameter disks of pure HA, 4% biphasic and 8% pure whitlockite samples. Human MG63 osteoblast cells were cultured on CPFS Mg-CaP discs and analysed for cell viability at days 1, 3 and 7 (Figure 5-15). At day 1, cell viability was lowest for both heat treated (4Mg-CaP HT and 8Mg-CaP HT) discs while both as prepared (4Mg-CaP AP and 8Mg-CaP AP) discs had significantly higher viability but this was only 50 % that of pure HA.

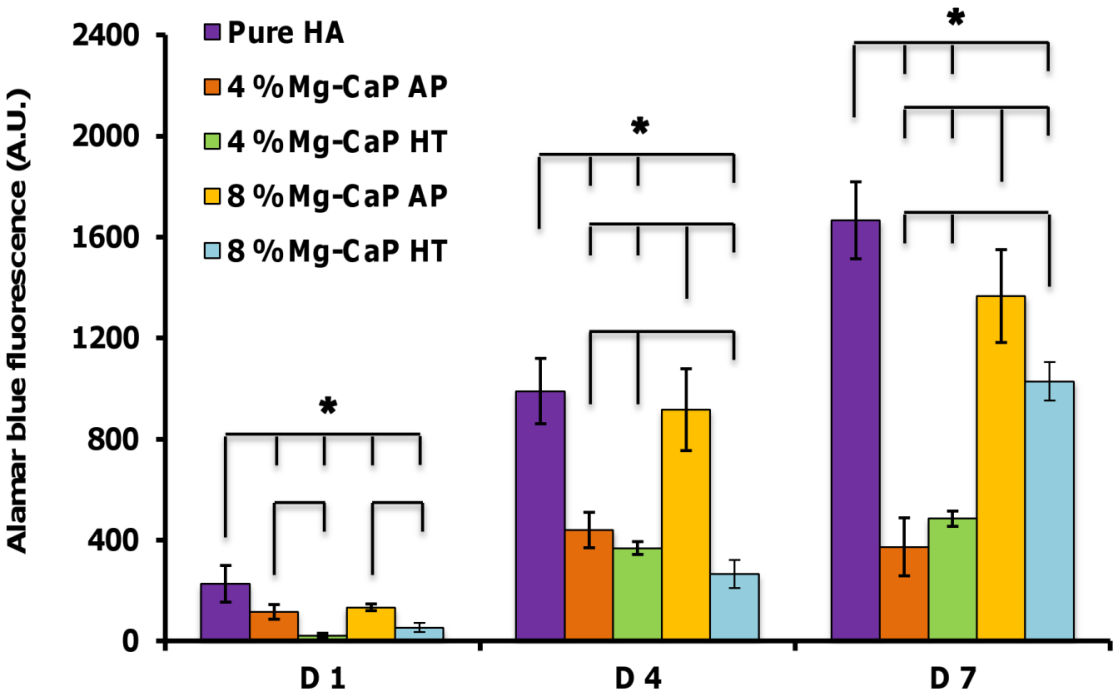

Figure 5-15 MG63 viability on CPFS Mg-CaP discs. Alamar blue viability assay was performed at days 1, 4, and 7 to observe MG63 viability on AP and HT CPFS Mg-CaP discs consisting of 4 % or 8 % Mg, as well as CPFS pure HA. Mean ± SD, * $p < 0.05$.

Cell viability increased on all compositions at day 4 suggesting that all discs supported cell proliferation, however, viability was significantly higher on as prepared 8Mg-CaP discs than all other Mg containing compositions and was similar to pure HA. At day 7, cell viability increased further for 8Mg-CaP discs and pure HA, with as prepared 8Mg-CaP discs having higher viability than heat-treated discs and similar levels to pure HA. However, there was no increase in cell viability on as prepared 4Mg-CaP discs, which

showed similar levels to day 4. These results indicate that as prepared discs encouraged greater cell attachment than heat-treated discs while the presence of 8Mg-CaP sample encouraged greater cell proliferation than 4 Mg-CaP.

Human osteoblast cell viability study was also carried out on selected as prepared samples of 5Sr-CaP, 10Sr-CaP and 20Sr-CaP, respectively. Pure HA sample made on the CPFS system was used as a control. It was observed that by increasing strontium content, cell viability increased. A considerable increase in cell viability was noted on day 7 for all three as prepared samples [5Sr-CaP, 10Sr-CaP and 20Sr-CaP]. It was determined that strontium substitution in calcium phosphate enhanced the cell viability as compare to pure HA as shown in Figure 5-16.

5.3.9 Cell Morphology

On pure HA, cells covered most of the surface and showed a typical osteoblastic morphology, with many cells overlapping in dense areas and some cells stretching out to other cells in less dense areas. There was a marked contrast in MG63 morphology and size between as prepared and heat-treated discs for both 4 % and 8 % Mg-CaP. Cells on as prepared discs had larger nuclei and expressed more actin than cells on heat-treated discs as well as showing a more osteoblast-like morphology. Many of the cells on heat-treated discs were rounded up and showed little spreading. Figure 5-17 also shows that cells on all 4Mg-CaP discs were sparser than cells on comparable 8Mg-CaP discs, which is in good agreement with cell viability results.

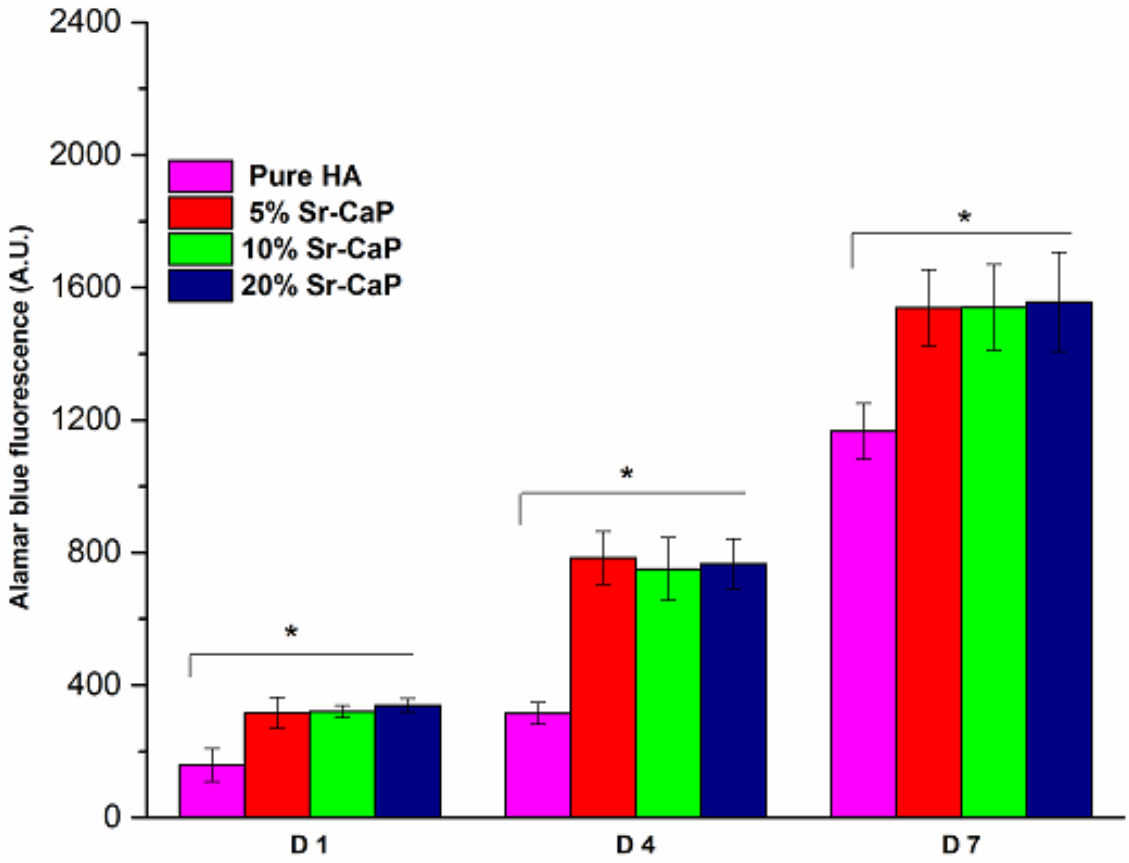

Figure 5-16 MG63 viability on CPFS Sr-CaP discs. Alamar blue viability assay was performed at days 1, 4, and 7 to observe MG63 viability on AP CPFS Sr-CaP discs consisting of 5 % or 10 % and 15 % Sr, as well as CPFS pure HA. Mean ± SD, * $p < 0.05$.

These results indicate that as prepared discs favour an osteoblastic morphology compared with heat-treated discs. The combined cell observations indicate that CPFS Mg-CaP are biocompatible, support cell attacment and proliferation and may serve as a potential biomaterial for bone regeneration/replacement therapies.

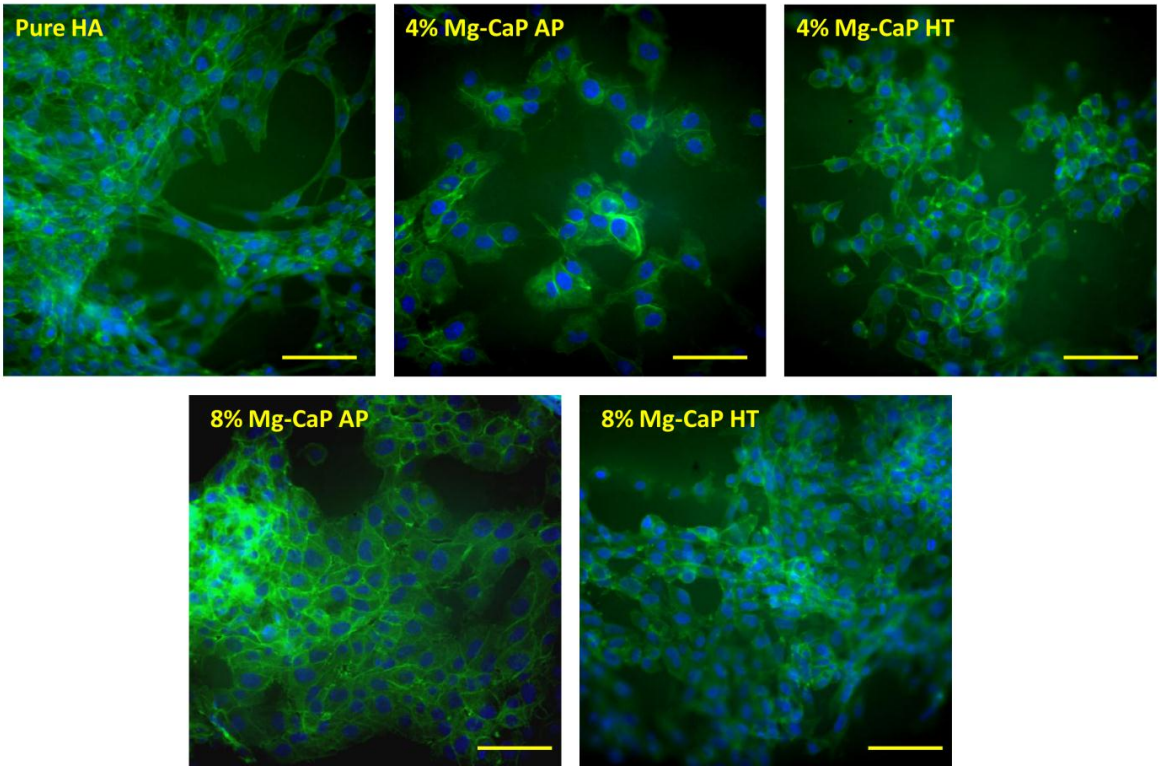

Figure 5-17 MG63 morphology of Mg-CaP discs made at 70 ˚C in a CPFS reactor. Cells were visualised at day 7 for cell nucleus (DAPI in blue) and cytoskeleton (phalloidin-FITC in green) for MG63s cultured on AP or HT Mg-CaP discs containing 4 % or 8 % Mg as well as pure HA. Scale bar is 100 µm.

Osteoblastic cell morphologys on some selected Sr-CaP samples (5Sr-CaP, 10Sr-CaP and 20Sr-CaP) were carried out on day 7. It was observed that cells formed bridges across the undulations and spread over them, which indicated that material was non-toxic for cells. Morphological images were taken of these cells on day 7 as shown in Figure 5-18. There were no substantial differences in the cell morphology of all three samples. The cells were round and almost flattened against the surface that showed the colony formation and attributed to continuous proliferation.

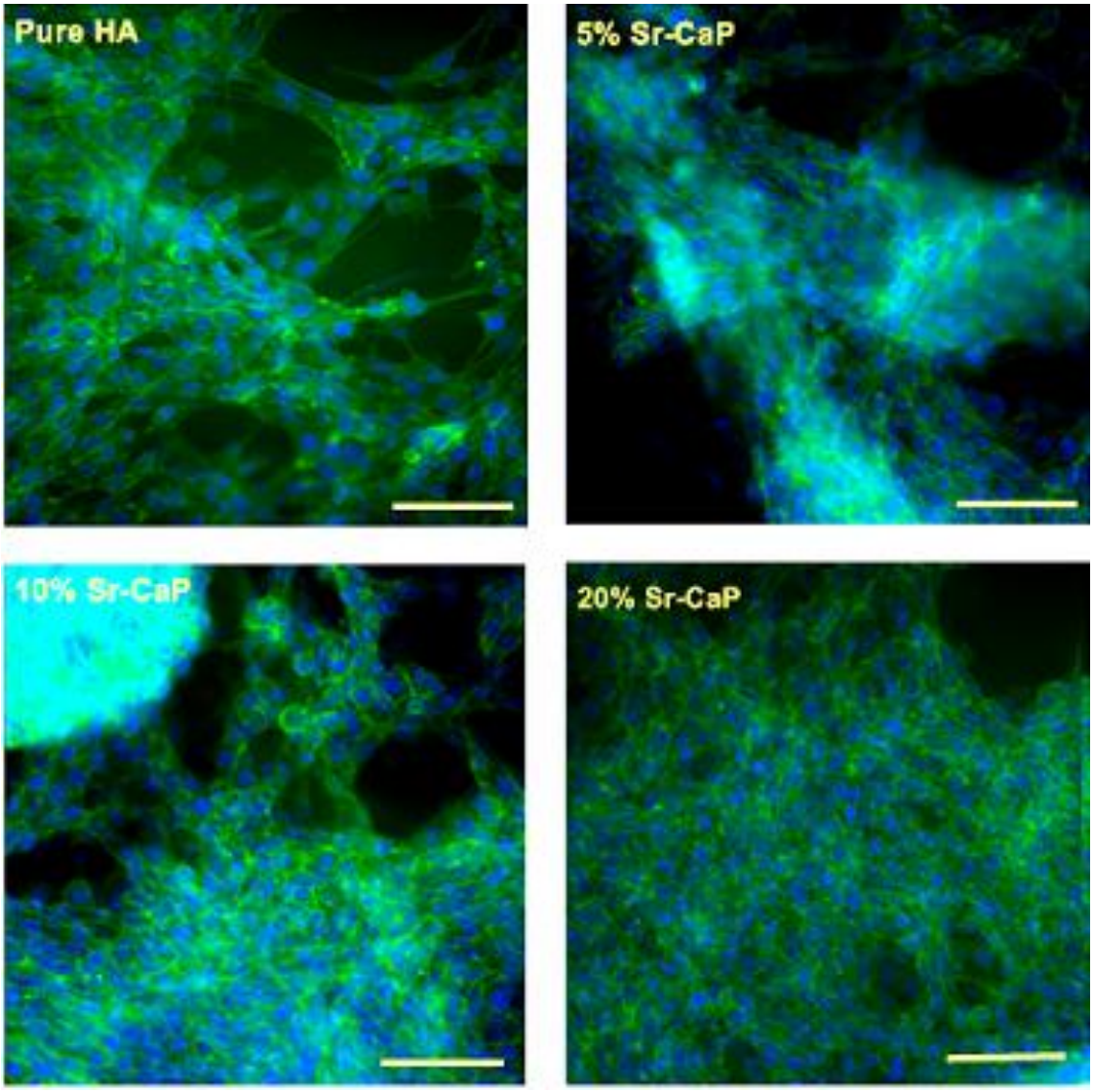

Figure 5-18 MG63 morphology of Mg-CaP discs made at 70 ˚C in a CPFS reactor. Cells were visualised at day 7 for cell nucleus (DAPI in blue) and cytoskeleton (phalloidin-FITC in green) for MG63s cultured on AP Sr-CaP discs containing 5 %, 10 % and 15 % Sr as well as pure HA. Scale bar is 100 μm.

5.4 Conclusions

Phase pure HA and a series of magnesium and strontium-substituted calcium phosphates were successfully synthesized using a CPFS system from calcium nitrate tetrahydrate [$Ca(NO_3)_2.4H_2O$], and diammonium hydrogen phosphate [$(NH_4)_2HPO_4$)] precursor solutions at (near) ambient conditions (70 °C, atmospheric pressure) in a rapid single step.

Careful control of the quantities of reactants used, resulted in phase pure nano-sized HA rods, biphasic mixture of HA and pure Mg-whitlockite. Cell toxicity analysis showed excellent biocompatiblity of these materials. Increase in magnesium content above 3% led to precipitation of biphasic mixture of magnesium substituted hydroxyapatite starting from sample (1MgCa-P) and Mg-whitlockite. Magnesium content above 7% (shown by XPS) led to the formation of pure Mg-whitlockite. Increasing magnesium content affected the morphology of obtained particles, beginning from roundening of HA-rods till the formation of small nano-sized hollow spherical particles of Mg-whitlockite.

The combined cell observations indicate that high surface area nanosized magnesium and strontium calcium phosphates made via CPFS were biocompatible and have the potential to be used for biomedical applications where bone regeneration /replacement is required.

It is concluded that the CPFS system is a versatile and useful tool for the synthesis of pure and ion substituted calcium phosphates with tailorable properties such as composition, particle size, and surface area. With its unique features, the obtained product is a promising material with biological properties and has potential to be used in biomedical applications where small size, fine particle size distribution control and bone regeneration /replacement or controlled resorbibility of bone grafts is a vital requirment.

5.5 Future Work

By using CPFS system parameters (temperature, flow rate / residence time, pH etc.) it would be interesting to improve cationic and anionic substitution levels in different calcium phosphates. Coupled ionic substitutions in calcium hydroxyapatite in the CPFS system would also be interesting.

The results of the present study have shown that the addition of strontium to calcium phosphate greatly enhanced the cell viability. In addition, because of its antibacterial nature and radiopacity properties, It could be a better tool for dental restorative materials. The findings reported here should be helpful in future clinical investigations.

Osteoblastic cell attachment and viability analysis confirmed the high biocompatiblity of magnesium and strontium-substituted materials. Future work should address the ability of CPFS to support osteogenic differentiation and what affect cationic [Mg^{2+}, Sr^{2+}] concentration and heat-treatment has on this.

Chapter 6
Synthesis and Characterization of Carbonate and Silicate-Substituted Calcium Phosphates Made via Continuous Plastic Flow Synthesis

6.1 Introduction

Synthetic hydroxyapatite, HA, [$Ca_{10}(PO_4)_6(OH)_2$], is a bioactive bioceramic that is chemically similar to the mineral component of hard tissues (biological apatite). HA is widely used in hard tissue replacement (Hench, 1991) because of its ability to stimulates bone formation, necessary for implant osseointegration. Rapid osseointegration is required to improve the implant efficiency and to decrease damage to adjacent tissues after implantation (Zdrenþu et al., 2004). HA properties can be enhanced by both cationic and anionic substitutions. Biological apatite is non-stoichiometric because of the presence of metal ions (Mg^{2+}, Mn^{2+}, Zn^{2+}, Na^{+}, Sr^{2+}, HPO_4^{2-} or CO_3^{2-}). HA is capable of accommodating substitute ions within its lattice. Trace ions substituted in apatites can have a dramatic effect on crystallinity, dissolution kinetics and other apatite properties like surface charge, lattice parameters etc. (Miao et al., 2005).

Human bone contains about 8 wt% (de Groot, 1983) of carbonate content, depending on the age of the individual (Rey et al., 1991, Burnell et al., 1980). Keeping in view the hydroxyapatite structure, carbonate groups can occupy both the hydroxyl and the phosphate site, offering both A-type and B-type carbonate substitution, respectively. In 1963, Kuhl and coworkers (Kühl and Nebergall, 1963) suggested the following formula for B-type substitution in HA.

$$Ca_{10-x+y}(CO_3)_x(PO_4)_{6-x}(OH)_{2-x+2y}$$

The B-type carbonate substitution is more favorable and found in the bone of a variety of species, with the A/B type ratio in the range of 0.7–0.9 (Rey et al., 1989). The presence of B-type carbonate in the apatite lattice was shown to cause a higher solubility but decrease in crystallinity for both *in vitro* and *in vivo* tests (LeGeros, 1990). Moreover the A-type carbonate surface shown less affinity (as compared to un-substituted HA)

towards human trabecular osteoblastic which was attributed by lower cell attachment as well as reduction in polar component of the surface of the A-type carbonate-substituted biomaterial (Redey et al., 1999, Redey et al., 2000). HA bonding to adjacent tissue is a slow process, therefore, carbonate-substituted HA is considered as an optimised biomaterial because of faster bonding ability between an implanted surface and human bone. Carbonate ion substitution for phosphate ions involves a reduction in the number of calcium ions to maintain charge balance (Ito et al., 1997, Tang et al., 2003).

Although HA is known to be bioactive and osteoconductive it has a slow dissolution rate and reduced ability to form a stable interface with its surrounding tissue, and to encourage the new bone formation (Hench, 1993). Also, undoped HA does not degrade substantially but rather remains as a permanent fixture susceptible to long term failure (Mastrogiacomo et al., 2005). The substitution of silicon in the HA lattice is one of the possible method to improve the osseointegration (Porter, 2006). In 1970, Carlisle and coworkers described the function of silicon in bone, wherein the presence of 0.5 wt% silicon was stated in mineralised osteoid regions in mice and rats (Carlisle, 1970).

According to Hench, the deterioration in the proliferation and function of osteoblasts due to osteoporosis are correlated with the loss of naturally existing silicon (Bianco et al., 2009, Hench, 1998b). Silicon has been reported to play a significant role in collagen formation (Carlisle, 1982)]. It has also been observed that silicon-substitution in HA leads to a smaller crystallite size and faster dissolution rate (Thian et al., 2006b, Porter et al., 2003, Botelho et al., 2006, Patel et al., 2002). Due to the significant role of silicon in calcified bone, attempts have been made to incorporate silicon in the HA lattice. Silicon-substituted HA has been synthesised using wet-precipitation and batch hydrothermal techniques (Kim et al., 2003, Gibson et al., 1999, Hing et al., 2006, Tang et al., 2005, Leventouri et al., 2003).

Gibson et al. produced phase pure Si-HA by wet precipitation method using calcium containing source and a phosphate source under basic pH by using silicon acetate as the

source of silicate ions (Gibson et al., 1999).

The efforts have also been made on the development of silicon-substituted HA coatings on metal implants for improved osseointegration (Thian et al., 2006a, Thian et al., 2007). Silicon enters the HA lattice in the form of silicate ions which substitute phosphate ions. Silicon content up to 4 wt% in HA has been reported in literature using a batch hydrothermal synthesis (Tang et al., 2005, Gibson et al., 2002).

6.2 Experimental

6.2.1 Synthesis of Carbonate (CO_3^{2-})-Substituted Calcium Phosphate

A series of Carbonate substitution reactions were carried out for this study. Urea (carbonate ion source) was added to diammonium hydrogen phosphate (adjusted pH 10). This solution was reacted with calcium nitrate solution (adjusted pH 11). A Ca:[PO_4^{3}+CO_3^{2-}] molar ratio of 1.67 was maintained in all precursor solutions. The pH of both the solutions was adjusted using neat ammonium hydroxide solution.

A continuous plastic flow synthesis system, which consists of two HPLC Gilson pumps fitted with 25 mL pump heads, was used for all synthesis. The details are described in section 2.2.1. The pH of both the solutions prior to the reaction was kept above pH 10. The initial mixture was pumped at 20 mL min^{-1} and connected to 8 m long tubing surrounded by a heating jacket whereupon reaction completed in 5 minutes which was the residence time for the reaction. All reactions were carried out at 70 °C and atmospheric pressure. The suspension was collected in a beaker at the exit point. The aqueous suspension obtained was centrifuged, washed and freeze dried as described in section 2.3.1.1. Samples are labelled as 2CHA, 4CHA, 6CHA and 8CHA. The initial numbers in the sample IDs show the nominal carbonate content (wt%).

6.2.2 Synthesis of Silicate (SiO_4^{2-})- Substituted Calcium Phosphate

A similar procedure was repeated for the synthesis of silicon substituted calcium phosphates using the CPFS system. In the process, 0.3 M diammonium hydrogen phosphate solution containing silicate ions and 0.5 M calcium nitrate solutions were pumped at 20 mL min^{-1} in the CPFS reactor (Ca:P molar ratio: 1.67). The pH of

diammonium hydrogen phosphate solution was adjusted to pH 10 using neat ammonium hydroxide solution. This initial mixture were connected to 8 m long PTFE tubing surrounded by a heating jacket whereupon the reaction has completed in 5 minutes. The suspension was collected in a beaker at the exit point. The aqueous suspension obtained was centrifuged, washed and freeze dried as described in section 2.3.1.1. All reactions were carried out at 70 °C and atmospheric pressure. The samples are labeled as 1Si-HA, 2Si-HA, 3Si-HA, 4Si-HA, 5Si-HA, 6Si-HA, 7Si-HA, and 8Si-HA. The numbers in the sample IDs represent the nominal silicon content (wt%) according to how much silicate precursor was used in the precursors.

The obtained powders were compacted into cylindrical discs of 13 mm diameter and 2 mm thickness by using a laboratory hydraulic press at 5 MPa. These samples were used for cell viability studies after sterilization in 70 % ethanol for 1 hour.

6.3 Results and discussion

6.3.1 Transmission Electron Microscopy

Transmission electron microscopy was used to analyse the particle size and morphology. Pure as prepared HA synthesized in the CPFS system had a rod like morphology as shown by TEM in Figure 6-1 (a) and 1(b) and average length along the longest axis of each particle was ~ 85 ±15 nm (200 particles sampled). TEM images of 4CHA sample as shown in Figure 6-2 (a) and (c) confirmed the synthesis of small crystallites. The average length along the longest axis of each particle was ~ 80 ± 15 nm (200 particles sampled), with the particles having rod-like morphology. Sample 8CHA revealed semi-rod shaped morphology, suggesting a slight deviation from the rod like morphology. The average length along the longest axis of each particle was ~ 70 ± 10 nm (200 particles sampled) as shown in Figure 6-2 (b) and (d).

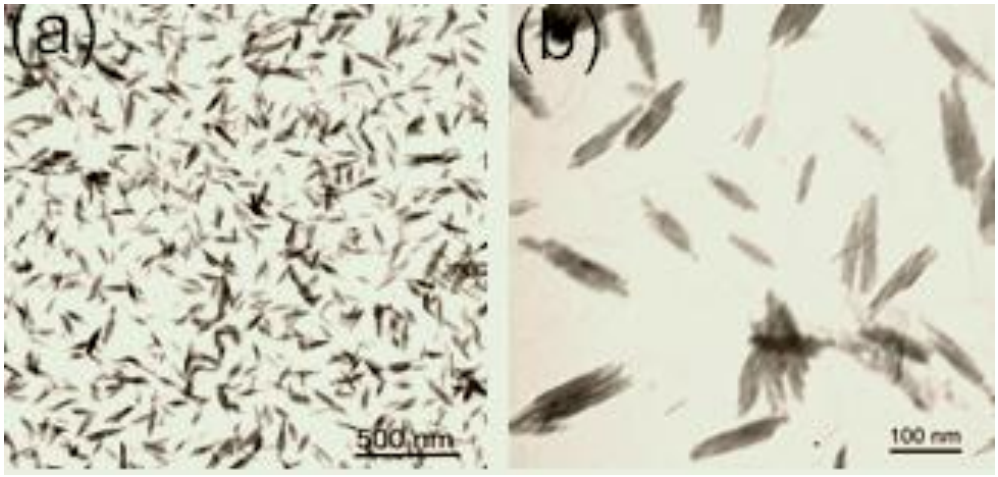

Figure 6-1 Transmission electron microscope images of hydroxyapatite nano-rods of (a), (bar = 500 nm), and for (b), (bar = 100 nm).

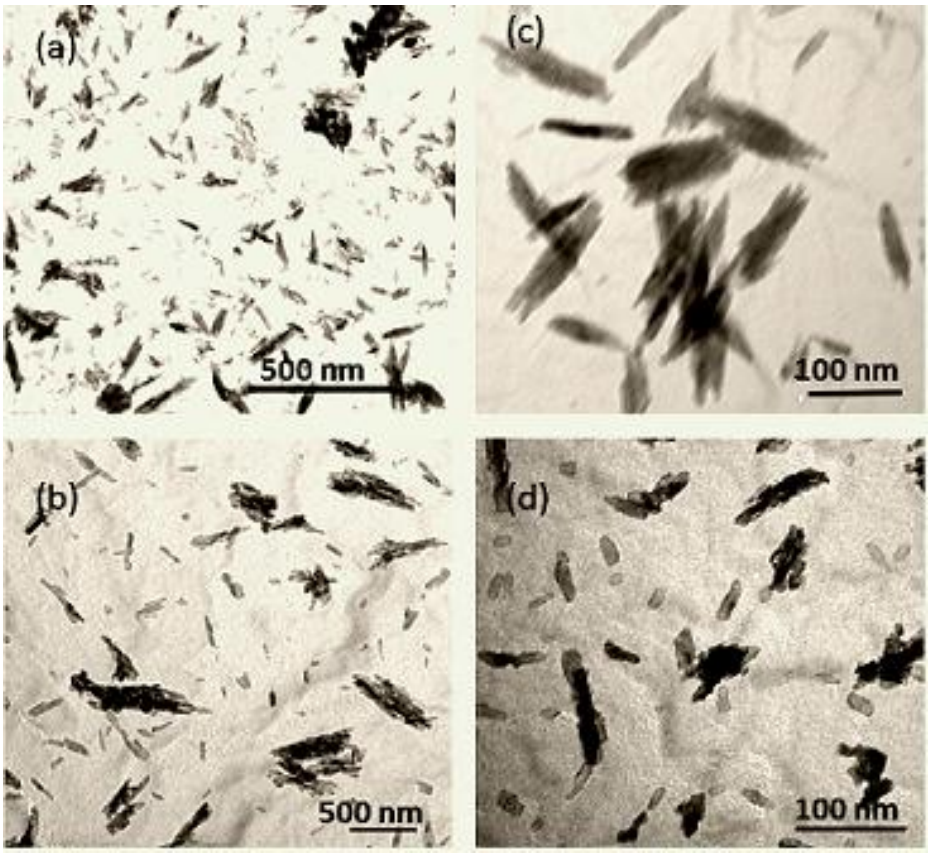

Figure 6-2 Transmission electron microscope images of 4CHA (a,c) and 8CHA(b,d) nano-rods made at 70 °C in five minutes residence time via CPFS, (a,b) (bar = 500 nm), and for (c,d) (bar = 100 nm).

TEM images were also collected for Si substituted HA to investigate the particle morphology and size with increasing silicon content. Figure 6-3 (a) and (c) for sample 4SiHA reveal distinct nanorods of size ~ 100 ± 15 nm (200 particles sampled), along the longest axis. Whilst the average length for 8SiHA particles along the longest axis was ~ 120 ± 15 nm (200 particles sampled) as shown in Figure 6-3 (b) and (d). It was observed that the presence of silicon in HA lattice slightly increased the particle size as compared to pure HA as shown in Figure 6-3.

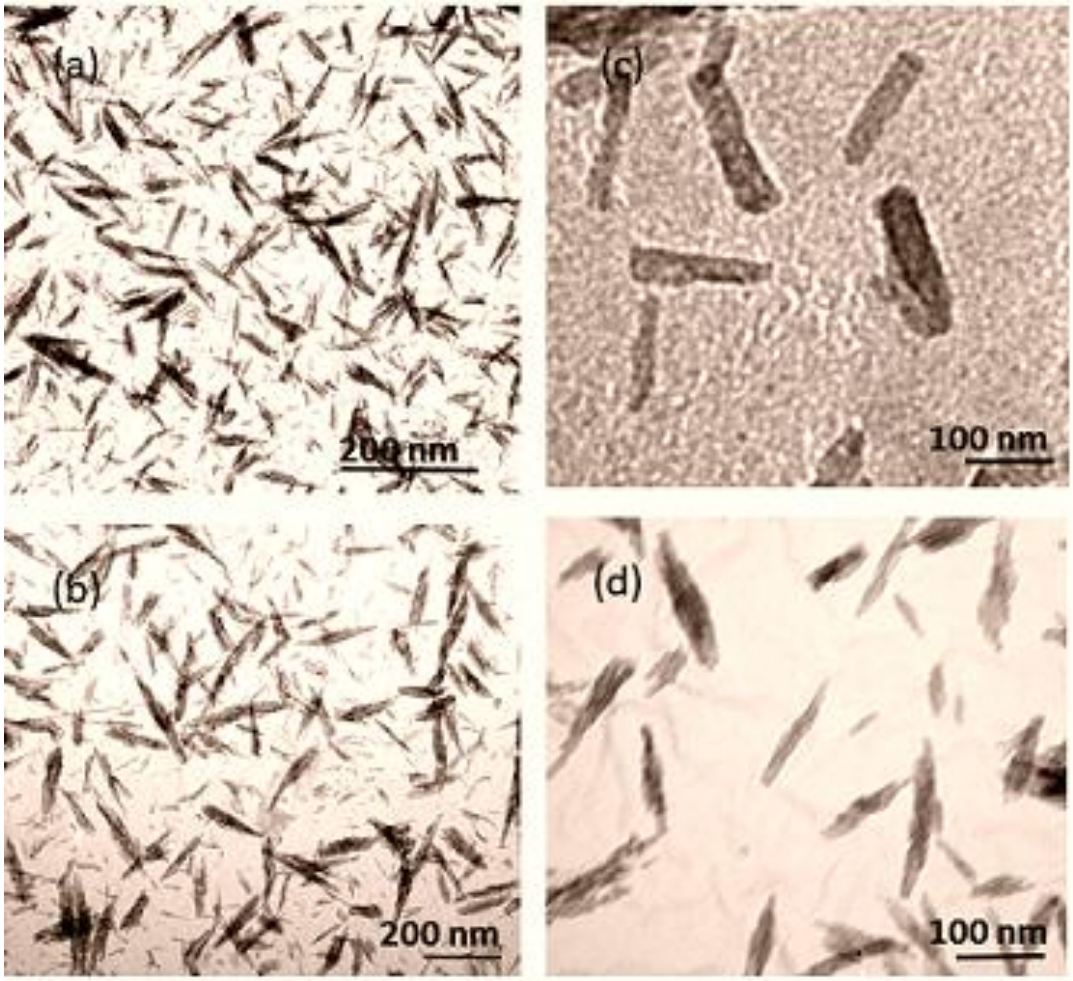

Figure 6-3 Transmission electron microscope images of 4SiHA (a,c) and 8SiHA (b,d) nano-rods made at 70 °C in five minutes residence time via CPFS, (a,b) (bar = 500 nm), and for (c,d) (bar = 100 nm).

6.3.2 BET Surface Area Analysis

Figure 6-4 shows the trends in BET surface areas for the carbonate substituted calcium phosphate samples (determined using XPS). There was a little change in the BET surface area by increasing urea content. All carbonate substituted samples had the surface areas in the range 111 - 136 m^2g^{-1}.

One of the possible reasons for lower surface area with small particle size was the increase in particle agglomeration with small size as observed in Figure 6-2. In contrast, silicon substituted HA samples showed a noticeable increase in surface area in the range 113 - 163 m^2g^{-1} which might be due to a slight difference in size or agglomeration as compared to the carbonate.

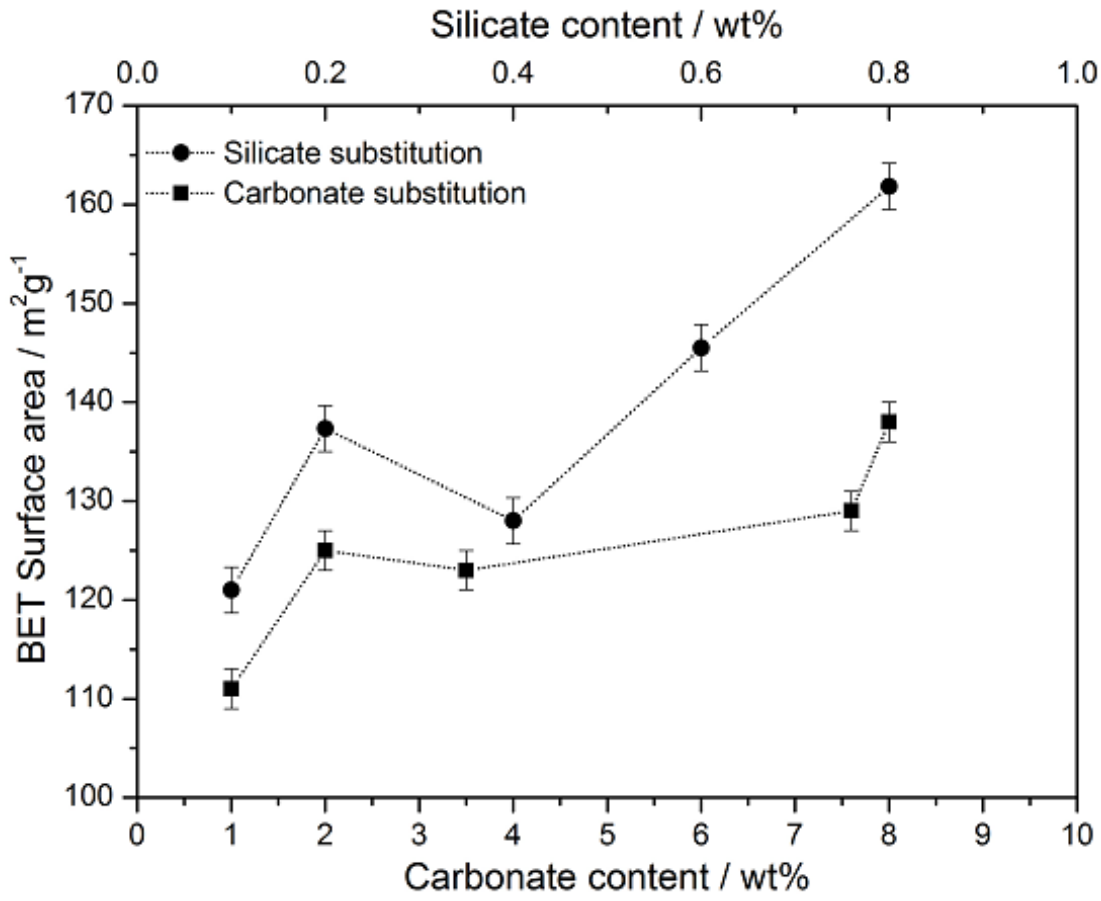

Figure 6-4 BET surface area of carbonate and silicate substituted samples (made at 70 °C in five minutes residence time via CPFS) as a function of substitution level.

6.3.3 Powder X-ray Diffraction

Powder X-ray diffraction data were obtained for all samples to investigate how carbonate and silicate substitution influenced phase composition and phase purity. The XRD pattern suggests an apatite-like structure (sample 2wt% CO_3-HA in Figure 6-5) and showed a good match to phase pure HA [compared to JCPDS pattern 09- 0432].

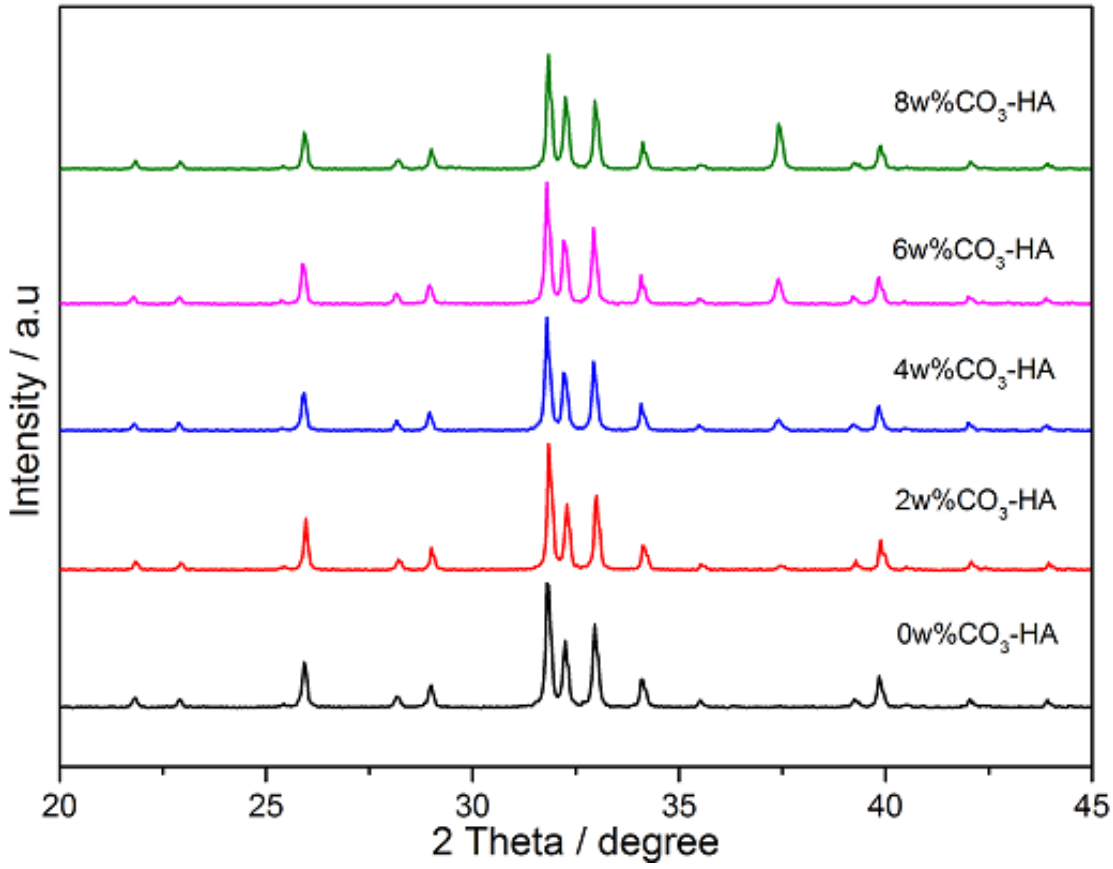

Figure 6-5 Powder X-ray diffraction patterns of heat treated (1000 °C, 2hr) CO_3^{2-}-substituted hydroxyapatite powders made using CPFS at 70°C in five minutes residence time.

All XRD patterns for silicate-substituted samples in Figure 6-6 have a good match to JCPDS pattern 09-432, and suggested no substantial effect of increasing silicon content on phase-purity, crystallinity or PXRD size of the HA phase.

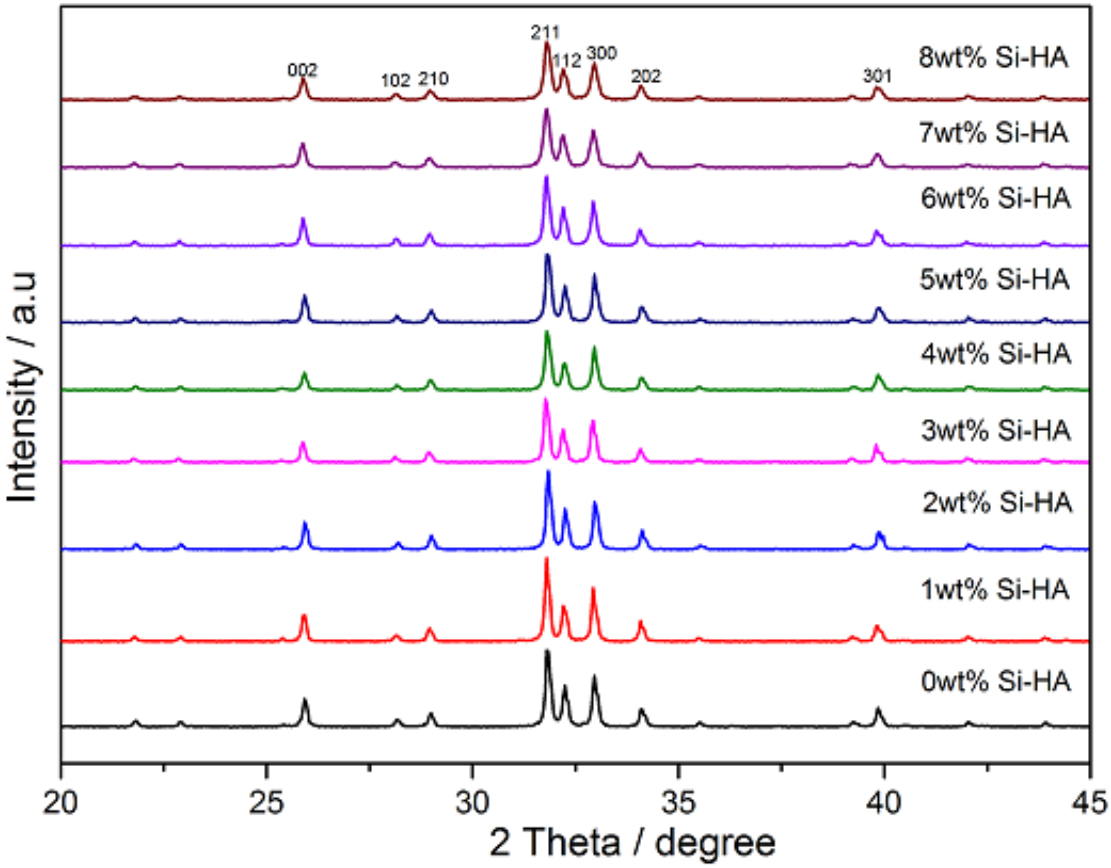

Figure 6-6 XRD patterns of heat-treated (1000 °C, 2hr in air) Si-substituted hydroxyapatite powders made using CPFS system at 70°C in five minutes residence time

6.3.4 Fourier Transform Infrared Spectroscopy

FTIR spectroscopy was carried out on all carbonate- and silicate-substituted samples in order to aid observations made using XRD. The FTIR analysis (Figure 6-7) detected strong peaks at the wavenumbers of the B-type CHA (870, 1430 and 1450 cm^{-1}). The typical peaks of the A-type CHA (880, 1450 and 1540 cm^{-1}) were not evident.

The FTIR spectrum for sample SiHA in Figure 6-8 revealed peaks similar to those observed for carbonate-substituted samples. However, the weak band in the range 1565–1380 cm^{-1} (corresponding to asymmetric stretching of the C–O band of CO_3^{2-} group in both A- and B-type carbonate substitutions in HA) was understandably much lower in intensity as compared to the similar band seen in the FTIR spectrum of the carbonate substitution samples in Figure 6-7.

The weak peak centred at 872 cm $^{-1}$ was due to the bending mode of the O–C–O linkage in a small amount of carbonate, which is present. This was also lower in intensity as compared to a similar peak observed at 876 cm $^{-1}$ in Figure 6-7 (due to higher amount of carbonate ions present in the carbonate-substituted samples).

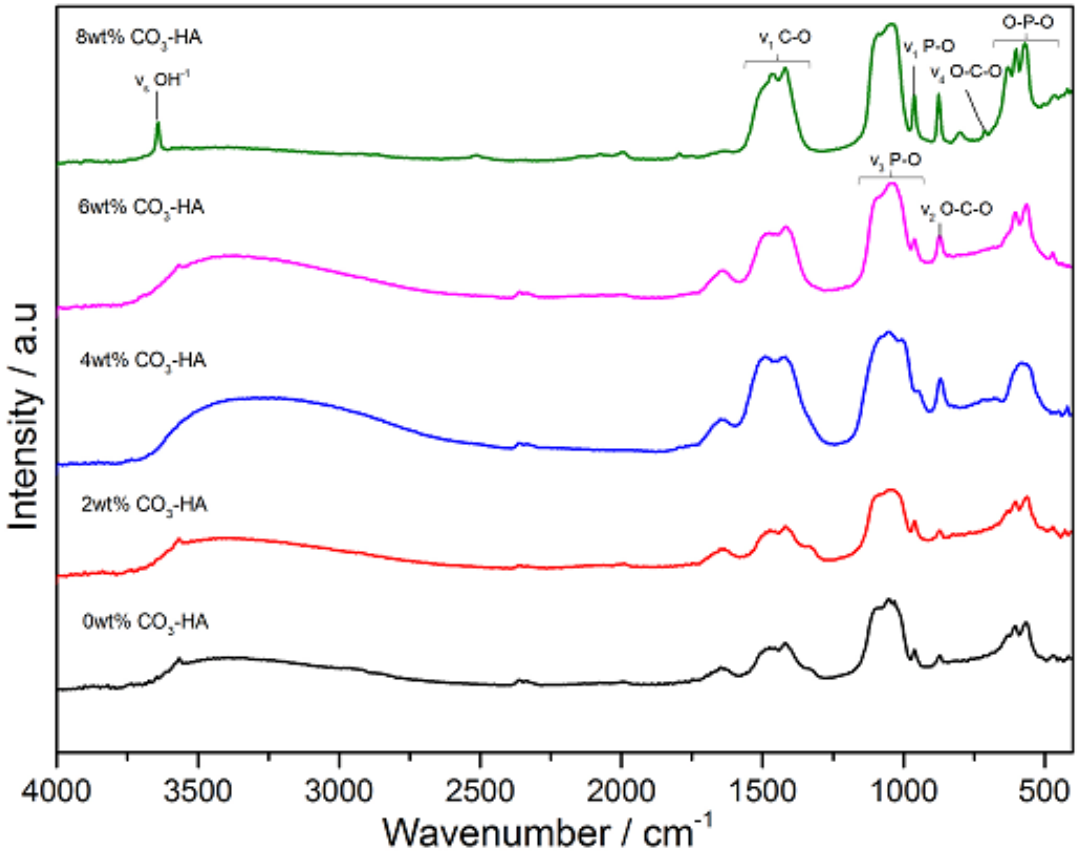

Figure 6-7 FTIR spectral data of CO_3^{2-} substituted hydroxyapatite powders made via CPFS system at 70°C in five minutes residence time

A notable difference from the FTIR spectra in Figure 6-8 was that the OH $^{-1}$ stretching peak at about 3571 cm $^{-1}$ decreased in intensity with increasing silicon substitution (Figure 6-8). This supported the hypothesis that silicon was being substituted in the HA lattice in the form of silicate, SiO_4^{-4} substituting phosphate, PO_3^{-4}. The most notable effect of silicon substitution on the FTIR spectra of hydroxyapatite is the changes in the PO_4 bands between 800 and 1100 cm^{-1} and 500–700 cm^{-1}.

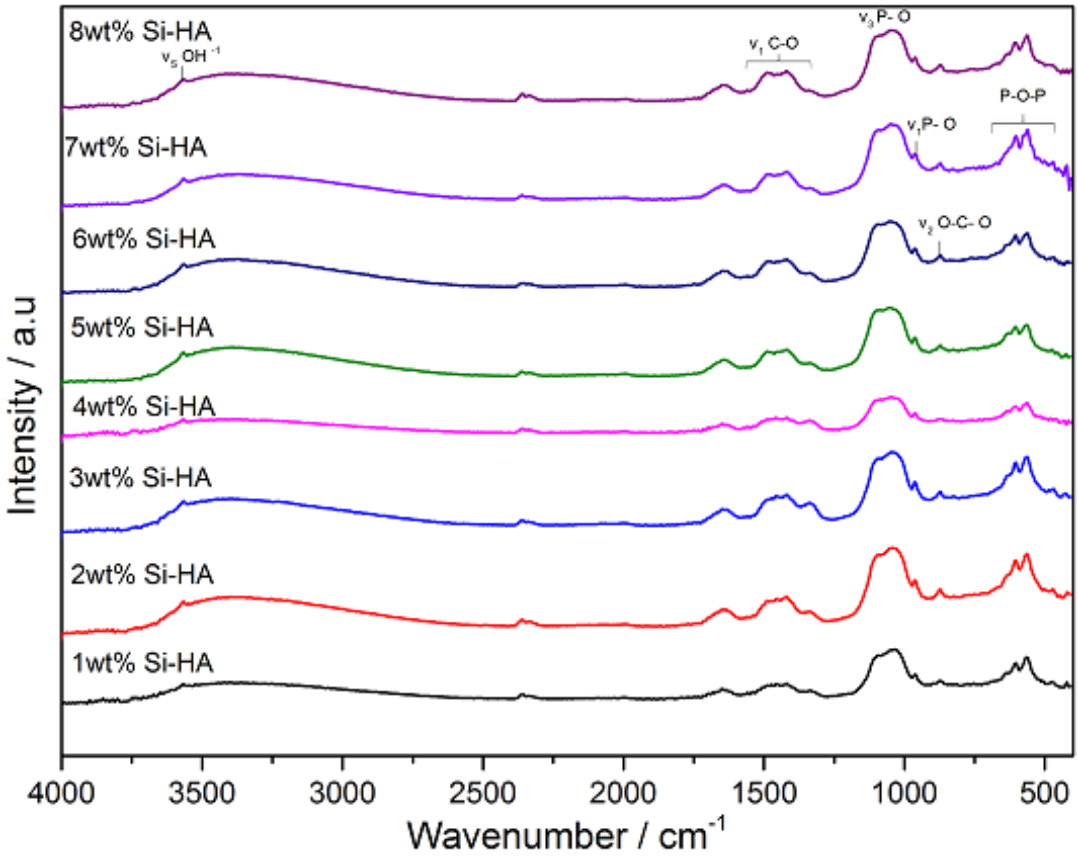

Figure 6-8 FTIR spectral data of Si-substituted substituted hydroxyapatite powders made using CPFS at 70°C

6.3.5 Raman Spectroscopy

Raman spectroscopy was conducted in order to supplement XRD data and investigate any structural changes with substitutions in the apatite lattice. Figure 6-9 shows Raman spectra for all the carbonate-substituted samples. The peak at 965cm^{-1} corresponded to a symmetric stretching mode of the P-O bonds in the phosphate groups. Peaks at 610 and 483 cm^{-1} are likely to correspond to the bending mode of the O-P-O linkage in the phosphate groups as shown in Figure 6-9. The band at 1070 cm^{-1} resulted due to a carbonate peak and intensity of the peak was largely dependent on the amount of carbonate ions present.

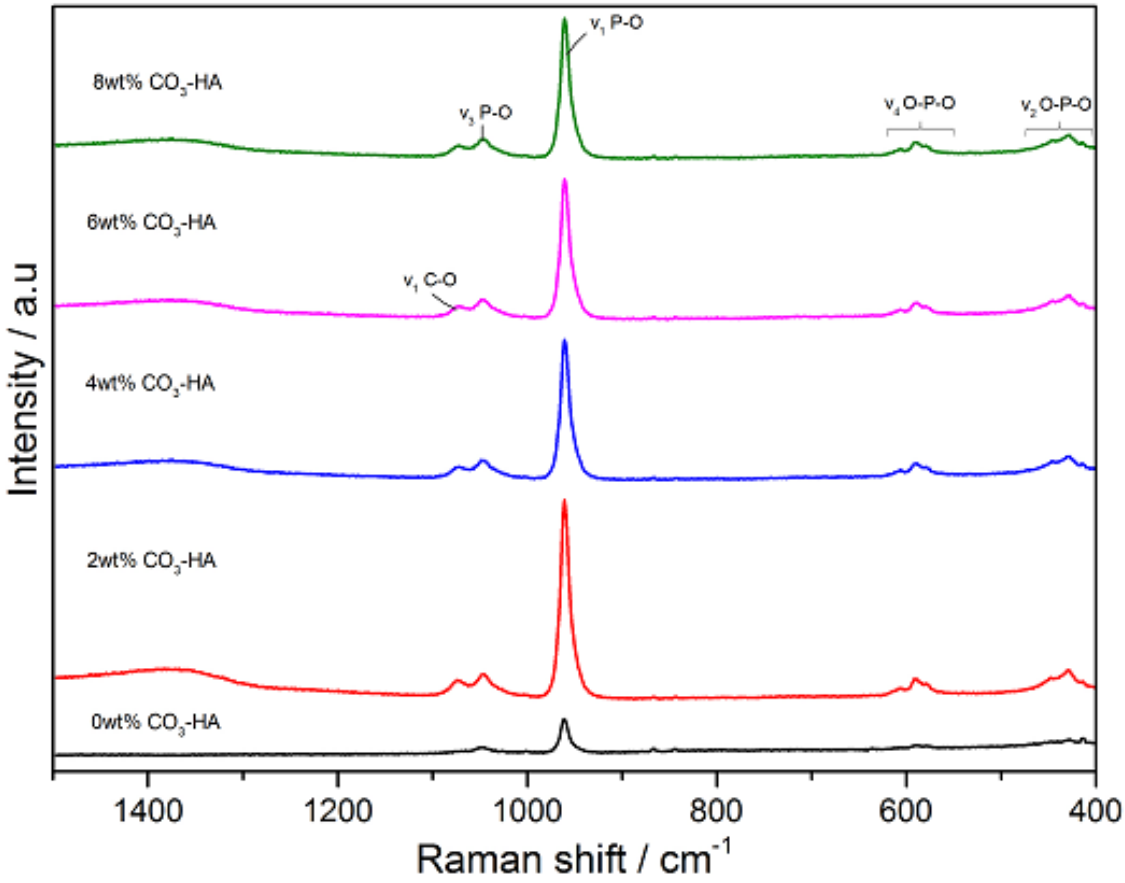

Figure 6-9 Raman data of CO_3^{2-}- substituted hydroxyapatite samples made using CPFS at 70°C

Raman spectra for all silicon-substituted samples are shown in Figure 6-10. The Raman spectra for SiHA samples revealed peaks at 1080 cm^{-1} and 1049 cm^{-1} attributed to asymmetric stretching of the P–O bonds in the phosphate groups. The peak around 960 cm^{-1} corresponded to the symmetric stretching mode of the P–O bonds in the phosphate groups. Peaks at 595 and 438 cm^{-1} corresponded to the bending modes of the O–P–O linkages.

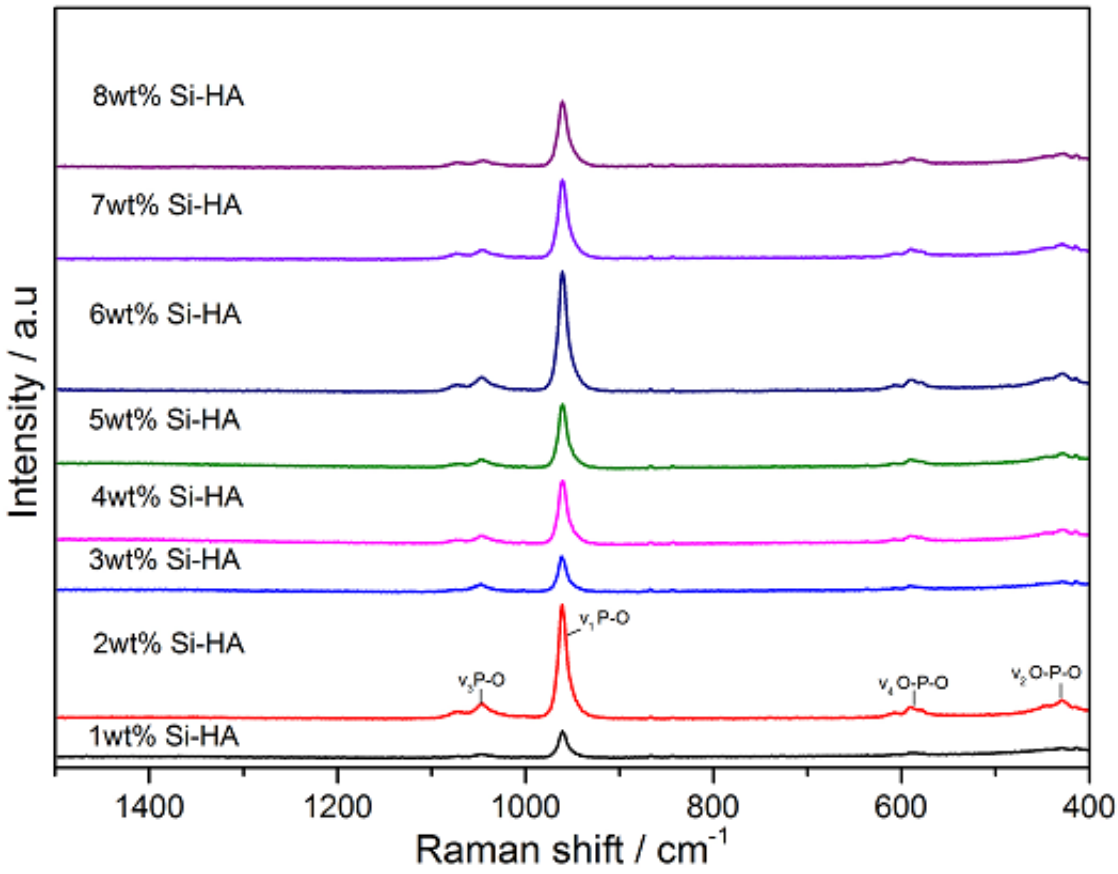

Figure 6-10 Raman spectra of Si-substituted hydroxyapatite powders made using CPFS at 70 °C

6.3.6 Dynamic Light Scattering

Particle size distribution was also conducted for some selected samples, pure HA, 2CHA, 4CHA, 8CHA, 2SiHA, 4SiHA and 8SiHA. DLS measurements of pure hydroxyapatite sample synthesized at 70 °C in 5 minutes residence time reveals average particle size of *ca.* 159 and PDI (polydispersity index) value of 0.231.

For samples 2CHA, 4CHA, 8CHA, 2SiHA, 4SiHA and 8SiHA, respectively, DLS measurements yielded average particle sizes of *ca.* 146, 149, 158, 159, 164, and 174 nm with unimodal distribution of particles. Whilst PDI values of 0.268, 0.264, 0.272, 0.207, 0.239 and 0.270 were recorded. DLS measured diameter (100-300nm) with PDI of 0.3 or less shows good dispersion. It was also observed that DLS measurement results are in good agreement with TEM determined distributions.

6.3.7 Cell Viability Study

A human osteoblast cell proliferation study was conducted on selected carbonate (2CHA, 4CHA, 6CHA) and silicate (2SiHA, 4SiHA, 8SiHA) samples. The pure HA sample made via CPFS at 70 °C (reaction time: 5 min.) was used as a control. The osteoblast cells cultured on all ceramic samples showed continuous proliferation. The cell viability was studied over the course of 7 days (Figure 6-11). At day 1, cell viability was almost similar on all samples indicating that initial cell attachment was not enhanced by any surface. At day 4, cell viability gradually increased on all 5 samples (pure HA, 4SiHA, 8SiHA, 4CHA and 8CHA) but a noticeable increase was observed for 4SiHA and 8SiHA samples.

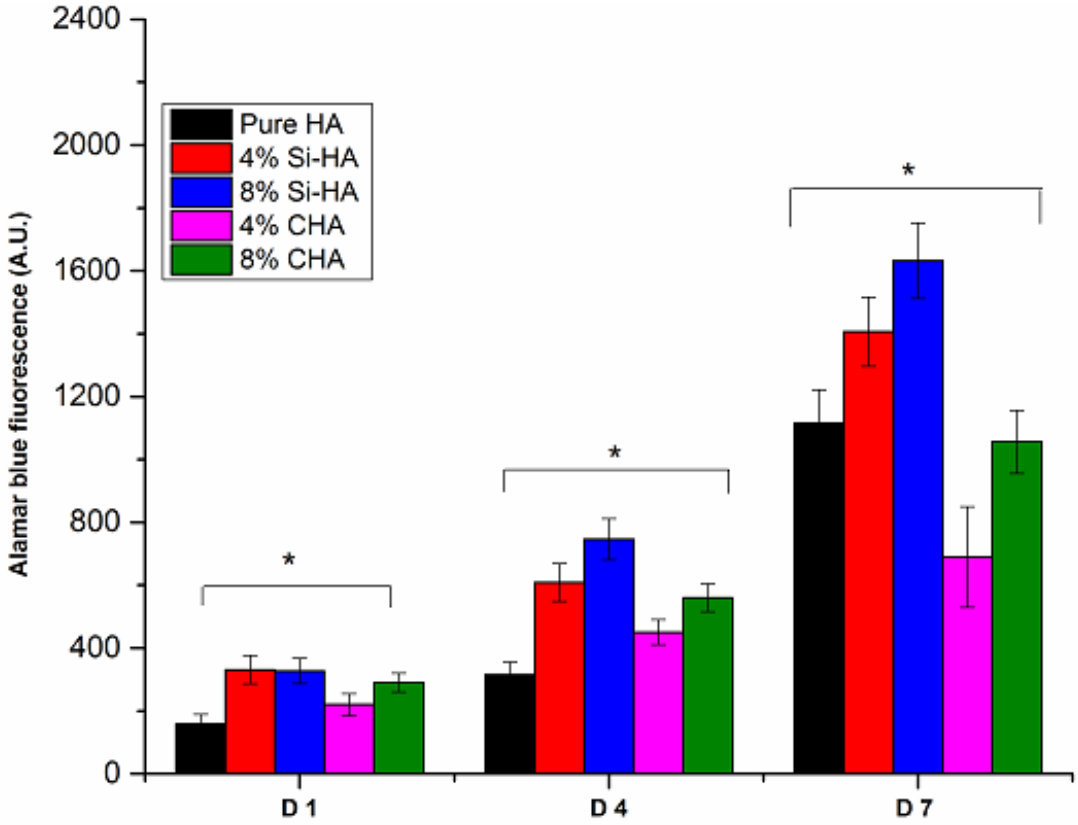

Figure 6-11 MG63 viability on CPFS, SiHA and CHA discs. Alamar blue viability assay was performed at days 1, 4, and 7 to observe MG63 viability on as prepared discs consisting of 4 % or 8 % SiHA and CHA as well as CPFS pure HA. Mean ± SD, * $p < 0.05$.

A similar trend was observed at day 7, however, all five samples had an increased cell viability compared with day 1 and 4. At both days 4 and 7, 4SiHA and 8SiHA had

significantly higher cell viability than 4CHA, 8CHA and pure HA. It was observed that silicon substitution in HA greatly enhance the osteoblatic cell proliferation.

6.3.8 Cell Morphology

MG63 morphology was observed at day 7 (Figure 6-13) on all five samples. Cells were seen to attach, spread and grow on all types of samples as shown in Figure 6-12. Cells were evenly distributed on pure HA and showed a typical square-like osteoblast morphology. On 4SiHA, cells were more sparse and generally less-well spread than those on pure HA and CHA, whilst cells were spread very well on 8SiHA sample as shown in Figure 6-12.

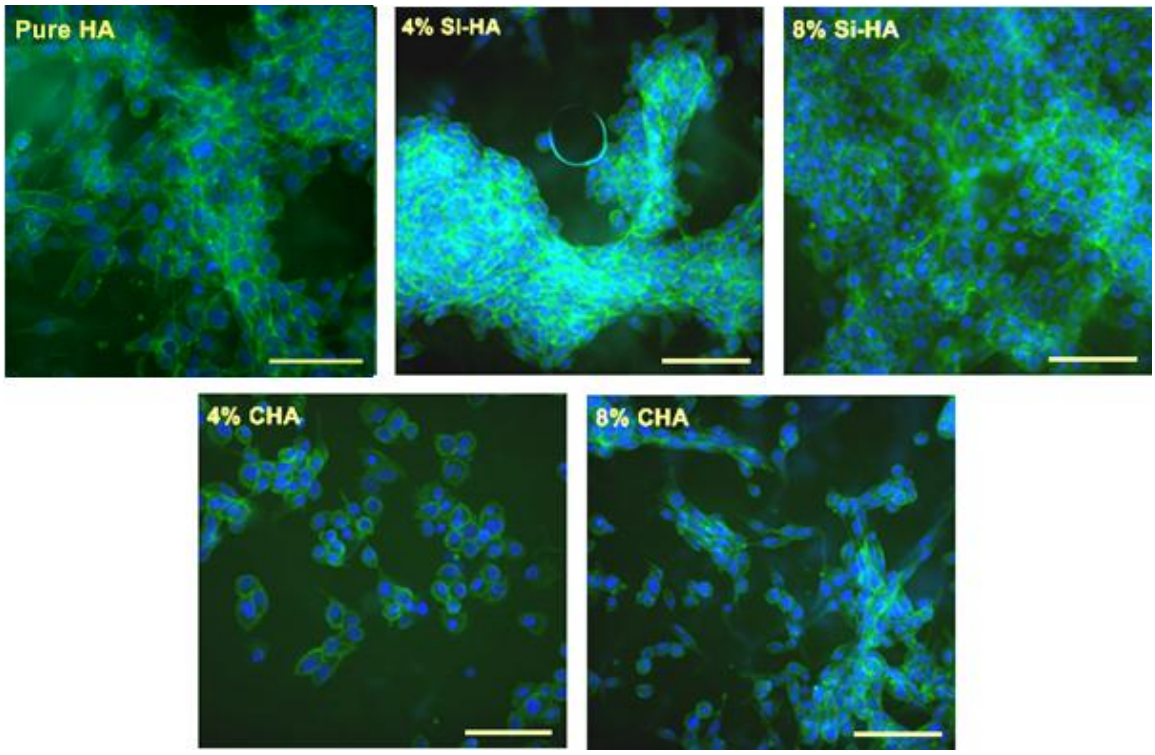

Figure 6-12 MG63 morphology of SiHA and CHA discs made at 70 ˚C in a CPFS reactor. Cells were visualised at day 7 for cell nucleus (DAPI in blue) and cytoskeleton (phalloidin-FITC in green) for MG63s cultured on as prepared discs containing 4 % or 8 % SiHA and CHA as well as pure HA. Scale bar is 100 µm.

On the other hand, cell spreading was less pronounced in carbonate samples compared to silicate substituted samples, with the majority showing a rounded morphology. Results revealed better bone cell cytoskeletal organisation and greater growth activity

for osteoblast cells cultured on SiHA than on CHA. This could be due to the faster dissolution or higher surface area of the SiHA samples compared to CHA.

6.4 Conclusions

A CPFS reactor was used to successfully synthesise ion substituted calcium phosphates from calcium nitrate tetrahydrate [($Ca(NO_3)_2.4H_2O$), and diammonium hydrogen phosphate ($(NH_4)_2HPO_4$)] precursor solutions at (near) ambient conditions in a rapid single step. Careful control of the quantities of reactants used, resulted in phase pure nano-sized carbonate and silicon substituted hydroxyapatite that retained the apatite structure even after heat-treatment at 1000 °C for two hours.

Cell toxicity analysis confirmed excellent biocompatiblity of these materials. These results indicate that newly developed CPFS technique for the production of pure HA and ion substituted HA, has made samples which are biocompatible and that support osteoblast proliferation. With its unique features, the obtained product is a promising material with biological properties and has potential to be used in biomedical applications where small size and fine particle size distribution control may be beneficial e.g. injectables for spinal fusion or as a filler in a biocomposite.

6.5 Future Work

Silicon substitution level may be enhanced by using different precursor solution (other than silicon tetraacetate) for better dissolution and more effective results. To further strengthen the proficiency of CPFS system, It would be interesting to correlate CPFS system parameters with different substitution levels in HA.

Osteoblastic cell attachment and viability analysis confirmed the high biocompatiblity of silicon-substituted materials. Future work should address the ability of CPFS to support osteogenic differentiation and what affect anionic [CO_3^{2-}, SiO_4^{2-}] substitution has on this.

Chapter 7
Synthesis and Surface Modification of Calcium, Strontium and Barium-Hydroxyapatite Nanorods Incorporating Functionalized Surfaces for Dental Restoration

7.1 Introduction

Hydroxyapatite (HA) is of interest as a synthetic bone substitute that has a wide range of applications in the dentistry health care products and medicine (Wei and Ma, 2004, Choi et al., 2006, Khan et al., 2008, Domingo et al., 2003, Sadat-Shojai et al., 2010). Dentine is a natural composite which forms part of teeth and is based on an organic matrix of mainly collagen, a small quantity of citrate, and an inorganic mineral phase (filler) consisting of nano-sized (<100 nm) biological apatite crystals. Synthetic HA resembles some of the properties of biological apatite found in natural teeth and bone offers numerous properties, which can be exploited for biomedical applications and in restorative dentistry (intrinsically radio-opaque, good polishability, high wear performance) (Arcís et al., 2002, Willems et al., 1992, Giannini et al., 2004). Synthetic HA potentially has a large amount of P–OH groups on the surface of particles, therefore many organic or inorganic substances have been introduced to HA surfaces via the P–OH groups. Increasing the number of surface P–OH groups is of interest because they can act as anionic surface charges and also offer a favourable environment for protein adsorption. Furthermore, increased numbers of P–OH groups can lead to increased electrophoretic mobility and good dispersibility in an aqueous phase (via the charge stabilization mechanism) groups (D'Andre and Fadeev, 2003, Borum-Nicholas and Wilson, 2003, Vega et al., 2003, Borum and Wilson, 2003, Tanaka et al., 2005, Tanaka et al., 2004, Choi et al., 2006).

There is considerable interest in the use of bioceramics as the hard segment in biomedical nanocomposites, particularly in dental applications. The reinforcement of a conventional dental resin with highly dispersed hydroxyapatite nanocrystals seems, in principle, a potential restorative material for non load bearing human tooth tissues as it

could mimic the tooth to some extent (Willems et al., 1992, Arcís et al., 2002, Saito et al., 1994). A key factor in the failure of many biomedical composites occurs at the interface between the hard / ceramic segment and polymer matrix. This is usually due to a weak mechanical bond between the two phases. Chemical coupling of ceramics to a polymer matrix provides a means of improving interfacial bonding between the hard particles and polymer in a composite. This can be achieved by creating reactive bonding sites/groups on the surface of the inorganic filler particle, which can be used to form bonds between the inorganic filler and polymer (Bonfield et al., 1998, Haque et al., 2007).

For the synthesis of HA and other biocermics, the method of preparation greatly influences the properties, nature and crystallinity of the precipitated powder. Reaction parameters for synthesis are also important such as temperature, pH, time and other precipitation conditions like aging time, variation in Ca:P ratio, concentration, mixing dynamics, choice of precursor, etc. (Raynaud et al., 2002, Ahn et al., 2001, Rodrıguez-Lorenzo et al., 2001). The majority of the reported literature methods for HA synthesis are multi-step, inconsistent, energy intensive or time consuming processes (Pang and Bao, 2003, Phillips et al., 2003, Lim et al., 1997, Kothapalli et al., 2005, Wang et al., 2006a, Kim et al., 2005) and almost always involve the need to have careful control over reaction pH during the mixing of reagents. In this report, we describe a rapid and direct route for the synthesis of phase pure surface grafted nano-HA using a continuous (plastic) flow synthesis (CPFS) reactor at 70 ˚C. The main objective of this work was to gain insights into the chemistry and use of surface functionalised hydroxyapatite as a reinforcing filler component for photo-cured BisGMA/TEGDMA dental restorative infiltrants.

Strontium and barium ions are divalent and have the ability to be incorporated into hydroxyapatite crystals. Among the many divalent cations that can be substituted for calcium in hydroxyapatite, strontium is of interest because of its beneficial effect on bone formation and prevention of bone resorption. Strontium and barium hydroxyapatite (with no calcium) have gained interest in recent years because of their high density and radiopaque properties. The doping of Sr in the hydroxyapatite structure for implants has been shown to increase bone mineral density (BMD), bone mineral content (BMC), bone volume and microarchitecture, reduced bone fracture risk and

improved the mechanical performance of whole bone without affecting the estimated material properties of the bone tissue (Bigi et al., 2007, Okayama et al., 1991).

Radiopaque dental materials are beneficial in making diagnosis and monitoring existing restoration. However, there is still a lack of dental material that is tooth coloured, minimally invasive and has satisfactory radiopacity. In a recent study on dental restorative materials containing Sr and Ba-HA (no calcium), it has been found that Sr-HA appeared to be a better radiopaque filler when it is mixed as a composite with a polymeric matrix.

In this chapter, a CPFS reactor is used to successfully synthesize surface grafted Group 2 metal phosphates and and to use these modified HA as filler component to develop a novel radiopaque resin infiltrant for dental applications.

7.2 Experimental

7.2.1 Synthesis Methodologies

7.2.1.1 Surface- Modified Calcium Hydroxyapatite Preparation

The pure nano-hydroxyapatite (HA) was prepared using a continuous (plastic) flow synthesis system (CPFS) the design of which is described in section 2.2.1. 0.3 M diammonium hydrogen phosphate solution and 0.5 M calcium nitrate solutions were pumped in the CPFS (Ca:P molar ratio:1.67) using pump 1 and pump 2, respectively. The pH of both the solutions prior to the reaction was kept above pH 10. 5.0 mL and 15.0 mL of ammonium hydroxide were added to calcium nitrate (500 mL) and diammonium hydrogen phosphate solution (500 mL), respectively. Both reagent solutions were pumped at 20 mL min^{-1} to meet at a T-piece. This initial mixture was connected to an 8 m long coiled tube surrounded by a heated jacket at 70 °C . For flow rates of calcium nitrate and diammonium hydrogen phosphate for P1 and P2, this gives 5 minutes residence time. The products were collected as a suspension in a beaker at the exit point and centrifuged and freeze dried as described earlier in section 2.3.1.1. The surface modified hydroxyapatites were obtained following a similar procedure as for pure nano-HA, except the calcium containing precursor additionally contained the appropriate amount of (0.05 M) the modifying organic chemical. Product was obtained as a fine white powder with ~ 85% yield. Resulting nanopowders were termed PVA-

HA (polyvinyl alcohol), A-HA (adipic acid), C-HA, (citric acid), VPA-HA (vinylphosphonic acid) and MA-HA (methacrylic acid).

7.2.1.2 Surface- Modified Strontium Hydroxyapatite Preparation

The surface modified strontium (containing no calcium) hydroxyapatite nanopowders were prepared at 70 °C using the continuous (plastic) flow synthesis system (CPFS), the details of which are described in section 2.2.1. In the synthesis process, 0.5M basic solutions of strontium nitrate with organic surface modifier ($Sr+RCO_2^-R$) / P = 1.67) and 0.3 M diammonium hydrogen phosphate, respectively, were pumped to meet at a T-piece. The pH of both the solutions prior to the reaction was ideally kept above pH 12. This initial mixture was connected to an 8 m long pipe, which was coiled inside an oil bath, which gave an effective 5 minutes residence time from the tee to the exit of the pipe. The obtained white precipitates were centrifuged and freeze dried as described previously (section 2.3.1.1).

7.2.1.3 Surface- Modified Barium Hydroxyapatite Preparation

A similar procedure was adopted for the synthesis of Ba-hydroxyapatite using the CPFS system as described earlier in section 2.2.1. In the synthesis process, basic solutions of barium hydroxide with organic surface modifier ($Ba+RCO_2^-R$) /P = 1.67) were used. The pH of both the solutions prior to the reaction was ideally kept above pH 12. This initial mixture was connected to an 8 m long plastic tube, which was coiled inside an oil bath, which gave an effective 5 minute residence time from the tee to the exit of the pipe. The obtained precipitates were centrifuged and freeze dried as described previously (section 2.3.1.1). All reactions were carried out at 70 °C and atmospheric pressure. Product was obtained as a fine white powder with ~ 85% yield.

7.2.2 Dental composite preparation

The organic matrix consisted of 60 wt% Bis-GMA and 40 wt% diluent TEGDMA as a comonomer. Various mass fractions of surface-modified hydroxyapatite,

nanoparticles were added into the monomer. The solution was stirred for 24 hours and shifted to a light sensitive vial to avoid photocuring prior to addition of further components (initiator, coinitiator, filler). 0.5 wt% camphorquinone and 2 wt% dimethylaminoethyl methacrylate along with 0.2 wt% N, N-Dimethyl-p-toluidine were added into the monomer solution as the initiator and coinitiators, respectively. After mixing thoroughly for 2 hours, the mixture was carefully transferred into a disk shaped Teflon mold (diameter 6mm, thickness 1mm). Then samples were photo-cured using a blue LED activation light (Demetron LC, Ser no 66004022, KERR corporation, Danbury). X-ray images were then taken of the samples after leaving the sample to cure for at least 30 minutes. The similar procedure was repeated for surface modified strontium and barium phosphates.

7.2.2.1 Radiopacity Investigation Procedure

For each sample, a Teflon mould was used to produce 3 disks, measuring 6 mm in diameter and 1 mm in thickness, in accordance to ISO 4049. The specimens were photo-polymerized using a blue LED light. The specimens were ground with 150-grit sandpaper to create a flat surface. Specimens were measured using a digital micrometer. One specimen of each sample and an aluminium wedge were placed side by side on an occlusal radiographic film. The step wedge served as a standard for each radiographic exposure. Films were exposed for 0.6 milliseconds with a radiography unit at 70 kV and 8 mA, the object to film distance was 300mm.

7.3 Results and Discussions

7.3.1 Transmission Electron Microscopy

Transmission electron microscope images of ungrafted hydroxyapatite samples as shown in Figure 7-1 confirmed that very small crystallites had been synthesised. The particles obtained at 60 °C possessed a small particle size of *ca.* 25 ± 5 nm (200 particles sampled) along the longest axis and of *ca.* 7 ± 2 nm along the smaller axis as shown in Figure 7-1 (a) and (b). Phase pure as prepared HA synthesized at 70 °C in the CPFS, the particles had a rod like morphology and average length along the longest axis was *ca.* 85 ± 15 nm (200 particles sampled) and average width was 15± 5 nm as shown in Figure 7-1 (c) and (d).

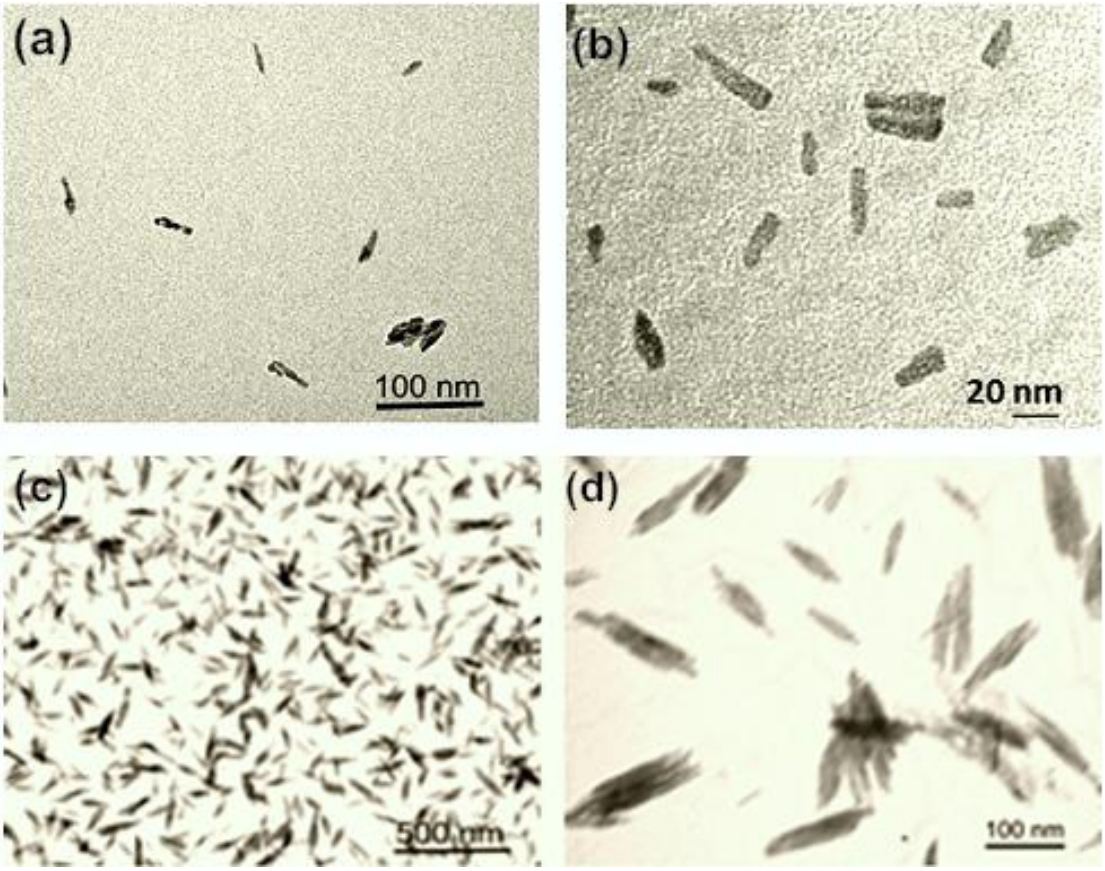

Figure 7-1 Transmission electron microscope images of hydroxyapatite nano-rods made at 60 °C (a,b) and 70 °C (c,d) in five minutes residence time via CPFS, ((bar = (a) and (c) = 100 nm, (b) = 20 nm, (c) = 500 nm

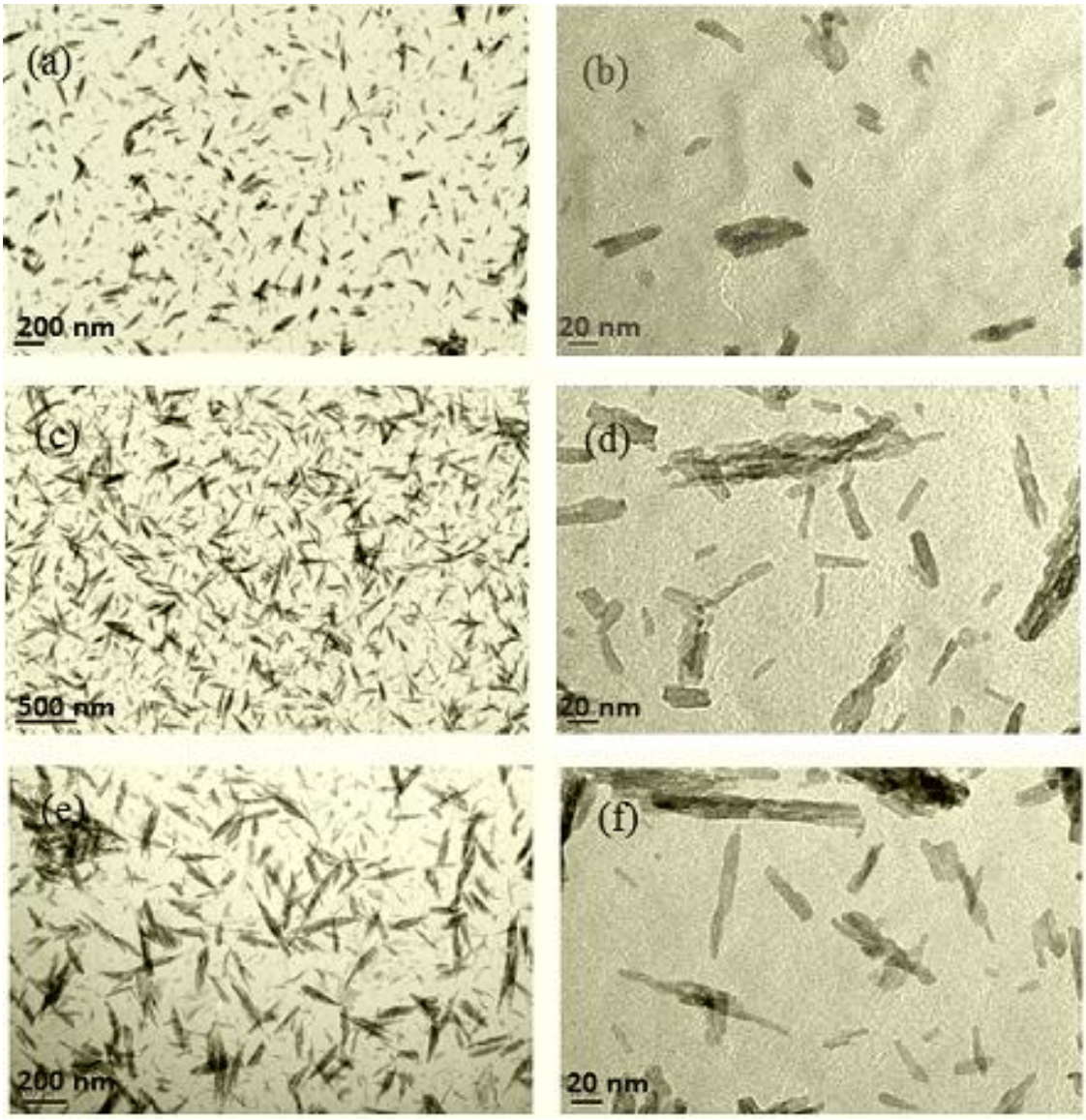

Figure 7-2 Transmission electron microscope images of surface modified hydroxyapatite nano-rods made at 70 °C in five minutes residence time via CPFS (a,b) methacrylic acid modified hydroxyapatite, (c,d) vinyphosphonic acid modified hydroxyapatite and (e,f) adipic acid modified hydroxyapatite with bar sizes (a), (c) and (e) = 500 nm, and for (b), (d) and (f) bar = 20 nm.

TEM images of surface grafted hydroxyapatite synthesized at 70 °C in five minutes residence time via CPFS were also recorded. It was observed that methacrylic acid grafted HA particles possessed a small particle size of *ca.* 25 ± 5 nm (200 particles sampled) along the longest axis and of *ca.* 7 ± 2 nm along the smaller axis as shown in Figure 7-2 (a) and (b).

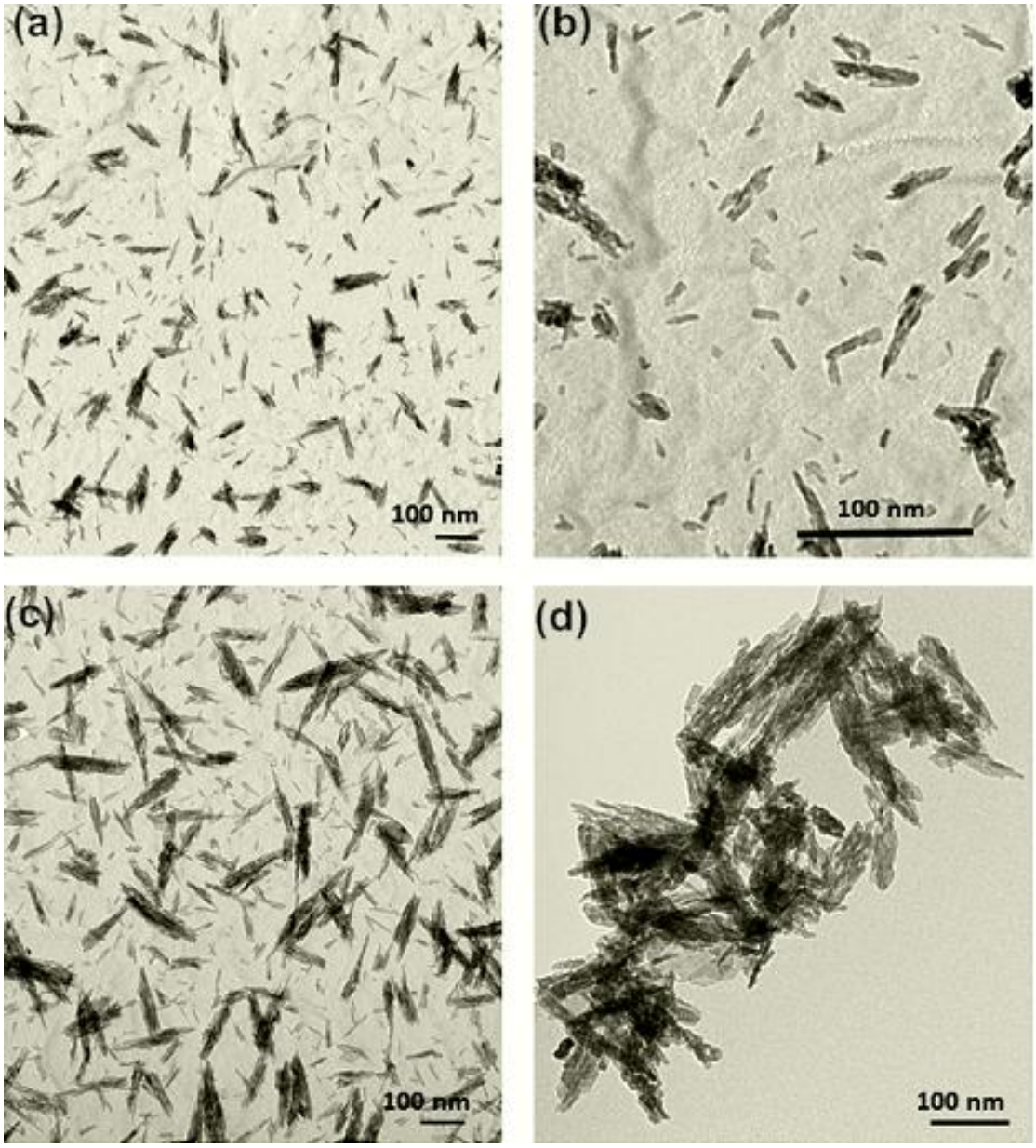

Figure 7-3 Transmission electron microscope images of surface modified strontium (a,b) and barium (c,d) hydroxyapatite nano-rods made at 70 °C in five minutes residence time via CPFS with bar sizes (a) and (c) = 500 nm, and for (b) and (d) = 100 nm.

On the other hand, vinylphosphonic and adipic acid based HA particles possessed a slightly larger particle size of *ca.* 35 ± 5 nm (200 particles sampled) along the longest axis and of *ca.* 7 ± 2 nm along the smaller axis as shown in Figure 7-2 [c-f].

Other surface functionalized Group 2 metal phosphates (Sr-HA, Ba-HA) were also synthesized successfully at 70 °C in five minutes residence time using CPFS system

parameters. It was observed that methacrylic acid grafted strontium hydroxyapatite nanoparticles possessed a particle size of *ca.* 40 ± 5 nm (200 particles sampled) along the longest axis and of *ca.* 7 ± 2 nm along the smaller axis as shown in Figure 7-3 (a) and (b). In comparison, methacrylic acid based barium hydroxyapatite nanoparticles revealed a relatively larger particle size of *ca.* 80 ± 15 nm (200 particles sampled) and average width was 15± 5 nm as shown in Figure 7-3 (c) and (d).

7.3.2 BET Surface Area Analysis

BET surface area measurements of the as prepared HA made at 70 °C in five minutes residence time via CPFS had a BET sufrace area of 195 $m^2g^{-1,}$ whilst surface modified PVA-HA (polyvinyl alcohol), A-HA (adipic acid), C-HA, (citric acid), VPA-HA (vinylphosphonic acid) and MA-HA (methacrylic acid) synthesized under the same conditions had BET surface areas of 143, 208, 201, 225 and 231 m^2g^{-1}, respectively, as shown in Figure 7-4. On the other hand, surface grafted strontium and barium hydroxyapatite nanoparticles revealed the BET surface area of 148 and 90 m^2g^{-1}, respectively.

7.3.2.1 Effect of Temperature on BET Surface Area

A comparative study based on pure HA and surface grafted HAs was carried out at different temperature regimes (60, 70 and 80 °C) in five minutes residence time via CPFS system. BET surface area measurements of as-prepared HA sample typically gave surface areas of 264, 195 and 113 m^2g^{-1} as shown in Figure 7-5.

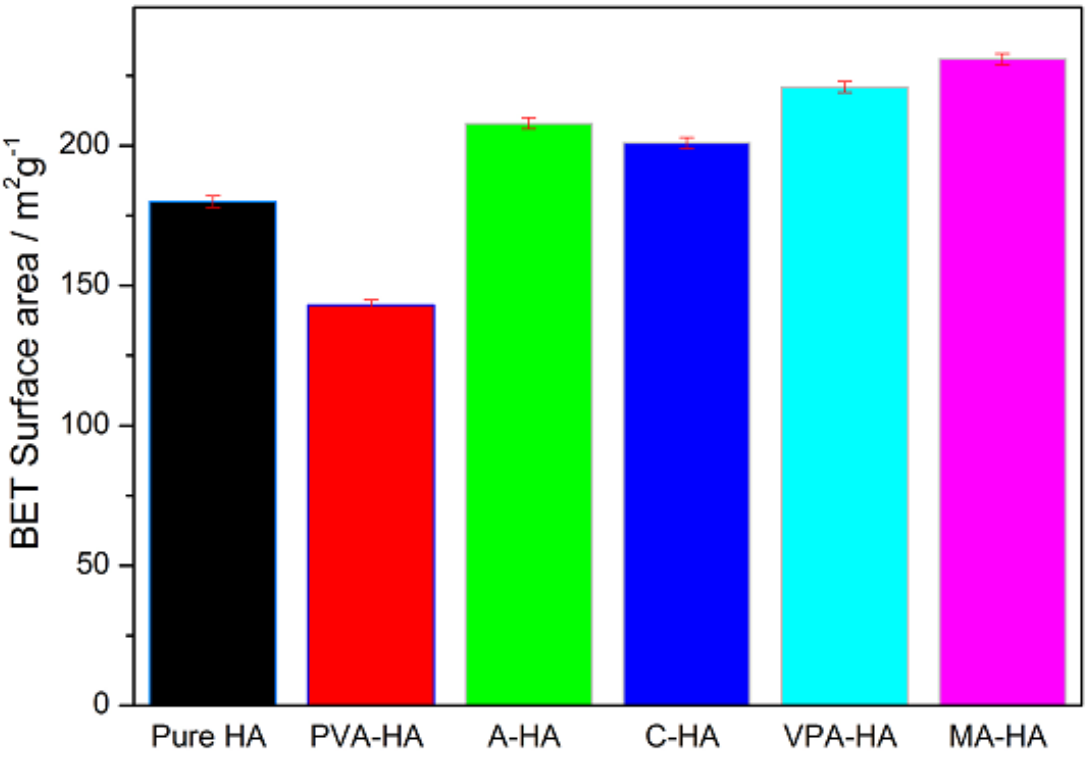

Figure 7-4 BET surface area analysis of pure HA, surface modified PVA-HA (polyvinyl alcohol), A-HA (adipic acid), C-HA, (citric acid), VPA-HA (vinylphosphonic acid) and MA-HA (methacrylic acid), respectively, made at 70 °C in five minutes residence time via CPFS system

Similar reactions were carried out using methacrylic acid and vinyphosphonic acid surface modifying agent on HA surface at 60, 70 and 80 °C. It was noticed that in the presence of surface grafted agents, the surface area remained high even on increasing temperature from 60 to 80 °C as shown in Figure 7-5. These exciting findings indicated that surface grafting agents restrict the particle growth, resulted in small size particles with very high surface area ranging from 220 to 265 m^2g^{-1}under all temperature regimes (60, 70, 80 °C).

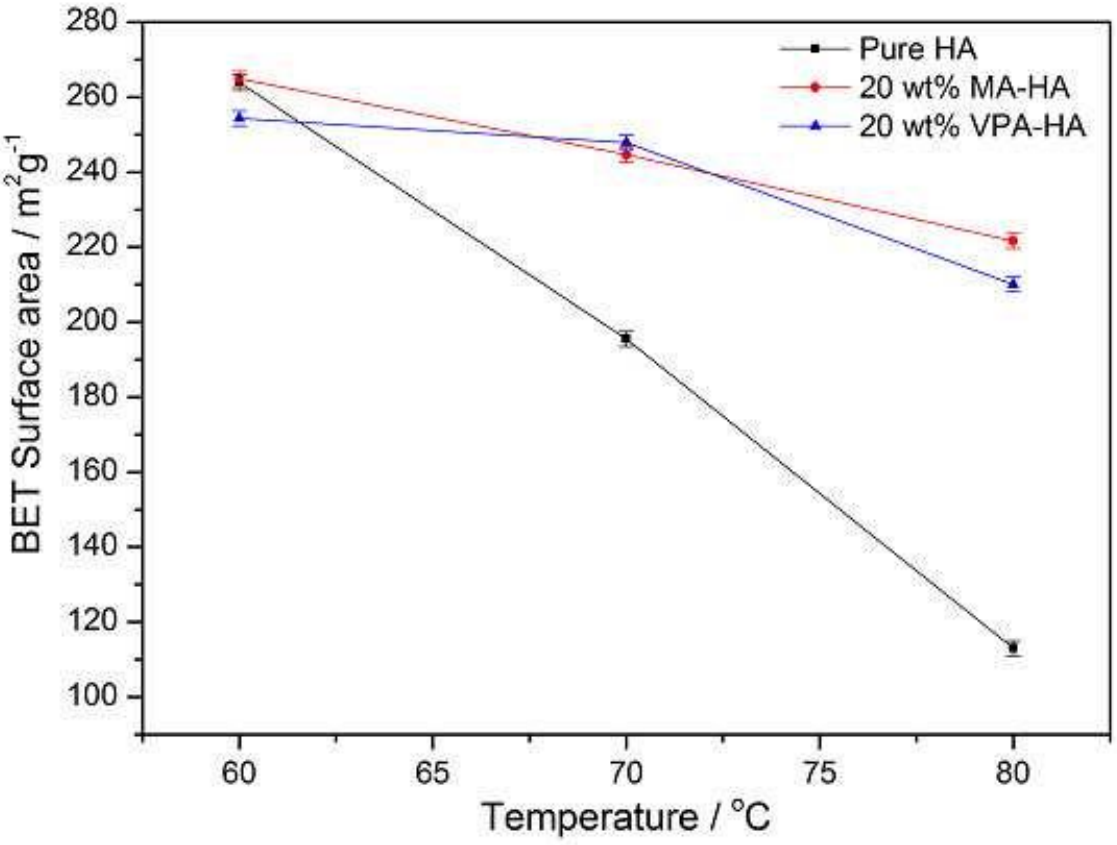

Figure 7-5 BET surface area analysis of pure HA, surface modified V-HA (vinylphosphonic acid) and M-HA (methacrylic acid), respectively, made at 60, 70 and 80 °C in five minutes residence time via CPFS system

7.3.3 Zeta Potential Measurements

Zeta potential measurements were performed on selected samples to investigate the colloidal stability related to surface charge of the pure HA and surface modified HA. Zeta potential gives the electrostatic potential of particles which is directly related to their dispersion stability; the higher the zeta potential values, the greater the electrostatic repulsion and therefore the higher will be the colloidal stability of the suspension. A zeta potential of -43.8 mV was measured for MA-HA (70 °C) and -40.6 mV for VPA-HA (70 °C), respectively which would be expected to stablise the particles from agglomeration as shown in Figure 7-6.

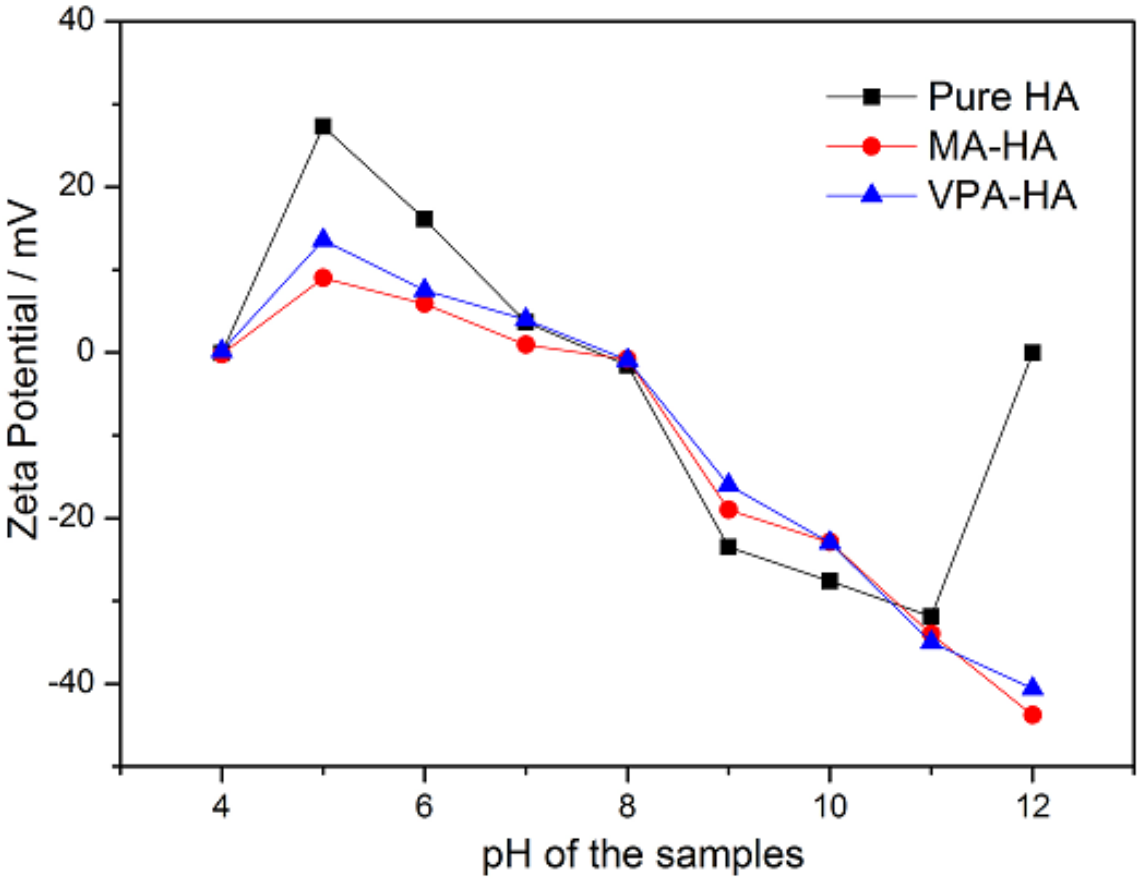

Figure 7-6 Zeta potential of pure HA and surface modified methacrylic acid and vinylphosphonic acid-HA samples made at 70 °C in five minutes residence time via CPFS.

7.3.4 Powder X-ray Diffraction

The powder X-ray diffraction data of the surface modified hydroxyapatites all displayed broad peaks, which were typical of an apatite structure (Figure 7-7). Upon heat-treatment (1000 °C for 2 hours) in air, the powder X-ray diffraction peaks of all samples became considerably sharper and well resolved and gave a good match to the phase pure hydroxyapatite reference pattern JCPDS [09-432]. No additional peaks due to secondary phases were observed in the XRD data after heat-treatment as shown in Figure 7-8.

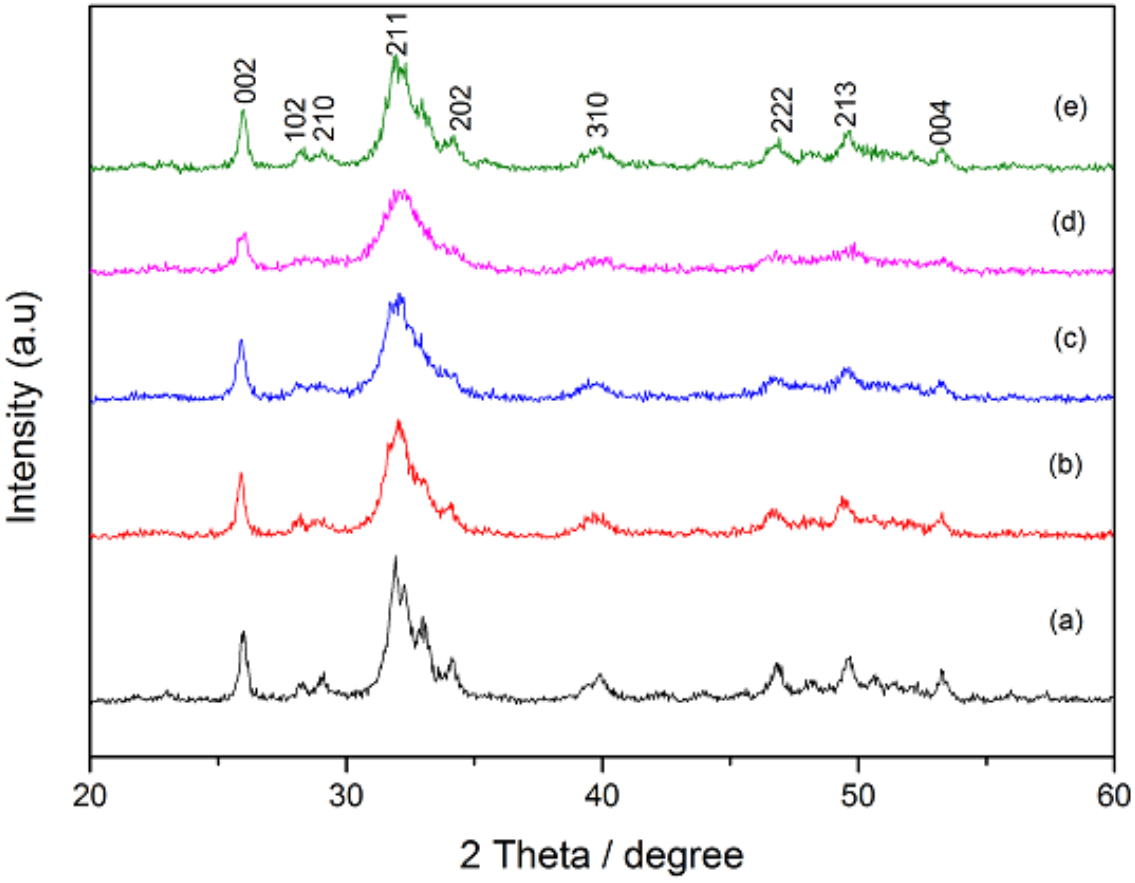

Figure 7-7 Powder X-ray diffraction patterns of surface modified hydroxyapatite with (a) = Polyvinylalcohol modified hydroxyapatite (b) = adipic acid modified hydroxyapatite (c)= citric acid modified hydroxyapatite (d) = vinyphosphonic acid modified hydroxyapatite (e) = methacrylic acid modified hydroxyapatite, respectively. All samples were made in a continuous plastic flow system at 70 °C with a residence time of 5 minutes.

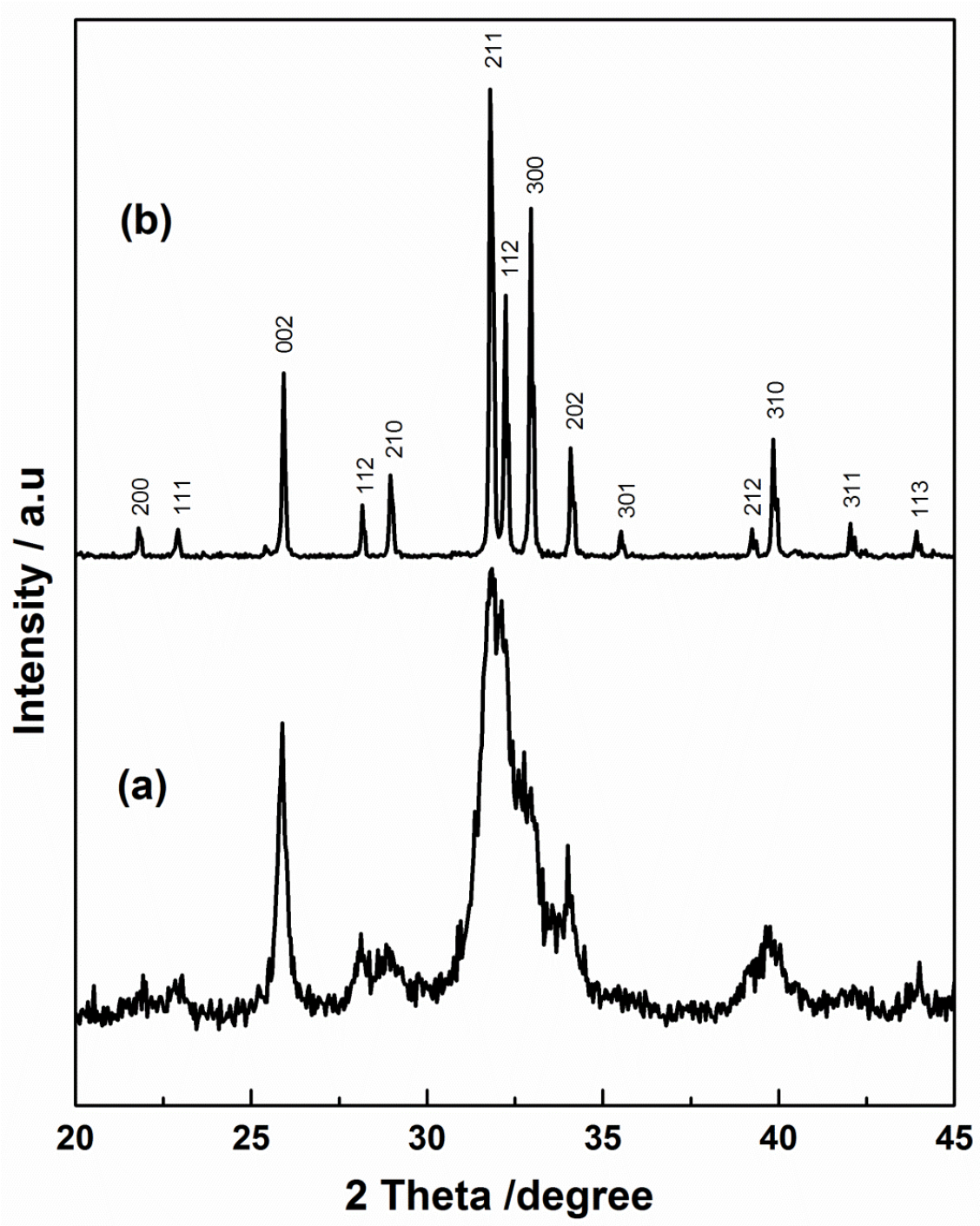

Figure 7-8 Powder X-ray diffraction patterns of as prepared and heat-treated (1000 °C, 2hrs) surface modified hydroxyapatite sample made in a continuous plastic flow system at 70 °C with a residence time of 5 minutes.

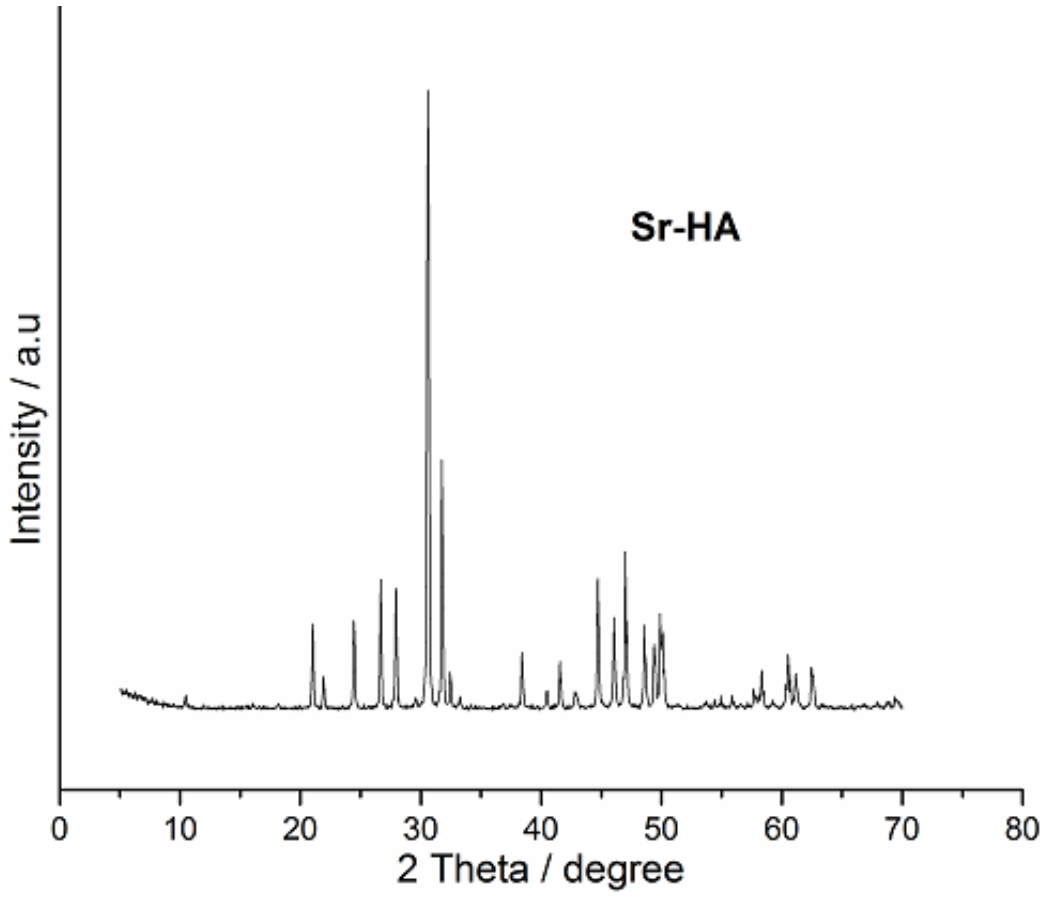

Figure 7-9 Powder X-ray diffraction patterns of as prepared methathacrylic acid grafted strontium hydroxyapatite nanoparticles made in a continuous plastic flow system at 70 °C with a residence time of 5 minutes.

The powder X-ray diffraction analysis of synthesized methacrylic acid grafted strontium hydroxyapatite product indicated that the products obtained at 70 °C in five minutes residence time was exclusively strontium hydroxyapatite particles. The XRD patterns shown in Figure 7-9 gave a good match to the phase pure strontium hydroxyapatite ($Sr_5(PO_4)_3(OH)$, reference pattern JCPDS [070-1511]).

The XRD data of as prepared methacrylic acid modified barium hydroxyapatite confirmed that the product obtained was pure Ba-HA and fairly well-crystallized as shown in Figure 7-10.

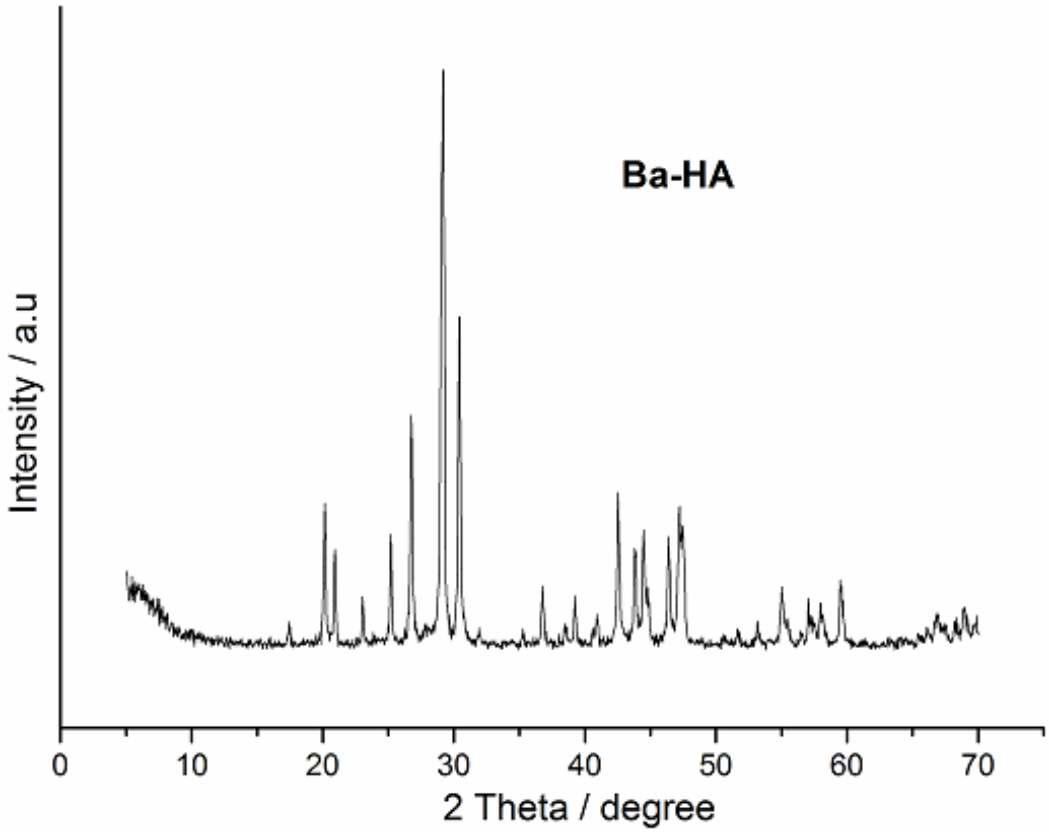

Figure 7-10 Powder X-ray diffraction patterns of as prepared methathacrylic acid grafted barium hydroxyapatite nanoparticles made in a continuous plastic flow system at 70 °C with a residence time of 5 minutes.

7.3.5 Fourier Transform Infrared Spectroscopy

The FTIR spectra of all five as-prepared surface modified HAs are shown in Figure 7-11. All spectra revealed peaks assigned to phosphate stretching and bending vibrations. The peaks at 1093 cm^{-1} and 1023 cm^{-1}correspond to asymmetric (P-O) stretching of the phosphate groups whilst peaks at 602 and 560 cm^{-1} correspond to the symmetric (P-O) stretch. The weak peak at 470 cm^{-1} was assigned to a phosphate bending mode.

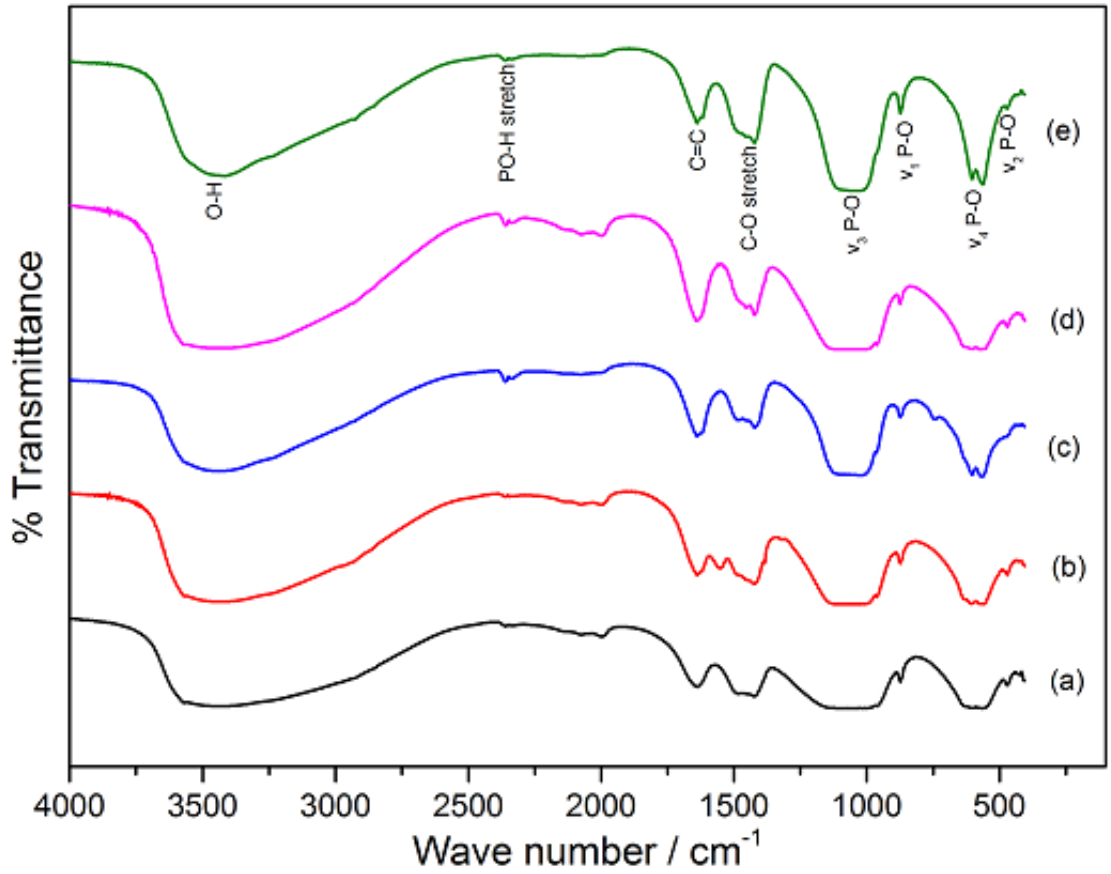

Figure 7-11 FTIR Spectra of surface modified hydroxyapatite with (a) = polyvinylalcohol modified hydroxyapatite, (b) = adipic acid modified hydroxyapatite, (c) = citric acid modified hydroxyapatite, (d) = vinyphosphonic acid modified hydroxyapatite, (e) = methacrylic acid modified hydroxyapatite, respectively. All samples were made in a continuous plastic flow system at 70 °C with a residence time of 5 minutes

7.3.6 X-ray Photoelectron Spectroscopy

A chemical analysis of VPA-HA sample made at 70 °C were conducted using XPS as shown in Figure 7-12. As a general observation, the ratio Ca/P was nearly stoichiometric in phase pure HA, whilst it was observed that in surface modified HAs, the Ca:P molar ratio decreased from 1.67 to 1.37 due to the addition of organic modifiers. The deconvoluted spectra for C, O, Ca and P in sample VPA-HA are presented in Figure 7-13. The Ca 2p spectrum could be resolved into two peaks for Ca $2p_{3/2}$ and $2p_{1/2}$ (two spin-orbit pairs) at 347.4 and 351.3 eV, respectively, which are related to hydroxyapatite. In Figure 7-13 (b), the 2p peak can also be deconvoluted into two peaks

with a spin orbit splitting for $p_{1/2}$ and $p_{3/2}$ levels with binding energy 134.2 and 133.4 eV, respectively (Mahabole et al., 2005, Costescu et al., 2010b, Lu et al., 2000).

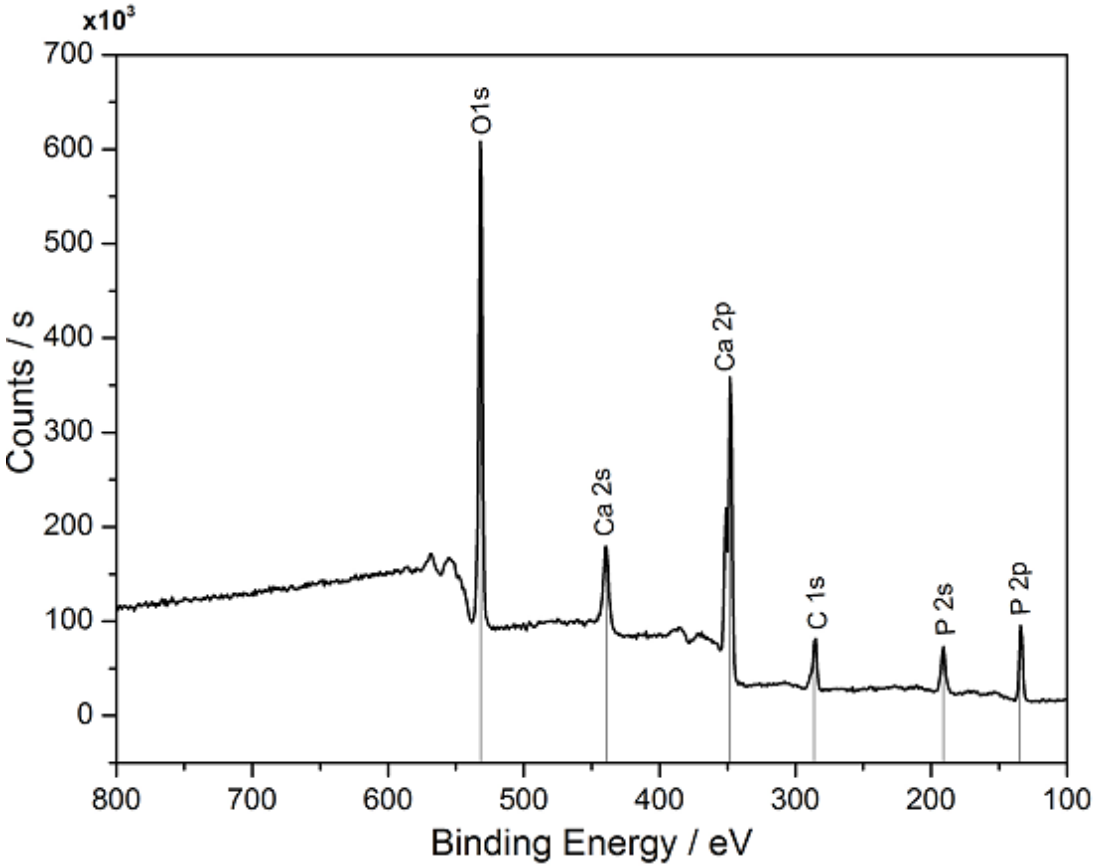

Figure 7-12 XPS survey spectrum of VPA-HA sample made via continuous plastic flow synthesis at 70 °C with a residence time of 5 minutes

Figure 7-13(c), depicts the core level XPS spectrum of O 1s and the peaks at 531.5.4, 532.1 eV and 533.6 eV are attributed to the hydroxy group, contribution of phosphate group and organic species, respectively. The peak at a binding energy of 288.5 eV in the C 1s spectrum was assigned to the $RCOO^-$ group (Casaletto et al., 2002) as shown in Figure 7-13 (d).

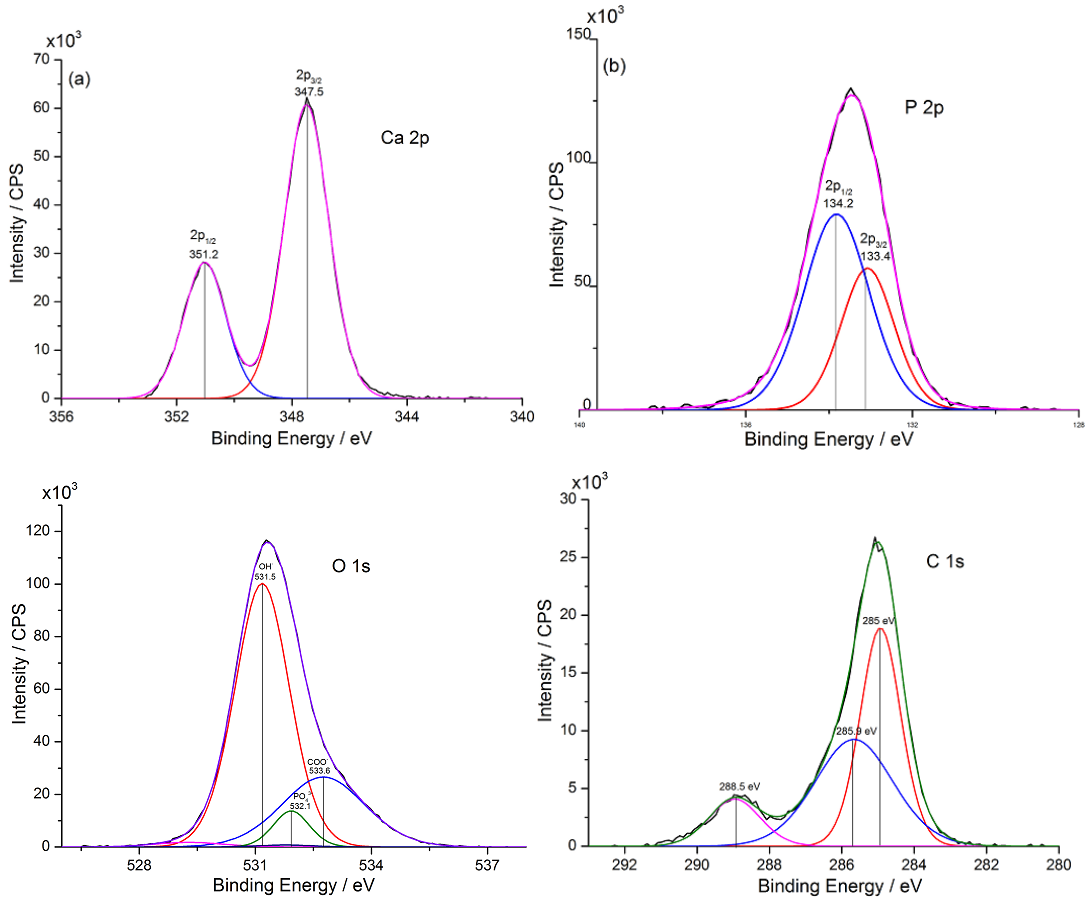

Figure 7-13 [a-d] XPS spectra of Ca 2p, P 2p, O 1s and C 1s for sample VPA-HA was made in a continuous plastic flow system at 70˚C with a residence time of 5 minutes

7.3.7 NMR Spectroscopy

The organic surface modifier molecules were investigated by NMR spectroscopy in solution, which required complete dissolution in a deuterated solvent. VPA dissolved very readily in D_2O and in d-methanol, d-concentrated sulfuric acid. However, only dilute solutions of VPA could be prepared in the solvents other than D_2O, therefore, the NMR data for VPA as dilute solution were recorded. The coupling interaction between different proton environments (doublet, triplet) in vinylphosphonic acid were evaluated as $2J(H_B, HA)$ = 21Hz, $3J(H_B, P)$ =44.8Hz, $3J(H_A, P)$ = 22.5 Hz, $3J(H_A, H_C)$ =19.1 Hz, $3J(H_B, H_C)$ =12.7 Hz, $2J(H_C, P)$ =19.1 Hz. The presence of different proton environments associated with the carbon atoms in VPA has proved that surface modification of VPA on HA has occurred.

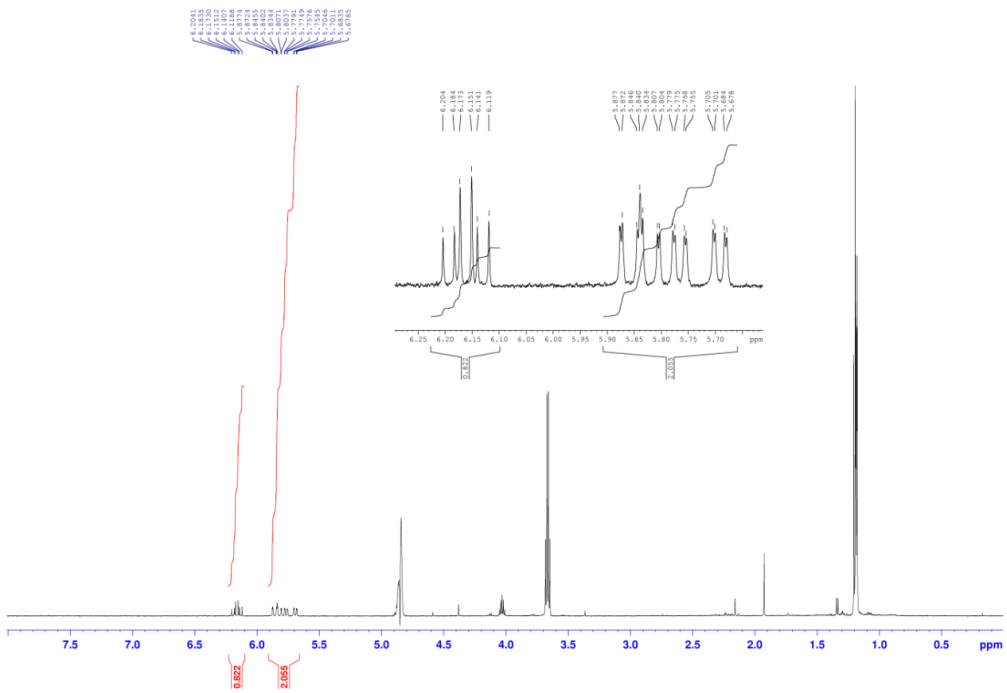

Figure 7-14 ^{1}H NMR spectrum of surface modified vinylphosphonic acid

Variables such as volume or mass fraction of inorganic fillers, particle size distribution, and nature and extend of bonding between resin matrix and filler particles have significant effect on chemical and mechanical properties of dental composites.

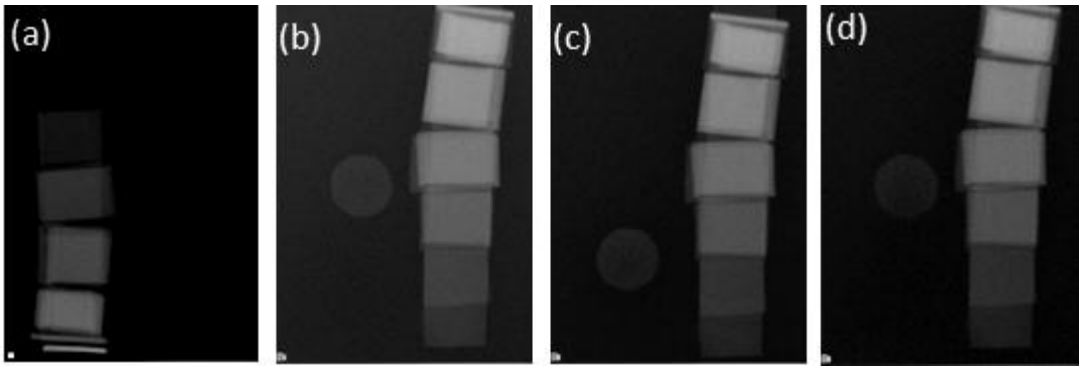

Figure 7-15 Radiographic images of (a) = commercially available dental composite (ICON), (b) = self- prepared dental composite with 20 wt% pure HA as a filler, (c) 20 wt% methacyrlic acid modified- HA based dental composite, (d) 20 wt% vinylphosphonic acid modified-HA based dental composite.

In the last decade, attention has been given to the dental composites with reduced size of the filler particles, from micrometric (traditional composites) to nanometric sizes (advanced composites). Nanometric particles have high surface area to volume ratio, and hence potentially a large interfacial area for interaction with the organic matrix. Stronger interaction between filler and matrix can be achieved by optimizing the amount of filler particles and/ or characteristics of the organic coupling agent.

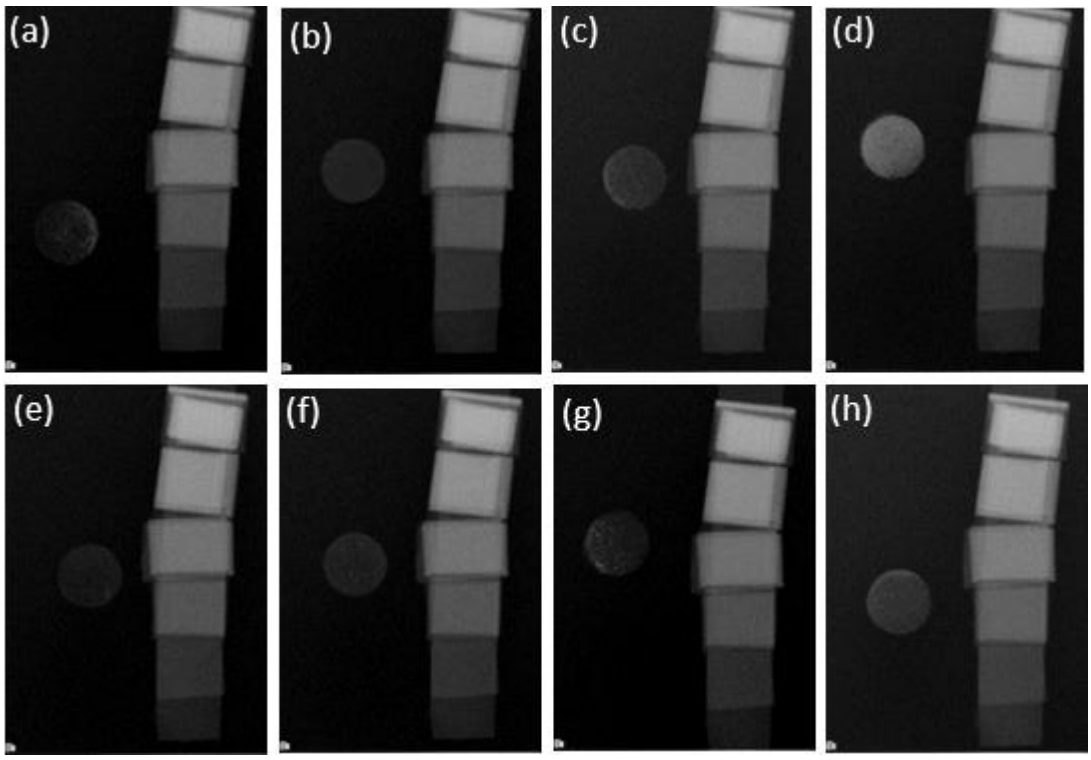

Figure 7-16 Radiographic images of surface functionalized strontium hydroxyapatite based dental composite with (a) = 5%, (b) = 10%, (c) = 15% and (d) = 20% and surface functionalized barium hydroxyapatite based dental composite with (e) = 5%, (f) = 10%, (g) = 15% and (h) = 20%, respectively.

A comparative study for radiographic examination of commercially available dental composite and self made dental composite with 20 wt% addition of ungrafted pure HA, methacrylic acid–HA and vinylphosphonic HA,respectively was carried out as shown in Figure 7-15. It was observed that self prepared dental nanocomposite with 20% loading of filler particles showed better radiopacity results as compared to a commercial sample.

A similar study was also carried out using different loadings of fillers (5, 10, 15 and 20%) of surface grafted strontium (a-d) and barium (e-h) hydroxyapatite as shown in Figure 7-16. The results indicated that surface functionalized strontium hydroxyapatite could be the better candidate for dental restorative materials because of its high radiopacity property.

7.4 Conclusions

The synthesis of surface modified HA for a range of surface modifiers was achieved in ca. 5 minutes in a continuous reaction at 70 °C. Surface modification with different carboxylic containing organic agents resulted in the production of nano-sized HA crystals which could be readily dispersed and possessed remarkably high surface areas. These fine, highly dispersed nanoparticles contain reactive groups on the surface; therefore they have great range of potential dental / biomedical applications.

The synthesis of surface modified HAs for a range of surface modifiers was achieved in *ca.* 5 minutes using a continuous flow reaction at 70 °C. Surface modification with different carboxylic containing organic agents resulted in the production of nano-sized HA crystals which could be readily dispersed and possessed remarkably high surface areas (> 250 m^2g^{-1}).

It was observed that surface modified VPA-HA (vinylphosphonic acid) and MA-HA (methacrylic acid synthesized at the same conditions as pure HA possessed a surface area of 254, 247, 210 m^2g^{-1} and 265, 244 and 221 m^2g^{-1}, respectively at reaction temperature of 60, 70 and 80 °C. This fact is attributed to the growth restriction of HA nanoparticle in the presence of surface modified agents and smooth increase in surface area at various selected temperatures.

It is concluded that these fine, highly dispersed nanoparticles (specifically Sr-HA) could be used as filler component to develop a novel radiopaque resin infiltrants for dental applications. As radiopaque dental materials are beneficial in making diagnosis and monitoring existing restoration. More research is needed to further improve the interaction of nanosized HA particles with the polymeric matrix, that allows to increase the total loading of the inorganic filler and, hence, to improve the mechanical properties.

7.5 Future Work

Surface functionalized Group 2 metal phosphates will be exploited as a component of a drug delivery system for the controlled release of a therapeutic agent or as an additive for a tooth paste.

It would be interesting to employ these newly formed nanoparticles as an injectable materials for bone repair, such as spinal fusion or other formulation in future application.

Furthermore, these surface functionalized high surface area Group 2 metal (Ca^{2+}, Sr^{2+}, Ba^{2+}) phosphates will be utilized to make porous scaffolds by freeze casting process by the addition of polyvinyl alcohol (PVA) as a binder and emulsifying agent. The purpose of study is to enhance the mechanical strength of HA for applications in bone tissue engineering.

Chapter 8

Continuous Plastic Flow Synthesis and In-Vitro Cytotoxicity Analysis of Hydroxyapatite-Titania and Hydroxyapatite-Magnetite Nanocomposites

8.1 Introduction

Increasing demands for smarter and smaller products call for the development of multiphase and multifunctional materials. Significant progress in ‘‘nanochemistry” has given birth to a newly emerging area called ‘‘nanohybrid” or ‘‘nanocomposite” materials, which results from the tuning of molecular level interactions of dissimilar inorganic components to form new, unique functional materials with improved properties (Loste et al., 2004).

Despite a large number of applications of hydroxyapatite (HA) ceramics in orthopedics and dental implantation it has some inherent mechanical drawbacks. These include the poor tensile strength and high brittleness that undermine its use as a safe, stable and durable in vivo implantation material (Loste et al., 2004, Kuo and Yen, 2002). One of the strategies proposed to tackle these intrinsic issues of HA is to increase the relative density of HA ceramics by making its composite with some metal/metal oxide (Webster et al., 2000).

Besides HA, many other implants usually metallic/metallic oxides have been widely employed in the body parts where load bearing properties of the implants are more significantly required like hip prostheses and dental implants. The excellent mechanical and corrosion-resistant properties and especially the cheaper availability and high biocompatibility of titanium/TiO_2 have made it a success in surgical implantations (Pushpakanth et al., 2008, Laing et al., 1967, Albrektsson et al., 1983). The major technical issue with the use of titanium and TiO_2 as bone implant is the bio-inertness of the oxide, which does not appreciably form an interface with surrounding bony tissue. Apart from its failure to form an active interface, titanium being much more stiff and hard than the surrounding bone tissue can result in the overall failure of the implant (Hayashi et al., 1991). So there is a strong need to resolve such issues with both HA

ceramics and titanium based implants.

On the other hand TiO_2 is a well-established photocatalytic and antimicrobial material used for the degradation of organic molecules and growth inhibition of bacteria (Nishikawa, 2003, Sunada et al., 2003). Therefore, the HA-TiO_2 composite materials may be expected to combat bacteria and toxic organic materials (Fu et al., 2005, Nonami et al., 1998, Wu and Nancollas, 1998) and possess high fracture toughness and excellent biocompatibility (Li et al., 2002).

The mechanical properties of hydroxyapatite can be enhanced by the addition of oxide phases particularly titania, alumina, zirconia, etc. (Prabakaran et al., 2005). These oxide materials are promising candidates for reinforcement due to their unique properties and low cost however, only a few research studies have been reported in this area (Lu and Yang, 2005, Teo et al., 2003).

Magnetic nanoparticles have drawn much attention due to their ability to generate heat in high frequency alternating magnetic field in hyperthermia. Many reports regarding the use of these particles in hyperthermia have been published (Wu et al., 2007, Ma et al., 2004, Konishi et al., 2004). Although these magnetic particles are biocompatible with the human body and target-directive, they have long-term toxic effects so mixing of a suitable bioactive substrate is desirable. In particular, magnetite incorporated HA nanocomposites are a most effective solution for hyperthermia therapy of malignant bone tumor (Johannsen et al., 2005, Tampieri et al., 2012, Gloria et al., 2013, Murakami et al., 2008, Andronescu et al., 2010) In recent studies, these nanocomposite materials have also been employed as adsorbents (Dong et al., 2010, Wang, 2011, Hongqin et al., 2012) and catalysts (Yang et al., 2010, Liu et al., 2010).

The conventional procedures (Murakami et al., 2008, Andronescu et al., 2010, Covaliu et al., 2009, Yang et al., 2010) for the synthesis of HA-Magnetite nanocomposites have drawbacks as long reaction time is required for completing the formation of HA and magnetite followed by subsequent heat treatment and aging. Thus, the literature syntheses of HA-Magnetite nanocomposites generally involve multi-step procedures. Therefore, a simple process is required to be developed for the rapid formation of these bioactive nanocomposites.

In this chapter, a range of HA-Titania and HA-Magnetite nanoparticles was fabricated using a facile one-pot continuous plastic flow synthetic route. The characterization and biocompatibility of these newly developed nanocomposites were evaluated using various optical and analytical techniques.

8.2 Experimental

8.2.1 Synthesis of Titania

Titania samples were made using a CPFS system, the details of which are described in section 2.2.1. In the synthesis process, 0.25 M titanium oxysulfate solution and 0.20 M basic solution of potassium hydroxide, were pumped to meet at a T-piece. The pH of both the solutions prior to the reaction was kept above pH 10. This initial mixture were connected to 8 m long PTFE tubing which was coiled inside an oil bath which gave an effective 5 minutes from the tee to the exit of the pipe. The suspension was collected in a beaker at the exit point and then centrifuged as described in section 2.3.1.1.

8.2.1.1 Synthesis of Hydroxyapatite-Titania Nanocomposite

The hydroxyapatites nanoparticles were obtained following a similar procedure as described in section 2.3.1.1. A range of HA-Titania nanocomposites were made using a CPFS system, the details of which are described in section 2.2.1. In the synthesis process, titania solution and basic solutions of calcium nitrate with diammonium hydrogen phosphate, were pumped to meet at a T-piece. The pH of both the solutions prior to the reaction was kept above pH 10. This initial mixture was connected to 8 m long 1/16 in. PTFE tubing, which was coiled inside an oil bath, which gave an effective 5 minutes residence time from the tee to the exit of the pipe. All reactions were carried out at 70 °C and atmospheric pressure. The suspension was collected in a beaker at the exit point and then centrifuged at 4500 rpm for 10 minutes. The obtained white precipitates were centrifuged and freeze dried as described previously (section 2.3.1.1).

The obtained powder was compacted into cylindrical discs of 13mm diameter and 2 mm thickness by using a laboratory hydraulic press at 5 MPa. These samples were used for cell viability studies after sterilization in 70 % ethanol for 1 hour.

8.2.2 Synthesis of Magnetite

Magnetite nanoparticles were rapidly synthesised using continuous plastic flow synthesis at 70 °C in 5 minutes residence time at the conditions of pH 10. In this process, 20.2g Iron nitrate and 11.52 g citric acid, were pumped to meet at a ‘‘Tee’’ piece mixer. This initial mixture was connected to 8 meter plastic tubing surrounded by heating jacket whereupon reaction was completed in 5 minutes, which is the residence time for the reaction. The suspension was collected in a beaker at the exit point. The dark brown precipitates of magnetite were centrifuged and dried by using freeze drier (as described in section 2.3.1.1).

8.2.2.1 Synthesis of Hydroxyapatite-Magnetite Nanocomposite

Hydroxyapatite nanoparticles were prepared using a similar method as described in section 2.3.1.1. HA-Magnetite composites were made by passing HA and magnetite samples through CPFS system. The initial mixture was connected to 8 meter plastic tubing surrounded by a heating jacket whereupon reaction was completed in 5 minutes, which is the residence time for the reaction. All reactions were carried out at 70 °C and atmospheric pressure. The suspension was collected in a beaker at the exit point and then centrifuged at 4500 rpm for 10 minutes. The obtained brown precipitates were centrifuged and freeze dried as described previously (section 2.3.1.1).

8.3 Results and Discussions

8.3.1 Powder X-ray Diffraction

Figure 8.1 shows the XRD patterns of sample with different compositions of HA-TiO_2 nanocomposites annealed at 600 °C for 1 h. All the samples, irrespective of TiO_2 composition, show well-defined peaks indicating the good crystallinity of these samples. All the diffraction peaks could be readily indexed with the pure hexagonal phase, which is in accordance with the bulk HA crystals (JCPDS card # 09-0432).

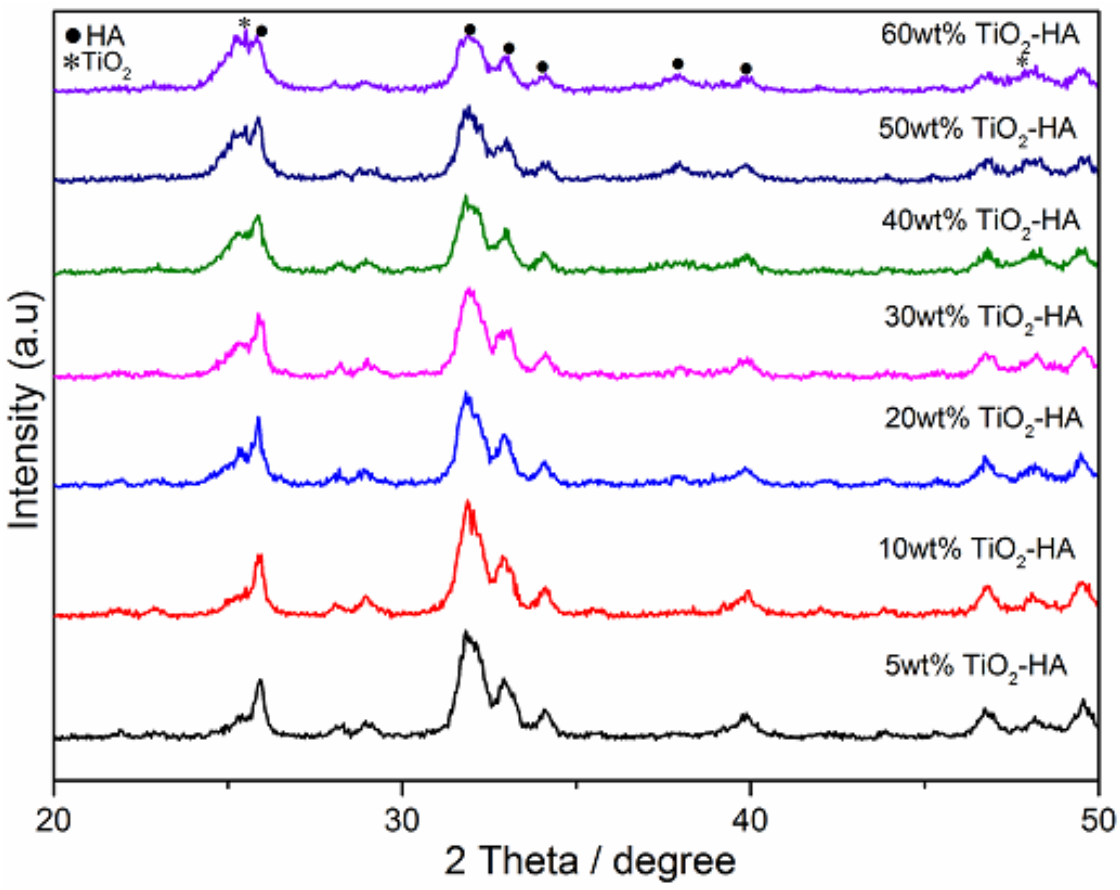

Figure 8-1 X-Ray diffraction analysis of TiO_2-HA composites made at 70 °C in 5 minutes (residence time) at the conditions of pH 10-11using CPFS reactor

The XRD pattern of HA-Magnetite nanopowder showed good correlation with stoichiometric hydroxyapatite (JCPDS 09-0432 card), with a small shifting in angles, probably due to increase in magnetite content. The magnetite peaks at 35.43^o and 43.05^o was observed in 25 and 30 mass % magnetite-HA samples as shown in Figure 8.2.

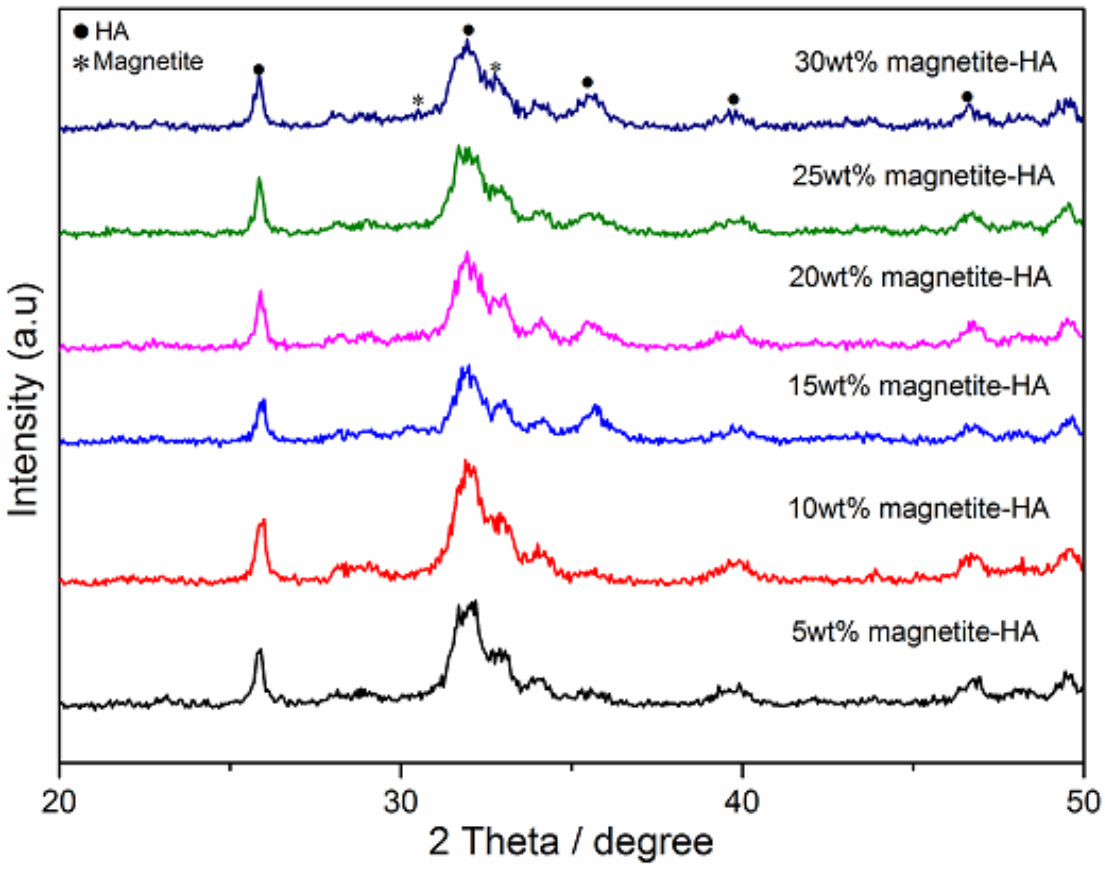

Figure 8-2 X-Ray diffraction analysis of Magnetite-HA nanocomposites made at 70 °C in 5 minutes (residence time) at the conditions of pH 10-11using CPFS reactor

8.3.2 Transmission Electron Microscopy

Transmission electron microscope images of Titania-HA composite as shown in Figure 8.3 confirmed the synthesis of small sphere like structures of Titania on the surface of HA rods.

The average length along the longest axis of rod shaped HA particle was *ca.* 85 ± 15 nm (200 particles sampled) with the titania particles of *ca.* 7nm ± 1.5 nm on the surface having sphere-like morphology. Transmission electron microscope images of 40 and 60 mass % HA-TiO_2 nanocomposite as shown in Figure 8.3 confirmed the synthesis of small sphere like structures of Titania on the surface of HA rods.

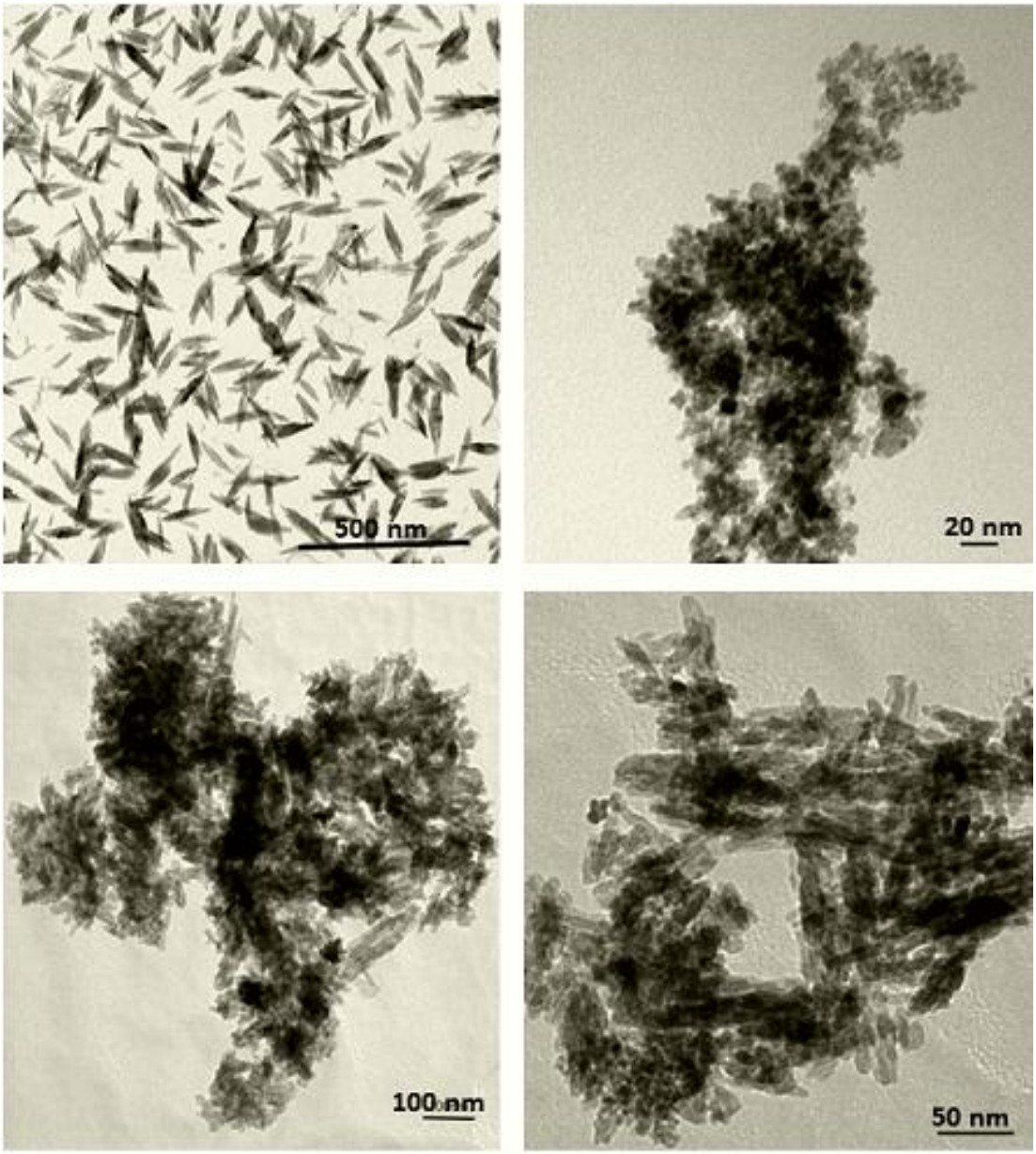

Figure 8-3 Transmission electron microscope images of pure hydroxyapatite nano-rods of sample HA60 (a),(bar = 200 nm), (b), (bar = 20 nm), (c), (bar = 50 nm) and (d), (bar = 100 nm).

TEM images of as precipitated magnetite samples with 1 M precursor concentration revealed moderate agglomeration. Figure 8.4 revealed the average particle size (total particles counted = 250) of 8 nm ±1.8 nm for pure magnetite as shown in Figure 8.4(c) while average particle size of 85 nm ± 15 nm was observed by pure HA samples [Figure 8.4(a) and (b)] made at 70 °C in five minutes residence time via CPFS. In Magnetite-

HA composite, sphere like magnetite structures on the surface of HA rods has been observed as shown in Figure 8.4(d).

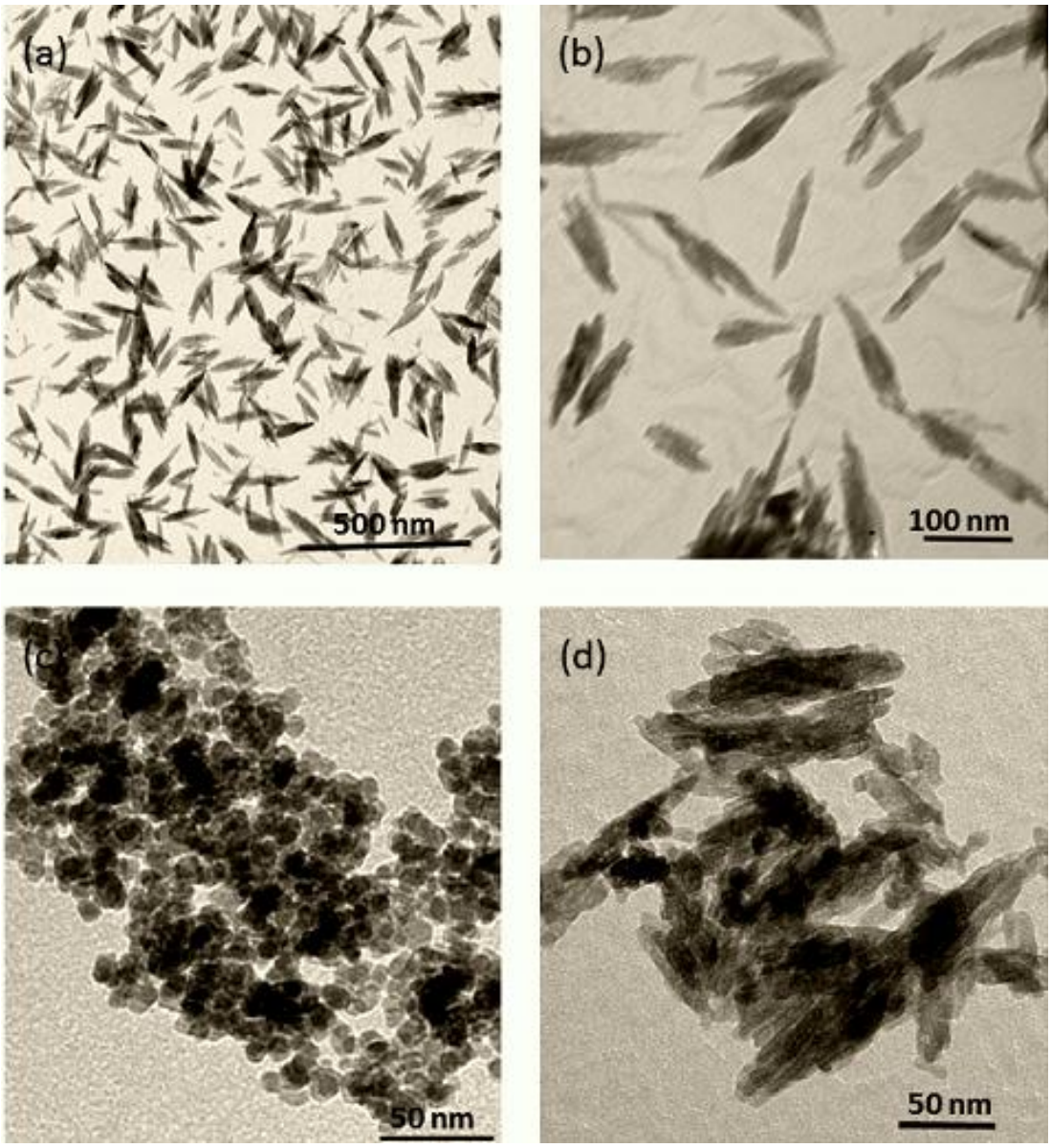

Figure 8-4 Transmission electron microscope images of pure hydroxyapatite nano-rods (a),(bar = 500 nm), (b), (bar = 100 nm), pure magnetite (c), (bar = 50 nm) and magnetite-HA composite with 30 wt% magnetite with the bar scale of ((d) =50nm

8.3.2 BET Surface Area Analysis

BET surface area analysis for the HA-TiO_2 composites revealed surface areas in the range of 147.6 m^2g^{-1} to 209.1 m^2g^{-1} on increasing the concentration of TiO_2 from 5 wt% to 60 wt % as shown in Figure 8-5.

The "as precipitated" amorphous HA-Magnetite samples made at 70°C temperature had a surface area range from 121.4 m^2g^{-1} to 142.3 m^2g^{-1} for the samples from 5 wt% to 30 wt% respectively as shown in Figure 8-6.

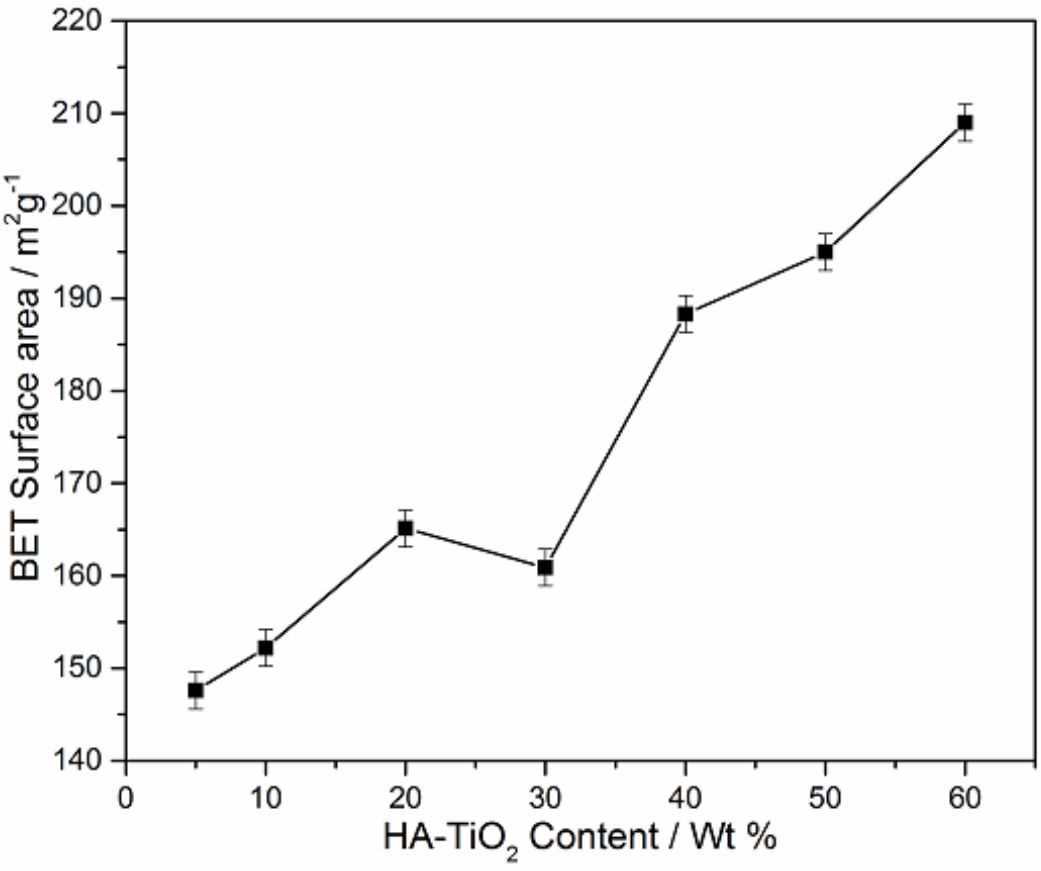

Figure 8-5 BET surface area of as precipitated HA-TiO_2 nanocomposites made at 70 °C in 5 minutes residence time via CPFS. The data points from left to right corresponded to samples 5wt% HA-TiO_2, 10wt% HA-TiO_2, 20wt% HA-TiO_2, 40wt% HA-TiO_2, 50wt% HA-TiO_2, 60wt% HA-TiO_2, respectively.

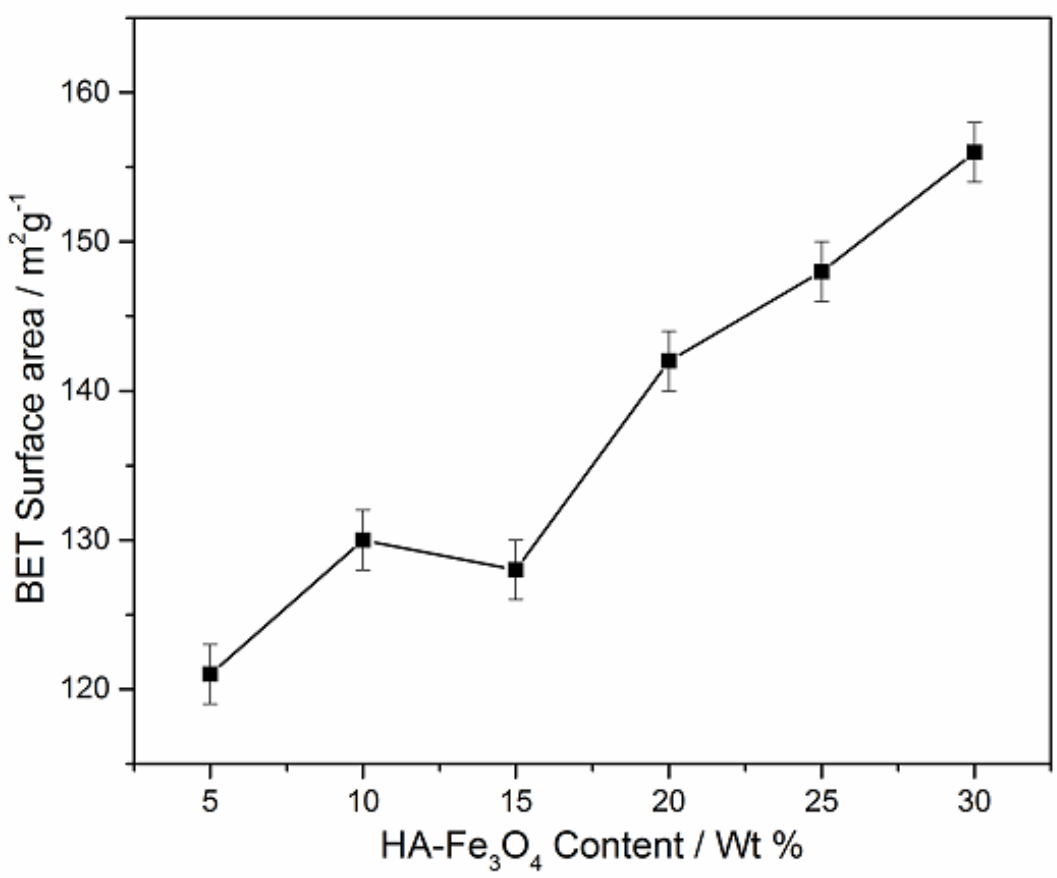

Figure 8-6 BET surface area of as precipitated HA-TiO_2 nanocomposites made at 70 °C in 5 minutes residence time via CPFS. The data points from left to right corresponded to samples 5wt% HA- Fe_3O_4, 10wt% HA- Fe_3O_4, 15wt% HA-Fe_3O_4, 20wt% HA- Fe_3O_4, 25wt% HA- Fe_3O_4, 30wt% HA- Fe_3O_4, respectively.

8.3.3 Zeta Potential Measurements

Zeta potential measurements were performed in order to investigate the colloidal stability related to surface charge of the nanocomposites. The greater the electrostatic repulsion, the higher the zeta potential values and therefore higher will be the colloidal stability of the suspension. Zeta potentials of -11.4, -19.6, -22.7 and -23.6 mV were obtained for 20, 30, 40 and 50 wt% HA-Titania composites, respectively, which indicates the high negative surface charge. The higher surface charge evident from the high zeta potential value, which protects the particle agglomeration resulting in a more stable dispersion.

8.3.4 X-ray Photoelectron Spectroscopy

X-ray photoelectron spectroscopy experiments were performed to investigate the concentration of the titania in the lattice, their oxidation state and the effect on the structure. Generally the survey spectra for all samples exhibited strong peaks for titanium, oxygen, phosphorous and calcium as shown in Figure 8-7. The peaks at 134 eV corresponded to P 2p spectra of hydroxyapatite. While the binding energy values for O 1s and Ca 2p were measured as 532 and 347 eV, respectively.

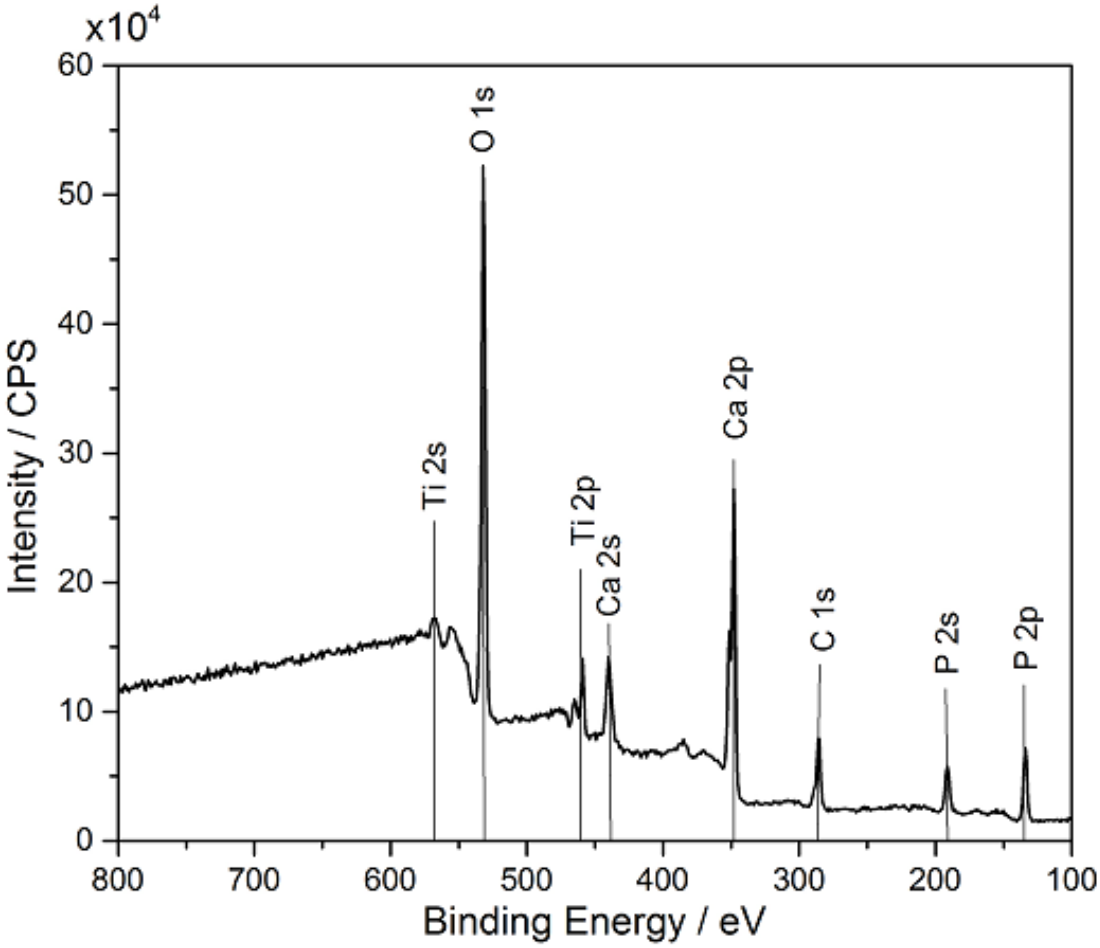

Figure 8-7 XPS survey spectrum of of 20HA-TiO_2 nanocomposite made via continuous plastic flow synthesis in 5 minutes residence time at 70 °C

The Ca 2p spectrum could be resolved into two peaks for Ca $2p_{3/2}$ and $2p_{1/2}$ (two spin-orbit pairs) at 347.4 and 351.3 eV, respectively, which are related to hydroxyapatite. In Figure 8-8(b), the 2p peak can also be deconvoluted into two peaks with a spin orbit

splitting for $p_{1/2}$ and $p_{3/2}$ levels with binding energies of 134.2 and 133.4 eV, respectively. Figure8-8(c), depicts the core level spectrum of O 1s peak, which showed that multiple O species were present on the surface. The sub-peak at the binding energy of 529.7 eV, could be assigned to O^{2-} in TiO_2, whilst the sub-peak at the binding energy of 531.5 eV corresponds to the contribution of surface O-H / adsorbed water in the apatite (Mahabole et al., 2005, Lu et al., 2000, Zhang et al., 1998).

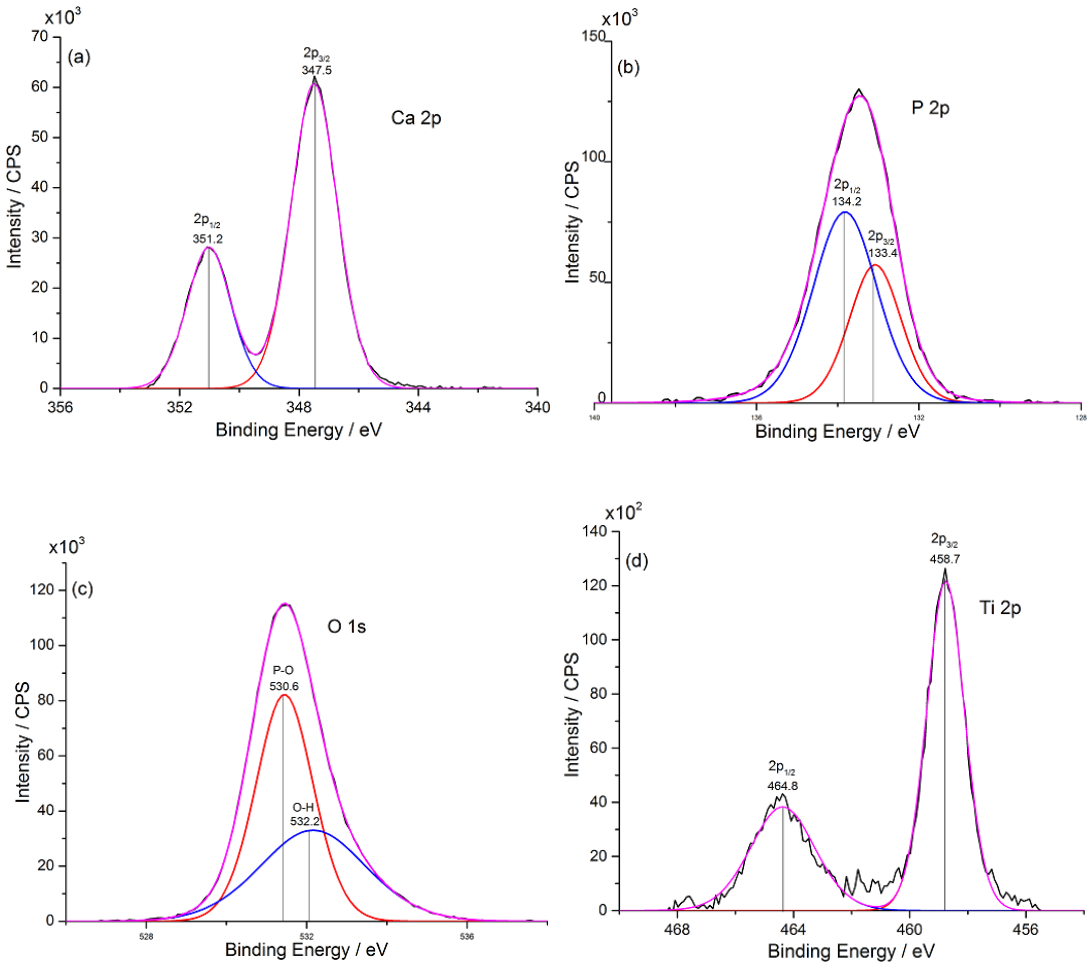

Figure 8-8[a-d] XPS Spectra of Ca 2p,O 1s and P 2p recorded from 20 HA-TiO_2 sample made at 70 °C in 5 minutes residence time via CPFS

In Figure 8-8(d) the Ti 2p spectrum could be resolved into two spin-orbit pairs 2p3/2 and 2p1/2 with binding energies of 458.7 and 464.8 eV, respectively, which are

characteristic of titanium in TiO_2.. The x-ray photoelectron spectroscopy results confirm the formation of HA-TiO_2 nanocomposite and also indicate that the HA-TiO_2 nanocomposite is stable under reaction conditions.

Chemical analysis of 20HA-Magnetite was conducted using XPS as shown in Figure 8-9. The peaks at 134 eV corresponded to P 2p spectra of hydroxyapatite. While the binding energy values for O 1s and Ca 2p and Fe 2p were measured as 532 and 347 and 712 eV, respectively.

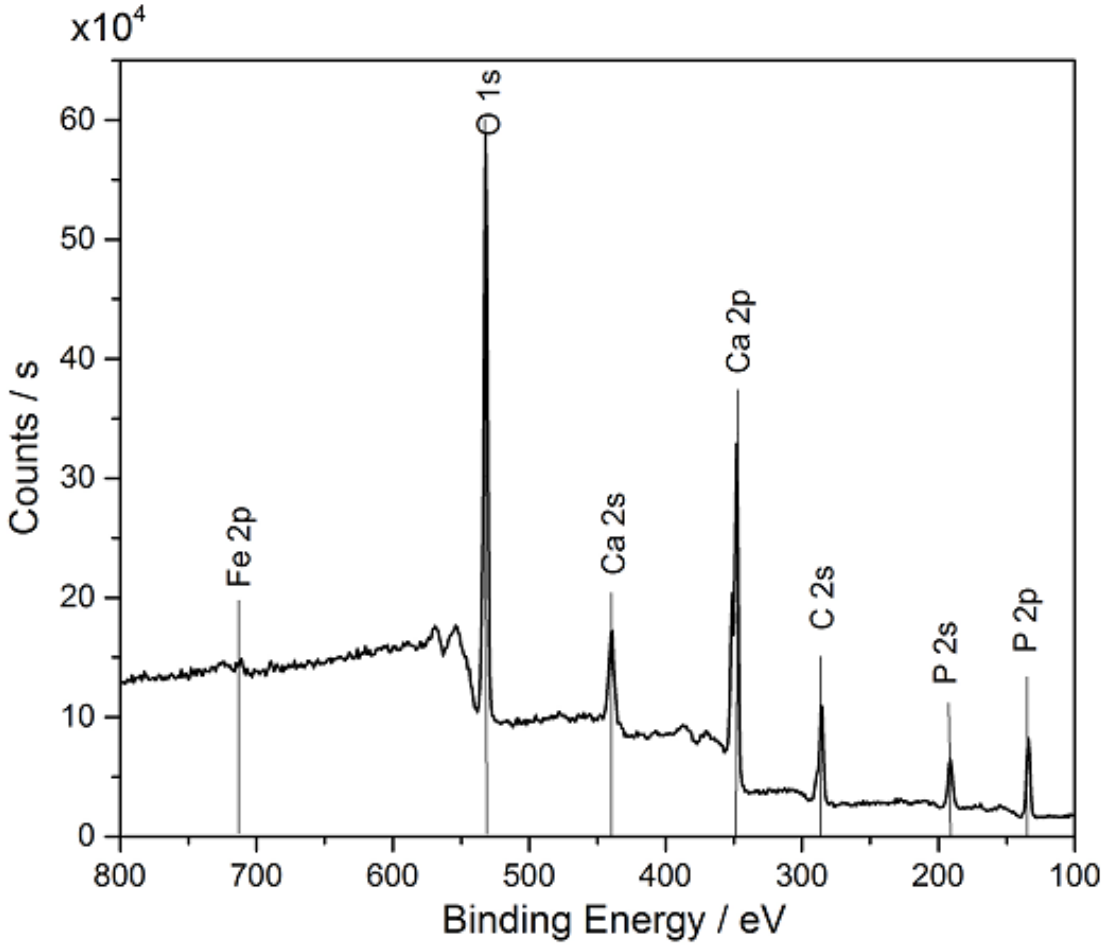

Figure 8-9 XPS survey spectrum of of 10wt% HA-Magnetite nanocomposite made via continuous plastic flow synthesis in 5 minutes residence time at 70 °C

8.3.5 Fourier Transform Infrared Spectroscopy

The saturated peak of TiO_2 below 700 cm^{-1} is assigned to Ti–O and Ti–O–Ti bonding of titania. The small peak at 3600 cm^{-1} is attributed to stretching of –OH groups in the

powder. The peaks at 600, 952, 1033 cm^{-1} are attributed to PO_4^{3-}. The intensity of –OH– absorption peaks at 358 and 627 cm^{-1} decreases in the nanocomposites with increasing titania concentration. The stretching vibration bands of PO_4 labeled at 958 and 1031 cm^{-1} are observed in all the samples. The peaks labeled at 569 and 600 cm^{-1} indicate the bending mode of PO_4^{3-}. The peak around 1400 cm^{-1} is attributed to CO_3^{2-}.

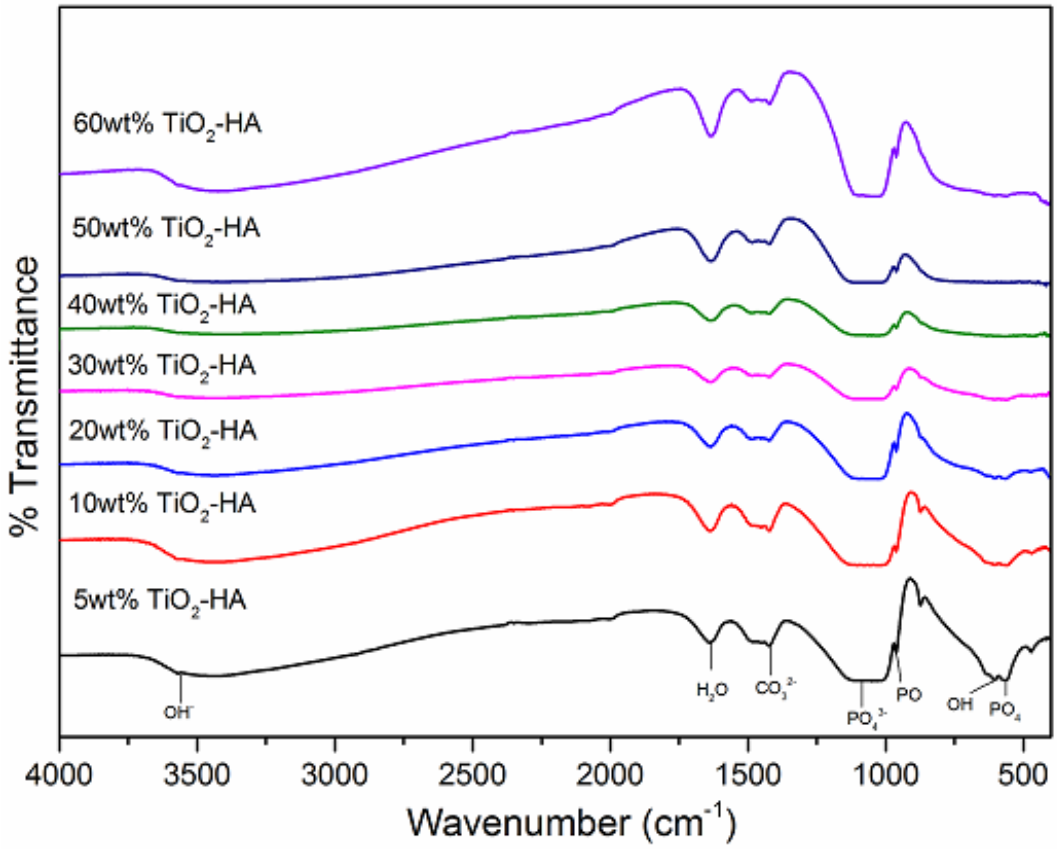

Figure 8-10 FTIR analysis of HA-TiO_2 nanocomposites made at 70 °C in 5 minutes residence time via CPFS

The intensity of –OH– absorption peaks at 358 and 627 cm^{-1} decreases in the nanocomposites with increasing titania concentration. The peaks at 569 and 600 cm^{-1} indicate the bending mode PO_4^{3-}. While peak around 1400 cm^{-1} is observed for CO_3^{2-} as shown in Figure 8-11.

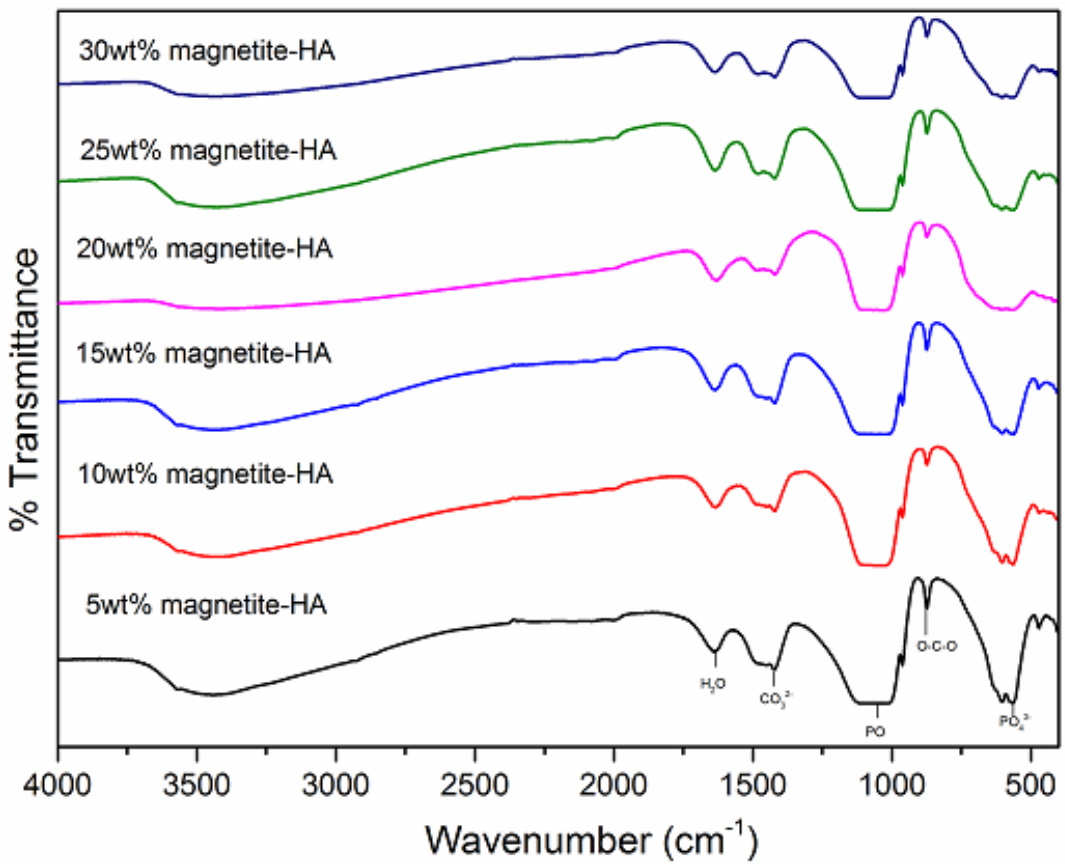

Figure 8-11 FTIR analysis of magnetite-HA nanocomposites made at 70 °C in 5 minutes residence time via CPFS

8.3.6 Raman Spectroscopy

Raman spectroscopy was conducted in order to supplement crystallographic data and detect substitutions in the apatite lattice. The peak at 965cm^{-1} corresponded to a symmetric stretching mode of the P-O bond in phosphate. Peaks at 610 and 483 cm^{-1} are likely corresponded to the bending mode of the O-P-O linkage in phosphate as in Figure 8-12.

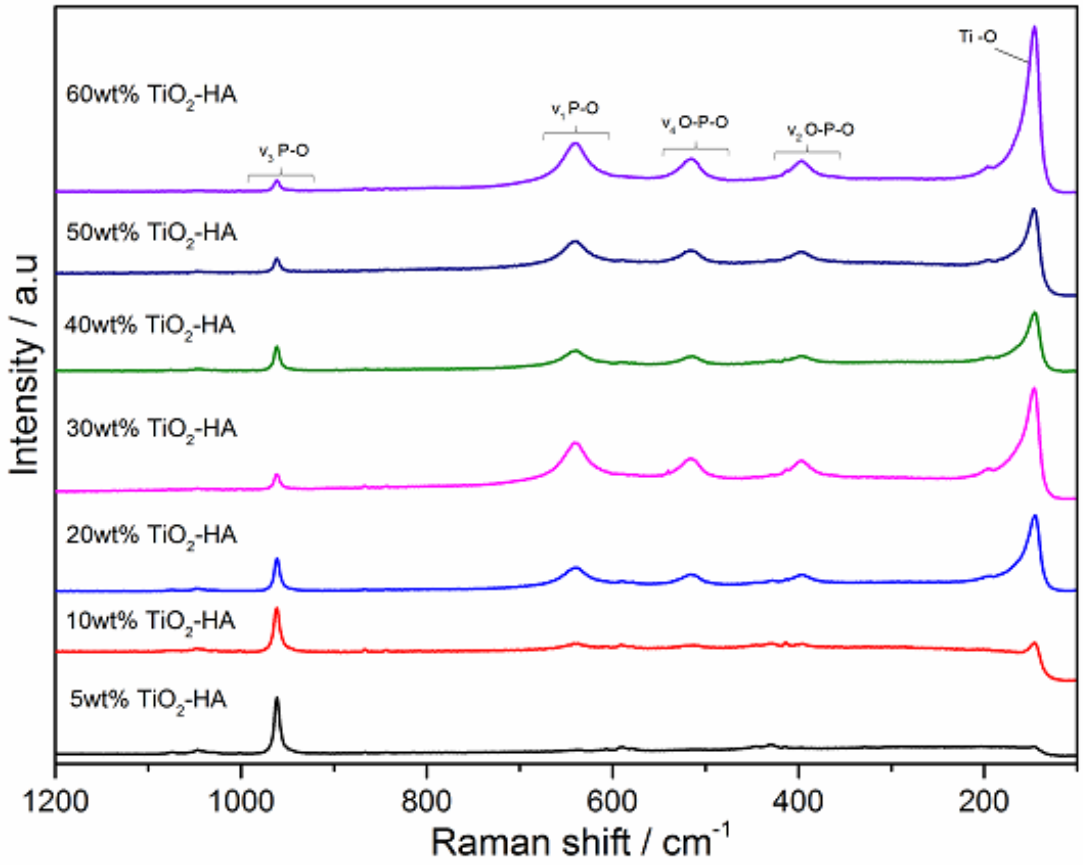

Figure 8-12 Raman Spectra of TiO_2-HA nanocomposites made at 70 °C in 5 minutes residence time via CPFS

8.3.7 Cell Viability Study

Human osteoblast cells (MG63) were cultured on pure HA and HA-TiO_2 composite disks and cell viability was studied over the course of 7 days as shown in Figure 8-13. The pure HA sample was used as a control. The osteoblasts cultivated on all ceramic samples showed continuous proliferation. At day 1, cell viability was almost similar on pure HA and 20HA-TiO_2 disks indicating that initial cell attachment was not enhanced by these surfaces, while slightly increased in 10HA-TiO_2 and 40HA-TiO_2. At day 4, cell viability increased on all sample, when compared with day 1. A similar trend was observed at day 7, however, all samples had an increased cell viability compared with day 1 and 4. At both days 4 and 7, pure HA and 40HA-TiO_2 had significantly higher cell viability than both 10HA-TiO_2 and 20HA-TiO_2, while 40HA-TiO_2 had significantly higher cell viability than pure HA. These results indicate that newly developed CPFS HA were biocompatible and supported osteoblast attachment and proliferation.

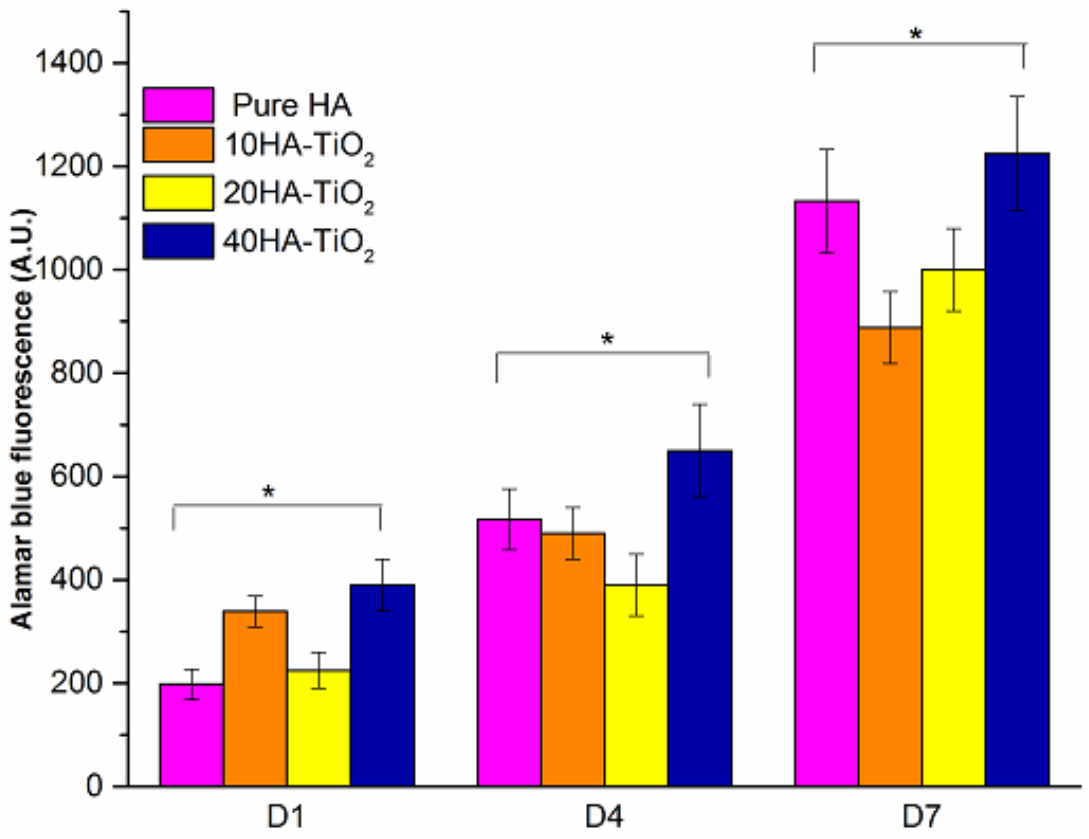

Figure 8-13 MG63 viability on pure HA and HA-TiO_2 discs. Cell viability was measured at days 1, 4 and 7 via Alamar blue assay for MG63s cultured on pure HA, 10HA-TiO_2, 20HA-TiO_2 and 40HA-TiO_2 (Mean ± SD, n = 6). * $p < 0.05$.

8.3.8 Cell Morphology

MG63 morphology was observed at day 7 (Figure 8-14) on each HA type. The cell proliferation results showed that there was a continuous growth of cells on all experimental samples. Cells were evenly distributed on pure HA and showed a typical square-like osteoblast morphology. MG63s were also evenly spread across the surface of the sample and showed an osteoblastic morphology. The cell cytoskeleton also appeared more elongated in pure HA sample than composites and the cells appeared to form cell-cell bridges. On 10HA-TiO_2, cells were more sparce and generally less-well spread than those on pure HA, with the majority showing a rounded morphology. MG63s on 20HA-TiO_2 and 40HA-TiO_2 were also generally quite rounded and formed clusters. Cell toxicity analyses confirm the biocompatiblity of this material.

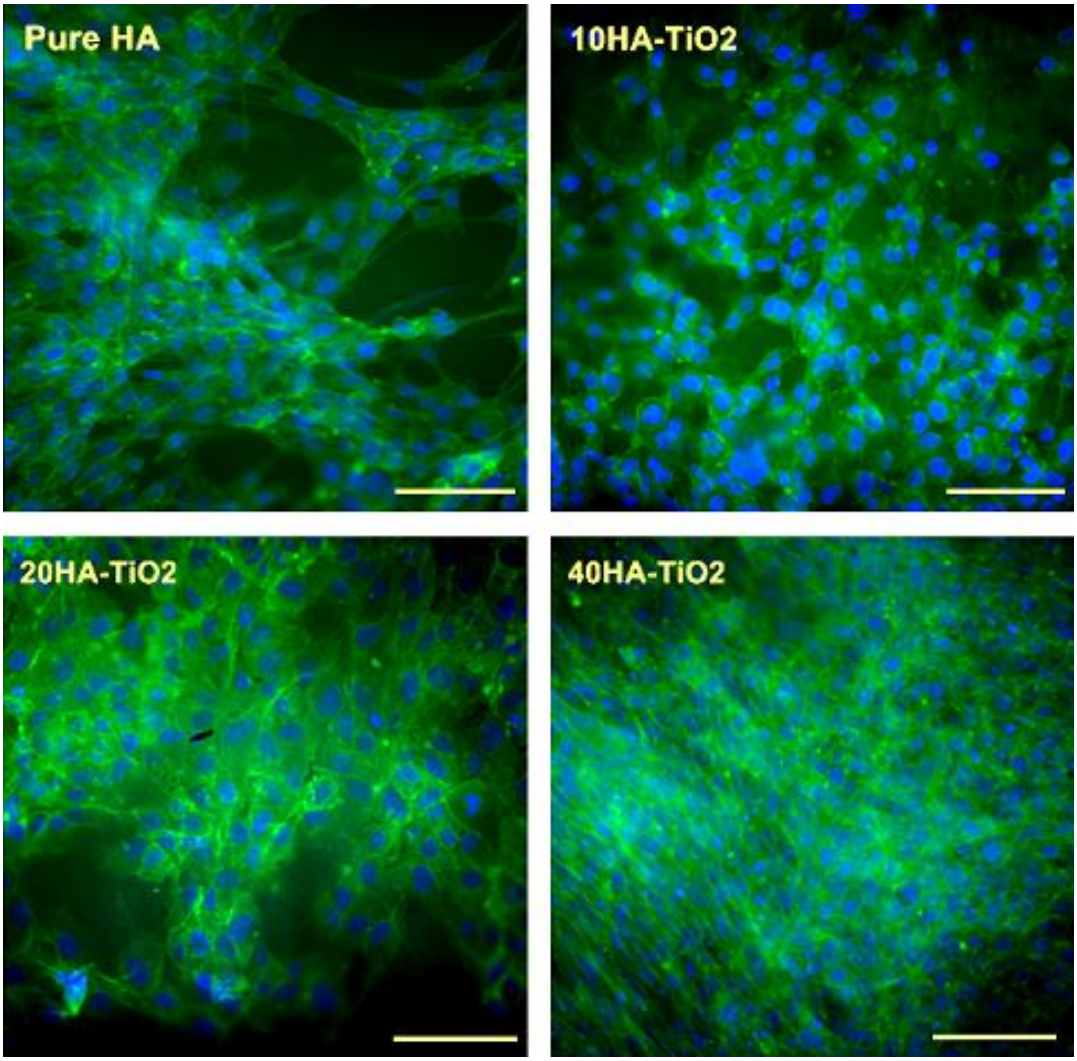

Figure 8-14 MG63 morphology on pure HA and HA-TiO_2 discs. Cells were visualized at day 7 for cell nucleus (DAPI in blue) and cytoskeleton (phalloidin-FITC in green) for MG63s cultured on pure HA, 10HA-TiO_2, 20HA-TiO_2 and 40HA-TiO_2. Scale bar is 100 µm.

8.4 Conclusions

In summary, Continuous Plastic Flow Synthesis (CPFS) reactor parameters were successful in synthesizing stoichiometric phase pure HA, Ion substituted calcium phosphates and nanocomposite materials for biomedical applications. The results have proved the versatility and rapidity of this particulate synthesis technology for the production of variety of nanobioceramics and other biomaterials. Hence the current work deals with the preparation of synthetic calcium phosphates with optimum properties closer to those of living hard tissues like bone and teeth, aiming at better and

more effective biomedical ceramics for use as powders or as nanocomposites in future efforts.

It was observed cell adhesion on 40HA-TiO_2 nanocomposite (highest surface area) was substantially greater than the control and low wt% HA-TiO_2 nanocomposite. So these results indicate that high surface area nanosized HA-TiO_2 nanocomposites have potential to be used in biomedical applications.

8.5 Future Work

It would be desirable to upgrade the CPFS systems to synthesize more quantity of aforementioned bioceramics and mixtures. Higher concentrations of calcium and phosphate source solutions or increased flow rate can also help to achieve this. Importantly, by using a flow system the work is readily scalable and thus has promise for scale-up.

Nano-sized HA composites can improve the sintering kinetics and subsequently improve mechanical properties, because of its higher surface area. As a consequence, large efforts would be focused on the synthesis of nano-sized, high surface area HA nanocomposites in future applications.

The combination of magnetic nanoparticles with the biocompatible hydroxyapatite suggests this composite material has potential to be used as drug delivery in future endeavor.

The novel simplified CPFS reactor system at near ambient reaction conditions (70 °C, atmospheric pressure) can be applied in future to synthesize a variety of apatite based nanocomposite materials on large scale for various biomedical applications where bone regeneration /replacement is required.

Chapter 9
Conclusions

A two-pump CPFS system was found to be suitable for the synthesis of group 2 metal phosphates. Different precursor solutions to provide the calcium (calcium nitrate, calcium hydroxide) and phosphate sources (diammonium hydrogen phosphate, orthophosphoric acid) were used in this synthesis. Both reagent solutions were pumped to meet at a T-piece mixer, which further connected to an 8 metre long plastic tubing coiled inside an oil bath, allowing the reaction to reach completion. A variety of phase-pure calcium (CaHA, CDHA, TCP, DCPD), barium and strontium phosphates were successfully synthesised using the novel CPFS reactor system at near ambient conditions (room temperature to 80 °C, atmospheric pressure). The Ca:P ratio, reaction pH and temperature were shown to play an important role in the formation of different phase-pure metal phosphates.

Based on these promising results, the synthesis of variety of biologically beneficial cations (Mg^{2+}, Sr^{2+}, Ba^{2+}) were addressed. Careful control of the quantities of the reactants used resulted in phase-pure nano-sized HA rods, biphasic mixture of HA and pure Mg-whitlockite. Cell toxicity analysis showed excellent biocompatiblity of these materials. An increase in magnesium content above 3% led to precipitation of a biphasic mixture of magnesium-substituted hydroxyapatite. Strontium- and barium-substituted calcium hydroxyapatite had great potential for use in dental nanocomposites because of radiopacity properties. It was observed that 100% substitution of strontium for calcium in the hydroxyapatite structure has the highest level of radiopacity as compared to 5, 20 and 50% substitution. Similarly, carbonate and silicate ions (CO_3^{2-}, SiO_4^{4-}) were also substituted into calcium phosphates. Carbonate substitution up to ~ 8 wt% was achieved successfully. However, high substitution level in silicon was difficult to achieve due to the low dissolution rate of silicon acetate. A maximum silicon content of ~ 0.8 wt% was attained.

In addition to ionic substitution, surface modification with different carboxylic containing organic agents (polyvinyl alcohol, adipic acid, citric acid, vinylphosphonic acid, and methacrylic acid) resulted in the production of nano-sized calcium phosphate

crystals which could be readily dispersed and possessed remarkably high surface areas. If the surface-functionalised bioceramics are heat-treated, they normally form non-stoichiometric calcium phosphates depending on the conditions. This is because some of the organic acid groups are incorporated, replacing some of the phosphate ions that, typically, would have been in the as-prepared material. BET surface areas of the as-prepared HA samples were 264, 195 and 113 m^2g^{-1}. While surface modified VPA-HA (vinylphosphonic acid) and MA-HA (methacrylic acid synthesised at the same conditions as pure HA possessed surface areas of 254, 247, 210 m^2g^{-1} and 265, 244 and 221 m^2g^{-1}, at reaction temperatures of 60, 70 and 80°C, respectively. This fact is attributed to the growth restriction of HA nanoparticles in the presence of surface modified agents and the smooth increase in surface area at various selected temperatures. These fine, highly dispersed nanoparticles contain reactive groups on their surfaces; therefore they have a great range of potential dental / biomedical applications.

Poor radiopacity of dental materials is an issue, since radiopaque dental materials are advantageous in making diagnosis and monitoring existing restoration. However, there is still a lack of dental material that is tooth coloured, minimally invasive and has satisfactory radiopacity. In this study on dental restorative materials containing surface grafted CaHA and surface grafted Sr and Ba-HA (no calcium), it was found that Sr-HA appeared to be a better radiopaque filler when it was mixed as a composite with a polymeric matrix. The *in vitro* biocompatibility study was also carried out on selected metal phosphates made via a novel CPFS. Cell toxicity analyses confirmed the biocompatiblity of these materials. The combined cell observations indicate that high surface area nanosized materials have the potential to be used for biomedical applications where bone regeneration or replacement is required.

The work presented in this thesis has shown that a wide range of nanomaterials can be produced using a CPFS reactor system. The properties of the precipitated nanoproduct depended on the temperature, concentration, pH and other precipitation conditions such as variation in Ca:P ratio and residence time. It was observed that by tuning the reaction parameters, products of any required particle size (ranging from 20-150 nm) and surface area (ranging from 95-300 m^2g^{-1}) can be produced using a CPFS system.

In closing, the CPFS system is a versatile and useful tool for the synthesis of pure, ion-substituted and surface-grafted group 2 metal phosphates with tailorable properties such as composition, particle size, and surface area. With these unique features, the products obtained possess a substantially superior high temperature stability (e.g., hydroxyapatite stable up to 1200°C can be synthesised because it is stoichiometric with a Ca:P ratio of 1.67) with remarkably high surface area (up to 264 m^2g^{-1}) and small particle size (typically 20 nm) compared to that reported in the literature. These high surface area materials (i.e., nanoparticles) are novel and have a great range of applications for use in replacement of living hard tissues, such as bone and teeth; as bone graft substitutes, injectables, coatings on metallic implants, as fillers or additives in commercial products, such as toothpastes; materials for the controlled release of drugs or other controlled release therapies, reinforcements in biomedical composites, and in bone and dental cements.

Chapter 10
Future Work

It has been shown that continuous plastic flow synthesis (CPFS) is a useful technique for the production of phase-pure, ion-substituted and surface-functionalised hydroxyapatite, and other group 2 metal phosphate nanoparticles produced in this thesis for a wide range of applications. The majority of the methods described in literature for the production of nanosized HA powders and other nanobioceramics were multi-step, inconsistent, energy intensive or time consuming and almost always required very careful control over reaction pH during the mixing of two or more reagents. For room temperature batch syntheses, failure to permit enough maturation time for the reagents gives a non-stoichiometric as-prepared powder, which then phase separates upon heat-treatment, which can badly affect biological properties *in vivo*. The key benefits of the use of high temperature routes for the continuous production of HA and its variants had already been identified and described in the existing literature. We also recognised the limitations of the process, namely that the continuous hydrothermal flow synthesis process uses high temperatures and pressures to generate bioceramics which are likely to be contaminated with metals from the reactors at levels that far exceed those than would be acceptable for use in clinical applications. The difficulties associated with working at high system pressures limited applications of this process for future work. Furthermore, many of the particle sizes obtained in such reactors are not particularly small and, indeed, are very similar to those obtained using more conventional synthesis methods. Smaller particles would open up and improve many applications, such as a more rapid dissolution (due to higher surface area) or use as a hard filler for bone replacement. Therefore, there was an aim to produce smaller nano-sized calcium phosphates using methods which permit fine control over particle sizes, preferably under relatively mild conditions of temperature and pressure, and with a purity acceptable for use in a clinical setting, such as for bone replacement.

This thesis has evaluated many of these aspects and applied the concept of a simple continuous plastic flow synthesis (CPFS) reactor to the rapid production (over a period of a few minutes) of phase-pure stoichiometric HA at (near) ambient conditions (60-80°C), and at atmospheric pressure. In this new flow system, aqueous solutions of

calcium nitrate tetrahydrate and diammonium hydrogen phosphate were mixed and heated for a residence time of five minutes at a pH in the range of 10-11. It was observed that particle properties could be altered, e.g, particle size and shape, by varying conditions including bath temperature, reaction pH, reaction time in flow and Ca:P ratio [Patent Filed, UK Patent Application No. 1317747.2].

In the early chapters of this thesis, a variety of phase-pure, high surface area group 2 metal phosphates were presented using continuous flow reactor followed by ion-substituted, surface-grafted and composite formation reaction towards the end chapters. A large area of the future work, underlined by the work presented in Chapters 7 and 8, aimed at the introduction of a surface modified agent and formation of nanocomposites materials using different surface-functionalised agents on the particle surface would be useful to investigate further. It would be beneficial to study the effect of different solvents on particle dispersion and colloidal stability. Similarly, an investigation into the large scale synthesis of nanoparticles modified with different chemical agents would also be of interest from a commercialisation point of view.

Furthermore, these high surface area HA products will be utilised to make porous scaffolds by freeze casting process through the addition of polyvinyl alcohol (PVA) as a binder and emulsifying agent. The purpose of study is to enhance the mechanical strength of HA for applications in bone tissue engineering. It would be interesting to perform reactions at different reaction pH to obtain different HA morphologies.

An area of materials chemistry that would be useful to investigate further is the use of nanoparticles made by CPFS in porous scaffold and surface coatings for bone tissue engineering / replacement applications. As mentioned previously, HA obtained from CPFS reactor is phase-pure, thermally stable up to 1200 °C, and has a tremendously high surface area, which makes it a suitable candidate for high temperature coatings, e.g., spray coating etc., in future applications.

The combined-cell observations indicate that high surface area nanosized HA rods, made via CPFS, were biocompatible and would have the potential to be used for biomedical applications where bone regeneration / replacement is required. Future work will address the ability of the CPFS nano-HA to support osteogenic differentiation.

Importantly, by using a flow system like this, the presented work is readily scalable and thus has promise for the large scale production of bioceramics.

The scale-up of a continuous plastic flow reactor has been recently designed for the large scale production of these nanobioceramics (Kg/hr) and will be in use soon. The scaled up reactions would be beneficial as there is high demand for these nanobioceramics as potential bone substitute materials, especially in countries with high rates of accidents or natural disasters. Thus the process has the potential to offer high purity HA as medical device for hospitals / orthopaedic surgery and research field. The world's top medical companies [Baxter (UK), Accentus (UK) and Polysciences (USA)] and hospitals are in collaboration with this project. By following HA ISO-Standards for sterilisation and packaging, further steps can be taken towards the commercialisation of this product.

Additionally, the highly dispersed, high surface area, very small size of calcium phosphate bioceramics made via CPFS would open up new horizons in dental / biomedical applications such as injectables, coatings on metallic implants, fillers or additives in commercial products, such as toothpastes; materials for the controlled release of drugs or other controlled release therapies, reinforcements in biomedical composites, and in bone and dental cements.

References

Afshar, A., Ghorbani, M., Ehsani, N., Saeri, M. & Sorrell, C. 2003. Some important factors in the wet precipitation process of hydroxyapatite. *Materials & Design,* 24**,** 197-202.

Ahn, E. S., Gleason, N. J., Nakahira, A. & Ying, J. Y. 2001. Nanostructure processing of hydroxyapatite-based bioceramics. *Nano Letters,* 1**,** 149-153.

Albee, F. H. 1920. Studies in bone growth: triple calcium phosphate as a stimulus to osteogenesis. *Annals of surgery,* 71**,** 32.

Albrektsson, T., Brånemark, P., Hansson, H.-A., Kasemo, B., Larsson, K., Lundström, I., McQueen, D. H. & Skalak, R. 1983. The interface zone of inorganic implantsIn vivo: Titanium implants in bone. *Annals of biomedical engineering,* 11**,** 1-27.

Andres-Verges, M., Fernandez-Gonzalez, C. & Martinez-Gallego, M. 1998. Hydrothermal synthesis of calcium deficient hydroxyapatites with controlled size and homogeneous morphology. *Journal of the European Ceramic Society,* 18**,** 1245-1250.

Andronescu, E., Ficai, M., Voicu, G., Ficai, D., Maganu, M. & Ficai, A. 2010. Synthesis and characterization of collagen/hydroxyapatite: magnetite composite material for bone cancer treatment. *Journal of Materials Science: Materials in Medicine,* 21**,** 2237-2242.

Aoki, H. 1991. *Science and medical applications of hydroxyapatite*, Ishiyaku Euroamerica.

Arce, H., Montero, M. L., Sáenz, A. & Castaño, V. M. 2004. Effect of pH and temperature on the formation of hydroxyapatite at low temperatures by decomposition of a Ca–EDTA complex. *Polyhedron,* 23**,** 1897-1901.

Arcıis, R. W., López-Macipe, A., Toledano, M., Osorio, E., Rodríguez-Clemente, R., Murtra, J., Fanovich, M. A. & Pascual, C. D. 2002. Mechanical properties of visible light-cured resins reinforced with hydroxyapatite for dental restoration. *Dental Materials,* 18**,** 49-57.

Arends, J., Christoffersen, J., Christoffersen, M., Eckert, H., Fowler, B., Heughebaert, J., Nancollas, G., Yesinowski, J. & Zawacki, S. 1987. A calcium hydroxyapatite precipitated from an aqueous solution: An international multimethod analysis. *Journal of Crystal Growth,* 84**,** 515-532.

Balla, V. K., Bodhak, S., Bose, S. & Bandyopadhyay, A. 2010. Porous tantalum structures for bone implants: fabrication, mechanical and in vitro biological properties. *Acta biomaterialia,* 6**,** 3349-3359.

Barralet, J., Best, S. & Bonfield, W. 1998. Carbonate substitution in precipitated hydroxyapatite: an investigation into the effects of reaction temperature and bicarbonate ion concentration. *Journal of biomedical materials research,* 41**,** 79-86.

Bertoni, E., Bigi, A., Cojazzi, G., Gandolfi, M., Panzavolta, S. & Roveri, N. 1998. Nanocrystals of magnesium and fluoride substituted hydroxyapatite. *Journal of inorganic biochemistry,* 72**,** 29-35.

Besra, L. & Liu, M. 2007. A review on fundamentals and applications of electrophoretic deposition (EPD). *Progress in materials science,* 52**,** 1-61.

Bianco, A., Cacciotti, I., Lombardi, M. & Montanaro, L. 2009. Si-substituted hydroxyapatite nanopowders: synthesis, thermal stability and sinterability. *Materials Research Bulletin,* 44**,** 345-354.

Bigi, A., Boanini, E., Capuccini, C. & Gazzano, M. 2007. Strontium-substituted hydroxyapatite nanocrystals. *Inorganica Chimica Acta,* 360**,** 1009-1016.

Bigi, A., Falini, G., Foresti, E., Ripamonti, A., Gazzano, M. & Roveri, N. 1993. Magnesium influence on hydroxyapatite crystallization. *Journal of Inorganic Biochemistry,* 49**,** 69-78.

Bigi, A., Falini, G., Gazzano, M., Roveri, N. & Tedesco, E. Structural refinements of strontium substituted hydroxylapatites. Materials Science Forum, 1998. Trans Tech Publ, 814-819.

Blake, G., Zivanovic, M., McEwan, A. & Ackery, D. 1986. Sr-89 therapy: strontium kinetics in disseminated carcinoma of the prostate. *European journal of nuclear medicine,* 12**,** 447-454.

Blumenthal, N. C. 1989. Mechanisms of inhibition of calcification. *Clinical orthopaedics and related research,* 247**,** 279-289.

Boccaccini, A. R. & Zhitomirsky, I. 2002. Application of electrophoretic and electrolytic deposition techniques in ceramics processing. *Current Opinion in Solid State and Materials Science,* 6**,** 251-260.

Bohner, M. 2000. Calcium orthophosphates in medicine: from ceramics to calcium phosphate cements. *Injury,* 31**,** D37-D47.

Bonfield, W., Wang, M. & Tanner, K. 1998. Interfaces in analogue biomaterials. *Acta Materialia,* 46**,** 2509-2518.

Borum-Nicholas, L. & Wilson, O. 2003. Surface modification of hydroxyapatite. Part I. Dodecyl alcohol. *Biomaterials,* 24**,** 3671-3679.

Borum, L. & Wilson, O. 2003. Surface modification of hydroxyapatite. Part II. Silica. *Biomaterials,* 24**,** 3681-3688.

Botelho, C., Brooks, R., Best, S., Lopes, M., Santos, J., Rushton, N. & Bonfield, W. 2006. Human osteoblast response to silicon-substituted hydroxyapatite. *Journal of Biomedical Materials Research Part A,* 79**,** 723-730.

Bozhevolnov, V. E., Komarov, V. F., Melikhov, I. V., Minaev, V. V., Orlov, A. Y. & Rudin, V. N. 2007. Method for producing nano-sized crystalline hydroxyapatite. Google Patents.

Burnell, J. M., Teubner, E. J. & Miller, A. G. 1980. Normal maturational changes in bone matrix, mineral, and crystal size in the rat. *Calcified tissue international,* 31**,** 13-19.

Byrappa, K. & Adschiri, T. 2007. Hydrothermal technology for nanotechnology. *Progress in Crystal Growth and Characterization of Materials,* 53**,** 117-166.

Canalis, E., Hott, M., Deloffre, P., Tsouderos, Y. & Marie, P. 1996. The divalent strontium salt S12911 enhances bone cell replication and bone formation in vitro. *Bone,* 18**,** 517-523.

Cao, J. M., Feng, J., Deng, S. G., Chang, X., Wang, J., Liu, J. S., Lu, P., Lu, H. X., Zheng, M. B. & Zhang, F. 2005. Microwave-assisted solid-state synthesis of hydroxyapatite nanorods at room temperature. *Journal of materials science,* 40**,** 6311-6313.

Cao, W. & Hench, L. L. 1996. Bioactive materials. *Ceramics international,* 22**,** 493-507.

Carlisle, E. M. 1970. Silicon: a possible factor in bone calcification. *Science,* 167**,** 279-280.

Carlisle, E. M. 1982. The nutritional essentiality of silicon. *Nutrition reviews,* 40**,** 193-198.

Casaletto, M., Kaciulis, S., Mattogno, G., Mezzi, A., Ambrosio, L. & Branda, F. 2002. XPS characterization of biocompatible hydroxyapatite–polymer coatings. *Surface and interface analysis,* 34**,** 45-49.

Charriere, E., Terrazzoni, S., Pittet, C., Mordasini, P., Dutoit, M., Lemaıtre, J. & Zysset, P. 2001. Mechanical characterization of brushite and hydroxyapatite cements. *Biomaterials,* 22**,** 2937-2945.

Chaudhry, A. A., Goodall, J., Vickers, M., Cockcroft, J. K., Rehman, I., Knowles, J. C. & Darr, J. A. 2008. Synthesis and characterisation of magnesium substituted calcium

phosphate bioceramic nanoparticles made via continuous hydrothermal flow synthesis. *Journal of Materials Chemistry,* 18**,** 5900-5908.

Chaudhry, A. A., Haque, S., Kellici, S., Boldrin, P., Rehman, I., Khalid, F. A. & Darr, J. A. 2006. Instant nano-hydroxyapatite: a continuous and rapid hydrothermal synthesis. *Chemical communications***,** 2286-2288.

Chaudhry, A. A., Knowles, J. C., Rehman, I. & Darr, J. A. 2012a. Rapid hydrothermal flow synthesis and characterisation of carbonate-and silicate-substituted calcium phosphates. *Journal of Biomaterials Applications*.

Chaudhry, A. A., Knowles, J. C., Rehman, I. & Darr, J. A. 2013. Rapid hydrothermal flow synthesis and characterisation of carbonate-and silicate-substituted calcium phosphates. *Journal of biomaterials applications,* 28**,** 448-461.

Chaudhry, A. A., Yan, H., Gong, K., Inam, F., Viola, G., Reece, M. J., Goodall, J., McNeil-Watson, F. K., Corbett, J. C. & Knowles, J. C. 2011. High-strength nanograined and translucent hydroxyapatite monoliths via continuous hydrothermal synthesis and optimized spark plasma sintering. *Acta biomaterialia,* 7**,** 791-799.

Chaudhry, A. A., Yan, H., Viola, G., Reece, M. J., Knowles, J. C., Gong, K., Rehman, I. & Darr, J. A. 2012b. Phase stability and rapid consolidation of hydroxyapatite–zirconia nano-coprecipitates made using continuous hydrothermal flow synthesis. *Journal of biomaterials applications*, 27**,** 79-90.

Chen, C.-W., Oakes, C. S., Byrappa, K., Riman, R. E., Brown, K., TenHuisen, K. S. & Janas, V. F. 2004. Synthesis, characterization, and dispersion properties of hydroxyapatite prepared by mechanochemical–hydrothermal methods. *J. Mater. Chem.,* 14**,** 2425-2432.

Chen, L., Yu, Q., Wang, Y. & Li, H. 2011. BisGMA/TEGDMA dental composite containing high aspect-ratio hydroxyapatite nanofibers. *Dental Materials,* 27**,** 1187-1195.

Chen, Q. Z., Thompson, I. D. & Boccaccini, A. R. 2006. 45S5 Bioglass< sup>®</sup>-derived glass–ceramic scaffolds for bone tissue engineering. *Biomaterials,* 27**,** 2414-2425.

Chevalier, J. 2006. What future for zirconia as a biomaterial? *Biomaterials,* 27**,** 535-543.

Choi, H. W., Lee, H. J., Kim, K. J., Kim, H.-M. & Lee, S. C. 2006. Surface modification of hydroxyapatite nanocrystals by grafting polymers containing phosphonic acid groups. *Journal of colloid and interface science,* 304**,** 277-281.

Costescu, A., Pasuk, I., Ungureanu, F., Dinischiotu, A., Costache, M., Huneau, F., Galaup, S., Coustumer, P. L. & Predoi, D. 2010a. Physico-chemical properties of nano-sized hexagonal hydroxyapatite powder synthesized by sol-gel. *Digest Journal of Nanomaterials & Biostructures (DJNB),* 5.

Costescu, A., Pasuk, I., Ungureanu, F., Dinischiotu, A., Costache, M., Huneau, F., Galaup, S., Le Coustumer, P. & Predoi, D. 2010b. Physico-chemical properties of nano-sized hexagonal hydroxyapatite powder synthesized by sol-gel. *Digest Journal of Nanomaterials and Biostructures,* 5**,** 989-1000.

Covaliu, I., Georgescu, G., Jitaru, I., Neamtu, J., Malaeru, T., Oprea, O. & Patroi, E. 2009. Synthesis and characterization of a hydroxyapatite coated magnetite for potential cancer treatment. *Rev Chim,* 60**,** 1254-1257.

Cushing, B. L., Kolesnichenko, V. L. & O'Connor, C. J. 2004. Recent advances in the liquid-phase syntheses of inorganic nanoparticles. *Chemical reviews,* 104**,** 3893-3946.

D'Andre, S. C. & Fadeev, A. Y. 2003. Covalent surface modification of calcium hydroxyapatite using n-alkyl-and n-fluoroalkylphosphonic acids. *Langmuir,* 19**,** 7904-7910.

Dahl, S., Allain, P., Marie, P., Mauras, Y., Boivin, G., Ammann, P., Tsouderos, Y., Delmas, P. & Christiansen, C. 2001. Incorporation and distribution of strontium in bone. *Bone,* 28**,** 446-453.

Darr, J., Guo, Z., Raman, V., Bououdina, M. & Rehman, I. 2004. Metal organic chemical vapour deposition (MOCVD) of bone mineral like carbonated hydroxyapatite coatings. *Chemical communications***,** 696-697.

Darr, J. A. & Poliakoff, M. 1999. New directions in inorganic and metal-organic coordination chemistry in supercritical fluids. *Chemical Reviews,* 99**,** 495-542.

de Groot, K. 1983. *Bioceramics of calcium phosphate,* CRC.

Dey, A., Mukhopadhyay, A. K., Gangadharan, S., Sinha, M. K. & Basu, D. 2009. Weibull modulus of nano-hardness and elastic modulus of hydroxyapatite coating. *Journal of materials science,* 44**,** 4911-4918.

Dislich, H. 1986. Sol-gel: science, processes and products. *Journal of non-crystalline solids,* 80**,** 115-121.

Domingo, C., Arcís, R., Osorio, E., Osorio, R., Fanovich, M. A., Rodríguez-Clemente, R. & Toledano, M. 2003. Hydrolytic stability of experimental hydroxyapatite-filled dental composite materials. *Dental Materials,* 19**,** 478-486.

Donadel, K., Laranjeira, M., Gonçalves, V. L., Fávere, V. T., De Lima, J. C. & Prates, L. H. 2005. Hydroxyapatites Produced by Wet-Chemical Methods. *Journal of the American Ceramic Society,* 88**,** 2230-2235.

Dong, L., Zhu, Z., Qiu, Y. & Zhao, J. 2010. Removal of lead from aqueous solution by hydroxyapatite/magnetite composite adsorbent. *Chemical Engineering Journal,* 165**,** 827-834.

Dorozhkin, S. V. 2000. Solid-state transformation of a non-stoichiometric calcium deficient apatite into the biphasic calcium phosphate. *Key Engineering Materials,* 192**,** 155-158.

Dorozhkin, S. V. 2009. Nanodimensional and nanocrystalline apatites and other calcium orthophosphates in biomedical engineering, biology and medicine. *Materials,* 2**,** 1975-2045.

Ducheyne, P., Radin, S. & King, L. 1993. The effect of calcium phosphate ceramic composition and structure on in vitro behavior. I. Dissolution. *Journal of biomedical materials research,* 27**,** 25-34.

Elliott, J. C. 1994. *Structure and chemistry of the apatites and other calcium orthophosphates,* Elsevier Amsterdam.

Fadeev, I., Shvorneva, L., Barinov, S. & Orlovskii, V. 2003. Synthesis and structure of magnesium-substituted hydroxyapatite. *Inorganic materials,* 39**,** 947-950.

Famery, R., Richard, N. & Boch, P. 1994. Preparation of α-and β-tricalcium phosphate ceramics, with and without magnesium addition. *Ceramics International,* 20**,** 327-336.

Fathi, M. & Doostmohammadi, A. 2009. Bioactive glass nanopowder and bioglass coating for biocompatibility improvement of metallic implant. *Journal of materials processing technology,* 209**,** 1385-1391.

Ferreira, A., Oliveira, C. & Rocha, F. 2003. The different phases in the precipitation of dicalcium phosphate dihydrate. *Journal of crystal growth,* 252**,** 599-611.

Fidancevska, E., Ruseska, G., Bossert, J., Lin, Y.-M. & Boccaccini, A. R. 2007. Fabrication and characterization of porous bioceramic composites based on hydroxyapatite and titania. *Materials chemistry and physics,* 103**,** 95-100.

Fratzl, P., Fratzl-Zelman, N., Klaushofer, K., Vogl, G. & Koller, K. 1991. Nucleation and growth of mineral crystals in bone studied by small-angle X-ray scattering. *Calcified tissue international,* 48**,** 407-413.

Fratzl, P., Gupta, H., Paschalis, E. & Roschger, P. 2004. Structure and mechanical quality of the collagen–mineral nano-composite in bone. *Journal of Materials Chemistry,* 14**,** 2115-2123.

Fu, G., Vary, P. S. & Lin, C.-T. 2005. Anatase TiO2 nanocomposites for antimicrobial coatings. *The Journal of Physical Chemistry B,* 109**,** 8889-8898.

Fulmer, M. T., Ison, I. C., Hankermayer, C. R., Constantz, B. R. & Ross, J. 2002. Measurements of the solubilities and dissolution rates of several hydroxyapatites. *Biomaterials,* 23**,** 751-755.

Geffcken, W. & Berger, E. 1939. German Patent 736,411. May.

Getman, E., Loboda, S., Ignatov, A. & Demchenko, P. 2004. Carbonate-containing barium hydroxyapatite synthesized by solid state reactions. *Polish journal of chemistry,* 78**,** 35-43.

Giannini, M., Soares, C. J. & de Carvalho, R. M. 2004. Ultimate tensile strength of tooth structures. *Dental Materials,* 20**,** 322-329.

Gibson, I., Best, S. & Bonfield, W. 1999. Chemical characterization of silicon-substituted hydroxyapatite. *Journal of Biomedical Materials Research,* 44**,** 422-428.

Gibson, I. R., Best, S. M. & Bonfield, W. 2002. Effect of silicon substitution on the sintering and microstructure of hydroxyapatite. *Journal of the American Ceramic Society,* 85**,** 2771-2777.

Ginebra, M., Driessens, F. & Planell, J. 2004. Effect of the particle size on the micro and nanostructural features of a calcium phosphate cement: a kinetic analysis. *Biomaterials,* 25**,** 3453-3462.

Gloria, A., Russo, T., D'Amora, U., Zeppetelli, S., D'Alessandro, T., Sandri, M., Banobre-Lopez, M., Piñeiro-Redondo, Y., Uhlarz, M. & Tampieri, A. 2013. Magnetic poly (ε-caprolactone)/iron-doped hydroxyapatite nanocomposite substrates for advanced bone tissue engineering. *Journal of The Royal Society Interface,* 10**,** 20120833.

Gruar, R. I., Tighe, C. J. & Darr, J. A. 2013. Scaling-up a confined jet reactor for the continuous hydrothermal manufacture of nanomaterials. *Industrial & Engineering Chemistry Research,* 52**,** 5270-5281.

Grynpas, M., Hamilton, E., Cheung, R., Tsouderos, Y., Deloffre, P., Hott, M. & Marie, P. 1996. Strontium increases vertebral bone volume in rats at a low dose that does not induce detectable mineralization defect. *Bone,* 18**,** 253-259.

Güler, H., Gündoğmaz, G., Kurtuluş, F., Çelik, G. & Gacanoğlu, Ş. 2011. Solid state synthesis of calcium borohydroxyapatite. *Solid State Sciences,* 13**,** 1916-1920.

Guo, X. & Xiao, P. 2006. Effects of solvents on properties of nanocrystalline hydroxyapatite produced from hydrothermal process. *Journal of the European Ceramic Society,* 26**,** 3383-3391.

Haque, S., Rehman, I. & Darr, J. A. 2007. Synthesis and characterization of grafted nanohydroxyapatites using functionalized surface agents. *Langmuir,* 23**,** 6671-6676.

Hayashi, K., Uenoyama, K., Matsuguchi, N. & Sugioka, Y. 1991. Quantitative analysis of in vivo tissue responses to titanium-oxide-and hydroxyapatite-coated titanium alloy. *Journal of biomedical materials research,* 25**,** 515-523.

Heavens, S. 1990. Electrophoretic deposition as a processing route for ceramics. *Noyes Publications, Advanced Ceramic Processing and Technology.,* 1**,** 255-283.

Hench, L. 1993. Bioceramics: from concept to clinic. *American Ceramic Society Bulletin,* 72**,** 93-98.

Hench, L. 2000. (ii) The challenge of orthopaedic materials. *Current orthopaedics,* 14**,** 7-15.

Hench, L. L. 1991. Bioceramics: from concept to clinic. *Journal of the American Ceramic Society,* 74**,** 1487-1510.

Hench, L. L. 1998a. Bioactive materials: the potential for tissue regeneration. *Journal of biomedical materials research,* 41**,** 511-518.

Hench, L. L. 1998b. Biomaterials: a forecast for the future. *Biomaterials,* 19**,** 1419-1423.

Hench, L. L. & West, J. K. 1990. The sol-gel process. *Chemical Reviews,* 90**,** 33-72.

Hench, L. L. & Wilson, J. 1993. *An introduction to bioceramics,* World Scientific.

Heness, G. & Ben-Nissan, B. 2004. Innovative bioceramics.

Hing, K. A., Revell, P. A., Smith, N. & Buckland, T. 2006. Effect of silicon level on rate, quality and progression of bone healing within silicate-substituted porous hydroxyapatite scaffolds. *Biomaterials,* 27**,** 5014-5026.

Hlady, V. & Füredi-Milhofer, H. 1979. Adsorption of human serum albumin on precipitated hydroxyapatite. *Journal of Colloid and Interface Science,* 69**,** 460-468.

Hongqin, X., Duilin, W., Zhe, J., Xiaowei, L., Shouwei, Z., Yan, L. & Cheng, C. 2012. Kinetic and thermodynamic sorption study of radiocobalt by magnetic hydroxyapatite nanoparticles. *Journal of Radioanalytical and Nuclear Chemistry,* 292**,** 637-647.

Hutchens, S. A., Benson, R. S., Evans, B. R., O'Neill, H. M. & Rawn, C. J. 2006. Biomimetic synthesis of calcium-deficient hydroxyapatite in a natural hydrogel. *Biomaterials,* 27**,** 4661-4670.

Iqbal, N., Nazir, R., Asif, A., Chaudhry, A. A., Akram, M., Fan, G. Y., Akram, A., Amin, R., Park, S. H. & Hussain, R. 2012. Electrophoretic deposition of PVA coated hydroxyapatite on 316L stainless steel. *Current Applied Physics,* 12**,** 755-759.

Ito, A., Maekawa, K., Tsutsumi, S., Ikazaki, F. & Tateishi, T. 1997. Solubility product of OH-carbonated hydroxyapatite. *Journal of biomedical materials research,* 36**,** 522-528.

Johannsen, M., Gneveckow, U., Eckelt, L., Feussner, A., Waldöfner, N., Scholz, R., Deger, S., Wust, P., Loening, S. & Jordan, A. 2005. Clinical hyperthermia of prostate cancer using magnetic nanoparticles: presentation of a new interstitial technique. *International Journal of Hyperthermia,* 21**,** 637-647.

Jokanović, V., Izvonar, D., Dramićanin, M., Jokanović, B., Živojinović, V., Marković, D. & Dačić, B. 2006. Hydrothermal synthesis and nanostructure of carbonated calcium hydroxyapatite. *Journal of Materials Science: Materials in Medicine,* 17**,** 539-546.

Jokanović, V. & Uskoković, D. 2005. Calcium hydroxyapatite thin films on titanium substrates prepared by ultrasonic spray pyrolysis.

Jones, F. 2001. Teeth and bones: applications of surface science to dental materials and related biomaterials. *Surface Science Reports,* 42**,** 75-205.

Joshi, V. S. & Joshi, M. J. 2003. FTIR spectroscopic, thermal and growth morphological studies of calcium hydrogen phosphate dihydrate crystals. *Crystal Research and Technology,* 38**,** 817-821.

Kaminski, E. J., Oglesby, R. J., Wood, N. K. & Sandrik, J. 1968. The behavior of biological materials at different sites of implantation. *Journal of biomedical materials research,* 2**,** 81-88.

Kannan, S. & Ferreira, J. 2006. Synthesis and thermal stability of hydroxyapatite-β-tricalcium phosphate composites with cosubstituted sodium, magnesium, and fluorine. *Chemistry of materials,* 18**,** 198-203.

Kannan, S., Lemos, I., Rocha, J. & Ferreira, J. 2005. Synthesis and characterization of magnesium substituted biphasic mixtures of controlled hydroxyapatite/< i> β</i>-tricalcium phosphate ratios. *Journal of Solid State Chemistry,* 178**,** 3190-3196.

Katti, K. S. 2004. Biomaterials in total joint replacement. *Colloids and Surfaces B: Biointerfaces,* 39**,** 133-142.

Khan, A., Ahmed, Z., Edirisinghe, M., Wong, F. & Rehman, I. 2008. Preparation and characterization of a novel bioactive restorative composite based on covalently coupled polyurethane–nanohydroxyapatite fibres. *Acta Biomaterialia,* 4**,** 1275-1287.

Kikuchi, M., Yamazaki, A., Otsuka, R., Akao, M. & Aoki, H. 1994. Crystal structure of Sr-substituted hydroxyapatite synthesized by hydrothermal method. *Journal of Solid State Chemistry,* 113**,** 373-378.

Kim, H., Miyaji, F., Kokubo, T. & Nakamura, T. 1997. Effect of heat treatment on apatite-forming ability of Ti metal induced by alkali treatment. *Journal of Materials Science: Materials in Medicine,* 8**,** 341-347.

Kim, S., Lee, J., Kim, Y., Riu, D.-H., Jung, S., Lee, Y., Chung, S. & Kim, Y. 2003. Synthesis of Si, Mg substituted hydroxyapatites and their sintering behaviors. *Biomaterials,* 24**,** 1389-1398.

Kim, S., Ryu, H.-S., Shin, H., Jung, H. S. & Hong, K. S. 2005. In situ observation of hydroxyapatite nanocrystal formation from amorphous calcium phosphate in calcium-rich solutions. *Materials Chemistry and Physics,* 91**,** 500-506.

Kimura, I. 2007. Synthesis of hydroxyapatite by interfacial reaction in a multiple emulsion. *Advances in Materials Science and Engineering,* 2007.

Klein, C., Driessen, A., De Groot, K. & Van Den Hooff, A. 1983. Biodegradation behavior of various calcium phosphate materials in bone tissue. *Journal of biomedical materials research,* 17**,** 769-784.

Klein, C. P., de Blieck-Hogemrst, J., Wolket, J. & De Groot, K. 1990. Studies of the solubility of different calcium phosphate ceramic particles< i> in vitro</i>. *Biomaterials,* 11**,** 509-512.

Kohri, M., Miki, K., Waite, D. E., Nakajima, H. & Okabe, T. 1993. < i> In vitro</i> stability of biphasic calcium phosphate ceramics. *Biomaterials,* 14**,** 299-304.

Konishi, K., Maehara, T., Kamimori, T., Aono, H., Naohara, T., Kikkawa, H., Watanabe, Y. & Kawachi, K. 2004. Heating ferrite powder with AC magnetic field for thermal coagulation therapy. *Journal of magnetism and magnetic materials,* 272**,** 2428-2429.

Kothapalli, C., Wei, M., Legeros, R. & Shaw, M. 2005. Influence of temperature and aging time on HA synthesized by the hydrothermal method. *Journal of Materials Science: Materials in Medicine,* 16**,** 441-446.

Koumoulidis, G. C., Katsoulidis, A. P., Ladavos, A. K., Pomonis, P. J., Trapalis, C. C., Sdoukos, A. T. & Vaimakis, T. C. 2003. Preparation of hydroxyapatite via microemulsion route. *Journal of colloid and interface science,* 259**,** 254-260.

Kühl, G. & Nebergall, W. H. 1963. Hydrogenphosphat-und Carbonatapatite. *Zeitschrift für anorganische und allgemeine Chemie,* 324**,** 313-320.

Kumar, M., Dasarathy, H. & Riley, C. 1999. Electrodeposition of brushite coatings and their transformation to hydroxyapatite in aqueous solutions. *Journal of biomedical materials research,* 45**,** 302-310.

Kundu, B., Lemos, A., Soundrapandian, C., Sen, P., Datta, S., Ferreira, J. & Basu, D. 2010a. Development of porous HAp and β-TCP scaffolds by starch consolidation with foaming method and drug-chitosan bilayered scaffold based drug delivery system. *Journal of Materials Science: Materials in Medicine,* 21**,** 2955-2969.

Kundu, B., Soundrapandian, C., Nandi, S. K., Mukherjee, P., Dandapat, N., Roy, S., Datta, B. K., Mandal, T. K., Basu, D. & Bhattacharya, R. N. 2010b. Development of new localized drug delivery system based on ceftriaxone-sulbactam composite drug impregnated porous hydroxyapatite: a systematic approach for in vitro and in vivo animal trial. *Pharmaceutical research,* 27**,** 1659-1676.

Kuo, M. & Yen, S. 2002. The process of electrochemical deposited hydroxyapatite coatings on biomedical titanium at room temperature. *Materials Science and Engineering: C,* 20**,** 153-160.

Kurzweg, H., Heimann, R., Troczynski, T. & Wayman, M. 1998. Development of plasma-sprayed bioceramic coatings with bond coats based on titania and zirconia. *Biomaterials,* 19**,** 1507-1511.

Lacefield, W. R. 1988. Hydroxyapatite coatings. *Annals of the New York academy of sciences,* 523**,** 72-80.

Laing, P. G., Ferguson, A. B. & Hodge, E. S. 1967. Tissue reaction in rabbit muscle exposed to metallic implants. *Journal of biomedical materials research,* 1**,** 135-149.

Landis, W. & Martin, J. 1984. X-ray photoelectron spectroscopy applied to gold-decorated mineral standards of biological interest. *Journal of Vacuum Science & Technology A,* 2**,** 1108-1111.

Lee, B.-H., Kim, Y. D. & Lee, K. H. 2003. XPS study of bioactive graded layer in Ti–In–Nb–Ta alloy prepared by alkali and heat treatments. *Biomaterials,* 24**,** 2257-2266.

LeGeros, R. Variability of HAP/b-TCP ratios in sintered apatites. Journal Of Dental Research, 1986. Amer Assoc Dental Research 1619 Duke St, Alexandria, VA 22314, 292-292.

LeGeros, R. Z. 1990. Calcium phosphates in oral biology and medicine. *Monographs in oral science,* 15**,** 1-201.

Lemaitre, J. 1995. Injectable calcium phosphate hydraulic cements: new developments and potential applications. *Innovation et technologie en biologie et médecine,* 16**,** 109-120.

Lemaitre, J., Mirtchi, A. & Mortier, A. 1987. Calcium phosphate cements for medical use: state of the art and perspectives of development. *Silicates industriels,* 52**,** 141-146.

Leventouri, T., Bunaciu, C. & Perdikatsis, V. 2003. Neutron powder diffraction studies of silicon-substituted hydroxyapatite. *Biomaterials,* 24**,** 4205-4211.

Li-yun, C., Chuan-bo, Z. & Jian-feng, H. 2005. Influence of temperature,[Ca^{2+}], Ca/P ratio and ultrasonic power on the crystallinity and morphology of hydroxyapatite nanoparticles prepared with a novel ultrasonic precipitation method. *Materials Letters,* 59**,** 1902-1906.

Li, B., Liao, X., Zheng, L., He, H., Wang, H., Fan, H. & Zhang, X. 2012. Preparation and cellular response of porous A-type carbonated hydroxyapatite nanoceramics. *Materials Science and Engineering: C,* 32**,** 929-936.

Li, H., Khor, K. & Cheang, P. 2002. Titanium dioxide reinforced hydroxyapatite coatings deposited by high velocity oxy-fuel (HVOF) spray. *Biomaterials,* 23**,** 85-91.

Li, Z., Lam, W., Yang, C., Xu, B., Ni, G., Abbah, S., Cheung, K., Luk, K. & Lu, W. 2007. Chemical composition, crystal size and lattice structural changes after incorporation of strontium into biomimetic apatite. *Biomaterials,* 28**,** 1452-1460.

Lim, G., Wang, J., Ng, S., Chew, C. & Gan, L. 1997. Processing of hydroxyapatite via microemulsion and emulsion routes. *Biomaterials,* 18**,** 1433-1439.

Linde, D. 1991. 1992. CRC Handbook of Chemistry and Physics. CRC Press, Boca Raton, Ann Arbor, Boston.

Liu, C., Huang, Y., Shen, W. & Cui, J. 2001a. Kinetics of hydroxyapatite precipitation at pH 10 to 11. *Biomaterials,* 22**,** 301-306.

Liu, D.-M., Troczynski, T. & Tseng, W. J. 2001b. Water-based sol–gel synthesis of hydroxyapatite: process development. *Biomaterials,* 22**,** 1721-1730.

Liu, J., Ye, X., Wang, H., Zhu, M., Wang, B. & Yan, H. 2003. The influence of pH and temperature on the morphology of hydroxyapatite synthesized by hydrothermal method. *Ceramics International,* 29**,** 629-633.

Liu, Y., Zhong, H., Li, L. & Zhang, C. 2010. Temperature dependence of magnetic property and photocatalytic activity of Fe_3O_4/hydroxyapatite nanoparticles. *Materials Research Bulletin,* 45**,** 2036-2039.

López-Quintela, M. A. & Rivas, J. 1993. Chemical reactions in microemulsions: a powerful method to obtain ultrafine particles. *Journal of colloid and interface science,* 158**,** 446-451.

López, T., Ortiz, E., Quintana, P. & González, R. 2007. A nanostructured titania bioceramic implantable device capable of drug delivery to the temporal lobe of the brain. *Colloids and Surfaces A: Physicochemical and Engineering Aspects,* 300**,** 3-10.

Loste, E., Fraile, J., Fanovich, M. A., Woerlee, G. F. & Domingo, C. 2004. Anhydrous supercritical carbon dioxide method for the controlled silanization of inorganic nanoparticles. *Advanced Materials,* 16**,** 739-744.

Lu, A. H., Salabas, E. e. L. & Schüth, F. 2007. Magnetic nanoparticles: synthesis, protection, functionalization, and application. *Angewandte Chemie International Edition,* 46**,** 1222-1244.

Lu, H. B., Campbell, C. T., Graham, D. J. & Ratner, B. D. 2000. Surface characterization of hydroxyapatite and related calcium phosphates by XPS and TOF-SIMS. *Analytical chemistry,* 72**,** 2886-2894.

Lu, J., Descamps, M., Dejou, J., Koubi, G., Hardouin, P., Lemaitre, J. & Proust, J. P. 2002. The biodegradation mechanism of calcium phosphate biomaterials in bone. *Journal of biomedical materials research,* 63**,** 408-412.

Lu, M.-D. & Yang, S.-M. 2005. Syntheses of polythiophene and titania nanotube composites. *Synthetic metals,* 154**,** 73-76.

Lu, X., Wang, Y.-b., Wang, J.-x., Qu, S.-x., Weng, J., Xin, R.-l. & Leng, Y. 2006. Calcium phosphate crystal growth under controlled environment through urea hydrolysis. *Journal of crystal growth,* 297**,** 396-402.

Lynn, A. & Bonfield, W. 2005. A novel method for the simultaneous, titrant-free control of pH and calcium phosphate mass yield. *Accounts of chemical research,* 38**,** 202-207.

Ma, M., Wu, Y., Zhou, J., Sun, Y., Zhang, Y. & Gu, N. 2004. Size dependence of specific power absorption of Fe_3O_4 particles in AC magnetic field. *Journal of Magnetism and Magnetic Materials,* 268**,** 33-39.

Mahabole, M., Aiyer, R., Ramakrishna, C., Sreedhar, B. & Khairnar, R. 2005. Synthesis, characterization and gas sensing property of hydroxyapatite ceramic. *Bulletin of Materials Science,* 28**,** 535-545.

Manafi, S. A. & Joughehdoust, S. 2009. Synthesis of hydroxyapatite nanostructure by hydrothermal condition for biomedical application. *Iran J. Pharm,* 5**,** 89.

Manicone, P. F., Rossi Iommetti, P. & Raffaelli, L. 2007. An overview of zirconia ceramics: basic properties and clinical applications. *Journal of dentistry,* 35**,** 819-826.

Marie, P., Ammann, P., Boivin, G. & Rey, C. 2001. Mechanisms of action and therapeutic potential of strontium in bone. *Calcified tissue international,* 69**,** 121-129.

Marie, P. J. 2005. Strontium as therapy for osteoporosis. *Current opinion in pharmacology,* 5**,** 633-636.

Marti, A. 2000. Inert bioceramics (Al_2O_3, $ZrO_2$for medical application. *Injury,* 31**,** D33-D36.

Martin, R. & Burr, D. 1989. The structure, function and adaptation of cortical bone. *Raven, New York.*

Martin, R. I. & Brown, P. W. 1997. Phase equilibria among acid calcium phosphates. *Journal of the American Ceramic Society,* 80**,** 1263-1266.

Mastrogiacomo, M., Muraglia, A., Komlev, V., Peyrin, F., Rustichelli, F., Crovace, A. & Cancedda, R. 2005. Tissue engineering of bone: search for a better scaffold. *Orthodontics & craniofacial research,* 8**,** 277-284.

Mayer, I., Schlam, R. & Featherstone, J. 1997. Magnesium-containing carbonate apatites. *Journal of inorganic biochemistry,* 66**,** 1-6.

McEwan, A. Unsealed source therapy of painful bone metastases: an update. Seminars in nuclear medicine, 1997. Elsevier, 165-182.

Miao, S., Weng, W., Cheng, K., Du, P., Shen, G., Han, G. & Zhang, S. 2005. Sol–gel preparation of Zn-doped fluoridated hydroxyapatite films. *Surface and Coatings Technology,* 198**,** 223-226.

Mirtchi, A. A., Lemaitre, J. & Terao, N. 1989. Calcium phosphate cements: study of the β-tricalcium phosphate—monocalcium phosphate system. *Biomaterials,* 10**,** 475-480.

Murakami, S., Hosono, T., Jeyadevan, B., Kamitakahara, M. & Ioku, K. 2008. Hydrothermal synthesis of magnetite/hydroxyapatite composite material for hyperthermia therapy for bone cancer. *Nippon seramikkusu kyokai gakujutsu ronbunshi,* 116**,** 950-954.

Murugan, R. & Ramakrishna, S. 2006. Production of ultra-fine bioresorbable carbonated hydroxyapatite. *Acta Biomaterialia,* 2**,** 201-206.

Nakahira, A., Karatani, C. & Nishida, S. 2004. Evaluation of cadmium removal in solution using various hydroxyapatites and cattle bone. *Phosphorus Research Bulletin,* 17**,** 148-152.

Nakahira, A., Okajima, T., Honma, T., Yoshioka, S. & Tanaka, I. 2006. Arsenic removal by hydroxyapatite-based ceramics. *Chemistry Letters,* 35**,** 856-857.

Narasaraju, T. & Phebe, D. 1996. Some physico-chemical aspects of hydroxylapatite. *Journal of Materials Science,* 31**,** 1-21.

Nazir, R., Samad Khan, A., Ahmed, A., Ur-Rehman, A., Anwar Chaudhry, A., Ur Rehman, I. & Wong, F. S. 2013. Synthesis and< i> in-vitro</i> cytotoxicity analysis of microwave irradiated nano-apatites. *Ceramics International,* 39**,** 4339-4347.

Ngankam, P., Schaaf, P., Voegel, J. & Cuisinier, F. 1999. Heterogeneous nucleation of calcium phosphate salts at a solid/liquid interface examined by scanning angle reflectometry. *Journal of crystal growth,* 197**,** 927-938.

Nilsson, M., Fernandez, E., Sarda, S., Lidgren, L. & Planell, J. 2002. Characterization of a novel calcium phosphate/sulphate bone cement. *Journal of biomedical materials research,* 61**,** 600-607.

Nishikawa, H. 2003. Surface changes and radical formation on hydroxyapatite by UV irradiation for inducing photocatalytic activation. *Journal of Molecular Catalysis A: Chemical,* 206**,** 331-338.

Nonami, T., Taoda, H., Hue, N. T., Watanabe, E., Iseda, K., Tazawa, M. & Fukaya, M. 1998. Apatite Formation on TiO_2 Photocatalyst Film in a Pseudo Body Solution. *Materials research bulletin,* 33**,** 125-131.

Norhidayu, D., Sopyan, I. & Ramesh, S. Development of Zinc doped hydroxyapatite for bone implant applications. International Conference on Construction and Building Technology, 2008.

O'Donnell, M., Fredholm, Y., De Rouffignac, A. & Hill, R. 2008. Structural analysis of a series of strontium-substituted apatites. *Acta biomaterialia,* 4**,** 1455-1464.

Okayama, S., Akao, M., Nakamura, S., Shin, Y., Higashikata, M. & Aoki, H. 1991. The mechanical properties and solubility of strontium-substituted hydroxyapatite. *Bio-medical materials and engineering,* 1**,** 11-17.

Oonishi, H. 1991. Orthopaedic applications of hydroxyapatite. *Biomaterials,* 12**,** 171-178.

Oonishi, H., Kushitani, S., Yasukawa, E., Iwaki, H., Hench, L. L., Wilson, J., Tsuji, E. & Sugihara, T. 1997. Particulate bioglass compared with hydroxyapatite as a bone graft substitute. *Clinical orthopaedics and related research,* 334**,** 316-325.

Paital, S. R. & Dahotre, N. B. 2009. Calcium phosphate coatings for bio-implant applications: materials, performance factors, and methodologies. *Materials Science and Engineering: R: Reports,* 66**,** 1-70.

Paital, S. R., He, W. & Dahotre, N. B. 2010. Laser pulse dependent micro textured calcium phosphate coatings for improved wettability and cell compatibility. *Journal of Materials Science: Materials in Medicine,* 21**,** 2187-2200.

Pan, Y., Huang, J.-L. & Shao, C. 2003. Preparation of β-TCP with high thermal stability by solid reaction route. *Journal of materials science,* 38**,** 1049-1056.

Pang, Y. & Bao, X. 2003. Influence of temperature, ripening time and calcination on the morphology and crystallinity of hydroxyapatite nanoparticles. *Journal of the European Ceramic Society,* 23**,** 1697-1704.

Panzavolta, S., Torricelli, P., Sturba, L., Bracci, B., Giardino, R. & Bigi, A. 2008. Setting properties and in vitro bioactivity of strontium-enriched gelatin–calcium phosphate bone cements. *Journal of Biomedical Materials Research Part A,* 84**,** 965-972.

Pasteris, J. D., Wopenka, B. & Valsami-Jones, E. 2008. Bone and tooth mineralization: Why apatite? *Elements,* 4**,** 97-104.

Patel, N., Best, S., Bonfield, W., Gibson, I., Hing, K., Damien, E. & Revell, P. 2002. A comparative study on the in vivo behavior of hydroxyapatite and silicon substituted hydroxyapatite granules. *Journal of Materials Science: Materials in Medicine,* 13**,** 1199-1206.

Penel, G., Leroy, G., Rey, C. & Bres, E. 1998. MicroRaman spectral study of the PO4 and CO3 vibrational modes in synthetic and biological apatites. *Calcified Tissue International,* 63**,** 475-481.

Phillips, M., Darr, J., Luklinska, Z. & Rehman, I. 2003. Synthesis and characterization of nano-biomaterials with potential osteological applications. *Journal of Materials Science: Materials in Medicine,* 14**,** 875-882.

Porter, A., Patel, N., Skepper, J., Best, S. & Bonfield, W. 2003. Comparison of in vivo dissolution processes in hydroxyapatite and silicon-substituted hydroxyapatite bioceramics. *Biomaterials,* 24**,** 4609-4620.

Porter, A. E. 2006. Nanoscale characterization of the interface between bone and hydroxyapatite implants and the effect of silicon on bone apposition. *Micron,* 37**,** 681-688.

Prabakaran, K., Kannan, S. & Rajeswari, S. 2005. Development and characterisation of zirconia and hydroxyapatite composites for orthopaedic applications. *Trends Biomater Artif Organs,* 18**,** 114-6.

Pushpakanth, S., Srinivasan, B., Sreedhar, B. & Sastry, T. 2008. An in situ approach to prepare nanorods of titania–hydroxyapatite (TiO< sub> 2</sub>–HAp) nanocomposite

by microwave hydrothermal technique. *Materials Chemistry and Physics,* 107**,** 492-498.

Puvvada, N., Panigrahi, P. K. & Pathak, A. 2010. Room temperature synthesis of highly hemocompatible hydroxyapatite, study of their physical properties and spectroscopic correlation of particle size. *Nanoscale,* 2**,** 2631-2638.

Radin, S. & Ducheyne, P. 1993. The effect of calcium phosphate ceramic composition and structure on in vitro behavior. II. Precipitation. *Journal of biomedical materials research,* 27**,** 35-45.

Raynaud, S., Champion, E., Bernache-Assollant, D. & Thomas, P. 2002. Calcium phosphate apatites with variable Ca/P atomic ratio I. Synthesis, characterisation and thermal stability of powders. *Biomaterials,* 23**,** 1065-1072.

Redey, S., Razzouk, S., Rey, C., Bernache-Assollant, D., Leroy, G., Nardin, M. & Cournot, G. 1999. Osteoclast adhesion and activity on synthetic hydroxyapatite, carbonated hydroxyapatite, and natural calcium carbonate: relationship to surface energies. *Journal of biomedical materials research,* 45**,** 140-147.

Redey, S. A., Nardin, M., Bernache–Assolant, D., Rey, C., Delannoy, P., Sedel, L. & Marie, P. J. 2000. Behavior of human osteoblastic cells on stoichiometric hydroxyapatite and type A carbonate apatite: role of surface energy. *Journal of biomedical materials research,* 50**,** 353-364.

Rehman, I. & Bonfield, W. 1997. Characterization of hydroxyapatite and carbonated apatite by photo acoustic FTIR spectroscopy. *Journal of Materials Science: Materials in Medicine,* 8**,** 1-4.

Rey, C., Collins, B., Goehl, T., Dickson, I. & Glimcher, M. 1989. The carbonate environment in bone mineral: a resolution-enhanced Fourier transform infrared spectroscopy study. *Calcified tissue international,* 45**,** 157-164.

Rey, C., Renugopalakrishman, V., Collins, B. & Glimcher, M. J. 1991. Fourier transform infrared spectroscopic study of the carbonate ions in bone mineral during aging. *Calcified tissue international,* 49**,** 251-258.

Rho, J.-Y., Kuhn-Spearing, L. & Zioupos, P. 1998. Mechanical properties and the hierarchical structure of bone. *Medical engineering & physics,* 20**,** 92-102.

Riman, R. E., Suchanek, W. L., Byrappa, K., Chen, C.-W., Shuk, P. & Oakes, C. S. 2002. Solution synthesis of hydroxyapatite designer particulates. *Solid State Ionics,* 151**,** 393-402.

Rodrıguez-Lorenzo, L., Vallet-Regı, M. & Ferreira, J. 2001. Fabrication of hydroxyapatite bodies by uniaxial pressing from a precipitated powder. *Biomaterials,* 22**,** 583-588.

Rodríguez-Lorenzo, L., Vallet-Regı, M. & Ferreira, J. 2001. Fabrication of hydroxyapatite bodies by uniaxial pressing from a precipitated powder. *Biomaterials,* 22**,** 583-588.

Roop Kumar, R. & Wang, M. 2001. Biomimetic deposition of hydroxyapatite on brushite single crystals grown by the gel technique. *Materials Letters,* 49**,** 15-19.

Ryan, G., Pandit, A. & Apatsidis, D. P. 2006. Fabrication methods of porous metals for use in orthopaedic applications. *Biomaterials,* 27**,** 2651-2670.

Sadat-Shojai, M., Atai, M., Nodehi, A. & Khanlar, L. N. 2010. Hydroxyapatite nanorods as novel fillers for improving the properties of dental adhesives: synthesis and application. *dental materials,* 26**,** 471-482.

Safronova, T., Reshotka, D., Putlyaev, V., Lukin, E. & Ivanov, V. 2009. Phase composition of powdered material based on calcium hydroxyapatite and sodium dihydrophosphate. *Glass and Ceramics,* 66**,** 293-296.

Saito, M., Maruoka, A., Mori, T., Sugano, N. & Hino, K. 1994. Experimental studies on a new bioactive bone cement: hydroxyapatite composite resin. *Biomaterials,* 15**,** 156-160.

Sarig, S. 2004. Aspartic acid nucleates the apatite crystallites of bone: a hypothesis. *Bone,* 35**,** 108-113.

Sarkar, P. & Nicholson, P. S. 1996. Electrophoretic deposition (EPD): mechanisms, kinetics, and application to ceramics. *Journal of the American Ceramic Society,* 79**,** 1987-2002.

Schaad, P., Thomann, J.-M., Voegel, J.-C. & Gramain, P. 1994. Adsorption of neutral and anionic polyacrylamides on hydroxyapatite and human enamel: influence on the dissolution kinetics. *Journal of colloid and interface science,* 164**,** 291-295.

Serre, C., Papillard, M., Chavassieux, P., Voegel, J. & Boivin, G. 1998. Influence of magnesium substitution on a collagen–apatite biomaterial on the production of a calcifying matrix by human osteoblasts. *Journal of biomedical materials research,* 42**,** 626-633.

Singh, S., Singh, V., Aggarwal, S. & Mandal, U. K. 2010. Synthesis of brushite nanoparticles at different temperatures. *Chemical Papers,* 64**,** 491-498.

Sivakumar, G., Girija, E., Narayana Kalkura, S. & Subramanian, C. 1998. Crystallization and characterization of calcium phosphates: brushite and monetite. *Crystal Research and Technology,* 33**,** 197-205.

Skytte Sørensen, J. & Lundager Madsen, H. E. 2000. The influence of magnetism on precipitation of calcium phosphate. *Journal of crystal growth,* 216**,** 399-406.

Stöber, W., Fink, A. & Bohn, E. Colloid Interface Sci. 1968, 26, 62. *CrossRef, Web of Science® Times Cited,* 3225.

Stoch, A., Brożek, A., Kmita, G., Stoch, J., Jastrzebski, W. & Rakowska, A. 2001. Electrophoretic coating of hydroxyapatite on titanium implants. *Journal of Molecular Structure,* 596**,** 191-200.

Suchanek, W. & Yoshimura, M. 1998. Processing and properties of hydroxyapatite-based biomaterials for use as hard tissue replacement implants. *Journal of Materials Research,* 13**,** 94-117.

Suchanek, W. L., Byrappa, K., Shuk, P., Riman, R. E., Janas, V. F. & TenHuisen, K. S. 2004a. Mechanochemical-hydrothermal synthesis of calcium phosphate powders with coupled magnesium and carbonate substitution. *Journal of Solid State Chemistry,* 177**,** 793-799.

Suchanek, W. L., Byrappa, K., Shuk, P., Riman, R. E., Janas, V. F. & TenHuisen, K. S. 2004b. Preparation of magnesium-substituted hydroxyapatite powders by the mechanochemical–hydrothermal method. *Biomaterials,* 25**,** 4647-4657.

Sue, K., Murata, K., Kimura, K. & Arai, K. 2003. Continuous synthesis of zinc oxide nanoparticles in supercritical water. *Green Chem.,* 5**,** 659-662.

Sun, Y., Guo, G., Tao, D. & Wang, Z. 2007. Reverse microemulsion-directed synthesis of hydroxyapatite nanoparticles under hydrothermal conditions. *Journal of Physics and Chemistry of Solids,* 68**,** 373-377.

Sunada, K., Watanabe, T. & Hashimoto, K. 2003. Bactericidal activity of copper-deposited TiO2 thin film under weak UV light illumination. *Environmental science & technology,* 37**,** 4785-4789.

Sygnatowicz, M. & Tiwari, A. 2009. Controlled synthesis of hydroxyapatite-based coatings for biomedical application. *Materials Science and Engineering: C,* 29**,** 1071-1076.

Tampieri, A., D'Alessandro, T., Sandri, M., Sprio, S., Landi, E., Bertinetti, L., Panseri, S., Pepponi, G., Goettlicher, J. & Bañobre-López, M. 2012. Intrinsic magnetism and hyperthermia in bioactive Fe-doped hydroxyapatite. *Acta biomaterialia,* 8**,** 843-851.

Tanaka, H., Futaoka, M. & Hino, R. 2004. Surface modification of calcium hydroxyapatite with pyrophosphoric acid. *Journal of colloid and interface science,* 269**,** 358-363.

Tanaka, H., Futaoka, M., Hino, R., Kandori, K. & Ishikawa, T. 2005. Structure of synthetic calcium hydroxyapatite particles modified with pyrophosphoric acid. *Journal of colloid and interface science,* 283**,** 609-612.

Tang, R., Hass, M., Wu, W., Gulde, S. & Nancollas, G. H. 2003. Constant composition dissolution of mixed phases: II. Selective dissolution of calcium phosphates. *Journal of colloid and Interface Science,* 260**,** 379-384.

Tang, X. L., Xiao, X. F. & Liu, R. F. 2005. Structural characterization of silicon-substituted hydroxyapatite synthesized by a hydrothermal method. *Materials Letters,* 59**,** 3841-3846.

Tas, A. C. & Bhaduri, S. B. Preparation of Brushite Powders and their in Vitro Conversion to Nanoapatites. Bioceramics: Materials and Applications V: Proceedings of the 106th Annual Meeting of The American Ceramic Society, Indianapolis, Indiana, USA 2004, Ceramic Transactions, 2005. Wiley-American Ceramic Society, 119.

Teo, B. K., Li, C., Sun, X., Wong, N. & Lee, S. 2003. Silicon-silica nanowires, nanotubes, and biaxial nanowires: inside, outside, and side-by-side growth of silicon versus silica on zeolite. *Inorganic chemistry,* 42**,** 6723-6728.

Thamaraiselvi, T. & Rajeswari, S. 2004. Biological evaluation of bioceramic materials-a review. *Carbon,* 24**,** 172.

Theiss, F., Apelt, D., Brand, B., Kutter, A., Zlinszky, K., Bohner, M., Matter, S., Frei, C., Auer, J. A. & Von Rechenberg, B. 2005. Biocompatibility and resorption of a brushite calcium phosphate cement. *Biomaterials,* 26**,** 4383-4394.

Thian, E., Huang, J., Best, S., Barber, Z. & Bonfield, W. 2006a. Novel silicon-doped hydroxyapatite (Si-HA) for biomedical coatings: An in vitro study using acellular simulated body fluid. *Journal of Biomedical Materials Research Part B: Applied Biomaterials,* 76**,** 326-333.

Thian, E., Huang, J., Best, S., Barber, Z. & Bonfield, W. 2007. Silicon-substituted hydroxyapatite: The next generation of bioactive coatings. *Materials Science and Engineering: C,* 27**,** 251-256.

Thian, E. S., Huang, J., Best, S. M., Barber, Z. H., Brooks, R. A., Rushton, N. & Bonfield, W. 2006b. The response of osteoblasts to nanocrystalline silicon-substituted hydroxyapatite thin films. *Biomaterials,* 27**,** 2692-2698.

Thompson, I. & Hench, L. 1998. Mechanical properties of bioactive glasses, glass-ceramics and composites. *Proceedings of the Institution of Mechanical Engineers, Part H: Journal of Engineering in Medicine,* 212**,** 127-136.

Vallet-Regi, M. & González-Calbet, J. M. 2004. Calcium phosphates as substitution of bone tissues. *Progress in Solid State Chemistry,* 32**,** 1-31.

Van der Biest, O. O. & Vandeperre, L. J. 1999. Electrophoretic deposition of materials. *Annual Review of Materials Science,* 29**,** 327-352.

Van Landuyt, P., Peter, B., Beluze, L. & Lemaitre, J. 1999. Reinforcement of osteosynthesis screws with brushite cement. *Bone,* 25**,** 95S-98S.

Vega, E. D., Narda, G. E. & Ferretti, F. H. 2003. Adsorption of citric acid from dilute aqueous solutions by hydroxyapatite. *Journal of colloid and interface science,* 268**,** 37-42.

Vereecke, G. & Lemaître, J. 1990. Calculation of the solubility diagrams in the system $Ca(OH)_2$-H_3PO_4-KOH-HNO_3 CO_2H_2O. *Journal of Crystal Growth,* 104**,** 820-832.

Wang, X. 2011. Preparation of magnetic hydroxyapatite and their use as recyclable adsorbent for phenol in wastewater. *CLEAN–Soil, Air, Water,* 39**,** 13-20.

Wang, Y., Chen, L., Yang, H., Guo, Q., Zhou, W. & Tao, M. 2010. Large-area self assembled monolayers of silica microspheres formed by dip coating. *Materials Science (0137-1339),* 28.

Wang, Y., Zhang, S., Wei, K., Zhao, N., Chen, J. & Wang, X. 2006a. Hydrothermal synthesis of hydroxyapatite nanopowders using cationic surfactant as a template. *Materials Letters,* 60**,** 1484-1487.

Wang, Y. J., Lai, C., Wei, K., Chen, X., Ding, Y. & Wang, Z. L. 2006b. Investigations on the formation mechanism of hydroxyapatite synthesized by the solvothermal method. *Nanotechnology,* 17**,** 4405.

Waters, N. Some mechanical and physical properties of teeth. Symposia of the Society for experimental Biology, 1979. 99-135.

Webster, T. J., Ergun, C., Doremus, R. H., Siegel, R. W. & Bizios, R. 2000. Enhanced functions of osteoblasts on nanophase ceramics. *Biomaterials,* 21**,** 1803-1810.

Wei, G. & Ma, P. X. 2004. Structure and properties of nano-hydroxyapatite/polymer composite scaffolds for bone tissue engineering. *Biomaterials,* 25**,** 4749-4757.

Wei, M., Ruys, A., Milthorpe, B., Sorrell, C. & Evans, J. 2001. Electrophoretic deposition of hydroxyapatite coatings on metal substrates: a nanoparticulate dual-coating approach. *Journal of Sol-Gel Science and Technology,* 21**,** 39-48.

Weiner, S. & Wagner, H. D. 1998. The material bone: structure-mechanical function relations. *Annual Review of Materials Science,* 28**,** 271-298.

Willems, G., Lambrechts, P., Braem, M., Celis, J.-P. & Vanherle, G. 1992. A classification of dental composites according to their morphological and mechanical characteristics. *Dental Materials,* 8**,** 310-319.

Wu, C., Chang, J., Wang, J., Ni, S. & Zhai, W. 2005. Preparation and characteristics of a calcium magnesium silicate (bredigite) bioactive ceramic. *Biomaterials,* 26**,** 2925-2931.

Wu, H.-C., Wang, T.-W., Sun, J.-S., Wang, W.-H. & Lin, F.-H. 2007. A novel biomagnetic nanoparticle based on hydroxyapatite. *Nanotechnology,* 18**,** 165601.

Wu, W. & Nancollas, G. H. 1998. Kinetics of heterogeneous nucleation of calcium phosphates on anatase and rutile surfaces. *Journal of colloid and interface science,* 199**,** 206-211.

Wu, Y., Hench, L. L., Du, J., Choy, K. L. & Guo, J. 2004. Preparation of hydroxyapatite fibers by electrospinning technique. *Journal of the American Ceramic Society,* 87**,** 1988-1991.

Xie, J., Riley, C., Kumar, M. & Chittur, K. 2002. FTIR/ATR study of protein adsorption and brushite transformation to hydroxyapatite. *Biomaterials,* 23**,** 3609-3616.

Yang, Z.-p., Gong, X.-y. & Zhang, C.-j. 2010. Recyclable Fe_3O_4/hydroxyapatite composite nanoparticles for photocatalytic applications. *Chemical Engineering Journal,* 165**,** 117-121.

Yang, Z., Jiang, Y., xin Yu, L., Wen, B., Li, F., Sun, S. & Hou, T. 2005. Preparation and characterization of magnesium doped hydroxyapatite–gelatin nanocomposite. *Journal of Materials Chemistry,* 15**,** 1807-1811.

Yano, T., Budiyanto, K., Yoshida, K. & Iseki, T. 1998. Fabrication of silicon carbide fiber-reinforced silicon carbide composite by hot-pressing. *Fusion engineering and design,* 41**,** 157-163.

Yasukawa, A., Ouchi, S., Kandori, K. & Ishikawa, T. 1996. Preparation and characterization of magnesium–calcium hydroxyapatites. *J. Mater. Chem.,* 6**,** 1401-1405.

Yoshida, K., Kondo, N., Kita, H., Mitamura, M., Hashimoto, K. & Toda, Y. 2005. Effect of Substitutional Monovalent and Divalent Metal Ions on Mechanical Properties of β-Tricalcium Phosphate. *Journal of the American Ceramic Society,* 88**,** 2315-2318.

Zaffe, D. 2005. Some considerations on biomaterials and bone. *Micron,* 36**,** 583-592.

Zdrenþu, L., Mihãilescu, I., Socol, G. & Lojkowski, W. 2004. Biocompatibility of hydroxyl-apatite thin films obtained by pulsed laser deposition. *Rev. Adv. Mater. Sci,* 8**,** 164-169.

Zhang, F., Zheng, Z., Chen, Y., Liu, X., Chen, A. & Jiang, Z. 1998. In vivo investigation of blood compatibility of titanium oxide films. *Journal of biomedical materials research,* 42**,** 128-133.

Zhang, X. & Vecchio, K. S. 2007. Hydrothermal synthesis of hydroxyapatite rods. *Journal of Crystal Growth,* 308**,** 133-140.

Zhang, Z., Goodall, J. B., Brown, S., Karlsson, L., Clark, R. J., Hutchison, J. L., Rehman, I. & Darr, J. A. 2010. Continuous hydrothermal synthesis of extensive 2D sodium titanate (Na2Ti3O7) nano-sheets. *Dalton Transactions,* 39**,** 711-714.

Zhitomirsky, I. & Gal-Or, L. 1997. Electrophoretic deposition of hydroxyapatite. *Journal of Materials Science: Materials in Medicine,* 8**,** 213-219.

Zhou, Z.-H., Zhou, P.-L., Yang, S.-P., Yu, X.-B. & Yang, L.-Z. 2007. Controllable synthesis of hydroxyapatite nanocrystals via a dendrimer-assisted hydrothermal process. *Materials research bulletin,* 42**,** 1611-1618.

Zhu, K., Yanagisawa, K., Shimanouchi, R., Onda, A. & Kajiyoshi, K. 2006. Preferential occupancy of metal ions in the hydroxyapatite solid solutions synthesized by hydrothermal method. *Journal of the European Ceramic Society,* 26**,** 509-513.

Zioupos, P. & Rogers, K. D. 2006. Complementary physical and mechanical techniques to characterise tooth: a bone-like tissue. *Journal of Bionic Engineering,* 3**,** 19-31.

Zyman, Z., Tkachenko, M., Epple, M., Polyakov, M. & Naboka, M. 2006. Magnesium-substituted hydroxyapatite ceramics. *Materialwissenschaft und Werkstofftechnik,* 37**,** 474-477.